Universidade do Minho
Escola de Ciências

Daniel António da Silva Miranda

Optimizing performance of rechargeable lithium-ion batteries through computer simulations

fevereiro de 2017

Optimizing performance of rechargeable lithium-ion batteries through computer simulations

Daniel António da Silva Miranda

UMinho | 2017

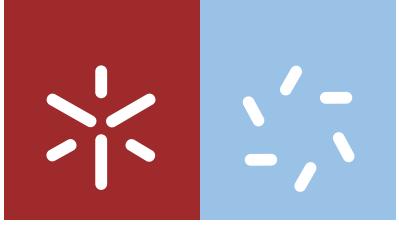

Universidade do Minho
Escola de Ciências

Daniel António da Silva Miranda

Optimizing performance of rechargeable lithium-ion batteries through computer simulations

Tese de Doutoramento em Ciências
Especialidade em Física

Trabalho efetuado sob a orientação do
Professor Doutor António Mário Lourenço da Fonseca Almeida

do
Professor Doutor Senentxu Lanceros-Méndez

e da
Professora Doutora Maria Manuela da Silva Pires da Siva

fevereiro de 2017

STATEMENT OF INTEGRITY

I hereby declare having conducted my thesis with integrity. I confirm that I have not used plagiarism or any form of falsification of results in the process of the thesis elaboration.

I further declare that I have fully acknowledged the Code of Ethical Conduct of the University of Minho.

University of Minho, 7 February, 2017

Full name:
Daniel António da Silva Miranda

Signature:
Daniel António da Silva Miranda

To my parents for everything

To my wife and my daughter for existing

"Não existem sonhos impossíveis para aqueles que realmente acreditam que o poder realizador reside no interior de cada ser humano. Sempre que alguém descobre esse poder, algo antes considerado impossível, se torna realidade."

Albert Einstein

Acknowledgements

To my supervisor Professor Mário Almeida, I appreciate the opportunity to work with him, all transmitted scientific knowledge and friendship built over the years of working together.

To my co-supervisors Professor Senentxu Lancers-Méndez and Maria Manuela Silva, thank you for all the support and helping me whenever I needed.

To my friend Carlos Costa for his availability and support.

To all the colleagues of the ESM group who helped me and encouraged. I have only these words: thank you very much.

To my family and friends who directly or indirectly contributed to this work and are not mentioned.

To my Parents, António and Rosa, my brother Francisco, my wife Vânia and my daughter Maria, my parents in law Ilda and Artur for all that signify to me: my strength to live.

Abstract

There is an increasing need for larger battery autonomy and performance related to rapid technological advances in portable electronic products such as mobile-phones, computers, e-labels, e-packaging and disposable medical testers, among others.

The advantages of lithium-ion batteries in comparison to other battery types, such as Ni-Cd ones, are the fact of being lighter and cheaper, showing high energy density (between 100 and 150 Wh kg^{-1}) and a large number of charge/discharge cycles.

The key issues for improving lithium-ion battery performance are specific energy, power, safety and reliability. Typically, the performance of a battery is optimized for either power or energy density through the improvement of electrodes and separator materials.

Computer simulations of battery performance are important and critical for optimizing materials and geometries. Models have been developed considering the physical-chemical properties of the materials to be used as electrodes and separators, the choice of the most suitable organic solvents for electrolytes, the geometry and dimensions of the components that make up the battery as well as the porosity of the electrodes.

The objective of the present work was the optimization of lithium-ion battery performance through computer simulations based on the Doyle/Fuller/Newman model for separators, electrodes (anode and cathode) and full/half-cells in order to understand the main processes that affect battery performance.

Thus, along this work, simulations were developed to improve the performance of a lithium-ion batteries. Thus, simulation of the different battery components (separator and electrodes) were developed. The first simulation explores the influence of the geometrical parameters of the separator (porosity, turtuosity and separator thickness) in the performance of the battery. Then, the optimal relationship between active material, binder and conductive additive for lithium-ion battery cathode was studied. Further, a simulation of an interdigitated battery was performed, where the effect of the number, thickness and the length of the digits on the delivered battery capacity was evaluated. Finally, different conventional and unconventional geometries were evaluated taking into account their suitability for different applications without and with consideration of

different thermal conditions. The different thermal conditions included isothermal, adiabatic, cold, regular and hot conditions.

In relation to the separator, it was observed that its ionic conductivity depends on the value of the Bruggeman coefficient, which is related to the degree of porosity and tortuosity of the membrane. It was determined that the optimal value of the degree of porosity is above 50% and the separator thickness should range between 1 μm and 32 μm for improved battery performance.

For the electrodes, it is shown that optimization of the electrode formulation is independent of the active material type but depends on the minimum value of n, defined as the percentage of binder content /percentage of conductive material, depending also on the discharge rate.

The influence of different geometries, including conventional, interdigitated, horseshoe, spiral, ring, antenna and gear, in the performance of lithium-ion batteries was analyzed and the delivered capacity depends on geometrical parameters such as the maximum distance that ions move until occurs intercalation process, the distance between the current collectors and the thickness of the separator and the electrodes.

For interdigitated structures, the delivered capacity of the battery increases with increasing the number of digits as well as with increasing thickness and length of the digits.

Finally, the influence of the thermal behavior on battery performance was evaluated for the aforementioned geometries under different conditions, isothermal, adiabatic, cold, regular and hot conditions. The gear and interdigitated batteries presented the highest delivery capacity at all thermal conditions.

In conclusion, in order to improve the performance of lithium ion batteries, it is necessary optimize the geometric parameters of the separator, the percentages of binder, active material and conductive additive in the cathode, as well as the battery geometry (conventional, interdigitated and unconventional geometries) at different thermal conditions.

Resumo

Nos dias de hoje, devido ao galopante avanço tecnológico, há uma crescente necessidade de maior autonomia e desempenho de baterias para uso em dispositivos eletrónicos portáteis (telemóveis, computadores, identificadores eletrónicos, embalagens eletrónicas e dispositivos médicos de diagnóstico descartáveis, etc).

As vantagens das baterias de iões de lítio, comparativamente com outros tipos de baterias tais como as de Ni-Cd, são o facto de serem mais leves e económicas, tendo elevada densidade de energia (entre 100 e 150 Wh kg^{-1}) e um elevado número de ciclos de carga/descarga.

As caraterísticas que permitem potenciar o desempenho da bateria de iões de lítio são energia específica, potência, segurança e confiabilidade. Tipicamente o desempenho de uma bateria é otimizado para uma melhor potência ou densidade de energia, o que é conseguido através da melhoria dos elétrodos e do material dos separadores.

As simulações computacionais que avaliam o desempenho das baterias são de uma enorme importância para a otimização de materiais e geometrias das mesmas. Os modelos têm sido desenvolvidos tendo em conta as propriedades físico-químicas dos materiais que são usados como elétrodos e separadores, a escolha de solventes orgânicos mais adequados para os eletrólitos, a geometria e dimensões dos componentes que constituem a bateria, assim como a porosidade dos elétrodos.

O objetivo do meu trabalho é a otimização do desempenho da bateria de iões de lítio através de simulações em computador baseadas no modelo de Doyle/Fuller/Newman para os separadores, elétrodos (ânodo e cátodo) e completas/meias-células de baterias de iões de lítio, para que se possam entender os principais processos que afetam o desempenho da bateria.

Assim, ao longo deste trabalho, foram desenvolvidas simulações para melhorar o desempenho das baterias de iões de lítio, tendo sido implementadas simulações dos diferentes componentes da bateria (separador e elétrodos). Numa primeira simulação explorou-se a influência dos parâmetros geométricos do separador (porosidade, tortuosidade e espessura do separador) no desempenho da bateria. De seguida, fez-se um estudo otimizado da relação entre o material ativo, o material ligante e o material condutor para o cátodo de uma bateria de iões de lítio. Além disso, foi realizada uma simulação de uma bateria interdigitada, onde foi avaliado o efeito do número, espessura e comprimento dos dígitos na capacidade da bateria. Finalmente foram avaliadas

diferentes geometrias convencionais e não convencionais tendo em conta a sua adequação para diferentes aplicações, considerando diferentes condições térmicas. As diferentes condições térmicas incluíram condições isotérmicas, adiabáticas, frias, regulares e quentes.

Em relação ao separador observou-se que a condutividade iónica depende do valor do coeficiente de Bruggeman, que está relacionado com o grau de porosidade e tortuosidade da membrana. Assim, foi determinado que o melhor valor para o grau de porosidade se situa acima de 50% e que a espessura do separador se deve situar entre 1 μm e 32 μm, para um melhor desempenho da bateria.

Para os elétrodos mostrou-se que a sua otimização é independente do tipo de material ativo, mas depende do valor mínimo de n, razão entre a percentagem de material ligante (C_2) e material condutor (C_3), dependendo também da taxa de descarga.

A influência das diferentes geometrias (convencional, interdigitada, ferradura, espiral, anel e roda dentada) no desempenho das baterias de iões de lítio foi analisada e o seu valor de capacidade depende de parâmetros geométricos tais como, a distância máxima que os iões se movem até que ocorra processo de intercalação, distância entre os coletores de corrente e a espessura do separador e elétrodos.

Para a geometria interdigitada a capacidade da bateria aumenta, não só com o aumento do número de dígitos, mas também com o aumento da espessura e do comprimento dos dígitos.

Por fim, a influência do comportamento térmico no desempenho da bateria sob diferentes condições (condição isotérmica, adiabática, frio, regular e quente) foi também avaliada para as diferentes geometrias. Neste aspeto, as geometrias roda dentada e interdigitada foram as que revelaram maior valor de capacidade para todas as condições térmicas.

Em conclusão, no sentido de aumentar o desempenho das baterias de iões de lítio é necessário otimizar os parâmetros geométricos do separador, as percentagens de material ligante, material ativo e material condutor no cátodo, bem como a geometria da bateria (convencional, interdigitada, e as não convencionais), para diferentes condições térmicas.

List of Symbols and Abbreviations

a	specific interfacial area, m^2/m^3
A_{aa}	area of active material in the not interdigitated part of the anode (m^2)
A_{bat}	cell cross section area, m^2
A_{cc1}	area of active material in the not interdigitated part of the cathode (m^2)
A_i	area of a given component in the battery *i*(*i* = a,s,c)
brugg	Brugg parameter in the electrodes
c_dig	digit length of the electrode, m
C_E	concentration of Li ions in the electrode, mol/m^3
C_L	concentration of Li ions in the electrolyte, mol/m^3
$C_{p,i}$	heat capacity at constant pressure of battery components *i*(*i* = a,s,c), J/(kg.K)
CNT	carbon nanotubes
C_1	percentage of the active material, %.
C_2	percentage of the binder, %.
C_3	percentage of carbon black, %.
D	diffusion coefficient of the salt in the electrolyte, m^2/s
d_cc	distance between of collectors
DEC	diethyl carbonate
D_{LI}	diffusion coefficient of Li ions in the electrode, m^2/s
d_max	maximum distance of ions from the collector positions
DMC	dimethyl carbonate
DMPU	N,N'-dimethyl propylene urea
D_1	density of the active material, g/m^3.
D_2	density of the binder, g/m^3.
D_3	density of carbon black, g/m^3.
$E_{ad,i}$	activation energy for diffusion in the electrodes *i*(*i* = a,c), J/mol
$E_{ak,i}$	activation energy for reaction in the electrodes *i*(*i* = a,c), J/mol
EC	ethylene carbonate
e_dig	digit thickness of the electrode, m
EMC	ethyl methyl carbonate
EV	electric vehicles
e_sep	separator thickness, m
F	Faraday's constant, 96487 C/mol
FEA	finite element analysis
FEM	finite element method

$f_{\pm}$	activity of the salt in the electrolyte, mol/m^3
grade GF/A	Whatman glass microfiber filters
h	heat transfer coefficient, W/(m^2.K)
HEV	hybrid electric vehicles
HOPG	highly ordered pyrolytic graphite
$\mathbf{i}_E$	current density in the electrode, A/m^2
$\mathbf{i}_L$	current density in the electrolyte, A/m^2
I_{TOTAL}	total current density, A/m^2
j_{Li^+}	pore wall flux of Li ions, mol/cm^2 s
L	width, m
L_dim	dimension of horseshoe, m
LFP	lithium iron phosphate
LMO	lithium manganese oxide
LTO	lithium titanium oxide
M	mass transport flux, mol/m^2
MCMB	mesocarbon microbeads
m_{Totalc}	total mass of cathode, g
N	number of digits for interdigitated and gear battery
NMP	N-methyl-2-pyrrolidone
ODE	ordinary differential equation
p	porosity of the separator
PAN	poly(acrylonitrile)
PC	propylene carbonate
PCM cooling	phase change materials cooling
PDA	principal differential analysis
PE	poly(ethylene)
PEO	poly(ethylene oxide)
PVDF	poly (vinylidene fluoride)
PVDF-TrFE	poly(vinylidene-co-trifluoroethylene)
PVDF-HFP	poly(vinylidene fluoride-co-hexafluoropropene)
PVDF-CTFE	poly(vinylidenefluoride-co-chlorotrifluoroethylene)
$Q_{ohmic,i}$	total ohmic heat generation rate of battery components *i* (*i* = a,s,c), W/m^3
$Q_{reaction,i}$	total reaction heat generation rate of electrodes *i* (*i* = a,c), W/m^3
$Q_{reversible}$	total reversible heat generation rate of electrodes *i* (*i* = a,c), W/m^3
$Q_{total,i}$	total heat generation rate of battery components *i* (*i* = a,s,c), W/m^3
R	reaction term of the mass balance equation, mol/m^3 s

R	gas constant, 8,314 J/mol K
r	radius of the electrode spherical particles, m
R_d	radius of ring geometry, m
R_f	film resistance, Ω m^2
R_g	radius of gear geometry, m
Super P-C45	carbon black
T	temperature, K
t	time, s
TMS	thermal management system
T∞	external temperature, K
t_+^0	transport number of the positive ions
u^0	open circuit voltage, V
V_{Totalc}	total volume of cathode, m^3
W	weight of the sample per unit area, g/m^2
1D	one dimension
2D	two dimension
3D	three dimension

Greek symbols

ε_i	porosity of the region *i* (*i* = a,s,c)
$\varepsilon_{f,i}$	volume fraction of the fillers in the electrode *i* (*i* = a,s,c)
η	over-potential, V
λ_i	thermal conductivity of battery components *i* (*i* = a,s,c), W/(m.K)
κ_l	ionic conductivity of the electrolyte, S/m
$\kappa_{ef,i}$	effective ionic conductivity of the electrolyte *i* (*i* = a,c), S/m
κ_f	effective ionic conductivity of the separator polymer film, S/m
ρ_i	density of battery components *i* (*i* = a,s,c), kg/m^3
σ	electronic conductivity of the solid phase of the electrode *i* (*i* = a,s,c), S/m
$\sigma_{ef,i}$	effective electronic conductivity of the solid phase of the electrode *i* (*i* = a,s,c), S/m
σ_{3Pure}	electronic conductivity of the carbon black (conductive material), S/m
τ	tortuosity of the separator
φ_E	potential of the electrodes, V
φ_L	potential of the electrolyte, V

ϕ_i	volume fraction of the material i (i=1, 2, 3)

Subscripts referring specific components of the battery and initial conditions

a	anode
adi	adiabatic condition
c	cathode
cc	current collector
cold	cold condition
hot	hot condition
reg	regular condition
s	separator
0	initial condition
1	active material
2	binder
3	carbon black

Table of contents

List of figures xxi
List of tables xxvii

1. Introduction 1
1.1 Introduction 3
1.1.2 Advantages and disadvantages of lithium ion batteries 5
1.1.3 Mathematical model for lithium ion batteries 7
1.1.4 Materials 9
1.1.4.1 Anode and cathode electrodes 9
1.1.4.2 Battery separator 10
1.1.5 General mathematical framework for the microscopic models of lithium-ion batteries 11
1.2 Objectives 17
1.3 Thesis structure and methodology 18
1.4 References 20

2. State of the art on microscopic theoretical models and simulations of lithium-ion rechargeable batteries 29
2.1 Microscopic modelling of lithium ion batteries 31
2.2 Simulation of the components of the battery: electrodes and separator/electrolyte 33
2.2.1 Electrodes 33
2.2.2 Separator and electrolyte 43
2.3 Thermal behavior simulation 45
2.4 Conclusions 48
2.5 References 50

3. Simulation of Lithium-ion Batteries: Methodology and Theoretical Models 55
3.1 Simulation of lithium-ion batteries 57
3.1.1 Methodology 57
3.1.2 Development and execution of the simulation 58

3.2 Theoretical models of lithium-ion batteries: Electrochemical and Thermal models 62
3.3 References 65

4. Modelling separator membranes physical characteristics for optimized lithium ion battery performance 67

4.1 Introduction 69
4.2 Theoretical model 71
4.2.1 General model 71
4.2.2 Separator 73
4.3 Parameters and simulation model 74
4.4 Results and Discussion 76
4.4.1 Effect of separator/electrolyte 76
4.4.2 Effect of the variation of separator membrane physical parameters on battery performance 78
4.4.2.1 Degree of porosity 78
4.4.2.2 Tortuosity 80
4.4.2.3 Dimension/thickness 82
4.5 Conclusions 84
4.6 References 85

5. Theoretical simulation of the optimal relationship between active material, binder and conductive additive for lithium-ion battery cathodes 89

5.1 Introduction 91
5.2 Preparation and characterization of the cathodes 92
5.3 Theoretical simulation model and model parameters 93
5.4 Results and discussion 96
5.4.1 LFP and LMO half-cells: validation of the theoretical model 96
5.4.2 Influence of the cathode components content in the performance of the half-cell 98
5.4.3 Impedance of the LFP and LMO half-cells 103
5.4.4 Electrolyte and Electrode Current Density for LFP half-cells 106
5.5 Conclusions 111
5.6 References 112

6. Computer simulation evaluation of the geometrical parameters affecting the performance of two dimensional interdigitated batteries..... 115
6.1 Introduction..... 117
6.2 Theoretical simulation model and parameters..... 119
6.3 Results..... 124
6.3.1 Conventional geometry..... 124
6.3.2 Interdigitated geometry..... 127
6.3.2.1 Influence of the number of digits at different scan rates..... 127
6.3.2.2 Influence of length and thickness of the digit..... 130
6.3.2.2.1 Influence of digit length from 60 μm to 480 μm..... 130
6.3.2.2.2 Influence of the digit thickness from 10 μm to 70 μm..... 132
6.3.2.2.3 Maximum limit for digit thickness and length at 200C and 400C..... 133
6.4. Discussion..... 136
6.5. Conclusions..... 137
6.6 References..... 138

7. Computer simulations of the influence of geometry in the performance of conventional and unconventional lithium-ion batteries..... 141
7.1 Introduction..... 143
7.2 Theoretical simulation model and specific parameters for each geometry..... 145
7.3 Results and Discussion..... 149
7.3.1 Effect of battery geometry..... 149
7.3.2 Influence of the geometrical parameters in battery performance..... 152
7.3.2.1 Effect of battery dimensions and current collector positions in the horseshoe geometry..... 152
7.3.2.1.1 Current collector positions..... 153
7.3.2.1.2. Dimensions of the battery..... 154
7.3.2.2 Influence of the radius in the ring geometry..... 157
7.3.2.3 Comparative performance of ring and gear battery geometries..... 158
7.4 Conclusions..... 163
7.5 References..... 164

8. Computer simulation of the effect of different thermal conditions in the performance of conventional and unconventional lithium-ion battery geometries.. 169
8.1 Introduction..... 171

8.2 Preparation and measurement of the full-cell 173
8.3 Theoretical model: parameters, initial values and boundary conditions 174
8.3.1 Theoretical simulation model 174
8.3.2 Specific parameters and initial values 175
8.3.3 Boundary conditions 180
8.4 Results and discussion 183
8.4.1 LiC_6/$LiFePO_4$ full-cell: Validation of the theoretical model 183
8.4.2 Battery performance of the various battery geometries at different thermal conditions 184
8.4.2.1 Isothermal condition 184
8.4.2.2 Adiabatic condition 186
8.4.2.3 Environmental conditions 188
8.4.3 Total heat at low and high discharge rates 192
8.4.4 Ohmic heat for ring geometry with different radius 197
8.5 Conclusions 203
8.6 References 204
9. Conclusions and future work 209
9.1 Conclusions 211
9.2 Future work 213

List of figures

Figure 1.1 - Battery evolution with respect to their energy density. 3
Figure 1.2 - Schematic representation of the main structure of a lithium ion battery and the process of insertion/extraction of lithium ions that occurs at the electrodes during discharge of a battery. 7
Figure 2.1 - 1C discharge voltage curve comparison between the rigorous model and the simplified model at different number of terms or node points through the Galerkin's approximation. Figure from [11]. 32
Figure 2.2 - Cell configuration (not to scale). The x-dimension corresponds to the length of the cell and the y-dimension corresponds to the height of the cell. Figure adapted from [24]. 33
Figure 2.3 - Experimental and simulated discharge curves for PLION® cells at low rates. The C rates for thin, medium and thick cells are 2.312, 2.906, and 3.229 mA/cm^2, respectively. The dots represent the experimental data and the solid lines correspond to the simulation results. Figure from [31]. 36
Figure 2.4 - Solution phase diffusion coefficient as a function of discharge rate used to fit experimental data for three different cells. 1C corresponds to 1.156, 1.937 and 2.691 A/m^2 for thin, medium and thick cells, respectively. Figure from [6]. 37
Figure 2.5 - Conduction phenomena in the $LiFePO_4$ cathode during battery charging. Figure from [32]. 39
Figure 2.6 - Illustration of the composition of the cathode electrode: complementary solid phase and electrolyte phase [35]. 42
Figure 2.7 - Schematic computation domain of a Li–air battery during discharge operation. The inset demonstrates the discharge products formation of Li_2O_2 and Li_2CO_3 covering the porous carbon surface. Figure from [45]. 44
Figure 2.8 - Temperature on the cell surface during 1C discharge process under different cooling conditions. Figure from [46]. 46
Figure 2.9 - Cell voltage for 1C discharge process under different cooling conditions. Figure from [46]. 46
Figure 3.1 - Steps for the implementation of the simulations. 58
Figure 3.2 - Representation of the dimension of the battery for the application of the theoretical model: a) 1D, b) 2D and c) 3D. 59
Figure 3.3 - Design of different geometries for lithium-ion batteries. 60

Figure 3.4 - Different size of the mesh: extremely fine, fine and normal. 61
Figure 4.1 - Schematic representation of the main structure of a lithium ion battery. .. 70
Figure 4.2 - Voltage as a function of delivered capacity at different scan rates for: a) free electrolyte and b) battery separator membrane with 70% of porosity and 3.8 of tortuosity. 76
Figure 4.3 - Delivered capacity as a function of the scan rate for free electrolyte and separator membrane batteries. 77
Figure 4.4 - Voltage as a function of delivered capacity for batteries with separator membranes with different degrees of porosity with tortuosity of 3.8 at scan rates of a) 0.15C and b) 5C. 78
Figure 4.5 - Delivered capacity as a function of the degree of porosity at different scan rates: 0.15C, 2C and 5C. 79
Figure 4.6 - Delivered capacity as a function of tortuosity for membranes with different degrees of porosity: a) low scan rate, 0.15C, b) moderate scan rate, 2C and c) high scan rate, 5C. 80
Figure 4.7 - Voltage as a function of the delivered capacity for battery separator membranes with different thicknesses, 70% of porosity and 3.8 of tortuosity: a) 0.15C and b) 5C. 82
Figure 4.8 - Delivered capacity as a function of the separator thickness at different scan rates: 0.15C, 2C and 5C. 83
Figure 5.1 - Voltage as a function of the delivered capacity at C/10 and C/2 discharge rates for the a) Li/LFP and b) Li/LMO half-cells. 97
Figure 5.2 - Voltage as a function of delivered capacity for Li/LFP half-cells with C_1: 95% a) and 50% b) at a discharge rate of 1C. 98
Figure 5.3 - Delivered capacity as a function of C_3 for different C_1 for Li/LFP (a) and Li/LMO (b) half-cells at a discharge rate of 1C. 99
Figure 5.4 - Minimum percentage of C_3 as a function of C_1 for both half-cells at a discharge rate of 1C. 100
Figure 5.5 - Delivered capacity and $Capacity_{sim}/Capacity_{theo}$ (%) ratio as a function of C_1 for the Li/LFP half-cell at 1C discharge rate. 101
Figure 5.6 - a) Delivered capacity as a function of minimum C_3 for the Li/LFP half-cells: a) C_1=95% at 1C, 5C and 10C discharge rates and b) C_1 = 95%, 75% and 50% at 5C discharge rate. 102

Figure 5.7 - Nyquist plot for the Li/LFP half-cell: a) C_1 = 95% with different C_3 values at 1C discharge rate and b) C_1 = 50% with different C_3 values at 1C discharge rate. Nyquist plot for Li/LMO half-cells: c) C_1 = 95% and 50% and C_3 = 1% and 10% at 1C discharge rate. 105
Figure 5.8 - Total impedance as a function of minimum C_3 for different C_1 at 1C discharge rate for: a) Li/LFP and b) Li/LMO half-cells. 106
Figure 5.9 - Schematic representation of a battery cathode and the corresponding intercalation process during the discharge mechanism. 107
Figure 5.10 - Electrolyte and electrode current density as a function of cathode length for a Li/LFP half-cell with C_1 = 95% and C_3 = 4% of at 1C discharge rate and at 500s. The blue line corresponds the sum of both current densities along the width of the cathode, showing that the divergence of the total electric charge is null. 108
Figure 5.11 - Electrolyte current density as a function of the cathode length for Li/LFP half-cell for various C_3 at 1C discharge rate and at 500s for C_1= 95% (a) and 50% (b). 109
Figure 5.12 - Electrode current density as a function of cathode length for Li/LFP half-cell for various C_3 at 1C discharge rate and 500s for C_1 = 95% (a) and 50% (b)..... 110
Figure 5.13 - Electrolyte and electrode current density as a function of time for a Li/LFP half-cell with C_1 = 95% and C_3 = 0.9% at 20 μm of position inside of cathode in relation to separator/cathode interface. The width of the cathode is 70 μm..... 110
Figure 6.1 - Schematic representation of a conventional (a) and an interdigitated (b) battery with indication of the main geometrical parameters. 120
Figure 6.2 - Schematic representation illustrating how the area of each component is maintained constant, while varying the number of digits..... 122
Figure 6.3 - Delivered capacity at 1C discharge rate as a function of the anode thickness for a fixed cathode thickness of 400 μm (a) and as a function of the cathode thickness for a fixed anode thickness of 200 μm (b). 125
Figure 6.4 - Delivered capacity as a function of the scan rate for three different anode thicknesses and fixed cathode thickness of 400 μm. 126
Figure 6.5 - Delivered capacity as a function of the scan rate (a and c) and number of digits (b). Separator thickness and battery width as a function of the number of digits with a fixed c_dig at 400 μm and e_dig at 20 μm (d)..... 128
Figure 6.6 - Nyquist plot for the conventional (a) and the interdigitated (b) geometry with 8 digits in frequency range of 1 mHz to 1MHz..... 129

Figure 6.7 - a) Delivered capacity and b) width of the battery as a function of digit length for a four digits battery for a constant (I) and a variable (II) separator. 131
Figure 6.8 - Nyquist plot of interdigitated geometries for three different digit lengths in the frequency range from 1 mHz to 1MHz..... 132
Figure 6.9 - a) Delivered capacity and b) width of the battery as a function of digit thickness for a constant (I) and a variable (II) separator. 132
Figure 6.10 - Nyquist plot of the interdigitated geometries for three different digit thicknesses in the frequency range from 1 mHz to 1MHz. 133
Figure 6.11 - Schematic representation of the: a) digit limit length and b) digit limit thickness for four digits. 134
Figure 6.12 - Delivered capacity as a function of digit limit thickness (a) and length (b) at 200C and 400C. c) Width of the battery as a function of the number of digits for c_dig= 100 μm and e_dig=20 μm at 200C and 400C. 135
Figure 7.1 – Delivered capacity as a function of scan rate for the different batteries. 149
Figure 7.2 - Delivered capacity for the different geometries as a function of a) maximum distance and b) distance between collectors. 150
Figure 7.3 - a) Schematic representation of the current collector positions and b) voltage as a function of the delivered capacity for the different current collector positions. 153
Figure 7.4 - Delivered capacity as a function of current collector positions and maximum distance of lithium ions. 154
Figure 7.5 - a) Schematic representation of the horseshoe battery dimension, L_dim, and b) delivered capacity as a function of L_dim. 155
Figure 7.6 - Maximum distance and distance between current collectors as a function of L_dim for the horseshoe geometry. 156
Figure 7.7 - a) Schematic representation of the ring geometry and b) delivered capacity as a function of the radius, R_d. 157
Figure 7.8 - Maximum distance, distance between current collectors and thickness of the separator as a function of R_d. 158
Figure 7.9 – Schematic representation of the gear geometry. 159
Figure 7.10 – Voltage as a function of the delivered capacity for the ring and gear geometries with different Rg: a) 93.9 μm and b) 20 μm. 160
Figure 7.11 - Electrolyte potential and electrolyte current density vectors for a) ring and b) gear geometries. 161

Figure 7.12 - Voltage as a function of the delivered capacity for the ring and gear geometries with different separator thickness. 162
Figure 8.1 - Schematic representation of the boundary conditions applied in the conventional geometry. 182
Figure 8.2 - Voltage as a function of the delivered capacity at C/10 rate for the $LiC_6/LiFePO_4$ full-cell with a conventional geometry. 183
Figure 8.3 - Delivered capacity as a function of scan rate for all geometries under isothermal condition. 185
Figure 8.4 - Delivered capacity (a) and temperature (b) as a function of the scan rate for all geometries under adiabatic condition. 186
Figure 8.5 - Nyquist plot for conventional and interdigitated geometries under adiabatic condition. 188
Figure 8.6 - Delivered capacity (left) and final temperature (right) as a function of the scan rate for all geometries under cold (a and b), regular (c and d) and hot (e and f) conditions. 190
Figure 8.7 - Total heat in the anode (a), separator (b) and cathode (c) for all geometries at 1C as a function of the time. d) Total heat along the battery for all geometries at 1C after 120 000s. 192
Figure 8.8 - Temperature of the battery as a function of time for all geometries at 1C. 194
Figure 8.9 - Total heat for anode (a), separator (b) and cathode (c) for all geometries at 300C as a function of time..... 195
Figure 8.10 - Total heat along the battery after 50 s at 300C for conventional and interdigitated geometries (a) and for the remaining geometries (b). 196
Figure 8.11 - Temperature as a function of time for all geometries at 300C. 197
Figure 8.12 - Schematic representation of the ring geometry for the radius of 93.9 µm and 430 µm. 198
Figure 8.13 - a) Capacity as a function of ring radius and b) temperature as a function of time for all ring radius at 500 C. 198
Figure 8.14 - Ohmic heat for anode (a), separator (b) and cathode (c) as a function of the time at 500 C for various ring radius. 199
Figure 8.15 - Ohmic heat along different places between the current collectors of the battery after 70 s at 500C for ring geometry with different radius. 200
Figure 8.16 - Nyquist plot for the ring geometry with different radius at 500 C. 201

Figure 8.17 - Ionic current density vectors of the ring geometry for a) R= 93.9 µm and b) R=430 µm. 202

List of tables

Table 1.1 - Main advantages and disadvantages of lithium ion batteries when compared to related battery systems [33–36]. 6

Table 1.2 - Nomenclature adopted for the variables of the mathematical models. 11

Table 1.3 - Summary of the main equations governing the different processes involved in lithium-ion batteries. 13

Table 1.4 - Summary of the boundary conditions or limits of the mathematical model adopted by [110] where La, Ls and Lc are the width of the anode, separator and cathode, respectively. 16

Table 3.1 - Equations governing various phenomena within a battery [1-4]..... 62

Table 4.1 - Boundary conditions applied in the simulation. The nomenclature is indicated in the List of Symbols and Abbreviations. 72

Table 4.2 - Parameters used in the simulations..... 75

Table 4.3 - Limit value of tortuosity for different degrees of porosity and scan rates. . 81

Table 5.1 - Parameters used for the simulations of the Li/LFP and Li/LMO half-cells.. 95

Table 5.2 - Minimum values of $n=C_2/C_3$ as a function of C_1 for the Li/LFP and Li/LMO half-cells at a discharge rate of 1C. 101

Table 5.3 - Minimum values of the *n* ratio for different C_1 for Li/LFP half-cells at 1C, 5C and 10C discharge rates. 103

Table 6.1 - Parameters used in the simulations of the conventional and interdigitated battery structures..... 123

Table 7.1 - Parameters used for the simulations, main characteristics and applications for the different battery geometries [44-46]. 146

Table 8.1 - Values of the parameter values used in the simulations. The nomenclature is indicated in the List of Symbols and Abbreviations. 175

Table 8.2 - Schematic representation of the different battery geometries and the corresponding dimensions. The nomenclature is indicated in the List of Symbols and Abbreviations. 177

Table 8.3 - Summary of the boundary conditions implemented in the conventional geometry. The nomenclature is indicated in the List of Symbols and Abbreviations.. 181

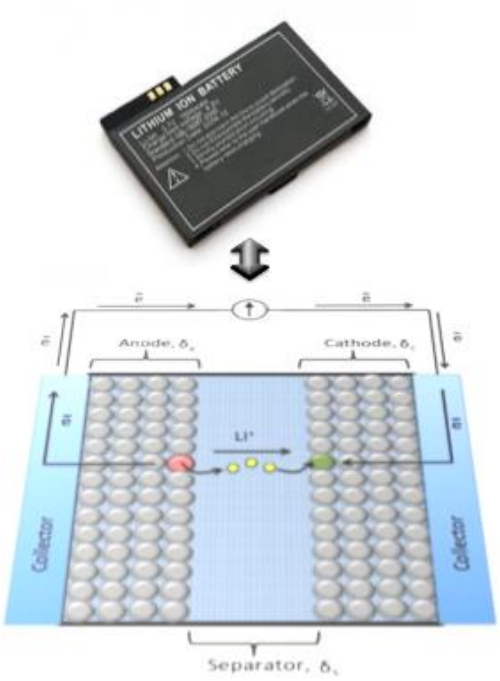

1. Introduction

This chapter is divided into three parts: the theme of the thesis is introduced, the main objectives are presented as well as the thesis structure and the applied methodology.

With respect to the introduction, it is shown the importance of lithium-ion batteries as energy storage systems, the mathematical models for lithium ion batteries, the description of the main materials used for each of the components of a battery (anode, cathode and separator) and how material characteristics affect battery performance. Finally, it is introduced the general mathematical framework for the microscopic models of lithium-ion batteries.

This chapter is partially based on the following publication:

"Lithium ion rechargeable batteries: State of the art and future needs of microscopic theoretical models and simulations", D. Miranda, C.M. Costa, S. Lanceros-Mendez, Journal of Electroanalytical Chemistry 739 (2015) 97-110.

1.1 Introduction

The XX and XXI centuries are characterized by rapid technological advances, in particular in the electronics, informatics and communication industries. The development of products such as computers, mobile phones, tablets and other portable devices lead to an increasing need for battery autonomy and performance [1–3].

Increasing battery performance (Figure 1) is associated to the use of novel materials and concepts leading to increasing loading capacity, cycle life and safety [4–7]. Figure 1.1 illustrates the evolution of batteries with respect to energy density.

Nowadays, large attention is being paid to the development of batteries for the automobile industry in order to reduce fossil fuel dependence and emission gases responsible for the greenhouse effect and therefore to reduce the environmental impact associated to the energies used for mobility [8–10].

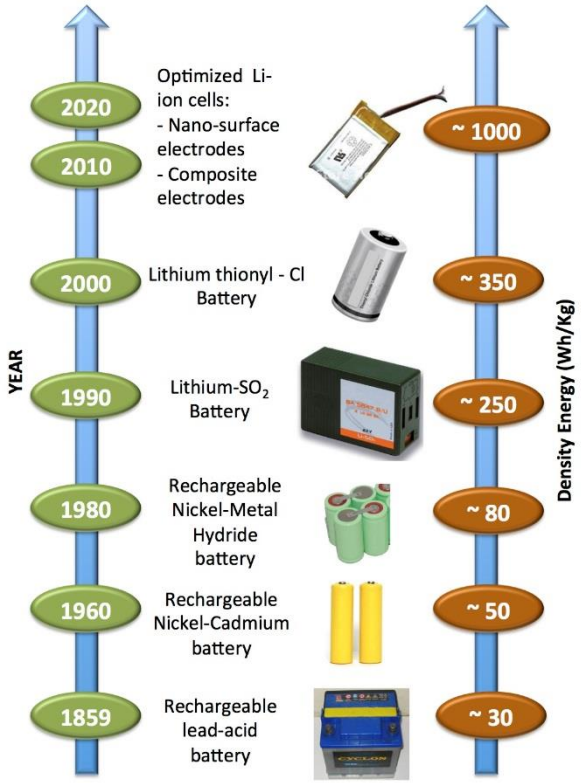

Figure 1.1 - Battery evolution with respect to their energy density.

The main goal of the battery industry is to obtain specific levels of battery performance for the different applications (e.g. applied voltage and capacity) with low production costs. In this context, intensive research is being devoted to the development of rechargeable or secondary batteries [11,12].

For many years, nickel–cadmium batteries (Ni–Cd) were the most suitable for portable communications systems and computing equipments. However, at the beginning of the 90s, lithium ion batteries increased in attention and acceptance by consumers. Nowadays, lithium ion batteries are the most widely used and still show a promising growth potential [13,14]. The pioneering work with lithium ion batteries began in 1912 and it was in the 70s that the first non-rechargeable lithium ion batteries were commercialized [15,16]. Lithium is the lightest of all metals, showing a large electrochemical potential and high energy density relative to its weight [17]. Several attempts to develop rechargeable lithium ion batteries failed due to safety problems [18,19], associated to the inherent instability of lithium metal, in particular during the charge cycle.

The lithium ion is safe provided that certain precautions are taken during battery charge and discharge cycles. The safety of the lithium-ion battery is one of the key issues for improving the performance of the battery. Thus, the interest in developing lithium-ion batteries increased and in 1991 the Sony Corporation commercialized the first lithium-ion batteries [20].

For increasing battery performance and optimizing materials and designs it is critical to have suitable theoretical models that allow battery simulation. The mathematical theoretical models for lithium-ion batteries describe the physical processes and mechanisms of the different components of the batteries and are essential for optimizing performance, design, durability and safety of lithium-ion batteries.

Mathematical models for lithium ion batteries have been developed at different scales of battery operation from the macro to the nano scales [21].

The mathematical models at the micro-scale are the most widely used for research, development and battery optimization as they allow the correlation of the theoretical results with experimental transport and electrochemistry data [22].

This review is divided into the following sections: first, the advantages and disadvantages of lithium-ion batteries in relation to other types of batteries are outlined; then, the process of insertion/extraction of lithium ions and each of the main components of the battery are described; finally, the microscopic mathematical models dealing with the description of the operation of lithium ion batteries are reviewed and their results discussed; the reviews finish with some concluding remarks on the open questions and future research directions in this specific topic.

1.1.2 Advantages and disadvantages of lithium ion batteries

A critical assessment on the main advantages and disadvantages should be performed for each type of battery [2]. The main advantages and disadvantages of the use of lithium ion batteries when com- pared to other types of batteries such as Ni–Cd, Lead–Acid battery and Nickel–Metal Hydride Cells are illustrated in Table 1. By comparing lithium ion batteries with nickel–cadmium batteries (Ni– Cd), the energy density of the lithium ion batteries is approximately twice as large as the energy density of nickel–cadmium batteries [23,24]. The charging cycle, on the other hand, shows similar characteristics for nickel–cadmium and lithium-ion batteries [25,26]. Lithium-ion electrochemical cells show high voltages and in case, for example, of an electrical apparatus requiring a voltage of 3.6 V, it requires just one cell instead of a package of three cells of 1.2 V for nickel–cadmium batteries. Lithium-ion batteries show no memory effect in their charge and discharge cycles which leads to increased life time [27]. Furthermore, their self-discharge effect is lower in comparison to nickel–cadmium batteries. Despite the mentioned advantages, lithium-ion batteries also show some disadvantages. In particular, lithium-ion batteries require a protection circuit to maintain safe operation. This protection circuit limits the peak voltage of each cell during charge and prevents the cell voltage to strongly decrease during discharge [28].

The temperature of lithium-ion batteries should be also con- trolled in order not to exceed 100 °C. The maximum charge and discharge current in the majority of these batteries is limited between 1C and 2C [29]. Aging is also a concern for most lithium-ion batteries and deterioration is observed after one year, approximately, whether in use or not [30–32]. However, in some specific applications the durability of lithium-ion batteries can extend up to about five years [7].

Table 1.1 - Main advantages and disadvantages of lithium ion batteries when compared to related battery systems [33–36].

Advantages	Disadvantages
High energy density, between 100 and 150 Wh kg^{-1}	A protection circuit is needed for maintaining constant voltage
One regular charge cycle is needed, not needing a long charging cycle.	Subject to aging, while not in use.
Low self-discharge when compared with Ni–Cd batteries.	Restrictions on transportation. Transportation of large quantities may be subjected to regulatory control.
Low maintenance and no memory effects.	High manufacturing costs due to the price of lithium.
Specific cells can provide high current for particular applications.	Lithium batteries show good operation range for discharge currents between 1C and 2C.

In the automotive industry there are many options for electric vehicle batteries, each system offering unique features with advantages and disadvantages [37–39]. Currently, some of the most promising approaches are based on lithium-ion batteries, due to their high energy density [7]. However, lithium-ion batteries show problems with sensitivity of overload that can reduce their life cycle. Other options under consideration include fuel cells with rechargeable batteries. In any case, it should be noted that these options do not provide the same amount of energy in comparison to fossil fuels: ~40 MJ/kg for fossil fuel against 1.5–0.25 MJ/kg for fuel cells and advanced batteries, respectively [34]. Although electric vehicles are being designed and built, currently there is no energy source that matches the power and energy of the internal combustion engine [40,41]. Nevertheless, research is conducted to develop a robust system capable of achieving reasonable acceleration for the vehicle and the ability to perform long distances [42]. In this sense, fuel cells and lithium-ion batteries are suitable alternatives for application in electric vehicles due to their large improvement potential based on novel materials and optimized design [43–45].

1.1.3 Mathematical model for lithium ion batteries

Lithium ion batteries are composed by three major components (Figure 1.2): anode, cathode and separator [46,47].

As in other types of batteries, it shows two electrodes with different electrical potentials related to the chemical nature of their active material which are the cathode and the anode [48–50]. The battery separator is located between the cathode and the anode and it is an ionic conductor but electronic insulator. Lithium ion batteries also need the electrolyte, which may be embedded in the separator, containing lithium salts dissolved in an organic solvent and that can be dispersed in the three battery components (electrodes and separator) as illustrated in Figure 1.2 [51,52].

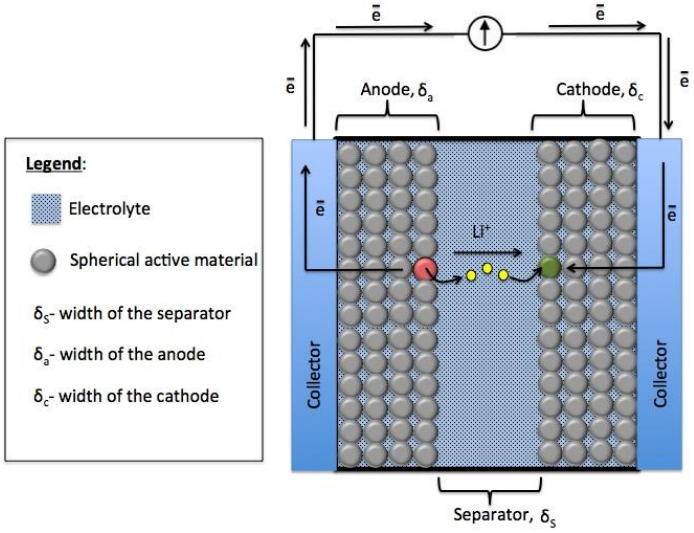

Figure 1.2 - Schematic representation of the main structure of a lithium ion battery and the process of insertion/extraction of lithium ions that occurs at the electrodes during discharge of a battery.

The operation of a lithium-ion battery is based on a process called ‘‘rocking chair’’ due to the extraction and insertion of lithium ions at the electrodes. During discharge of a battery, extraction of lithium ions from the anode occurs, providing electrons to the cathode through an external circuit (Figure 1.2). When the lithium ions reach the cathode, capture of electrons from the external circuit occurs together with the insertion process of lithium ions. During the discharge process, therefore, electrons and Li-ions move from the anode to the cathode.

The insertion/extraction process has advantages and disadvantages when compared to the others traditional battery processes (such as the ones in Ni–Cd) [53]. Insertion and

extraction processes are highly reversible but, on the other hand, they are associated to a change in the volume of the electrodes that, depending on their nature, leads to matrix degradation over the lifecycle [54].

The majority of the theoretical models consider that the active material in both electrodes is spherical and that it is supported by a material that is not involved in the battery operation reactions, i.e., an inert material.

The process of insertion/extraction of lithium ions and the over- all battery operation can be studied from different points of view and at different physical and chemical scales: nanoscale, mesoscale, microscale and macroscale, as illustrated in Figure 3. Two recent reviews [21,55] describe the theoretical simulations for anode, cathode and separator as well as the interface between electrodes and electrolyte considering a nano- and meso scale approach, mainly focusing on the ion transport phenomena at the meso scale.

For all models developed at the different physico-chemical scales, there are a number of variables available for manipulation, particularly relevant for battery performance. The electrodes, for example, are studied taking into account different scales and particle shapes, among others, based on computer-aided reconstruction. Effects of mechanical stress and thermal heterogeneities are also studied from the atomic to the macroscopic scales.

The development of models at different scales (multi-scale approach) are suggested in order to prove battery operation coupling at different physical levels [21], as nano- and mesoscale models are suitable for understanding and improving the different components of the battery from a materials science point of view but lack for proper validation with respect to improvement in batteries performance. Suitable extrapolation from the lower to the higher scales are needed in order to achieve the final goal, which is to allow proper battery design.

Thus, a more detailed physico-chemical description of the materials is necessary for improving battery design optimization by increasing predictability of multiscale models [55].

On the other hand, the purpose of mathematical models at the microscopic level is to study parameters directly affecting battery performance, such as energy density, capacity, voltage and discharge time which are readily modeled considering overall properties of different materials, their microstructures, electrolytes and boundary conditions.

1.1.4 Materials

1.1.4.1 Anode and cathode electrodes

The electrodes in most batteries are porous [56], although in some cases may be compact and flat. Several materials have been used for electrodes, the most frequently used being graphite as anode material [57–59] and $LiCoO_2$, $LiNiO_2$, $LiMn_2O_4$, $LiMn_{1/3}Ni_{1/3}$ $Co_{1/3}O_2$ and $LiFePO_4$ as cathodes [60–63]. The most promising cathode materials are from the $LiMPO_4$ family in which phosphorous occupies tetrahedral sites and the transition metal (M) occupies octahedral sites. In this family, the most used cathode material is lithium iron phosphate ($LiFePO_4$), which shows high open circuit voltages >3.5V but low capacities around ~170$mAhg^{-1}$ [64].

At the present moment, the most commonly used cathode material in lithium-ion batteries for portable applications is $LiCoO_2$ [65], but cobalt is less available and shows a higher price than other transition metals. The cost of $LiNiO_2$ is lower and shows higher energy density but is less stable and has a less ordered structure when compared with $LiCoO_2$ [65]. In this sense, cathodes with different amounts of three transition metals Li(Ni, Mn, Co)O_2 are increasingly being used as they show high capacity, good rate capability and can operate at high voltages [60,65]. The main characteristics of the materials used for cathode development are the presence of a transition metal ion for maximizing cell voltage, the possibility of preparation of a composite with the active material to allow insertion/extraction of a large quantity of lithium ions for maximizing the capacity of the cell and, finally, the composite material must possess minimal structural changes depending on the composition of lithium, which ensures good reversibility of the process. Relatively of the anode material, graphite improves the insertion or intercalation, being able to store lithium through the interstitial sites between two graphite planes. This process is directly related to the energy storage density of Li-ion batteries. Graphite also shows low expansion, which is directly related to their facility to maintain their charge capacity after many charge–discharge cycles. Further, it is cheap, shows cycle efficiency and moderate capacity, 373 $mAhg^{-1}$ [66]. Carbon nanotubes (CNT) are also used as anode material. Single walled CNT show higher capacity, up to 1000 $mAhg^{-1}$, than graphite and can be used as a support matrix. Finally, they have adequate properties for electrode materials such as high tensile strength and high conductivity. The disadvantage of CNT is their irreversible lithium ion capacity loss that occurs during the first cycle. [67].

1.1.4.2 Battery separator

The separator is a key component in all electrochemical devices and is located between the anode and the cathode [68,69]. The role of the separators is to serve as the medium for the transfer of the lithium ions between both electrodes and to control lithium ion flow and mobility [70]. The key requirements of a separators for lithium ion batteries are thickness, permeability, gurley, porosity and pore size, wettability by liquid electrolyte, electrolyte absorption and retention, resistance to chemical degradation by electrolyte impurities, dimensional stability, puncture strength, thermal stability, mechanical and dimensional stability and skew [68,71].

The separator membrane is often a polymer matrix, in which the membrane is impregnated by the electrolyte solution. The liquid electrolyte solution is constituted by salts dissolved in solvents, water or organic molecules. The solvent must meet the requirements of low viscosity, medium to high dielectric constant for dissolving the salts, low viscosity for facility the ion transportation, to be inert to all cell components and remain in liquid state in the temperature range of cell operation cell [72,73]. The most used solvents in electrolyte solutions are ethylene carbonate (EC), propylene carbonate (PC), dimethyl carbonate (DMC), diethyl carbonate (DEC) and ethyl methyl carbonate (EMC) [74–77].

The lithium salts most used in electrolyte solution are $Li(CF_3SO_2)_2N$ [78], $LiAsF_6$ [79], $LiPF_6$ [80], $LiClO_4$ [81], $LiBF_4$ [82], $LiCF_3SO_3$ [83] in which the size of the anions is an important factor that determines the properties of the salts [84].

The materials used as separator materials are polymers with/ without dispersed fillers. Among the used polymers stand out poly(ethylene) (PE) [85], poly(propylene) (PP) [86], poly(ethylene oxide) (PEO) [87,88], poly(acrylonitrile) (PAN) [88,89] and poly (vinylidene fluoride), PVDF, and its copolymers [90–92] (poly(vinylidene-co-trifluoroethylene), PVDF-TrFE [93], poly(vinylidene fluoride-co-hexafluoropropene), PVDF-HFP [94] and poly(vinylidenefluoride-co-chlorotrifluoroethylene), PVDF-CTFE. PVDF and copolymers show important advantages in comparison to polyolefins and other materials for their use as separators due to their polarity (high dipole moment) and high dielectric constant for a polymer, which can assist the ionization of lithium salts. It is possible to control their porosity, they are wetted by organic sol- vents and are chemically inert. They also show good contact between electrode and electrolyte and are stable in cathodic environment [95]. The fillers incorporated (dispersed directly) into

the polymer hosts may be inert oxide ceramic (Al_2O_3, SiO_2, TiO_2), molecular sieves (zeolites), ferroelectric materials ($BaTiO_3$) and carbonaceous fillers, among others, with the goal to increase the electrochemical properties, mechanical and thermal stability of the separator [96].

1.1.5 General mathematical framework for the microscopic models of lithium-ion batteries

Most mathematical models for lithium ion batteries are developed to study the performance of the battery in one and two-dimensions by considering electrochemical and transport processes in the different components of the battery. Some models also allow to study of the influence of temperature in the performance of the battery [97]. The different microscopic models are based on the Doyle/Fuller/Newman model [98–109], considering the same mathematical framework for the electrochemical phenomena and transport occurring in the different components of the battery: anode, cathode and separator with electrolyte. The main differences between the developed theoretical studies are thus reduced to border and boundary conditions, specific for each of the studies, which simplify the general mathematical model for each particular case under study [98–109] and/or in the materials used for the different components. In the following, the nomenclature adopted for the variables of the mathematical models is introduced in Table 1.2.

Table 1.2 - Nomenclature adopted for the variables of the mathematical models.

Nomenclature	
a	specific interfacial area, m^2/m^3
C_L	concentration of Li ions in the electrolyte, mol/m^3
C_E	concentration of Li ions in the electrode, mol/m^3
D	diffusion coefficient of the salt in the electrolyte, m^2/s
D_{LI}	diffusion coefficient of Li ions in the electrode, m^2/s
F	faraday's constant, 96487 C/mol
$f_{\pm}$	activity of the salt in the electrolyte, mol/m^3
$\mathbf{i}_E$	current density in the electrode, A/m^2
$\mathbf{i}_L$	current density in the electrolyte phase, A/m^2
I_{TOTAL}	total current density, A/m^2

j_{Li^+}	pore wall flux of Li ions, mol/cm^2 s
L	width
M	mass transport flux, mol/m^2
R	reaction term of the mass balance equation, mol/m^3 s
R	gas constant, 8,314 J/mol K
R_f	film resistance, Ω m^2
r	radius of electrode spherical particle, m
T	temperature
t	time, s
t_+^0	transport number of the positive ion
u^0	open circuit voltage, V
ε_i	porosity of region *i*(*i* = a,s,c)
$\varepsilon_{f,i}$	volume fraction of fillers in electrode *i* (*i* = a,s,c)
η	over-potential, V
φ_E	potential of the electrodes, V
φ_L	potential of electrolyte,V
κ	ionic conductivity of the electrolyte, S/m
κ_{ef}	effective ionic conductivity of the electrolyte, S/m
σ	electronic conductivity of the solid phase of the electrode *i* (*i* = a,s,c), S/m
$\sigma_{ef,i}$	effective electronic conductivity of the solid phase of the electrode *i* (*i* = a,s,c), S/m
Subscripts	
a	anode
c	cathode
s	separator
0	initial condition

Thus, the general mathematical model presented in this review is based on the Doyle/Fuller/Newman model which describes the fundamental equations governing the main phenomena that occur in the operation process of a lithium-ion battery. The main equations governing the different processes during operation of a battery are presented in Table 1.3.

Table 1.3 - Summary of the main equations governing the different processes involved in lithium-ion batteries.

	Governing Equation	**Description**
Cathode	$\varepsilon_c \frac{\partial C_L}{\partial t} = \frac{D_{ef,c}}{\partial^2} \frac{\partial^2 C_L}{\partial x^2} + a(1-t_+^0) j_{Li^+}$	Diffusion of lithium ions in the electrolyte applied to the cathode.
	$-\frac{\sigma_{ef,c}}{\partial^2} \frac{\partial^2 \varphi_E}{\partial x^2} = -Faj_{Li^+}$	Electrode potential calculated by the Ohm Law where the current density gradient is substituted by its equivalent in terms of lithium ion flux according to Faraday's Laws.
	$-\frac{k_{ef,c}}{\partial^2} \frac{\partial^2 \varphi_L}{\partial x^2} = Faj_{Li^+} + \frac{2kRT}{F}(1-t_+^0) \frac{\partial \ln C_L}{\partial x^2}$	This equation relates the potential of the electrolyte with the local current density in the cathode (Ohm Law).
Anode	**Governing Equation**	**Description**
	$\varepsilon_a \frac{\partial C_L}{\partial t} = \frac{D_{ef,a}}{\partial^2} \frac{\partial^2 C_L}{\partial x^2} + a(1-t_+^0) j_{Li^+}$	Diffusion of lithium ions in the electrolyte applied to the anode.
	$-\frac{\sigma_{ef,a}}{\partial^2} \frac{\partial^2 \varphi_E}{\partial x^2} = -Faj_{Li^+}$	Electrode potential calculated by the Ohm Law where the current density gradient is substituted by its equivalent in terms of lithium ion flux according to Faraday's Laws.
	$-\frac{k_{ef,a}}{\partial^2} \frac{\partial^2 \varphi_L}{\partial x^2} = Faj_{Li^+} + \frac{2kRT}{F}(1-t_+^0) \frac{\partial \ln C_L}{\partial x^2}$	This equation relates the potential of the electrolyte with the local current density in the anode (Ohm Law).
Electrolyte/ Separator	**Governing Equation**	**Description**
	$\varepsilon_s \frac{\partial C_L}{\partial t} = \frac{D_{ef,s}}{\partial^2} \frac{\partial^2 C_L}{\partial x^2}$	Lithium ion diffusion in the electrolyte.
	$-\frac{k_{ef,s}}{\partial^2} \frac{\partial^2 \varphi_L}{\partial x^2} = Faj_{Li^+} + \frac{2kRT}{F}(1-t_+^0) \frac{\partial \ln C_L}{\partial x^2}$	This equation relates the potential of the electrolyte with the local current density (Ohm Law).

Active material	Governing Equation	Description
	$\frac{\partial C_E}{\partial t} = D_{Li}\left[\frac{\partial^2 C_E}{\partial r^2} + \frac{2}{r}\frac{\partial C_E}{\partial r}\right]$	Diffusion of lithium ions in the active material.
General equations	**Governing Equation**	**Description**
Faraday's law (electrodes)	$\nabla i_L = Faj_{Li^+}$	Faraday's law express the relationship between the insertion/extraction of lithium ions into the electrodes with the electrical charge flow Relation between the lithium ions flux and the current density in the electrodes.
Faraday's law (electrolyte)	$\nabla i_E = Faj_{Li^+}$	Relation between the lithium ions flux and the current density in the electrolyte (Faraday´ s Law).
Total current density	$i_E + i_L = I_{TOTAL}$	Conservation of charge. The current density is preserved between the electrode and the electrolyte.
Butler-Volmer equation (kinetics)	$j_n = i_0\left\{\exp\left(\frac{F}{2RT(\eta - u^0)}\right) - \exp\left(\frac{-F}{2RT(\eta - u^0)}\right)\right\}$	Kinetics of the heterogeneous reaction at the electrode/electrolyte interface, described by the Butler–Volmer equation.
Variable over-potential	$\eta = \varphi_E - \varphi_L - u^0$	The variable over-potential relates the potential of the electrodes/electrolyte and the open circuit voltage.
Mass transport process	$M_+^{Total} = -D\left(1 - \frac{\partial \ln C_{L_0}}{\partial \ln C_L}\right)\nabla CL + \frac{i_L t_+^0}{F}$	Mass transport flux.
Term of the reaction	$R = -\frac{a}{v_+}(1 - t_+^0)\, j_{Li^+}$	Reaction term of the mass balance equation.

Overall mass balance	$\frac{\partial C_L}{\partial t} = -\nabla .M + R$	Overall mass balance.
Auxiliary equations	**Governing Equation**	
	$\int_{L_a+L_s}^{L_a+L_s+L_C} Faj_{Li^+}(\varphi_{E,0})dx = -I_{TOTAL}$	
	$\int_{0}^{L_s} Faj_{Li^+}(\varphi_{L,0})dx = I_{TOTAL}$	
	$kef,i = (4.1253\times10^{-2} + 5.007\times10^{-4}c - 4.7212\times10^{-7}c^2 + 1.509\times10^{-10}c^3 - 1.6018\times10^{-14}c^4) \quad i = c,s,a$	
	$\sigma_{ef,i} = \varepsilon_i(1-\varepsilon_i-\varepsilon_{f,i})$	
	$D_{ef,i} = D_i\varepsilon_i^{brugg},\ i = c,a$	

The different models found in the literature involve simplifications and specific boundary conditions of the previous equations in order to account for specific phenomena [98–109]. The auxiliary equations are important as they reflect the effect of the microstructure (porosity) in the ionic conductivity and diffusion process in all components of the battery. These effects are described through the Bruggeman equation for highly conductive isotropic materials [106]. This equation applies to the ionic conductivity in liquid-electrolyte-soaked porous media, not being suitable for electronic conductivity based on networks of touching particles or for solid polymer composite electrolytes [106].

The model of the battery in one dimension is considered taking into account the three main components of the battery (separator, anode and cathode) in dimension x and sub-dimension r (spherical particles of active material). In the following, the boundary conditions adopted for the different equations at the interfaces between the regions will be presented.

The diffusion of lithium ions in the electrolyte occurs at the three cell components (anode, cathode and separator). The collectors of the battery are a wall impermeable to the electrolyte, so the flow of lithium ions is null at these limits. The interfaces of the three components show a condition of continuity that is expressed as an equal mass that flows on both sides of the interface, i.e.

- at the interfaces:

$$\left.\frac{\partial C_L}{\partial x}\right|_{x^+=L_a} = \left.\frac{\partial C_L}{\partial x}\right|_{x^-=L_a} \quad (1)$$

$$\left.\frac{\partial C_L}{\partial x}\right|_{x^+=L_a+L_S} = \left.\frac{\partial C_L}{\partial x}\right|_{x^-=L_a+L_S} \quad (2)$$

- at the current collectors:

$$\left.\frac{\partial C_L}{\partial x}\right|_{x=0} = 0 \quad (3)$$

$$\left.\frac{\partial C_L}{\partial x}\right|_{x=L_a+L_s+L_c} = 0 \quad (4)$$

• Diffusion of lithium ions in the active material:

$$\left.\frac{\partial C_E}{\partial r}\right|_{r=0} = 0 \quad (5)$$

$$\left.\frac{\partial C_E}{\partial r}\right|_{r=R_{sp}} = -\frac{j_{Li^+}}{D_{Li}} \quad (6)$$

Table 1.4 summarizes the boundary conditions or limits adopted in the model.

Table 1.4 - Summary of the boundary conditions or limits of the mathematical model adopted by [110] where La, Ls and Lc are the width of the anode, separator and cathode, respectively.

Region battery	Equation	x = 0	x = L_a	x = L_a + L_S	x = L_a+ L_S+ L_c
Electrolyte	Li^+ diffusion	$\frac{\partial C_L}{\partial x} = 0$	Continuity	Continuity	$\frac{\partial C_L}{\partial x} = 0$
	Ohm's law	$\varphi_L = \varphi_{L,0}$	Continuity	Continuity	$\frac{\partial \varphi_L}{\partial x} = 0$
Electrodes	Ohm's law	$\varphi_E = 0$	$\frac{\partial \varphi_E}{\partial x} = 0$	$\varphi_E = \varphi_{E,0}$	$\frac{\partial \varphi_E}{\partial x} = -\frac{I_{TOTAL}}{\sigma}$
	Li^+ diffusion	$r = 0$ $\frac{\partial C_E}{\partial r} = 0$	$r = R_s$ $\frac{\partial C_E}{\partial r} = -\frac{j_{Li^+}}{D_{Li}}$		

1.2 Objectives

The main objective of the present work is the optimization of the performance of lithium-ion batteries through of computer simulations. This optimization is performed through the development of theoretical simulations for separators, electrodes and full/half-cells of lithium ion batteries. For this purpose, the understanding of the main processes that affect the battery performance is critical, and may be achieved through adequate simulation based on optimization of electrodes, separators and battery geometry.

The main specific objectives of this work are:

1) Optimizing the performance of the separator (porous membrane) of lithium ion batteries through the evaluation of the influence of geometrical parameters such as degree of porosity, tortuosity, Bruggeman coefficient and thickness. Understand the relationship of Bruggeman coefficient with the degree of porosity and tortuosity.

2) Obtain the optimal relationship between active material, binder and conductive additive for lithium-ion battery cathodes. Evaluate the effect of the relative percentages of active material, binder and conductive additive in cathodes with different active materials, such as $LiMn_2O_4$ and $LiFePO_4$.

3) Evaluate the effect of the geometrical parameters of interdigitated batteries, including the number, thickness and the length of the digits, on the delivered battery capacity.

4) Study the influence of the geometry in the performance of conventional and unconventional lithium-ion batteries. Develop new high performance battery geometries for different applications.

5) Understand the thermal behavior in unconventional geometries for lithium-ion batteries. Evaluate the heat produced by the different geometries and test the performance of these batteries at different temperatures and thermal conditions (isothermal, adiabatic, cold, regular and hot conditions).

1.3 Thesis structure and methodology

The present thesis is divided into nine chapters showing the evolution of the work during this investigation.

Six of those chapters are based on published or submitted scientific articles.

Chapter 1 presents the introduction to the theme of this thesis, describes the main objectives of the work and presents the thesis structure and methodology.

Chapter 2 shows the state of the art on the theoretical models for the simulation of the performance of lithium ion batteries and shows a description of the main theoretical studies describing the operation and performance of a battery. This chapter also presents the objectives of the study as well as the structure of the document.

Chapter 3 describes the methodology implemented in the simulations developed in the different studies. It is also shown the theoretical models used in the different simulations, such as the electrochemical and thermal models.

The effect of geometrical parameters of the separator, such as degree of porosity, tortuosity and thickness, in the performance of lithium-ion batteries is presented in chapter 4. This chapter also shows the relation of Bruggeman coefficient (applied in equations of ionic diffusion/conductivity) with the degree of porosity and tortuosity of separator.

Chapter 5 reports the optimal relationship between active material, binder and conductive additive for lithium-ion battery cathodes. The effect of different percentages of active material, binder and conductive additive on the performance of two cathodes with different active materials ($LiMn_2O_4$ and $LiFePO_4$) is presented.

The effect of the geometrical parameters of interdigitated batteries, including the number, thickness and the length of the digits, on the delivered battery capacity is presented in chapter 6.

The influence of geometry in the performance of conventional and unconventional lithium-ion batteries is provided in chapter 7. In order to optimize battery performance, different geometries have been evaluated taking into account their suitability for different applications, as presented in chapter 7.

The thermal behavior of conventional and unconventional lithium-ion battery geometries is evaluated in chapter 8. The performance of different battery geometries in several thermal conditions (isothermal, adiabatic, cold, regular and hot conditions) is presented.

Finally, chapter 9 provides the general conclusions as well as suggestions for future work.

1.4 References

1. Crompton, T.P.J., *Battery Reference Book*2000: Elsevier Science.
2. Munshi, Z.A., *Handbook of Solid State Batteries & Capacitors*1995: World Scientific Pub.
3. Wakihara, M. and O. Yamamoto, *Lithium ion batteries: fundamentals and performance*1998: Kodansha.
4. Bates, J.B., et al., *Thin-film lithium and lithium-ion batteries.* Solid State Ionics, 2000. **135**(1–4): p. 33-45.
5. Megahed, S. and B. Scrosati, *Lithium-ion rechargeable batteries.* Journal of Power Sources, 1994. **51**(1–2): p. 79-104.
6. Scrosati, B., *Recent advances in lithium ion battery materials.* Electrochimica Acta, 2000. **45**(15–16): p. 2461-2466.
7. Scrosati, B. and J. Garche, *Lithium batteries: Status, prospects and future.* Journal of Power Sources, 2010. **195**(9): p. 2419-2430.
8. Dincer, I., *Renewable energy and sustainable development: a crucial review.* Renewable and Sustainable Energy Reviews, 2000. **4**(2): p. 157-175.
9. Hill, J., et al., *Environmental, economic, and energetic costs and benefits of biodiesel and ethanol biofuels.* Proceedings of the National Academy of Sciences, 2006. **103**(30): p. 11206-11210.
10. Johansson, T.B. and L. Burnham, *Renewable energy: sources for fuels and electricity*1993: ISLAND Press.
11. Products, G.E., *Rechargeable Batteries Applications Handbook*1998: Elsevier Science.
12. Graham, R.W., *Rechargeable batteries: advances since 1977*1980: Noyes Data Corp.
13. Consulting, P.R., *Advanced Batteries for Portable Power Applications*, 2011.
14. Nagaura, T. and K. Tozawa, Progress in Batteries and Solar Cells, 1990. **209**.
15. Ozawa, K., *Lithium-ion rechargeable batteries with LiCoO2 and carbon electrodes: the LiCoO2/C system.* Solid State Ionics, 1994. **69**(3–4): p. 212-221.
16. Colin A, V., *Lithium batteries: a 50-year perspective, 1959–2009.* Solid State Ionics, 2000. **134**(1-2): p. 159-167.
17. Sapse, A.M. and P. von R. Schleyer, *Lithium Chemistry: A Theoretical and Experimental Overview*1995: Wiley.

18. Dusastre, V., J.M. Tarascon, and M. Grätzel, *Materials for Sustainable Energy: A Collection of Peer-Reviewed Research and Review Articles from Nature Publishing Group*2010: World Scientific.
19. Balakrishnan, P.G., R. Ramesh, and T. Prem Kumar, *Safety mechanisms in lithium-ion batteries.* Journal of Power Sources, 2006. **155**(2): p. 401-414.
20. Johnson, B.A. and R.E. White, *Characterization of commercially available lithium-ion batteries.* Journal of Power Sources, 1998. **70**(1): p. 48-54.
21. Franco, A.A., *Multiscale Modeling of Rechargeable Lithium Ion Batteries: Concepts, Methods and Challenges.* RSC Advances, 2013.
22. Arora, P., et al., *Comparison between computer simulations and experimental data for high-rate discharges of plastic lithium-ion batteries.* Journal of Power Sources, 2000. **88**(2): p. 219-231.
23. Section, G.E.C.B.P., D.L. Barney, and R.L. Falzone, *Nickel-cadmium battery application engineering handbook*1971: General Electric.
24. Thackeray, M.M., J.O. Thomas, and M.S. Whittingham, *Science and Applications of Mixed Conductors for Lithium Batteries.* MRS Bulletin, 2000. **25**(03): p. 39-46.
25. Besenhard, J.O., J. Yang, and M. Winter, *Will advanced lithium-alloy anodes have a chance in lithium-ion batteries?* Journal of Power Sources, 1997. **68**(1): p. 87-90.
26. van Schalkwijk, W. and B. Scrosati, *Advances in Lithium-Ion Batteries*2002: Springer.
27. Chen, J., C. Buhrmester, and J.R. Dahn, *Chemical Overcharge and Overdischarge Protection for Lithium-Ion Batteries.* Electrochemical and Solid-State Letters, 2005. **8**(1): p. A59-A62.
28. Arora, P., R.E. White, and M. Doyle, *Capacity Fade Mechanisms and Side Reactions in Lithium-Ion Batteries.* Journal of The Electrochemical Society, 1998. **145**(10): p. 3647-3667.
29. Lijun, G., S. Liu, and R.A. Dougal, *Dynamic lithium-ion battery model for system simulation.* Components and Packaging Technologies, IEEE Transactions on, 2002. **25**(3): p. 495-505.
30. Vetter, J., et al., *Ageing mechanisms in lithium-ion batteries.* Journal of Power Sources, 2005. **147**(1–2): p. 269-281.

31. Broussely, M., et al., *Main aging mechanisms in Li ion batteries.* Journal of Power Sources, 2005. **146**(1–2): p. 90-96.
32. Broussely, M., et al., *Aging mechanism in Li ion cells and calendar life predictions.* Journal of Power Sources, 2001. **97–98**(0): p. 13-21.
33. Bruce, P.G., B. Scrosati, and J.-M. Tarascon, *Nanomaterials for Rechargeable Lithium Batteries.* Angewandte Chemie International Edition, 2008. **47**(16): p. 2930-2946.
34. Linden, D. and T.B. Reddy, *Handbook of Batteries*2002: McGraw-Hill.
35. Kiehne, H.A., *Battery Technology Handbook*2003: Marcel Dekker.
36. Pistoia, G., *Batteries for Portable Devices*2005: Elsevier Science.
37. Broussely, M., et al., *Lithium-ion batteries for electric vehicles: performances of 100 Ah cells.* Journal of Power Sources, 1997. **68**(1): p. 8-12.
38. Kennedy, B., D. Patterson, and S. Camilleri, *Use of lithium-ion batteries in electric vehicles.* Journal of Power Sources, 2000. **90**(2): p. 156-162.
39. Zhang, X., et al., *Diagnostic Characterization of High Power Lithium-Ion Batteries for Use in Hybrid Electric Vehicles.* Journal of The Electrochemical Society, 2001. **148**(5): p. A463-A470.
40. Holdren, J.P., *The Energy Innovation Imperative: Addressing Oil Dependence, Climate Change, and Other 21st Century Energy Challenges.* Innovations: Technology, Governance, Globalization, 2006. **1**(2): p. 3-23.
41. Mabro, R.E. and O.o.P.E. Countries, *Oil in the 21st Century: Issues, Challenges and Opportunities*2006: Oxford University Press.
42. Cairns, E.J., & Albertus, P. , *Batteries for electric and hybrid-electric vehicles.* Annual Review of Chemical and Biomolecular Engineering, 2010. **1**: p. 299–320.
43. Chu, A. and P. Braatz, *Comparison of commercial supercapacitors and high-power lithium-ion batteries for power-assist applications in hybrid electric vehicles: I. Initial characterization.* Journal of Power Sources, 2002. **112**(1): p. 236-246.
44. Smith, K. and C.-Y. Wang, *Power and thermal characterization of a lithium-ion battery pack for hybrid-electric vehicles.* Journal of Power Sources, 2006. **160**(1): p. 662-673.
45. Burke, A.F., *Batteries and Ultracapacitors for Electric, Hybrid, and Fuel Cell Vehicles.* Proceedings of the IEEE, 2007. **95**(4): p. 806-820.

46. Yuan, X., H. Liu, and J. Zhang, *Lithium-ion Batteries: Advanced Materials and Technologies*2011: Taylor & Francis.
47. Yoshio, M., R.J. Brodd, and A. Kozawa, *Lithium-Ion Batteries: Science and Technologies*2009: Springer-Verlag New York.
48. Aravindan, V., et al., *LiMnPO4 - A next generation cathode material for lithium-ion batteries.* Journal of Materials Chemistry A, 2013. **1**(11): p. 3518-3539.
49. Hayner, C.M., X. Zhao, and H.H. Kung, *Materials for Rechargeable Lithium-Ion Batteries.* Annual Review of Chemical and Biomolecular Engineering, 2012. **3**(1): p. 445-471.
50. Zhang, W.-J., *A review of the electrochemical performance of alloy anodes for lithium-ion batteries.* Journal of Power Sources, 2011. **196**(1): p. 13-24.
51. Meyer, W.H., *Polymer Electrolytes for Lithium-Ion Batteries.* Advanced Materials, 1998. **10**(6): p. 439-448.
52. Song, J.Y., Y.Y. Wang, and C.C. Wan, *Review of gel-type polymer electrolytes for lithium-ion batteries.* Journal of Power Sources, 1999. **77**(2): p. 183-197.
53. Wang, G.X., et al., *Nanosize cobalt oxides as anode materials for lithium-ion batteries.* Journal of Alloys and Compounds, 2002. **340**(1–2): p. L5-L10.
54. Liaw, B.Y., et al., *Modeling capacity fade in lithium-ion cells.* Journal of Power Sources, 2005. **140**(1): p. 157-161.
55. Ramadesigan, V., et al., *Modeling and Simulation of Lithium-Ion Batteries from a Systems Engineering Perspective.* Journal of The Electrochemical Society, 2012. **159**(3): p. R31-R45.
56. Vu, A., Y. Qian, and A. Stein, *Porous Electrode Materials for Lithium-Ion Batteries – How to Prepare Them and What Makes Them Special.* Advanced Energy Materials, 2012. **2**(9): p. 1056-1085.
57. Chung, G.C., et al., *Effect of Surface Structure on the Irreversible Capacity of Various Graphitic Carbon Electrodes.* Journal of The Electrochemical Society, 1999. **146**(5): p. 1664-1671.
58. Inagaki, M., *Carbon materials Structure, texture and intercalation.* Solid State Ionics, 1996. **86–88, Part 2**(0): p. 833-839.
59. Tran, T.D., et al., *Commercial Carbonaceous Materials as Lithium Intercalation Anodes.* Journal of The Electrochemical Society, 1995. **142**(10): p. 3297-3302.

60. Delmas, C. and I. Saadoune, *Electrochemical and physical properties of the LixNi1−yCoyO2 phases.* Solid State Ionics, 1992. **53–56, Part 1**(0): p. 370-375.
61. Myung, S.-T., et al., *Structural, Electrochemical, and Thermal Aspects of Li [(Ni0.5Mn0.5) 1 − x Co x] O2 (0 ≤ x ≤ 0.2) for High-Voltage Application of Lithium-Ion Secondary Batteries.* Journal of The Electrochemical Society, 2008. **155**(5): p. A374-A383.
62. Shin, J.H., et al., *Rechargeable Li/LiFePO4 cells using N-methyl-N-butyl pyrrolidinium bis(trifluoromethane sulfonyl)imide–LiTFSI electrolyte incorporating polymer additives.* Electrochimica Acta, 2008. **54**(2): p. 410-414.
63. Wang, G.X., et al. *Structural and electro-chemical characteristics of Li1+x Mn2−x O4 and LiMn2 O4 for Secondary Lithium batteries.* in *Battery Conference on Applications and Advances, 1998., The Thirteenth Annual*. 1998.
64. Han, D.-W., et al., *Tailoring Crystal Structure and Morphology of LiFePO4/C Cathode Materials Synthesized by Heterogeneous Growth on Nanostructured LiFePO4 Seed Crystals.* ACS Applied Materials & Interfaces, 2013. **5**(4): p. 1342-1347.
65. Fergus, J.W., *Recent developments in cathode materials for lithium ion batteries.* Journal of Power Sources, 2010. **195**(4): p. 939-954.
66. de las Casas, C. and W. Li, *A review of application of carbon nanotubes for lithium ion battery anode material.* Journal of Power Sources, 2012. **208**(0): p. 74-85.
67. Iijima, S., *Helical microtubules of graphitic carbon.* Nature, 1991. **354**(6348): p. 56-58.
68. Arora, P. and Z. Zhang, *Battery Separators.* Chemical Reviews, 2004. **104**(10): p. 4419-4462.
69. A, M.S., *Review on gel polymer electrolytes for lithium batteries.* European Polymer Journal, 2006. **42**(1): p. 21-42.
70. Millet, P., F. Andolfatto, and R. Durand, *Preparation of solid polymer electrolyte composites: investigation of the precipitation process.* Journal of Applied Electrochemistry, 1995. **25**(3): p. 233-239.
71. Xu, K., *Nonaqueous Liquid Electrolytes for Lithium-Based Rechargeable Batteries.* Chemical Reviews, 2004. **104**(10): p. 4303-4418.
72. Saunier, J., et al., *Plasticized microporous poly(vinylidene fluoride) separators for lithium-ion batteries. I. Swelling behavior of dense membranes with respect*

to a liquid electrolyte—Characterization of the swelling equilibrium. Journal of Polymer Science Part B: Polymer Physics, 2004. **42**(3): p. 532-543.

73. Saunier, J., et al., *Plasticized microporous poly(vinylidene fluoride) separators for lithium-ion batteries. III. Gel properties and irreversible modifications of poly(vinylidene fluoride) membranes under swelling in liquid electrolytes.* Journal of Polymer Science Part B: Polymer Physics, 2004. **42**(12): p. 2308-2317.
74. Li, W. and J.R. Dahn, *Lithium-Ion Cells with Aqueous Electrolytes.* Journal of The Electrochemical Society, 1995. **142**(6): p. 1742-1746.
75. Barthel, J., R. Wachter, and H.J. Gores, *Temperature Dependence of Conductance of Electrolytes in Nonaqueous Solutions*, in *Modern Aspects of Electrochemistry*, B.E. Conway and J.O.M. Bockris, Editors. 1979, Springer US. p. 1-79.
76. Xiao, Q., et al., *A novel sandwiched membrane as polymer electrolyte for application in lithium-ion battery.* Journal of Membrane Science, 2009. **326**(2): p. 260-264.
77. Wachtler, M., et al., *A study on PVdF-based SiO2-containing composite gel-type polymer electrolytes for lithium batteries.* Electrochimica Acta, 2004. **50**(2–3): p. 357-361.
78. Webber, A., *Conductivity and Viscosity of Solutions of LiCF3 SO 3, Li (CF 3 SO 2) 2 N , and Their Mixtures.* Journal of The Electrochemical Society, 1991. **138**(9): p. 2586-2590.
79. Muniyandi, N., et al., *Optimisation of PVdF-based polymer electrolytes.* Journal of Power Sources, 2001. **96**(1): p. 14-19.
80. Yang, H., G.V. Zhuang, and P.N. Ross Jr, *Thermal stability of LiPF6 salt and Li-ion battery electrolytes containing LiPF6.* Journal of Power Sources, 2006. **161**(1): p. 573-579.
81. Angulakshmi, N., et al., *Electrochemical and mechanical properties of nanochitin-incorporated PVDF-HFP-based polymer electrolytes for lithium batteries.* Ionics, 2011. **17**(5): p. 407-414.
82. Shimizu, H., et al., *Sol-gel transitions of poly(vinylidene fluoride) in organic solvents containing LiBF4.* Polym J, 2011. **43**(6): p. 540-544.
83. Verdolotti, L., et al., *Effects of the addition of LiCl, LiClO4, and LiCF3SO3 salts on the chemical structure, density, electrical, and mechanical properties of*

rigid polyurethane foam composite. Polymer Engineering & Science, 2011. **51**(6): p. 1137-1144.

84. Park, J.K., *Principles and Applications of Lithium Secondary Batteries*2012: Wiley.
85. Chung, Y.S., S.H. Yoo, and C.K. Kim, *Enhancement of Meltdown Temperature of the Polyethylene Lithium-Ion Battery Separator via Surface Coating with Polymers Having High Thermal Resistance.* Industrial & Engineering Chemistry Research, 2009. **48**(9): p. 4346-4351.
86. Venugopal, G., et al., *Characterization of microporous separators for lithium-ion batteries.* Journal of Power Sources, 1999. **77**(1): p. 34-41.
87. Kang, Y., et al., *Photocured PEO-based solid polymer electrolyte and its application to lithium–polymer batteries.* Journal of Power Sources, 2001. **92**(1–2): p. 255-259.
88. Choi, B.K., K.H. Shin, and Y.W. Kim, *Lithium ion conduction in PEO–salt electrolytes gelled with PAN.* Solid State Ionics, 1998. **113–115**(0): p. 123-127.
89. Cho, T.-H., et al., *Battery performances and thermal stability of polyacrylonitrile nano-fiber-based nonwoven separators for Li-ion battery.* Journal of Power Sources, 2008. **181**(1): p. 155-160.
90. Djian, D., et al., *Macroporous poly(vinylidene fluoride) membrane as a separator for lithium-ion batteries with high charge rate capacity.* Journal of Power Sources, 2009. **187**(2): p. 575-580.
91. Gao, K., et al., *Crystal structures of electrospun PVDF membranes and its separator application for rechargeable lithium metal cells.* Materials Science and Engineering: B, 2006. **131**(1–3): p. 100-105.
92. Shen, Y.J., M.J. Reddy, and P.P. Chu, *Porous PVDF with LiClO4 complex as 'solid' and 'wet' polymer electrolyte.* Solid State Ionics, 2004. **175**(1–4): p. 747-750.
93. Costa, C.M., et al., *Effect of degree of porosity on the properties of poly(vinylidene fluoride–trifluorethylene) for Li-ion battery separators.* Journal of Membrane Science, 2012. **407–408**(0): p. 193-201.
94. Miao, R., et al., *PVDF-HFP-based porous polymer electrolyte membranes for lithium-ion batteries.* Journal of Power Sources, 2008. **184**(2): p. 420-426.
95. Costa, C.M., et al., *Evaluation of the main processing parameters influencing the performance of poly(vinylidene fluoride–trifluoroethylene) lithium-ion*

battery separators. Journal of Solid State Electrochemistry, 2013. **17**(3): p. 861-870.

96. Srun Jung, et al., *Fillers for Solid-State Polymer Electrolytes: Highlight.* Bull. Korean Chem. Soc, 2009. **30**(10).
97. Cai, L. and R.E. White, *Mathematical modeling of a lithium ion battery with thermal effects in COMSOL Inc. Multiphysics (MP) software.* Journal of Power Sources, 2011. **196**(14): p. 5985-5989.
98. Sikha, G., R.E. White, and B.N. Popov, *A Mathematical Model for a Lithium-Ion Battery/Electrochemical Capacitor Hybrid System.* Journal of The Electrochemical Society, 2005. **152**(8): p. A1682-A1693.
99. Chirkov, Y.G., V.I. Rostokin, and A.M. Skundin, *Computer simulation of operation of lithium-ion battery: Galvanostatics, central problem of theory, calculation of characteristics of thin active layers with low diffusion coefficients.* Russian Journal of Electrochemistry, 2011. **47**(11): p. 1239-1249.
100. Subramanian, V.R., V. Boovaragavan, and V.D. Diwakar, *Toward Real-Time Simulation of Physics Based Lithium-Ion Battery Models.* Electrochemical and Solid-State Letters, 2007. **10**(11): p. A255-A260.
101. Ramadesigan, V., et al., *Efficient Reformulation of Solid-Phase Diffusion in Physics-Based Lithium-Ion Battery Models.* Journal of The Electrochemical Society, 2010. **157**(7): p. A854-A860.
102. Subramanian, V.R., et al., *Mathematical Model Reformulation for Lithium-Ion Battery Simulations: Galvanostatic Boundary Conditions.* Journal of The Electrochemical Society, 2009. **156**(4): p. A260-A271.
103. Gomadam, P.M., et al., *Mathematical modeling of lithium-ion and nickel battery systems.* Journal of Power Sources, 2002. **110**(2): p. 267-284.
104. García, R.E., et al., *Microstructural Modeling and Design of Rechargeable Lithium-Ion Batteries.* Journal of The Electrochemical Society, 2005. **152**(1): p. A255-A263.
105. Sikha, G., B.N. Popov, and R.E. White, *Effect of Porosity on the Capacity Fade of a Lithium-Ion Battery: Theory.* Journal of The Electrochemical Society, 2004. **151**(7): p. A1104-A1114.
106. Ferguson, T.R. and M.Z. Bazant, *Nonequilibrium Thermodynamics of Porous Electrodes.* Journal of The Electrochemical Society, 2012. **159**(12): p. A1967-A1985.

107. Renganathan, S., et al., *Theoretical Analysis of Stresses in a Lithium Ion Cell.* Journal of The Electrochemical Society, 2010. **157**(2): p. A155-A163.

108. Dao, T.-S., C.P. Vyasarayani, and J. McPhee, *Simplification and order reduction of lithium-ion battery model based on porous-electrode theory.* Journal of Power Sources, 2012. **198**(0): p. 329-337.

109. Lee, J.-W., Y.K. Anguchamy, and B.N. Popov, *Simulation of charge–discharge cycling of lithium-ion batteries under low-earth-orbit conditions.* Journal of Power Sources, 2006. **162**(2): p. 1395-1400.

110. Martinez-Rosas, E., R. Vasquez-Medrano, and A. Flores-Tlacuahuac, *Modeling and simulation of lithium-ion batteries.* Computers & Chemical Engineering, 2011. **35**(9): p. 1937-1948.

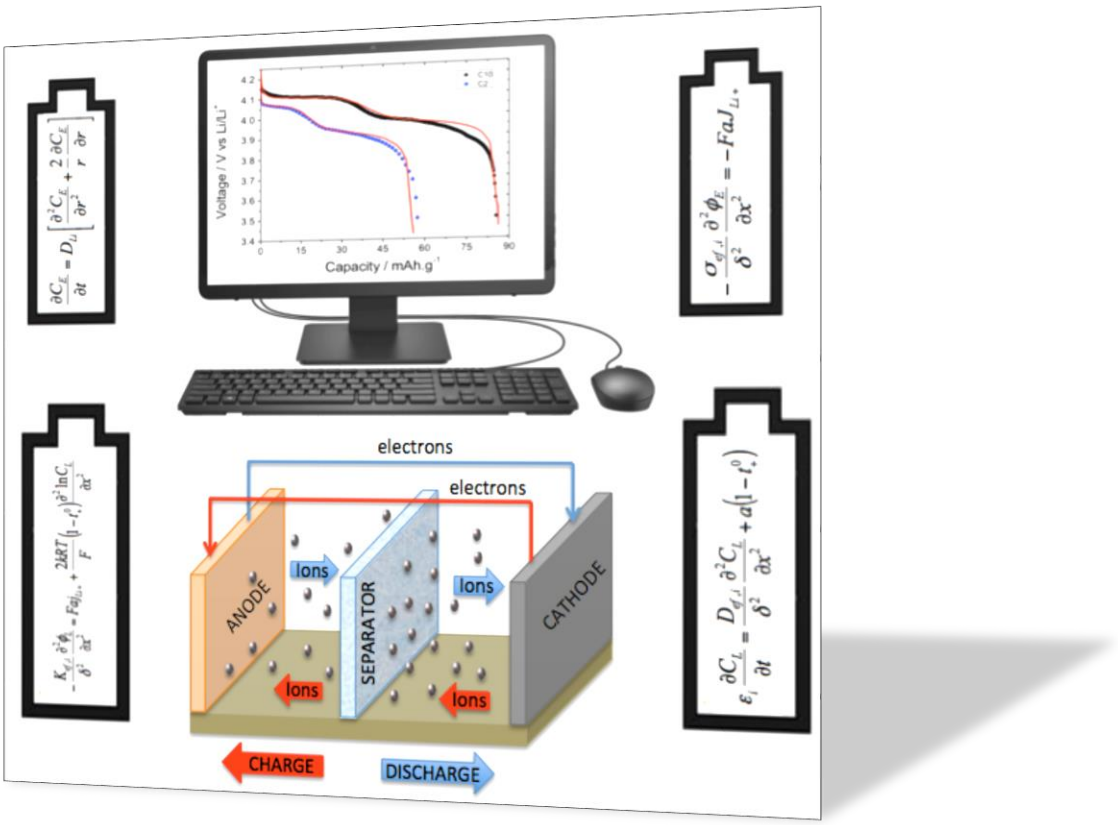

2. State of the art on microscopic theoretical models and simulations of lithium-ion rechargeable batteries

This chapter describes the state of art on the theoretical models for the simulation of the performance of lithium ion batteries. The main theoretical studies that describe the operation and performance of a battery are presented. Finally, the influence of the most relevant parameters of the models, such as boundary conditions, geometry and material characteristics are discussed.

This chapter is based on the following publication:

"Lithium ion rechargeable batteries: State of the art and future needs of microscopic theoretical models and simulations", D. Miranda, C.M. Costa, S. Lanceros-Mendez, Journal of Electroanalytical Chemistry 739 (2015) 97-110.

2.1 Microscopic modelling of lithium ion batteries

With the appearance of lithium batteries, several theoretical studies and models have been performed for understanding their main processes and for improving their performance. The developed models include parameters for the understanding of materials and microstructure of the electrodes, the most suitable organic solvents for electrolytes, geometry, dimensions of the different components of the battery and the materials and microstructure of the separator, among other variables [1–12]. Simulations and modeling have been performed through different programming languages, including C++ [13], MatLab [14], Simulink [15], Fluent [16], Battery Design Studio [17] and COMSOL Multiphysics [18], among others.

The microscopic models for the operation of lithium-ion batteries are based on the mathematical expressions of the fundamental physical and chemical processes associated to the electrochemical phenomena, ionic diffusion and mass transport. However, the models are simplified according to the boundary conditions selected as a function of the main goals of each study. Some models introduce also thermal conditions. The research in the development of models for lithium-ion batteries introduced important parameters in battery performance such as the parameter of porosity for electrodes and separators.

The majority of the theoretical models using the electrodes Li_xC_6–$Li_yMn_2O_4$ are based on the Doyle/Fuller/Newman model [19,20] with specific boundary conditions [21] in order to describe the three components of battery.

With the evolution of the complexity and accuracy of the models, higher processing time was required and reformulation of the mathematical models had to be performed in order to improve computational efficiency [5].

In this way, a simplified model for lithium-ion batteries based on the porous-electrode theory was presented [11], Figure 2.1. The model incorporates the concentrated solution theory, the porous electrode theory, and the variations in electronic/ionic conductivities and diffusivities, the simplification being based in exploiting the nature of the model and the structure of the governing equations.

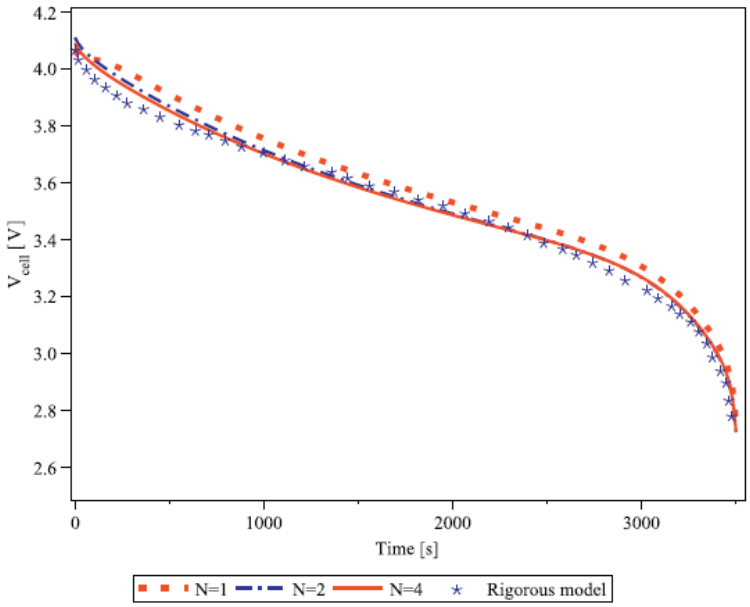

Figure 2.1 - 1C discharge voltage curve comparison between the rigorous model and the simplified model at different number of terms or node points through the Galerkin's approximation. Figure from [11].

The simplification of the model has been achieved through the Galerkin's approximation, which allows converting a continuous operator problem into a discrete problem, allowing to reduce computational time significantly while still retaining the accuracy compared to the full-order rigorous model.

A major difficulty to simulate lithium-ion batteries is the need to account for diffusion in the solid phase (active material) taking into account the spherical coordinates (dimension r). This fact increases the complexity of the models developed for lithium-ion batteries, as well as the computation time. In this context, a computationally efficient representation for solid phase diffusion was presented in [4] using an eigenfunction based Galerkin method and a mixed order finite difference method for approximating/representing solid-phase concentration variations within the active materials of the porous electrodes for a pseudo-two dimensional model for lithium ion batteries.

The complexity of the battery systems affects the speed and accuracy of the different numerical methods including operating and boundary conditions at the microscale.

2.2 Simulation of the components of the battery: electrodes and separator/electrolyte

In this section, the main results of the theoretical simulation developed for the different components of the lithium ion battery (electrodes and separator/electrolyte) will be presented. The models account for the study of undesirable phenomena in the battery performance (e.g. deposition of lithium ions at the cathode), the influence of the dimensions of the electrodes, the porosity and the particle size of the active material, as well as for a better under- standing of ionic conduction phenomena in lithium ion batteries. Typically, the theoretical models of the lithium-ion battery are 1-D and 2-D, being also developed models for spirally wound cells [22] in 3-dimensions [23].

2.2.1 Electrodes

In the study of lithium ion batteries, it was verified the importance given to phenomena occurring at the interface between electrodes and electrolytes (margins or edges). These effects were accounted for in the model of Kennell & Evitts [24] which focused on the prediction of the effects associated to electrode length and extent of the cathode and electrolyte in lithium ion batteries (Figure 2.2).

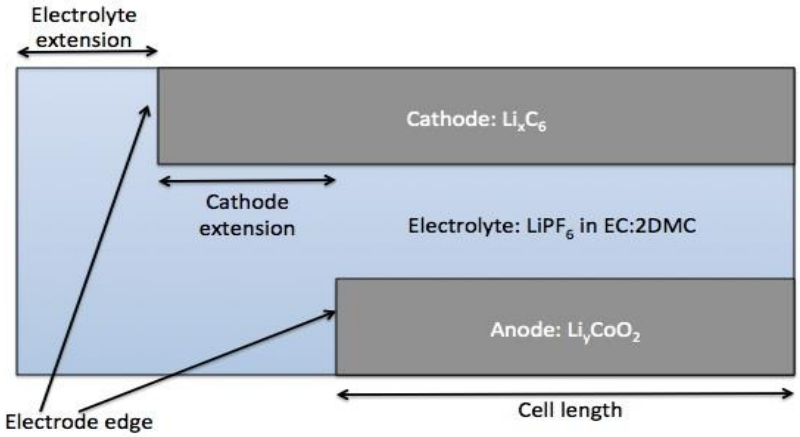

Figure 2.2 - Cell configuration (not to scale). The x-dimension corresponds to the length of the cell and the y-dimension corresponds to the height of the cell. Figure adapted from [24].

Lithium ions are produced and consumed at the electrode/electrolyte interfaces when the electrode comes into contact with the electrolyte, for example, when the electrolyte overflows the edges of the electrodes. At the ends of flooded electrodes (edges) the edge geometry can cause multidimensional effects, such as concentration gradients in the electrolyte and the electrodes, and also electrical potential gradients in the electrolyte. In [24], the authors explored the effects of the edges of the electrodes of the battery during charging and the effect of the gradient of the stoichiometric coefficient inside the electrode. It was shown that increasing effective conductivity relative to the electrolyte which extends beyond the edges of the electrodes does not have a significant effect on the rates of the anodic and cathodic reactions occurring at the edge regions of the electrodes. Furthermore, it is predicted that whereas lithium concentration gradients within the cathode have an impact on reaction rates of the cathode, lithium concentration gradients inside the anode have no significant impact on the rates of the anodic reactions during the early charge cell. It was verified that the rates of the anodic reactions are significantly affected by the surface area of the anode that is in contact with the electrolyte and not by the concentration gradient of lithium at the anode. It was also concluded that during the final stages of battery charge, the concentration gradients within the cathode (for equal lengths of electrodes) are more likely and may lead to deposition of lithium on the edge region of the cathode. In this study, simulations were performed for the case in which the tip of the cathode was extended beyond the edge of the anode to reduce the possibility of deposition of lithium at the edge region of the cathode. The simulations indicate that stoichiometric lithium in an extended edge of the cathode would be of little value, however, this extension may cause a high electric potential drop along the length of electrolyte during the initial battery charge. It was observed that a decreasing gradient equilibrium potential during charging of the battery causes a reduction in the rate of cathodic reactions which occurs along the extended cathode. This reduction in cathodic reactions along the extended region of the cathode reduces the risk for deposition of lithium on the cathode edge.

It is thus important to avoid the negative consequences for the performance of the cell that may arise due to concentration gradients associated with edges (interfaces) of the electrodes flooded by the electrolyte. These consequences include an increased risk of deposition of lithium on the cathode region. Therefore, the cathode extension beyond the edge of the anode can reduce the probability of deposition of lithium on the cathode

edge region. On the other hand, this may result in other problems, such as high drop in electrical potential along the length of the electrolyte in parallel with the electrodes and associated with the extended edge of the cathode [25,26].

West et al. [27] developed a one-dimensional model using porous electrodes and a liquid electrolyte, demonstrating that depletion in the electrolyte was the main factor that limits the discharge capacity of the battery. This depletion is a consequence of the mobility of the non-inserted ions, so the performance of this type of electrode is optimized by the choice of electrolyte through of the number of transport as close to unity as possible for the inserted ion.

Doyle et al. [19] presented a one dimensional model for a lithium ion battery and verified that the concentration of lithium decreased on the cathode material, illustrating the necessity of high concentrations of lithium. This model was developed in [28] considering a porous anode rather than a lithium foil anode. Transport in the electrolyte is described within the scope of the concentrated solution theory in the $Li_xC_6/Li_yMn_2O_4$ system with 1 M $LiClO_4$ in PC. Further, a two-dimensional model was also developed for the investigation of deposition of lithium [29] assuming:

- Concentration of electrolyte and conductivity are constant and uniform.
- Uniform concentration at the anode (the same concentration along the anode).
- Application of the linearization model of the Tafel kinetics.
- Solid film electrodes.
- Electroneutrality of the electrolyte.

It was shown that extending the cathode 0.4 mm is enough to prevent the occurrence of deposition of lithium.

Eberman et al. [30] used a two dimensional model based on the theory of concentrated solution for modeling the effects of decreased dimensions of a cathode in order to perform an analysis of various parameters on the risk of deposition of lithium. It was found that the three most important factors that affect the deposition are the open circuit potential, the rate of decreasing of the dimensions of the cathode and the charging rate.

A further two dimensional model for the study of the effects of concentration, distribution of current and electric field versus time profile in a lithium ion batteries [24] demonstrated that it is possible to predict not only the deposition of lithium on the cathode edge during higher charge times, but also the high electric gradients which were

observed experimentally in [25,26] along the electrolyte during the initial charging.

The influence of the variation of the electrode width and porosity of the electrodes in battery performance was also studied [21] leading to the conclusion that the width of the electrodes deter- mines two main factors in the function of the battery: the quantity of active material and the resistance to mass transport. The width of both electrodes was varied uniformly in a range of 80–120% of the baseline. It was found a slight increase in battery capacity when the width of the electrode increases. Further, the porosity of the electrodes affects the effective conductivity and the resistance to mass transfer. The variation of the porosity was performed in the same range used for the study of the width of the electrodes and it was verified that there is no linear relationship but the parameters can be optimized.

For plastic lithium-ion batteries it was developed a simulation model taking account the thickness value of the electrodes, active material loadings and initial salt concentrations with the objective of better understanding the transport processes of the plasticized polymer electrolyte system [31] in Bellcore PLION® cells. The results obtained in the simulation were compared with experimental data as shown in Figure 2.3.

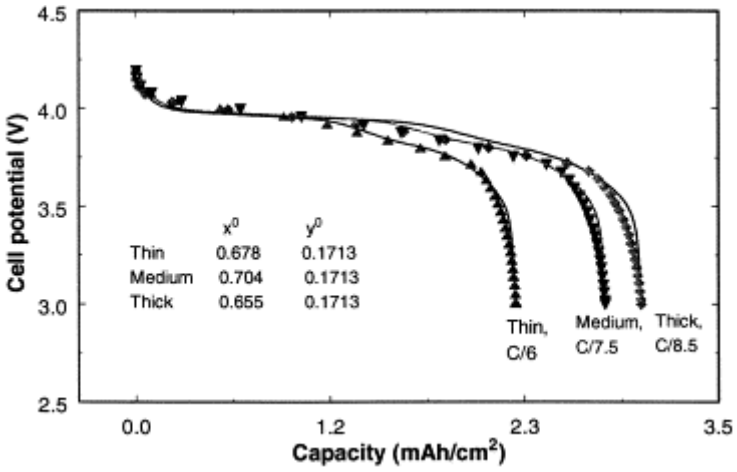

Figure 2.3 - Experimental and simulated discharge curves for PLION® cells at low rates. The C rates for thin, medium and thick cells are 2.312, 2.906, and 3.229 mA/cm^2, respectively. The dots represent the experimental data and the solid lines correspond to the simulation results. Figure from [31].

It is observed a good agreement between simulation and experimental data due to the use of a contact resistance at the interface between the current collector and the electrode, this being an adjustable parameter for different batteries. The diffusion coefficient of the salt at high discharge rates was also reduced to approximate the results of simulation with the experimental ones.

Regarding the dimensions of the electrodes (fine, medium and thick batteries) the diffusion limitations are most significant for thicker than fine and medium batteries and the limitations of diffusion in the solution phase are the main limiting factor for proper battery performance at high rate discharge [31].

Battery systems with lithium and nickel [6] have been simulated to account for the behavior of particles in a single electrode, individual cells and complete batteries (complete set of cells) based on varying operation conditions such as constant current discharge, pulse discharge, cyclic voltammetry and impedance. A review of the theoretical models for nickel, simulating the performance of complete cells, including the behavior of the active material (nickel hydroxide) was presented. It was concluded that the diffusion coefficient depends on the size of the cells as shown in Figure 2.4.

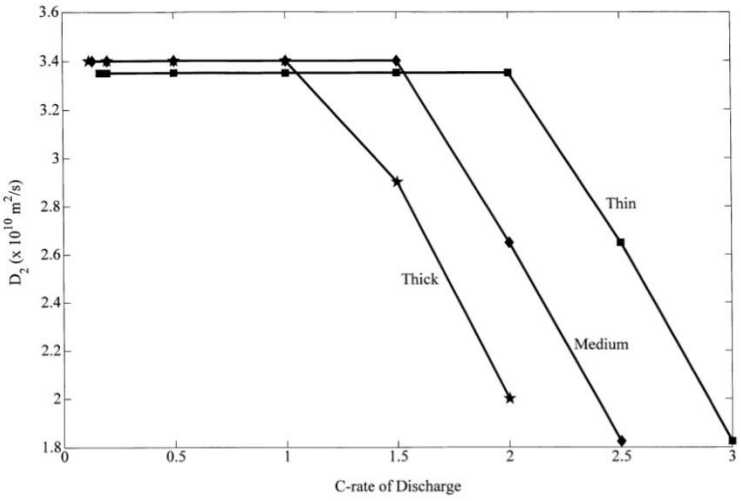

Figure 2.4 - Solution phase diffusion coefficient as a function of discharge rate used to fit experimental data for three different cells. 1C corresponds to 1.156, 1.937 and 2.691 A/m^2 for thin, medium and thick cells, respectively. Figure from [6].

In the study ($Li_yC_6/Li_xMn_2O_4$) [7], the properties of recharge- able lithium-ion batteries was calculated considering the electro- chemical properties of the materials and focusing on the influence of their microstructure. The main conclusion is that the

battery performance can be improved by controlling the transport paths to the back of the porous positive electrode, maximizing the surface area for intercalating lithium ions, and carefully controlling the distribution and particle size of the active material.

The model developed for the calculation of the effect of porosity on the capacity fade of a lithium-ion battery [8] includes the changes in the porosity of the material due to the reversible intercalation processes and irreversible parasitic reactions. Thus, a general method for the capacity fade prediction of a lithium ion battery system was presented. The variation in porosity due to the side reaction products formed during cycling causes the discharge voltage plateau to drop with cycling.

With respect to the theoretical analysis of stresses in a lithium ion cell [10], the mathematical model is developed to simulate the generation of mechanical stress during the discharge process in a dual porous insertion electrode cell sandwich comprised of lithium cobalt oxide and carbon. This model shows that the accumulation of stress within intercalation electrodes leads to changes in the lattice volume due to the intercalation and phase transformation during charge/discharge. The model provides the main parameters influencing the magnitude of the battery generation of stress, such as thickness, porosity and particle size of the electrodes. The developed model is used to understand the mechanical degradation of a porous electrode during the process of insertion/ extraction of lithium ions.

Other studies are based on the effort to gain a better under- standing of conduction phenomena of the lithium ion [32] in order to allow innovative technologies and a comprehensive understanding of the phenomena of conduction in all components of a lithium-ion battery incorporating theoretical analyses of the fundamentals of electrical and ionic conduction at the cathode, anode and electrolyte. A review of the relationship between electrical and ionic conduction of three cathode materials: $LiCoO_2$, $LiMn_2O_4$, $LiFePO_4$, is presented in [32], discussing the phase shift in graphite anodes and how they relate to diffusivity and conductivity. The phenomenon of electrical and ionic conduction has been one of the main objectives of the study for the development of models of lithium-ion batteries. The review work presented in [32] refers to various aspects of this problem that have been dis- cussed for each of the main components of a lithium-ion battery (anode, cathode and electrolyte) as previously stated.

Efforts to optimize the electrical and ionic conductivity and the cathode have focused largely on doping methods (liquid–solid method, spray drying method, etc.) to

improve the electrical conductivity and ionic conductivity. Viable methods for improving the electrical conductivity are based on covering the cathode surface using a conductive material and by using micro and nanoparticles [32] as shown in Figure 2.5 for $LiFePO_4$ active material.

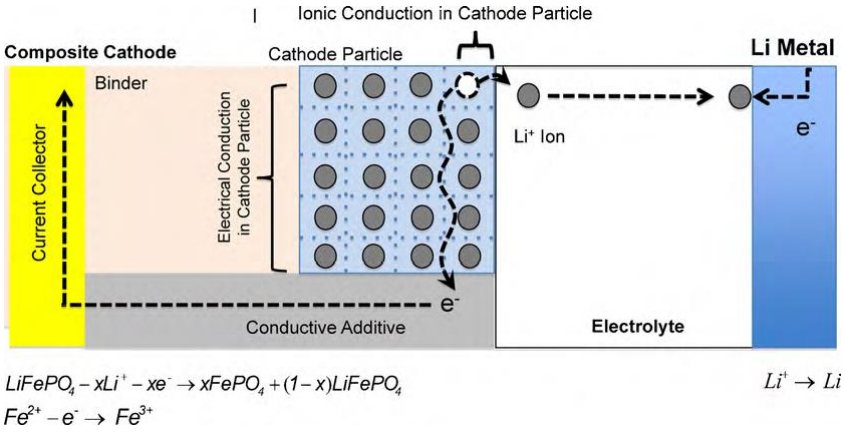

Figure 2.5 - Conduction phenomena in the $LiFePO_4$ cathode during battery charging. Figure from [32].

Mathematical developments suggest that fibrous architectures, such as carbon–silicon-nanocomposites, show better results with respect to improving ionic conductivity [33].

With respect to the anodes, importance is attributed to the intercalation process. The most commonly used materials for the anode are carbonaceous materials including graphites (natural graphite and Highly Ordered Pyrolytic Graphite (HOPG)), modified graphites (MesoCarbon MicroBeads (MCMB), carbon fiber, metal deposited carbon fiber) and non-graphitic carbons. The diffusivity of lithium ion in graphite is complicated by the constant change in the phase intercalation compound Li–graphite, which can cause disorder in the original structure [32].

It is observed that with increasing degree of intercalation the diffusivity becomes smaller. For this reason, the diffusivity must be understood as a function of electrode voltage or intercalation. Further, the optimization between the crystalline and amorphous phases is an important strategy for improving conductivity in carbon electrodes.

Computer simulation models [2] are used for studying the operation of a lithium-ion battery discharge galvanostatic mode based on the central problem and calculation of the characteristics of thin active layers with low diffusion coefficients. The authors

showed the mathematical model of the processes occurring in the active layers of the electrodes. The central problem of the theory of lithium ion batteries is the possibility of analyzing two processes in space and time: the recovery or filling of active substance (intercalating agent) grains with lithium atoms and redistribution of electrode potentials over the active layer width, which related to ohmic limitations. The authors report that the diffusion coefficient of lithium atoms in the grain intercalating agent is important. In the electrodes with high diffusion coefficients, the size of the intercalating agent grain is limited, whereas in the electrodes with low diffusion coefficient, there are no restrictions on the grain size.

In this study, the advantages and disadvantages of the electrodes in relation to the high and low diffusion coefficients are reported. The calculation of these parameters of the electrolyte is achieved for active layers with low diffusion coefficients such as $\leq 10^{-13}$ cm^2/s. The thickness of the active layer, the time of full dis- charge, electrical capacitance and specific potential within the interface layer/interactive electrodes are determined where the grain size is commonly limited to approximately 10μm.

The importance of the electrode design, i.e., its performance through of the optimization of parameters (the weight fraction of electronic particle additives, electrode thickness and electrode density or porosity) was shown in [34]. Numerical model simulation also proved that ion transport in the electrolyte phase becomes more difficult in dense electrodes and that high electrode compression to obtain high energy density may cause severe transport loss. However, the discharge current will decrease with increasing grain size.

Chen et al. [35], showed that design of cathode electrodes for high specific energy also creates higher operation and specific power. It is observed that for improving the performance of the cathode, the most important issue is to properly consider the cathode thickness and volume fraction of active material with respect to ion transportation, cathode capacity and mass balance effect of active material. The addition of additives (for example, carbon back) improves the specific energy through optimization of the cathode composition and cathode design but penalizes both volumetric and gravimetric properties of the cathode.

The prediction of the impedance response of a dual insertion electrode cell separated by an ionically conduction membrane was presented in [36]. The used expressions take into account the reaction kinetics and double-layer adsorption processes at the

electrode–electrolyte interface, transport of electroactive species in the electrolyte phase and solid phase of the electrodes. The prediction of the impedance response was obtained through the analytical expression development of a lithium-ion cell consisting on a porous $LiCoO_2$ cathode and mesocarbon microbead anode [36].

The lithium-ion concentration profile simulation in the cathode for a half-cell was studied in [37]. The model used in this work describes the discharge behavior of a rechargeable cell based on the simulated concentration profile. The cathode material used of this work was $LiMn_2O_4$.

In secondary batteries, the battery design was optimized through the efficient design of porous electrodes using a physics based porous electrode theory model with increased computational efficiency [38]. This model optimizes the discharge capacity given size constraints, rather than time constraints and minimizing the temperature gradient across a cell for sage operation and prevention of thermal runaway.

Cooper et al., quantified the effect of tortuosity of the porous electrode on the diffusion through the material. No correlation was observed between the measured tortuosities and the ones determined by Bruggeman equation [39] in which an isotropic and homogeneous material is considered.

These simulations demonstrate thus that tortuosity is not a simple scalar quantity, but instead both geometrical and transport tortuosities show a marked dependence on direction, i.e., a vectorial representation of tortuosity should be developed [39].

The capacity of lithium-ion batteries has been improved by adding conducting species in the battery materials, more specifically the cathode [35]. The addition of conducting species shall not limit the transport and performance at high discharge rates. This work [35] developed a technique to optimize the cathode with respect to ionic and electrical conductivity and specific energy. Figure 2.6 illustrates the composition of the simulated structure of the complementary solid phase and electrolyte phase obtained by finite element conduction model.

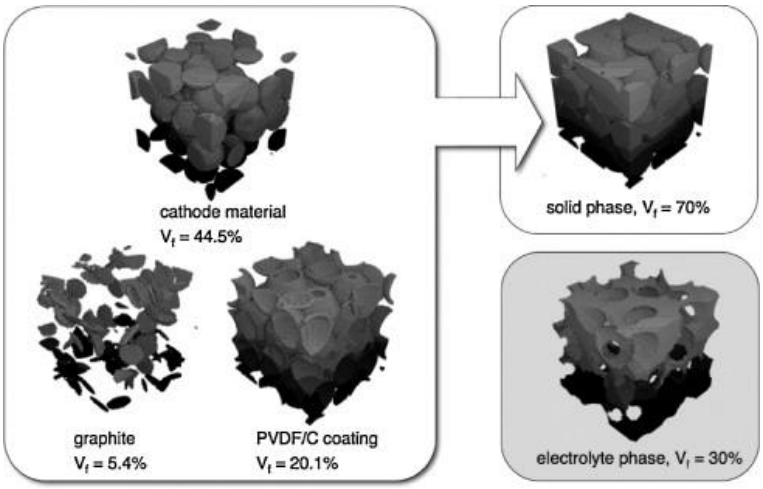

Figure 2.6 - Illustration of the composition of the cathode electrode: complementary solid phase and electrolyte phase [35].

It is shown in this way the importance of the design of the cathode and how to optimize the composition of the cathode with additives for improved specific energy.

The influence of different electrode ($LiFePO_4$) parameters on the performance of the battery, including conflicting effects of the conductor ratio (the weight fraction of electronic particle additives), electrode thickness and density (porosity), were addressed on the basis of experimental results and simulations [34]. In the context of the simulation model, it was concluded that the transport of ions decreases for thicker electrodes. Although the compression of the electrodes increases the energy density, it can cause a decrease in ion transport by reducing the diffusion and ionic conductivity from the electrolyte phase to the electrode. Further, at high discharge rates, very thick or very dense electrodes show a significant loss of tension due to a slowdown of the transport of ions in the liquid phase (so-called limited transport). Increased thickness and density of the electrode above a certain critical values lead to a small increase in the discharge capacity of the cell [34].

The influence of the microstructural morphology of the electrode ($LiCoO_2$, $LiFePO_4$ and $LiMn_2O_4$) in the performance of the battery is analyzed in [40]. An analytical approach is presented that properly reproduces the experimental results obtained after measuring the resistance of the electrode, capturing the most important effects of the microstructure of the electrode in battery performance. For $LiCoO_2$ and $LiFePO_4$ the relevance of solid surface characteristics and microstructure are significant due to losses in the electrical charge transport efficiency, including reduced charge

transfer kinetics [40].

The effect of tortuosity anisotropy in lithium-ion battery electrodes was shown for $LiNi_{1/3}Mn_{1/3}Co_{1/3}O_2$ and $LiCoO_2$ [41]. For these active materials, Bruggeman exponents are estimated to be 0.66 and 1.94 for $LiNi_{1/3}Mn_{1/3}Co_{1/3}O_2$ and $LiCoO_2$, respectively. These Bruggeman exponents are in agreement with those calculated through the numerical diffusion simulations performed directly on the tomography data [41]. Independently of the active material, alignment of the particles parallel to the current collector during electrode manufacturing affects the tortuosity and porosity value of the electrodes.

Mathematical models for lithium-ion cells with blended-electrodes were also developed [42]. These dynamic models allow simulations under various operating conditions such as C-rate and temperature by solving physico-chemical governing equations. The results of the models show good agreement with the experiment data, confirming that the present model is useful for evaluating possible active material compositions [42].

2.2.2 Separator and electrolyte

The key issues for conduction in organic liquid, solid state electrolytes and ionic liquids are summarized in [32], together with the ionic conductivity for various electrolytes (organic solvents, ionic liquids and electrolytes in solid state) indicating that $LiPF_6$ in 1M EC/DMC shows high ionic conductivity (10.7 mS/cm), rapid solvation and good interface between electrodes but is sensitive to ambient moisture and solvents.

The study of the performance of lithium-ion batteries by varying initial concentration of salt in the electrolyte [21] shows that the concentration of lithium ions in the electrolyte influences the conductivity (κ) in a non-linear way. A battery with an initial concentration in 2000 mol/m^3 gives rise to a low battery capacity ~0.6 mAh/m^2.

Above this concentration, the improvements on the capacity of the cell are smaller up to 1.8 mAh/m^2, leading to the conclusion that this parameter can be optimized contributing also to a decrease of the battery manufacturing cost.

In relation to battery separators (single polymer, composites and polymer blends) it is verified that the ionic conductivity depends not only on the characteristics of the electrolyte solution but also on the properties of the membrane (in particular porosity

and pore size) [43] as also reported in [44]. Typically, the ionic conductivity of the separator is described through of the Bruggeman equation. Theoretical and experimental evidence show that a Bruggeman exponent of 1.5 is often not valid for real electrodes or separator materials [44]. It was observed that only idealized morphologies, based on spherical or ellipsoids give rise to a Bruggeman law with an exponent of about 1.3. Polymer membranes with different morphologies or composite materials increase the tortuous path for ionic conductivity and result either in a significant increase of the exponent α or in a complete deviation from the power law. It is found that the MacMullin number increases with increasing anisotropy, i.e. approximately linear function of $1/\varepsilon$ [44]. The diffusion limitations in thick cells has been also reported [31]. Rate-dependent salt diffusion coefficients are probably an artifact of tortuous and inhomogeneous paths for salt diffusion inside the electrode/gelled polymer regions and reflect the inadequacy of the present simplified treatment of salt transport based on a binary electrolyte.

In order to understand the effect of electrolyte deterioration in the performance of Li–air batteries, a micro–macro model was constructed that includes the homogeneous phenomenon associated with the formation of Li_2CO_3 that occurs by degradation of the electrolyte during battery cycles, as shown in Figure 2.7 [45].

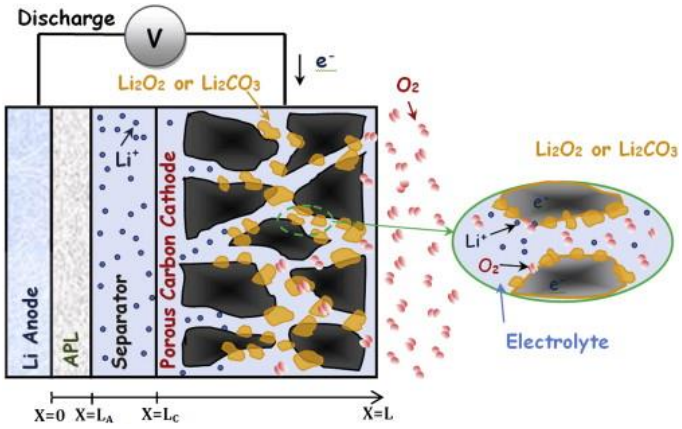

Figure 2.7 - Schematic computation domain of a Li–air battery during discharge operation. The inset demonstrates the discharge products formation of Li_2O_2 and Li_2CO_3 covering the porous carbon surface. Figure from [45].

The deterioration of the cycle performance is measured in terms of retention of discharge capacity, the model including the irreversible effect of the Li_2CO_3 in the discharge. A good relationship between the simulation model and experimental data was obtained, the results indicating a gradual decrease for retention of discharge capacity with increasing number of cycles due to the effect of irreversible formation of the Li_2CO_3 discharge product [45].

Due of the advances/improvements in battery separators, morphology parameters such as porosity, pore size, tortuosity, MacMullin number and polymer density have to be included in the computer simulation models in order to properly design and optimize battery performance.

The knowledge and correlation between ionic conductivity, porosity, pore size, mechanical and thermal properties are essential to achieve adequate battery separators with high performance for lithium ion batteries. It is a new field for computer simulation that can certainly provide new hints on battery materials optimization, in particular with respect to future trends in which conventional electrolytes can be replaced by gel electrolytes, ionic liquids and solid systems.

2.3 Thermal behavior simulation

In this section models for the influence of the thermal behavior in lithium ion battery performance will be presented as well as other relevant studies for the development and evaluation of predictive models for efficient battery performance.

A two-dimensional model for the thermal effect on the performance of lithium-ion battery [46] was developed using a binary electrolyte and thermal conditions ranging from adiabatic to isothermal. For adiabatic conditions, Figure 2.5, the temperature of the battery increasing rapidly during the discharge at 1C, resulting in a higher diffusion coefficient value for the binary electrolyte, thereby reducing the limitations of diffusion. This fact can be verified by comparing the profile of the concentration of the electrolyte at different cooling conditions. It was found that the concentration profile under the adiabatic condition presents a smaller variation along the length of the battery, unlike what happens in the case isothermal conditions. This observation indicates better diffusion properties of the electrolyte under the adiabatic condition in relation to isothermal condition. Figure 2.8 shows the temperature on the cell surface during 1C

discharge process under different cooling conditions and Figure 2.9 shows the cell voltage for 1C discharge process under different cooling conditions [46].

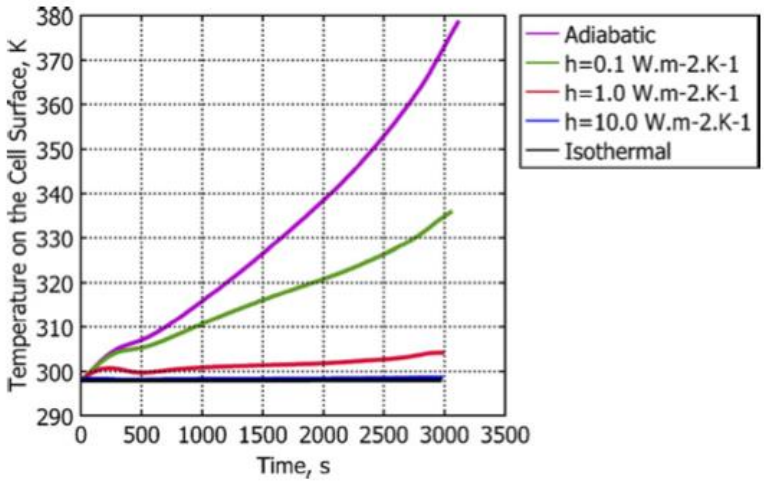

Figure 2.8 - Temperature on the cell surface during 1C discharge process under different cooling conditions. Figure from [46].

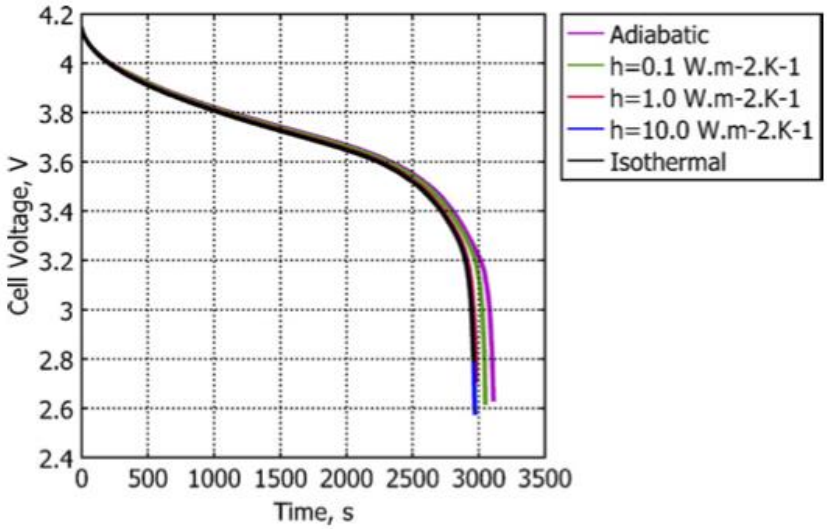

Figure 2.9 - Cell voltage for 1C discharge process under different cooling conditions. Figure from [46].

On the other hand, although good thermal insulation improves the discharge capacity, the high temperature that the battery reaches causes an increase in the risk of degradation of the battery.

The analysis of the electrochemical and thermal behavior of lithium ion batteries

[47] through a model based on two-dimensional thermal-electrochemical principles incorporating reversible, irreversible and ohmic heats in the solid and solution phases has been performed. The temperature dependence of the various trans- port, kinetic, and mass transfer parameters based on Arrhenius expressions are obtained.

The model incorporates experimental data on the entropic contribution for the manganese oxide spinel and carbon electrodes with the objective of evaluating the importance of this term in the overall heat generation.

The simulations were used to estimate the thermal and electric energy and the active material at various rates with the objective of understanding the effect of temperature on electrochemistry.

Simulations were performed at different rates to evaluate the importance of the different contributions to the total heat generated in the battery. The reversible heat was found to be important in all rates, contributing both to the final temperature of the battery at all rates and to the evolution of the temperature during discharge.

The non-uniform reaction distribution in the porous electrode was significant at higher rates, which in turn introduces error in estimating the heat generation based on the average cell voltage and open-circuit voltage [47].

Predictive models for commercial lithium-ion batteries have been also performed with the objective of evaluating the efficiency of the developed models. The study [48] compares battery performance simulations from a commercial lithium-ion battery modeling software package against manufacturer performance specifications and laboratory tests to assess model validity. The authors used the Battery Design Studio ® (BDS) software to create a mathematical model of each battery. The authors concluded that BDS can provide sufficient accuracy in discharge performance simulations for many applications.

An analytical model for the prediction of the remaining battery capacity of lithium-ion batteries was presented in [49]. The model allows to predict the residual energy of the battery source that powers a portable electronic device based on a design and management policy for the dynamic energy efficient device. The precision of the model was validated by comparison with simulation results DUALFOIL [50], with low discrepancy (maximum 5%) between the predicted and simulated results.

Other models coupling thermal and electrochemical responses are developed to predict the performance of lithium-ion batteries when those are subjected to different

temperatures during the operation of the battery [51]. The models are in agreement with the experimental results obtained for constant and pulsing charging and discharging conditions characteristic of hybrid electric vehicles (HEV). This model opens the possibility to predict and prevent situations of deposition of lithium resulting in the loss of capacity of lithium ions battery in vehicles, allowing the study of the degradation process and the life cycle of the batteries.

Other studies show the development of a thermal model applied to lithium ion batteries. The models include equations related to the diffusion coefficient and reaction rate coefficient of the electrodes as a function of temperature. These equations also include the activation energy for diffusion and the activation energy for reaction of electrodes, respectively E_{ad} and E_{ak}. The values of both activation energies depend on the active material. Further, the ionic conductivity and diffusion coefficient of the salt in the electrolyte as a function of temperature are also shown [52,53].

2.4 Conclusions

This chapter summarizes the main results of the theoretical models evaluating the contributions of each of the components of a battery, anode, cathode and separator, the performance of a lithium- ion battery. The main materials are described as well as the main mathematical framework of the models.

Parameters affecting separator performance such as degree of porosity, pore size and tortuosity, among others, have not been taken into account, the separator being considered, in most studies, as a continuous medium with porosity and described by the Bruggeman equation.

With respect to the electrodes (anode and cathode), simulations have taken into account porosity, with no emphasis in pore size, which is a relevant parameter. The models developed for electrodes take into account the radius of the particles of the active material and their influence in the insertion/extraction of lithium ions to/from the electrodes, the nature of the composite used in electrodes and their electrical characteristics, the mechanical stability and degree of crystallinity. Theoretical models were developed to describe the operation of a lithium-ion battery, focusing mainly on the variation of the boundary conditions. The models also account for the influence of

temperature, battery geometry and dimensions of their components (such as extension of the cathode in order to reduce the risk of deposition of lithium on the cathode edges) on battery performance.

Recent studies are focusing on the insertion of new species of ions such as sodium and magnesium ions, and future research should focus on theoretical models for the optimization of separators and electrodes for sodium and magnesium-ion batteries.

Regarding the implementation of the optimized models for electrodes, future studies may focus on the use of different active materials and evaluate the influence of electrical potential, porosity and capabilities of electrodes on insertion and extraction of lithium, magnesium and sodium ions, in order to find more efficient electrodes. Future work may focus on nano- and micro-porous electrode structures based on pure polymers and nanocomposites, combining selected fillers with organic matrix.

Studies related to the separator membranes should improve knowledge on the influence of the degree of porosity, pore size, the tortuosity, MacMullin number, Bruggeman coefficient. The characteristics of the material for the separator, including electrical insulation capacity (electrical properties), flexibility and mechanical stability (mechanical properties), degree of degradation with the electrolyte, relative performance against short circuits, ease of insertion into the electrolyte, effect of thickness and ionic conductivity in battery performance should be further addressed. Finally, once materials have been improved, charging characteristics, energy density and discharge capacity of the batteries must be studied and models of Li, Mg and Na-ion batteries should be optimized taking into account the influence of variables such as temperature, pressure and geometry.

2.5 References

1. Sikha, G., R.E. White, and B.N. Popov, *A Mathematical Model for a Lithium-Ion Battery/Electrochemical Capacitor Hybrid System.* Journal of The Electrochemical Society, 2005. **152**(8): p. A1682-A1693.
2. Chirkov, Y.G., V.I. Rostokin, and A.M. Skundin, *Computer simulation of operation of lithium-ion battery: Galvanostatics, central problem of theory, calculation of characteristics of thin active layers with low diffusion coefficients.* Russian Journal of Electrochemistry, 2011. **47**(11): p. 1239-1249.
3. Subramanian, V.R., V. Boovaragavan, and V.D. Diwakar, *Toward Real-Time Simulation of Physics Based Lithium-Ion Battery Models.* Electrochemical and Solid-State Letters, 2007. **10**(11): p. A255-A260.
4. Ramadesigan, V., et al., *Efficient Reformulation of Solid-Phase Diffusion in Physics-Based Lithium-Ion Battery Models.* Journal of The Electrochemical Society, 2010. **157**(7): p. A854-A860.
5. Subramanian, V.R., et al., *Mathematical Model Reformulation for Lithium-Ion Battery Simulations: Galvanostatic Boundary Conditions.* Journal of The Electrochemical Society, 2009. **156**(4): p. A260-A271.
6. Gomadam, P.M., et al., *Mathematical modeling of lithium-ion and nickel battery systems.* Journal of Power Sources, 2002. **110**(2): p. 267-284.
7. García, R.E., et al., *Microstructural Modeling and Design of Rechargeable Lithium-Ion Batteries.* Journal of The Electrochemical Society, 2005. **152**(1): p. A255-A263.
8. Sikha, G., B.N. Popov, and R.E. White, *Effect of Porosity on the Capacity Fade of a Lithium-Ion Battery: Theory.* Journal of The Electrochemical Society, 2004. **151**(7): p. A1104-A1114.
9. Ferguson, T.R. and M.Z. Bazant, *Nonequilibrium Thermodynamics of Porous Electrodes.* Journal of The Electrochemical Society, 2012. **159**(12): p. A1967-A1985.
10. Renganathan, S., et al., *Theoretical Analysis of Stresses in a Lithium Ion Cell.* Journal of The Electrochemical Society, 2010. **157**(2): p. A155-A163.

11. Dao, T.-S., C.P. Vyasarayani, and J. McPhee, *Simplification and order reduction of lithium-ion battery model based on porous-electrode theory.* Journal of Power Sources, 2012. **198**(0): p. 329-337.
12. Lee, J.-W., Y.K. Anguchamy, and B.N. Popov, *Simulation of charge–discharge cycling of lithium-ion batteries under low-earth-orbit conditions.* Journal of Power Sources, 2006. **162**(2): p. 1395-1400.
13. C++. http://www.cplusplus.com/. Available from: http://www.cplusplus.com/.
14. MatLab. http://www.mathworks.com/products/matlab/. Available from: http://www.mathworks.com/products/matlab/.
15. Simulink. http://www.mathworks.com/products/simulink/. Available from: http://www.mathworks.com/products/simulink/.
16. Fluent. http://www.ansys.com/. Available from: http://www.ansys.com/.
17. Studio, B.D. http://www.batterydesignstudio.com/. Available from: http://www.batterydesignstudio.com/.
18. Multiphysics, C. http://www.comsol.com/. Available from: http://www.comsol.com/.
19. Doyle, M., T.F. Fuller, and J. Newman, *Modeling of Galvanostatic Charge and Discharge of the Lithium/Polymer/Insertion Cell.* Journal of The Electrochemical Society, 1993. **140**(6): p. 1526-1533.
20. Doyle, M., et al., *Comparison of Modeling Predictions with Experimental Data from Plastic Lithium Ion Cells.* Journal of The Electrochemical Society, 1996. **143**(6): p. 1890-1903.
21. Martinez-Rosas, E., R. Vasquez-Medrano, and A. Flores-Tlacuahuac, *Modeling and simulation of lithium-ion batteries.* Computers & Chemical Engineering, 2011. **35**(9): p. 1937-1948.
22. Harb, J.N. and R.M. LaFollette, *Mathematical Model of the Discharge Behavior of a Spirally Wound Lead - Acid Cell.* Journal of The Electrochemical Society, 1999. **146**(3): p. 809-818.
23. Long, J.W., et al., *Three-Dimensional Battery Architectures.* Chemical Reviews, 2004. **104**(10): p. 4463-4492.
24. Evitts, G.F.K.a.R.W., *Two-Dimensional Lithium-Ion Battery Modeling with Electrolyte and Cathode Extensions,.* Advances in Chemical Engineering and Science, 2012. **2 No. 4**: p. 423-434.

25. E. Scott, G.T., B. Anderson and C. Schmidt, *Anoma- lous Potentials in Lithium Ion Cells: Making the Case for 3-D Modeling of 3-D Systems.* The Electrochemical So- ciety Meeting, Orlando, 13 October 2003.
26. E. Scott, G.T., B. Anderson and C. Schmidt, *Observation and Mechanism of Anomalous Local Potentials during Charging of Lithium Ion Cells.* The Electrochemical Society Meeting, Paris, 29 April 2003.
27. West, K., T. Jacobsen, and S. Atlung, *Modeling of Porous Insertion Electrodes with Liquid Electrolyte.* Journal of The Electrochemical Society, 1982. **129**(7): p. 1480-1485.
28. Fuller, T.F., M. Doyle, and J. Newman, *Simulation and Optimization of the Dual Lithium Ion Insertion Cell.* Journal of The Electrochemical Society, 1994. **141**(1): p. 1-10.
29. Tang, M., P. Albertus, and J. Newman, *Two-Dimensional Modeling of Lithium Deposition during Cell Charging.* Journal of The Electrochemical Society, 2009. **156**(5): p. A390-A399.
30. Eberman, K., et al., *Material and Design Options for Avoiding Lithium Plating during Charging.* ECS Transactions, 2010. **25**(35): p. 47-58.
31. Arora, P., et al., *Comparison between computer simulations and experimental data for high-rate discharges of plastic lithium-ion batteries.* Journal of Power Sources, 2000. **88**(2): p. 219-231.
32. Park, M., et al., *A review of conduction phenomena in Li-ion batteries.* Journal of Power Sources, 2010. **195**(24): p. 7904-7929.
33. Wolf, H., et al., *Carbon–fiber–silicon-nanocomposites for lithium-ion battery anodes by microwave plasma chemical vapor deposition.* Journal of Power Sources, 2009. **190**(1): p. 157-161.
34. Yu, S., et al., *Investigation of design parameter effects on high current performance of lithium-ion cells with LiFePO4/graphite electrodes.* Journal of Applied Electrochemistry, 2012. **42**(6): p. 443-453.
35. Chen, Y.H., et al., *Porous cathode optimization for lithium cells: Ionic and electronic conductivity, capacity, and selection of materials.* Journal of Power Sources, 2010. **195**(9): p. 2851-2862.

36. Sikha, G. and R.E. White, *Analytical Expression for the Impedance Response for a Lithium-Ion Cell.* Journal of The Electrochemical Society, 2008. **155**(12): p. A893-A902.
37. Yusof, N., A.S.H. Basari, and N.K. Ibrahim. *Prediction of the lithium-ion cell performance via concentration profile simulation*. in *Green and Ubiquitous Technology (GUT), 2012 International Conference on*. 2012.
38. De, S., et al., *Model-based simultaneous optimization of multiple design parameters for lithium-ion batteries for maximization of energy density.* Journal of Power Sources, 2013. **227**(0): p. 161-170.
39. Cooper, S.J., et al., *Image based modelling of microstructural heterogeneity in LiFePO4 electrodes for Li-ion batteries.* Journal of Power Sources, (0).
40. Nelson, G.J., et al., *Microstructural Effects on Electronic Charge Transfer in Li-Ion Battery Cathodes.* Journal of The Electrochemical Society, 2012. **159**(5): p. A598-A603.
41. Ebner, M., et al., *Tortuosity Anisotropy in Lithium-Ion Battery Electrodes.* Advanced Energy Materials, 2014. **4**(5): p. n/a-n/a.
42. Jung, S., *Mathematical model of lithium-ion batteries with blended-electrode system.* Journal of Power Sources, 2014. **264**(0): p. 184-194.
43. Costa, C.M., M.M. Silva, and S. Lanceros-Mendez, *Battery separators based on vinylidene fluoride (VDF) polymers and copolymers for lithium ion battery applications.* RSC Advances, 2013.
44. Patel, K.K., J.M. Paulsen, and J. Desilvestro, *Numerical simulation of porous networks in relation to battery electrodes and separators.* Journal of Power Sources, 2003. **122**(2): p. 144-152.
45. Sahapatsombut, U., H. Cheng, and K. Scott, *Modelling of electrolyte degradation and cycling behaviour in a lithium–air battery.* Journal of Power Sources, 2013. **243**(0): p. 409-418.
46. Cai, L. and R.E. White, *Mathematical modeling of a lithium ion battery with thermal effects in COMSOL Inc. Multiphysics (MP) software.* Journal of Power Sources, 2011. **196**(14): p. 5985-5989.
47. Srinivasan, V. and C.Y. Wang, *Analysis of Electrochemical and Thermal Behavior of Li-Ion Cells.* Journal of The Electrochemical Society, 2003. **150**(1): p. A98-A106.

48. Sakti, A., et al., *A validation study of lithium-ion cell constant c-rate discharge simulation with Battery Design Studio®.* International Journal of Energy Research, 2012: p. n/a-n/a.

49. Peng, R. and M. Pedram, *An analytical model for predicting the remaining battery capacity of lithium-ion batteries.* Very Large Scale Integration (VLSI) Systems, IEEE Transactions on, 2006. **14**(5): p. 441-451.

50. DualFoil. http://www.cchem.berkeley.edu/jsngrp/fortran.html. Available from: http://www.cchem.berkeley.edu/jsngrp/fortran.html.

51. Fang, W., O.J. Kwon, and C.-Y. Wang, *Electrochemical–thermal modeling of automotive Li-ion batteries and experimental validation using a three-electrode cell.* International Journal of Energy Research, 2010. **34**(2): p. 107-115.

52. Gerver, R.E. and J.P. Meyers, Three-Dimensional Modeling of Electrochemical Performance and Heat Generation of Lithium-Ion Batteries in Tabbed Planar Configurations. Journal of The Electrochemical Society, 2011. **158**(7): p. A835-A843.

53. Bae, S., et al., Quantitative performance analysis of graphite-LiFePO4 battery working at low temperature. Chemical Engineering Science, 2014. **118**: p. 74-82.

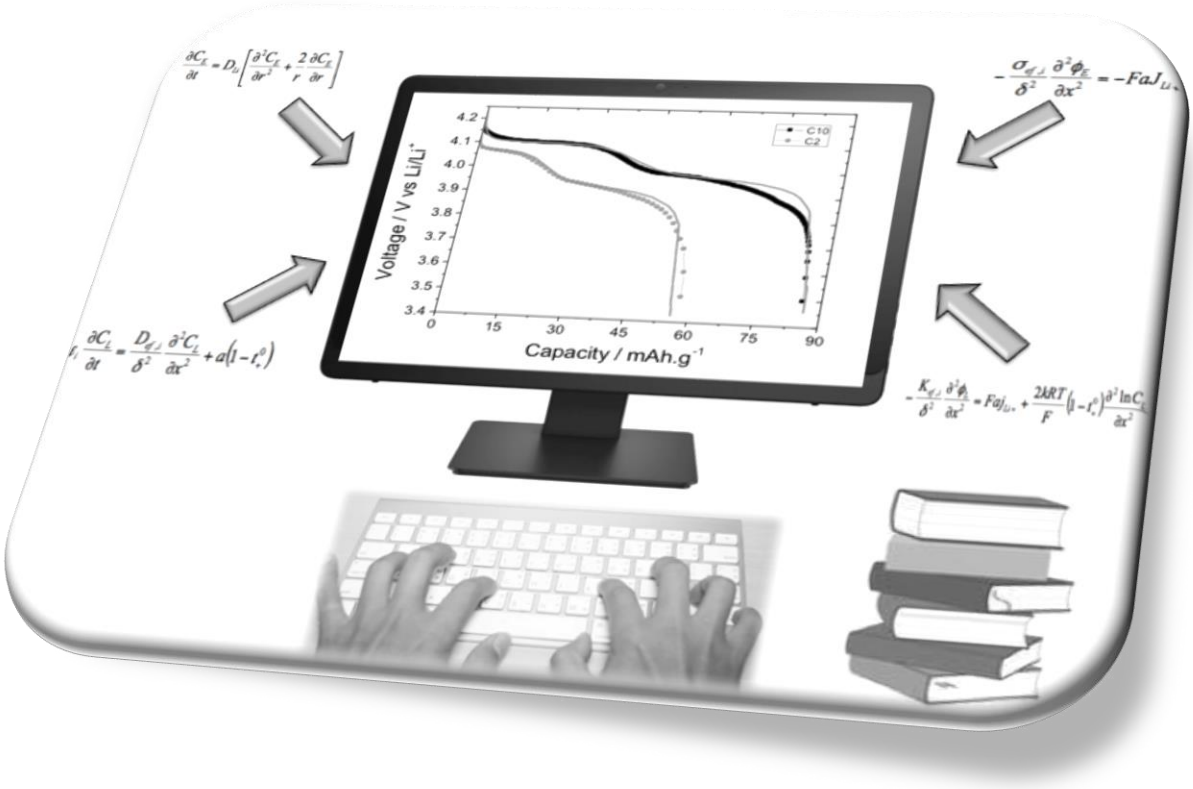

3. Simulation of Lithium-ion Batteries: Methodology and Theoretical Models

This chapter describes the methodology implemented in the simulations performed in the different studies presented in the various chapters. The theoretical models used in these simulations, such as the electrochemical and thermal models, are presented.

3.1 Simulation of lithium-ion batteries

3.1.1 Methodology

The simulation intends to reproduce the main phenomena and processes of the system under study based on physical, chemical and mathematical models. So, it is important to understand the equations governing the phenomena and processes that occurs in the different components of the battery, including electrodes, electrolyte/separator and current collectors, Thus, it is important to identify the appropriate theoretical models to describe the operation of lithium-ion batteries.

The main four steps that should be followed to implement a consistent simulation of the battery are:

- ✓ **First step:** Perform the state of the art on the work about modeling and simulation of lithium-ion batteries that is present in the literature;
- ✓ **Second Step:** Study and understand the physical and electrochemical equations that describe the lithium-ions battery operation;
- ✓ **Third Step:** Implementation of the model by finite element method (FEM) through commercial software or programming language such as C++, Matlab etc. Input of l the partial and ordinary differential equations (PDA and ODE) in the software;
- ✓ **Fourth Step:** Run the simulation and analyze the obtained data.

Figure 3.1 summarizes these steps.

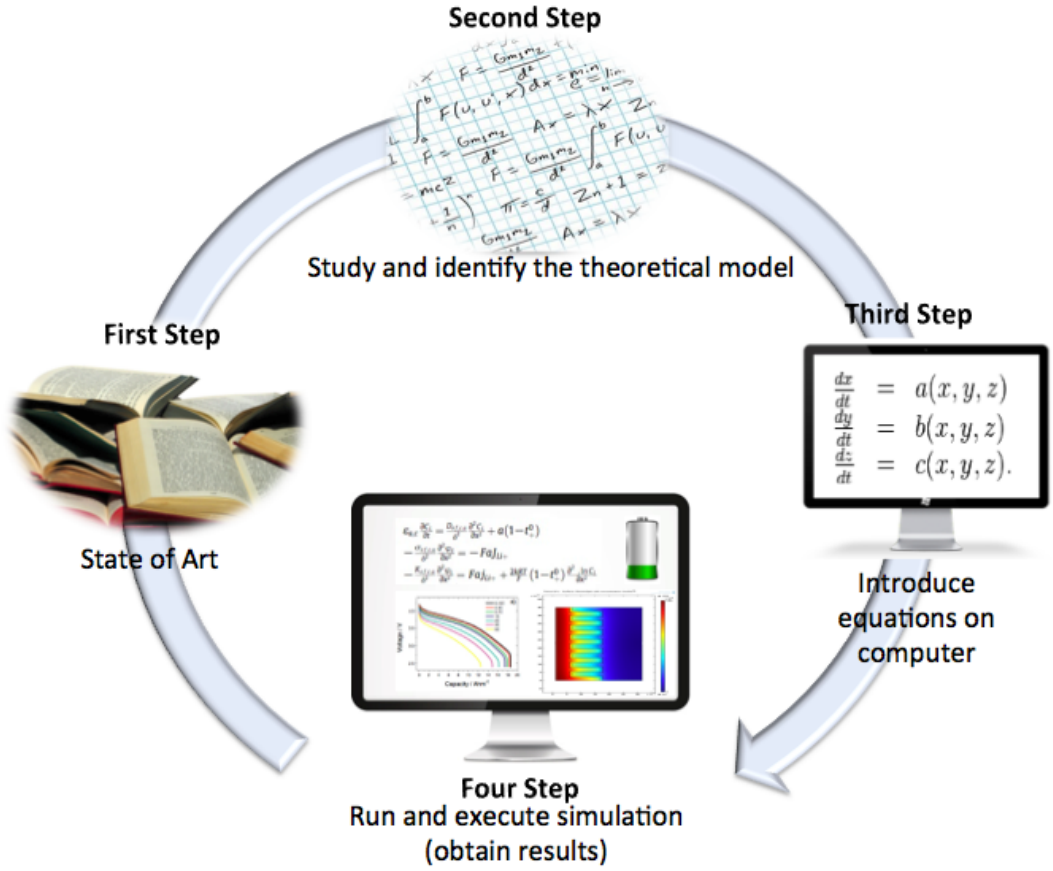

Figure 3.1 - Steps for the implementation of the simulations.

3.1.2 Development and execution of the simulation

This section presents the different phases that should be followed in the construction of a simulation after identifying the theoretical models that will be applied. In first the phase of construction of a simulation it is necessary to define the dimension (1D, 2D and 3D) of the model to be applied in the lithium-ion battery, as shown in figure 3.2. The battery can be represented in 1D, 2D and 3D. If the battery is developed in 1D, only the values of several physical variables along the x-axis will be measured. Thus, the three components of the battery (electrodes, separator/electrolyte and current collectors) are represented by a line, as shown in figure 3.2a). In relation to the 2D representation of the battery, the physical variables in the xx and yy axes will be measured, i.e., the values of physical quantities will be obtained in different points with the coordinates (x, y) of the battery. The battery components are defined as planes, as

shown in figure 3.2b). Finally, in the 3D representation, the physical quantities are obtained in the (coordinates (x, y, z)) points of the battery. In this case, the battery components are represented by volumes, as shown in Figure 3.2.c).

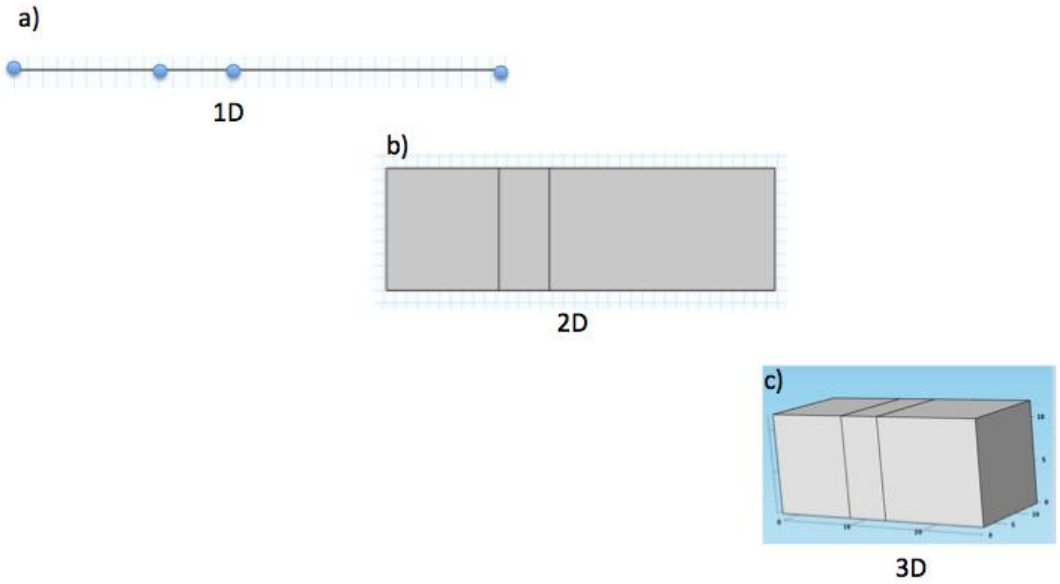

Figure 3.2 - Representation of the dimension of the battery for the application of the theoretical model: a) 1D, b) 2D and c) 3D.

Then, it is necessary to draw the geometry of the battery and its components (collectors, electrodes and separator/electrolyte), as shown in figure 3.3. Different geometries can be defined for lithium ion batteries according to the objective of the study.

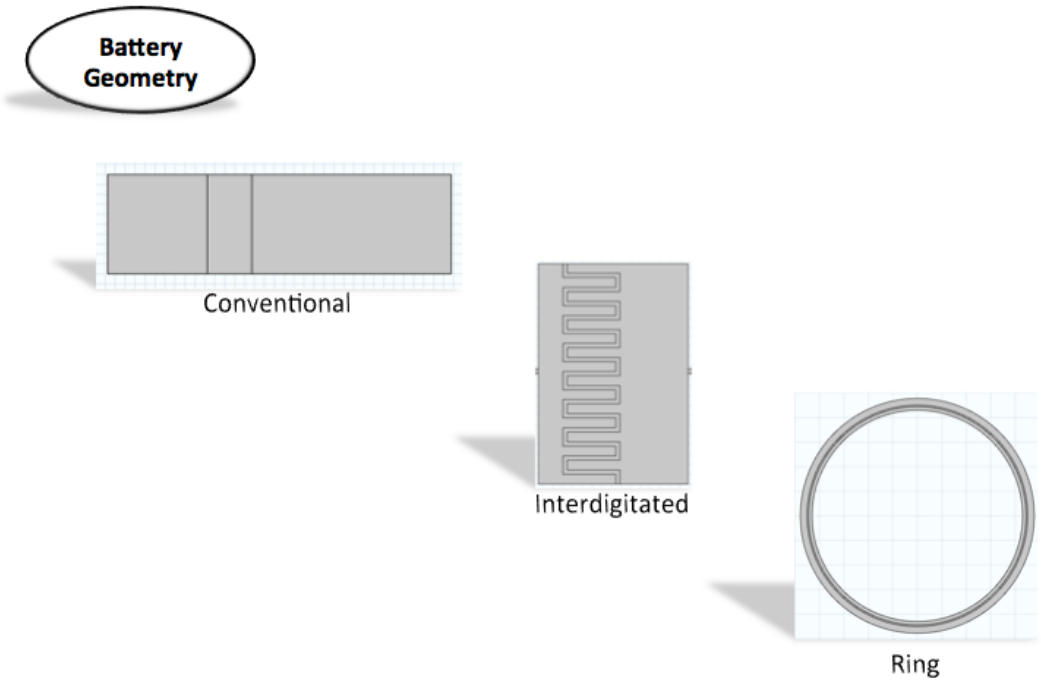

Figure 3.3 - Design of different geometries for lithium-ion batteries.

The next phase is characterized by the introduction of the equations governing the phenomena that occur in the various components of the battery (collectors, electrodes, separator/electrolyte). Then, it is important to define the active materials of electrodes and electrolyte/separator. In this phase, all parameters and physical, chemical and electrochemical constants of the materials of the battery components will be introduced. Also, the boundary conditions and the initial values of the different variables should be defined.

Once the physical and electrochemical quantities are measured at different battery locations, it is necessary to define the mesh. The mesh should be defined according to the dimensions of the battery.

Figure 3.4 shows that the mesh can be normal, fine or extremely fine. When the mesh is extremely fine, it will be required a higher computational performance to obtained the results. In contrast, if the mesh is normal, the element size of the mesh can be large and the obtained results will show a larger associated error. Thus, the choice of the element size of the mesh should take into account the order of magnitude of the dimensions of the simulated battery. Typically, the element size of the mesh has an order of magnitude below the order of magnitude of the battery.

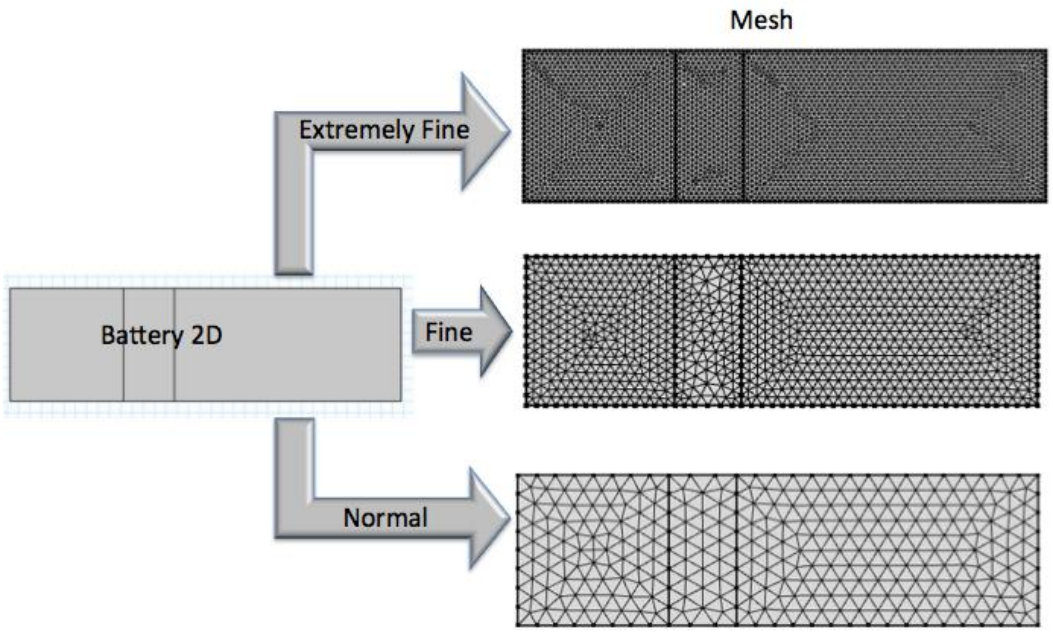

Figure 3.4 - Different size of the mesh: extremely fine, fine and normal.

After defining the size of the mesh of the battery, the study to be performed should be selected: time dependent or stationary. Finally, the simulation will be performed. The possible solutions from the electrochemical and thermal models of lithium-ion batteries will be determined and the plots (1D, 2D or 3D) of the relevant parameters obtained according to the objective of the study. Some examples of plots are: discharge curves (delivery capacity), Nyquist plot, electrolyte salt concentration, solid lithium concentration, electrolyte and electrode potential, electrode and electrolyte current density, temperature, total heat generation rate of battery components, total ohmic heat generation rate of battery components, total reversible heat generation rate of electrodes and total reaction heat generation rate of electrodes as a function of time or space.

3.2 Theoretical models of lithium-ion batteries: Electrochemical and Thermal models

The simulations developed in this thesis are based on theoretical models that govern the phenomena that occur in the different components of the lithium ion battery (electrodes, separator/electrolyte and current collectors). The theoretical models applied in the simulations are the electrochemical and thermal models.

As the electrochemical and thermal models are constituted by partial and ordinary differential equations, the numerical resolution method used in the simulations was based on the Finite Element Method. The batteries were simulated in 1 and 2 dimensions. The choice of these dimensions (1D and 2D) for the simulations is due to the computational efficiency. The application of 3-dimensional models increases substantially the number of points of the space to be measured and decreases computational performance. Further, the 1D and 2D simulations properly represent the performance of the battery.

The simulations developed on the various batteries are based on the electrochemical model. The electrochemical model is based on the Doyle/Newman model [1-3], which shows all the physical, chemical and electrochemical phenomena associated with the operation of lithium ion batteries. When the thermal model is introduced, the aim is to account the heats produced by the battery in its operation, taking into account the corresponding thermal equations [4].

Then, the fundamental equations of the electrochemical and thermal models are presented in table 3.1. These equations are applied to the different components of the battery (electrodes, separator and current collectors), as shown in table 3.1.

Table 3.1 - Equations governing various phenomena within a battery [1-4].

Electrochemical model (Newman/Doyle/Fuller)		
Physical process	**Governing Equation**	**Region**
Solid phase conduction	$-\frac{\sigma_{ef,i}}{\delta^2}\frac{\partial^2\phi_E}{\partial x^2} = -Faj_{Li+}$	Electrodes
Electrolyte phase conduction	$-\frac{K_{ef,i}}{\delta^2}\frac{\partial^2\phi_L}{\partial x^2} = Faj_{Li+} + \frac{2kRT}{F}\left(1-t_+^0\right)\frac{\partial^2 \ln C_L}{\partial x^2}$	Electrodes, Separator

Electrolyte phase diffusion	$\varepsilon_i \frac{\partial C_L}{\partial t} = \frac{D_{ef,i}}{\delta^2} \frac{\partial^2 C_L}{\partial x^2} + a\left(1 - t_+^0\right)$	Electrodes, Separator
Solid phase diffusion	$\frac{\partial C_E}{\partial t} = D_{Li}\left[\frac{\partial^2 C_E}{\partial r^2} + \frac{2}{r}\frac{\partial C_E}{\partial r}\right]$	Electrodes
Activation reaction (Butler-Volmer Kinetics)	$j_{Li+} = 2k_i\left(c_{E,\max,i} - c_{E,i}\big\|_{r=R_i}\right)^{0.5}\left(c_{E,i}\big\|_{r=R_i}\right)^{0.5} c^{0.5} \sinh\left[\frac{0.5F}{RT}\left(\varphi_E - \varphi_L - U_i\right)\right]$	Electrodes
Diffusion/ionic and electronic conductuvity	$k_{ef,i} = k_l \varepsilon_i^{brugg}, brugg = 1.5$	Electrodes, Separator
	$D_{ef,i} = D_l \varepsilon_i^{brugg}, brugg = 1.5$	Electrodes, Separator
	$\sigma_{ef,c} = \sigma_c\left(1 - \varepsilon_c - \varepsilon_{f,c}\right)$	Electrodes
Specific interfacial area	$a_c = \frac{3}{R_i}\left(1 - \varepsilon_c - \varepsilon_{f,c}\right)$	Electrodes
Thermal model		
Physical process	**Governing Equation**	**Region**
Energy balance	$\rho_i C_{p,i} \frac{dT}{dt} = \lambda_i \frac{\partial^2 T}{\partial x^2} + \lambda_i \frac{\partial^2 T}{\partial y^2} + Q_{total,i}$	Electrodes, Separator
Total heat generation rate of the electrodes	$Q_{total,i} = Q_{reaction,i} + Q_{reversible,i} + Q_{ohmic,i}, i = n, p$	Electrodes
Total heat generation rate of the separator	$Q_{total,i} = Q_{ohmic,i}, i = s$	Separator
Total reaction heat generation rate	$Q_{reaction,i} = FaJ\left(\phi_E - \phi_L - U\right), i = n, p$	Electrodes
Total reversible heat generation rate	$Q_{reversible,i} = FaJT\frac{\partial U}{\partial T}, i = n, p$	Electrodes
Total ohmic heat generation rate of the electrodes	$Q_{ohmic,i} = \sigma_{ef,i}\left(\frac{\partial \phi_1}{\partial x}\right)^2 + \sigma_{ef,i}\left(\frac{\partial \phi_1}{\partial y}\right)^2 + k_{ef,i}\left(\frac{\partial \phi_2}{\partial x}\right)^2 + k_{ef,i}\left(\frac{\partial \phi_2}{\partial y}\right)^2 + \frac{2k_{ef,i}RT}{F}\left(1 - t_+\right)\frac{\partial\left(\ln c_i\right)}{\partial x}\frac{\partial \phi_2}{\partial x} + \frac{2k_{ef,i}RT}{F}\left(1 - t_+\right)\frac{\partial\left(\ln c_i\right)}{\partial y}\frac{\partial \phi_2}{\partial y}, i = n, p$	Electrodes

Total ohmic heat generation rate of the separator	$Q_{ohmic,i} = k_{ef,i}\left(\frac{\partial \phi_2}{\partial x}\right)^2 + k_{ef,i}\left(\frac{\partial \phi_2}{\partial y}\right)^2 + \frac{2k_{ef,i}RT}{F}(1-t_+)\frac{\partial(\ln c_i)}{\partial x}\frac{\partial \phi_2}{\partial x} + \frac{2k_{ef,i}RT}{F}(1-t_+)\frac{\partial(\ln c_i)}{\partial y}\frac{\partial \phi_2}{\partial y}, i = s$	Separator
Temperature dependent open circuit potential of the electrode	$U_i = U_{ref,i} + (T - T_{ref})\left[\frac{dU}{dT}\right], i = n, p$	Electrodes
Heat flux transfer between the battery and the external environment	$-\lambda_i \nabla T = h(T_{external} - T), i = n, s, p$	All boundaries between the battery and the external environment

Auxiliary equations:

a) Ionic conductivity as a function of temperature [5]:
$k_i(T) = c \times (-10.5+(0.0740 \times T)-((6.96 \times 10^{-5}) \times (T^2))+(0.668 \times c)-(0.0178 \times c \times T)+((2.8 \times 10^{-5}) \times c \times (T^2))+(0.494 \times c^2)-((8.86 \times 10^{-4}) \times (c^2)*(T)))^2$

b) Reaction rate coefficient of the electrodes as a function of temperature [5]:
$K_{t,i}(T) = k_{t298,15,i} \times exp(-(E_{ak,i}/R) \times (1/T-1/298,15))$

c) Diffusion coefficient of the salt in the electrolyte as a function of temperature [5]:
$D_i(T) = 10\text{^}(-(0.22 \times c)-4.43-((54)/(T-229-(5 \times c))))$

d) Diffusion coefficient of Li ions in the electrode as a function of temperature [6]:
$D_{LI}(T) = D_{LI} \times exp(-(E_{ad,i}/R) \times (1/T-1/298,15))$

The boundary conditions, parameters and initial values are defined according to the objective of the study, so they will be presented in each study developed in chapters 4, 5, 6, 7 and 8.

3.3 References

1. Doyle, M., T.F. Fuller, and J. Newman, Modeling of Galvanostatic Charge and Discharge of the Lithium/Polymer/Insertion Cell. Journal of The Electrochemical Society, 1993. **140**(6): p. 1526-1533.
2. Doyle, M., et al., Comparison of Modeling Predictions with Experimental Data from Plastic Lithium Ion Cells. Journal of The Electrochemical Society, 1996. **143**(6): p. 1890-1903.
3. Fuller, T.F., M. Doyle, and J. Newman, Simulation and Optimization of the Dual Lithium Ion Insertion Cell. Journal of The Electrochemical Society, 1994. **141**(1): p. 1-10.
4. Cai, L. and R.E. White, Mathematical modeling of a lithium ion battery with thermal effects in COMSOL Inc. Multiphysics (MP) software. Journal of Power Sources, 2011. **196**(14): p. 5985-5989.
5. Gerver, R.E. and J.P. Meyers, Three-Dimensional Modeling of Electrochemical Performance and Heat Generation of Lithium-Ion Batteries in Tabbed Planar Configurations. Journal of The Electrochemical Society, 2011. **158**(7): p. A835-A843.
6. Bae, S., et al., Quantitative performance analysis of graphite-LiFePO4 battery working at low temperature. Chemical Engineering Science, 2014. **118**: p. 74-82.

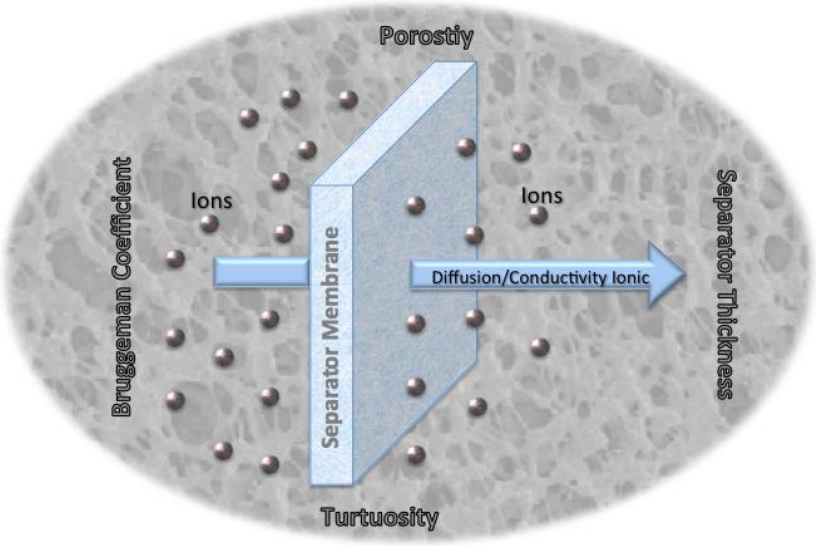

4. Modelling separator membranes physical characteristics for optimized lithium ion battery performance

This chapter presents the evaluation of the influence of different geometrical parameters of the separator in the performance of lithium ion batteries. The effect of varying separator membrane physical parameters such as degree of porosity, tortuosity and thickness, on battery delivered capacity was studied. This was achieved by a theoretical mathematical model relating the Bruggeman coefficient with the degree of porosity and tortuosity. The ionic conductivity of the separator and consequently the delivered capacity values obtained at different discharge rates depends on the value of the Bruggeman coefficient, which is related with the degree of porosity and tortuosity of the membrane.

This chapter is based on the following publication:

"Modeling separator membranes physical characteristics for optimized lithium ion battery performance", D. Miranda, C.M. Costa, A.M. Almeida, S. Lanceros-Méndez, Solid State Ionics 278 (2015) 78-84.

4.1 Introduction

Taking into account the rapid technological advances in portable electronic devices, such as mobile-phone, computers, e-labels, e-packaging and disposable medical testers, there is an increasing need for improving the autonomy and performance of batteries independently of the battery type [1]. One of the types of the battery with the best properties is the Lithium ion batteries, as they are lighter, cheaper, with higher energy density (210Wh kg^{-1}), no memory effect, prolonged service-life and higher number of charge/discharge cycles when compared to other battery solutions [2].

In order to improve the autonomy and performance of lithium-ion batteries it is necessary new advances in novel materials for improved delivery capacity, lifetime and safety [3, 4].

In all battery devices, the separator membrane is located between the anode and cathode and its main function is transferring the charge and prevent over-potential [5, 6].

The main characteristics of separator membranes for lithium ion batteries are thickness, permeability, porosity and pore size, wettability by liquid electrolyte, mechanical and dimensional stability [7, 8].

The separator is typically constituted by a polymer matrix, in which the membrane is soaked by the electrolyte solution, i.e, salts are dissolved in solvents, water or organic molecules.

For optimizing separator and electrodes materials (cathode and anode) it is essential and critical the use of computer simulations of the battery performance [9].

These computer simulations are based on mathematical models that take into account the physico-chemical properties of the materials to be used as electrodes and separators, the organic solvents for electrolytes, and the geometry and dimensions of the battery components [10, 11].

The computer simulation of the separator/electrolyte includes the correlation of ionic conductivity of the polymeric membrane and the conductivity of the electrolyte solution. Also the effective diffusivity is related to the Bruggeman coefficient. This correlation is described through the Bruggeman equation which reflects the importance of porosity and tortuosity of the material [12], the Bruggeman exponent being 1.5 for ideal electrodes [7] and 2.4 at 4.5 for different electrolyte solution and polymer membranes [13, 14]. In relation of electrodes materials, experimental results indicate

that the complexity of the porous electrodes induces tortuosity values that greatly deviate from the classical Bruggeman ideal [15].

For same degree of porosity and polymeric membrane, was revealed through of the utilization the different salts ($LiBF_4$, LiTFSI and etc) in electrolyte solution that tortuosity value varies between 3.3 at 4.1 [16].

In this work [17], the Bruggeman parameters for the commercial separators membranes differ from the parameters reported in previous studies of separator tortuosity.

It has been proven, on the other hand, that this exponent in not valid for real electrodes or separator materials [12]. This is mainly due to effects in the separators that are typically not accounted for. In this way, diffusion limitations in thick cells have been reported [13], which become more prominent as the thickness of the electrodes increases.

It is thus necessary for a proper description of separator performance, to take into account the morphology parameters of separators that are important for the performance of separator membranes such as porosity, pore size, tortuosity and thickness [18].

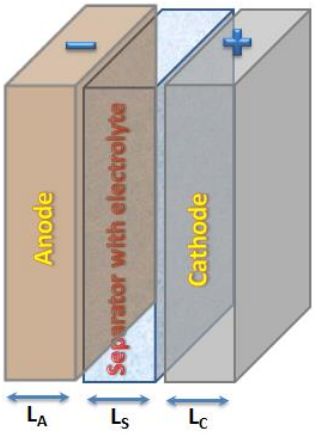

Figure 4.1 - Schematic representation of the main structure of a lithium ion battery.

The relevance of this work is to include these parameters in the computer simulation models in order to optimize and improve battery performance.

A finite element method simulation has been thus carried out by in order to quantitatively evaluate the effects of the dimensions of separator, porosity and tortuosity towards optimization of its performance in lithium-ion batteries for the same electrodes (anode and cathode) and independently of the electrolyte solution.

4.2 Theoretical model

4.2.1 General model

Anode, cathode and separator are the components of the lithium ion batteries (Figure 4.1). Each constituent has a specific function in the operation of a lithium-ion battery. The fundamental equations governing the main phenomena of the operation process of a lithium-ion battery are based on the Doyle/Fuller/Newman model [19].

The Chapter 3 shows the main equations governing the different components of the battery (cathode, anode and electrolyte/separator) and Table 4.1 shows the boundary conditions applied in this study. The model takes into account all the variables corresponding to the phenomena occurring in the electrodes and electrolyte/separator, including: the diffusion and ionic conductivity of lithium ions in the electrolyte and electrodes, the relation between the potential of the electrolyte and the local current density on the electrodes (Ohm's law), the relation between the potential of the electrolyte and the local current density on electrolyte/separator (Ohm's law), the diffusion of lithium ions in the active material, the kinetics of the heterogeneous reaction at the electrode/electrolyte interface, the open circuit voltage and the mass transport flux (Chapter 3).

Table 4.1 - Boundary conditions applied in the simulation. The nomenclature is indicated in the List of Symbols and Abbreviations.

	Boundary Conditions
Electrodes (Anode and cathode)	Cathode: $\left.\frac{\partial C_L}{\partial x}\right\|_{x=L_a+L_s+L_c} = 0$ $\left.\frac{\partial C_L}{\partial x}\right\|_{x^+=L_a+L_s} = \left.\frac{\partial C_L}{\partial x}\right\|_{x^-=L_a+L_s}$ $D_{ef,s}\left.\frac{\partial C_L}{\partial x}\right\|_{x=L_a+L_s^-} = D_{ef,c}\left.\frac{\partial C_L}{\partial x}\right\|_{x^-=L_a+L_s^+}$ $D_{ef,c}\left.\frac{\partial C_L}{\partial x}\right\|_{x=L_a+L_s+L_p} = 0$ $\left.\frac{\partial \varphi_E}{\partial x}\right\|_{x=L_a+L_s+L_c} = -\frac{I_{TOTAL}}{\sigma_{ef,c}}$ $\varphi_E\|_{x=L_a+L_s} = \varphi_{E,0}$ $k_f\left.\frac{\partial \varphi_L}{\partial x}\right\|_{x=L_a+L_s^-} = k_{ef,c}\left.\frac{\partial \varphi_L}{\partial x}\right\|_{x=L_a+L_s^+}$ $k_{ef,c}\left.\frac{\partial \varphi_L}{\partial x}\right\|_{x=L_a+L_s+L_c} = 0$
	Anode: $\left.\frac{\partial C_L}{\partial x}\right\|_{x=0} = 0, \quad \left.\frac{\partial C_L}{\partial x}\right\|_{x^+=L_a} = \left.\frac{\partial C_L}{\partial x}\right\|_{x^-=L_a}$ $D_{ef,c}\left.\frac{\partial C_L}{\partial x}\right\|_{x=0} = 0$ $D_{ef,a}\left.\frac{\partial C_L}{\partial x}\right\|_{x=L_a^-} = D_{ef,s}\left.\frac{\partial C_L}{\partial x}\right\|_{x=L_a+}$ $\varphi_E\|_{x=0} = 0, \quad \left.\frac{\partial \varphi_E}{\partial x}\right\|_{x=L_a} = 0$ $k_{ef,a}\left.\frac{\partial \varphi_L}{\partial x}\right\|_{x=L_a^-} = k_f\left.\frac{\partial \varphi_L}{\partial x}\right\|_{x=L_a^+},$ $k_{ef,a}\left.\frac{\partial \varphi_L}{\partial x}\right\|_{x=0} = 0$

Separator/Electrolyte	$$D_{ef,a}\left.\frac{\partial C_L}{\partial x}\right\|_{x=L_a^-} = D_{ef,s}\left.\frac{\partial C_L}{\partial x}\right\|_{x^-=L_a^+}$$ $$D_{ef,s}\left.\frac{\partial C_L}{\partial x}\right\|_{x=L_a+L_s^-} = D_{ef,c}\left.\frac{\partial C_L}{\partial x}\right\|_{x^-=L_a+L_s^+}$$ $$k_{ef,a}\left.\frac{\partial \varphi_L}{\partial x}\right\|_{x=L_a^-} = k_f\left.\frac{\partial \varphi_L}{\partial x}\right\|_{x=L_a^+}$$ $$k_f\left.\frac{\partial \varphi_L}{\partial x}\right\|_{x=L_a+L_s^-} = k_{ef,c}\left.\frac{\partial \varphi_L}{\partial x}\right\|_{x=L_a+L_s^+}$$
Active Material	$$\left.\frac{\partial C_E}{\partial r}\right\|_{r=0} = 0,\ \left.\frac{\partial C_E}{\partial r}\right\|_{r=R_{sp}} = -\frac{J_{Li^+}}{D_{Li}}$$

4.2.2 Separator

The effective conductivity of separator is described through of the following equation:

$$\kappa_f = \kappa_l.\varepsilon_s^{\ p} \tag{1}$$

where κ_f is the effective ionic conductivity of the polymer separator, κ_l is the ionic conductivity of the electrolyte, ε_s is the porosity of separator and *p* is the Bruggeman exponent.

Usually, the value of *p* is 1.5, as it is admitted that the separator pores show an ideal shape [20].

For battery separators it has been shown that Bruggeman exponent ranges between 2.4 [13] and 4.5 [19].

One important parameter influencing the battery separator performance is the tortuosity (τ), which is defined by the ratio between the effective capillarity length and the thickness of the sample [21]:

$$\kappa_f = \kappa_l \frac{\varepsilon_s}{\tau^2} \tag{2}$$

Taking account the equation 2, the tortuosity value is related with the ionic transport and provides information about pore blockage which describes the average pore connectivity of a solid. The ideal value of tortuosity is 1 for an ideal porous body with cylindrical and parallel pores.

By relating equations 1 and 2, one obtains

$$p = 1 - \frac{\ln(\tau^2)}{\ln(\varepsilon_s)} \tag{3}$$

which shows how the Bruggeman exponent depends on the values of the tortuosity and the porosity.

Also the salt diffusion coefficient is described through the following equation:

$$D_f = D_l \varepsilon_s^p \tag{4}$$

where *p* is determined by equation 3.

4.3 Parameters and simulation model

The finite element method simulation implemented in this work is based on the mathematical model of Newman group [22], considering the electrochemical and transport processes in a 1D lithium ion battery structure consisting on a [positive electrode | separator | negative electrode]. The equations describing the electrochemical and transport processes of the separator were modified to include equation 3. The values of the ionic conductivity and porosity included in this simulation model are the ones of the P(VDF-TrFE) copolymer [16, 23, 24]. The choice of this separator/electrolyte is due to its high ionic conductivity at room temperature, and very stable in function of temperature, good mechanical properties and excellent electrochemical stability up to 4V [16, 23]. The values of the parameters used for each component of the battery are listed in Table 4.2.

Table 4.2 - Parameters used in the simulations.

Parameter	**Unit**	**Anode** (Li_xC_6)	**Separator**	**Cathode** ($Li_xMn_2O_4$)
$C_{E,i,0}$	mol/m^3	14870		3900
$C_{E,i,max}$	mol/m^3	26390		22860
C_L	mol/m^3		1000	
r	m	$12,5\times10^{-6}$		8×10^{-6}
L_i	m	100×10^{-6}	L_s	183×10^{-6}
κ_i	S/m	$(6,5\times10^{-1}) \times0,357^{1,5}$	$(6,5\times10^{-1}) \times\varepsilon_s^p$	$(6,5\times10^{-1}) \times0,444^{1,5}$
D_i	m^2/s	$(4,0\times10^{-10}) \times0,357^{1,5}$	$(4,0\times10^{-10}) \times\varepsilon_s^p$	$(4,0\times10^{-10}) \times0,444^{1,5}$
D_{LI}	m^2/s	$3,9\times10^{-14}$		1×10^{-13}
Brugg or p		1,5	p	1,5
$\varepsilon_{f,i}$		0,172		0,259
ε_i		0,357	ε_s	0,444
σ_i	S/m	100		3,8
i_{1C}	A/m^2		17,5	
F	C/mol		96487	
T	K		298,15	
R	J/mol K		8,314	

For the electrodes, the values of the different parameters are constant and are presented in Table 4.2. Relatively to the parameters of the separator, the ones indicated in the table are considered fixed, and thickness (L_s), Bruggeman exponent (p) and porosity (ε_s) were varied in the simulations. The discharge protocol is the continuous current system where the voltage cut-off occurs around of 2.65V at room temperature. For each effect studied, were realized 3 simulations with < 0.1% error due that errors associated with the finite element solution of equations is minimized with care in the physical configuration of the problem.

4.4 Results and Discussion

4.4.1 Effect of separator/electrolyte

The behavior of the battery at different scan rates for a battery including a polymer porous membrane or free electrolyte is shown in figure 4.2.

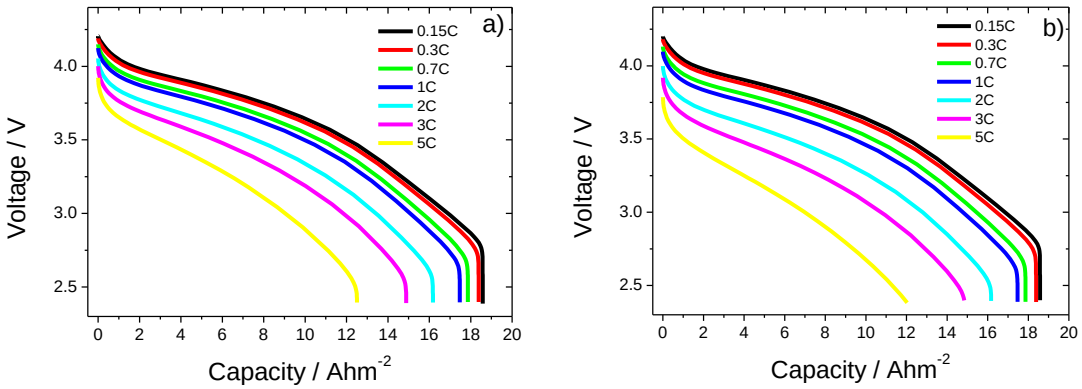

Figure 4.2 - Voltage as a function of delivered capacity at different scan rates for: a) free electrolyte and b) battery separator membrane with 70% of porosity and 3.8 of tortuosity.

Figure 4.2 shows the voltage as a function of delivered capacity for the free electrolyte without membrane (figure 4.2a)) and for a porous membrane with 70% of porosity and 3.8 of tortuosity (figure 4.2b)). Independently of electrolyte type (figure 4.2), as expected is observed, a progressive decrease of the discharge value with increasing the current density due to the ohmic drop. This fact is observed in experimental results but this simulation model assumes a constant value for the solid-phase diffusion coefficient [18].

Figure 4.2 shows that for low (0.15C) and medium (2C) discharge rates there is no variation in the results obtained for the delivered capacity of batteries with free electrolyte or polymer separator membrane. The separator membrane, therefore, does not influence negatively the performance of the battery up to medium discharge rates (2C).

On the other hand, at high discharge rates (5C), the values of the delivered capacity for the separator membranes are slightly smaller when compared with the samples with free electrolyte. Thus, Figure 4.3 shows the delivered capacity as a function of the scan rate for the aforementioned systems.

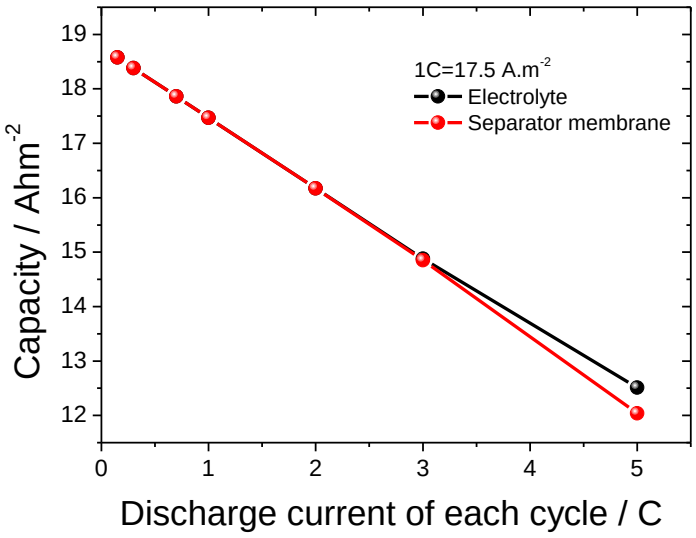

Figure 4.3 - Delivered capacity as a function of the scan rate for free electrolyte and separator membrane batteries.

Figure 4.3 shows that there are differences in the delivered capacity for both systems for scan rates above 3C, the delivered capacity being slightly smaller for battery systems with separator membranes.

This is due to the fact that, for high discharge rates, the diffusion and mobility of lithium ions should be larger in order to cross through the separator membrane. The ionic conductivity of the separator membrane is lower in comparison to the free electrolyte, which is reflected in the lower performance of the battery system with separator membrane.

Although it is observed a decrease in the performance of the battery system with separator membrane for the higher discharge rates, the differences in the delivered capacity values between the separator membrane and the free electrolyte are not significant. In this way, the introduction of a polymer membrane in the battery separator will not strongly hinder the battery performance for low, medium and high battery discharge rates.

4.4.2 Effect of the variation of separator membrane physical parameters on battery performance

Considering that the inclusion of the polymer membrane in the separator does not significantly affects the performance of the battery, the effect of the variation of relevant physical parameter of the separator membrane such as degree of porosity, tortuosity and thickness on battery performance will be addressed.

4.4.2.1 Degree of porosity

Figure 4.4 illustrates the effect of the degree of porosity on the voltage vs. capacity characteristics for separator membranes with a fixed tortuosity value of 3.8 at low (0.15 C, figure 4.4a)) and high scan rate (5C, figure 4.4b)).

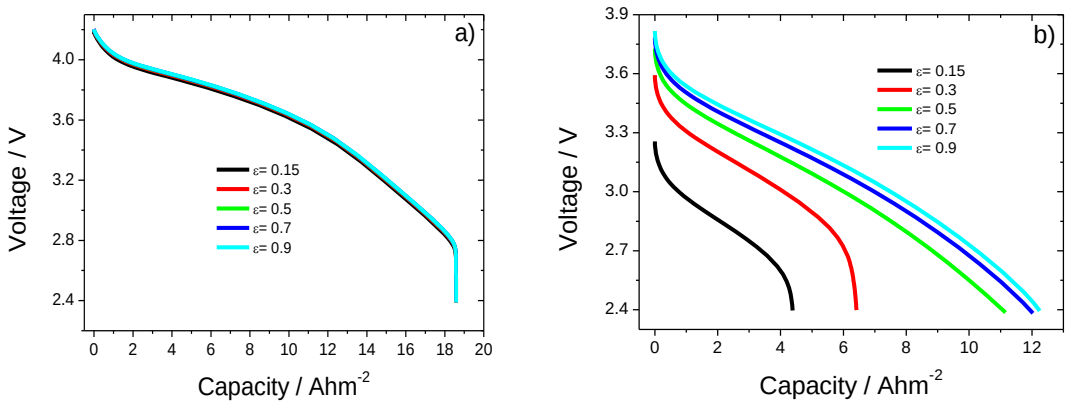

Figure 4.4 - Voltage as a function of delivered capacity for batteries with separator membranes with different degrees of porosity with tortuosity of 3.8 at scan rates of a) 0.15C and b) 5C.

Figure 4.4a) shows that for 0.15C and degrees of porosity between 15% and 90% there is no relevant variation in the performance of the battery system, the degree of porosity not affecting therefore the performance of the battery.

On the other hand, for high discharge rates (figure 4.4b)) it is observed a strong decrease in the battery performance for degrees of porosity below 50%, which further decreases with decreasing degree of porosity.

For degrees of porosity above 50%, the delivered capacity just slightly increases with increasing the degree of porosity with capacity values between 11 Ah/m^2 to 12 Ah/m^2 for degrees of porosity between 50% and 90%.

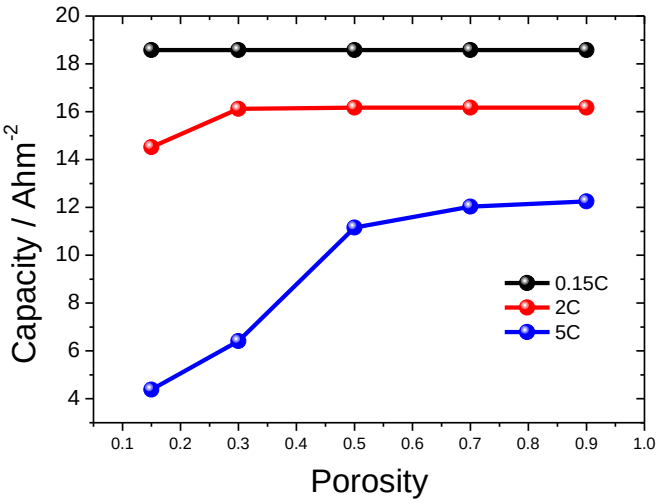

Figure 4.5 - Delivered capacity as a function of the degree of porosity at different scan rates: 0.15C, 2C and 5C.

Figure 4.5 shows the effect of the degree of porosity in the delivered capacity at different scan rates, 0.15C, 2C and 5C, for separator membranes with tortuosity value of 3.8.

For the scan rate of 0.15C, the performance of the battery measured through the delivered capacity is independent of the degree of porosity of the separator membrane. For a scan rate of 2C, the delivered capacity increases with increasing degree of porosity up to 30%, remaining constant for higher degrees of porosity.

However, at high scan rates, 5C, the delivered capacity increases strongly with increasing degree of porosity up to 50%. Taking account this behavior and the results shown in Figures 4.4 and 4.5, it is considered that good battery performances are obtained for degrees of porosity above 50%. It is to notice that the degree of porosity is correlated with the uptake value but also the affinity between salt and polymer chain which in turn affects the ionic conductivity value of the separator [25]. On the other

hand, the ionic conductivity and transport occurs mainly in the amorphous region which undergo swelling to accommodate the electrolyte but with mechanical integrity [26, 27]. The mechanical integrity depend the degree of porosity and pore size of the separator membrane but also the degree of crystallinity [27].

4.4.2.2 Tortuosity

In the simulations above, the value of the tortuosity has been considered fixed for all membranes. It is nevertheless important to have in mind that this is one of the most important characteristics of a separator membrane, as the tortuosity value is correlated with the ionic conductivity of the separator.

Figure 4.6 shows the effect of the different tortuosity values in the delivered capacity of the battery system at different scan rates for different degrees of porosity.

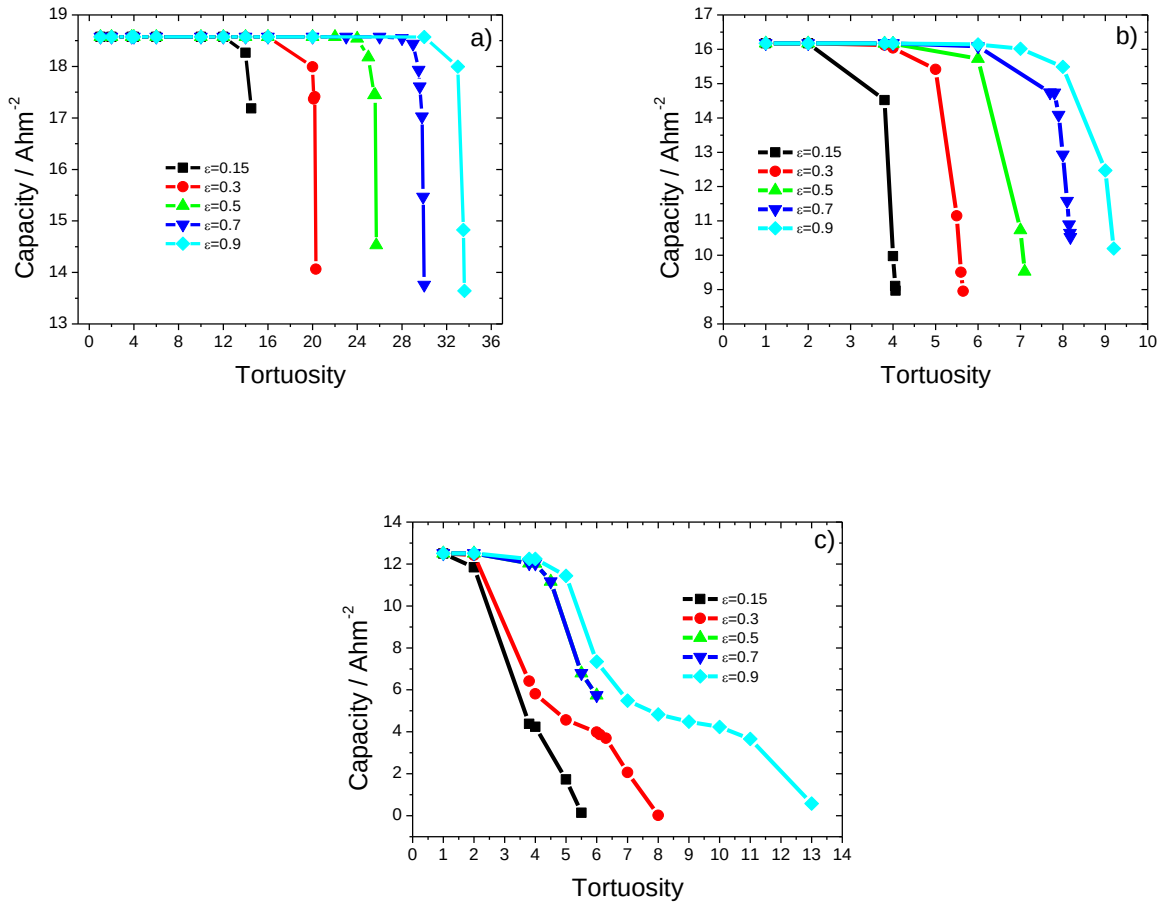

Figure 4.6 - Delivered capacity as a function of tortuosity for membranes with different degrees of porosity: a) low scan rate, 0.15C, b) moderate scan rate, 2C and c) high scan rate, 5C.

Figure 4.6a) shows the limit values of tortuosity for each degree of porosity at 0.15C at which there is no decreases of the capacity value of the battery.

It is verified that for a degree of porosity of 15%, the limit tortuosity value is around 14, but for a degree of porosity of 90% this value increases up to 33, followed by a drastic decrease in the delivered capacity value.

A similar behavior is observed for the scan rates of 2C (figure 4.6b)) and 5C (figure 4.6c)), the main differences being the limit value of the tortuosity at the best performance of the battery.

Table 4.3 shows the limit value of tortuosity for the different degrees of porosity and scan rates, as obtained from figure 4.6.

Table 4.3 - Limit value of tortuosity for different degrees of porosity and scan rates.

	0.15C	**2C**	**5C**
ε=0.15	12	2	1
ε=0.30	16	3.8	2
ε=0.50	24	4	2
ε=0.70	26	4	4
ε=0.90	30	6	5

Table 4.3 shows that for higher values of porosity, the limit value of tortuosity, at which a constant delivered capacity is maintained, increases.

Thus for a given degree of porosity and a discharge rate it is observed that the tortuosity has a limit value to maintain a good performance of the separator and, consequently, a good battery performance.

After the limit value of tortuosity for a given degree of porosity it is observed a significant decrease in the delivered capacity, strongly decreasing the performance of the battery.

It is observed that for higher values of the degree of porosity, the limit value of tortuosity can be higher without affecting the performance of battery as it is reflected in equation 2. As the capacity of the battery is related with the ionic conductivity of the separator/electrolyte, increasing the value of the tortuosity for a given degree of porosity and discharge rate results in a decrease of the ionic conductivity decreases, leading to a reduction in capacity [25, 26].

4.4.2.3 Dimension/thickness

Another important parameter of the separator is its thickness. Figure 4.7 shows the voltage vs delivered capacity, at 0.15C and 5C scan rates, of a battery as a function of the separator membrane thickness for a membrane with 70% of porosity and 3.8 of tortuosity knowing that separator membrane presents mechanical integrity. The mechanical integrity depends the degree of porosity but also pore size.

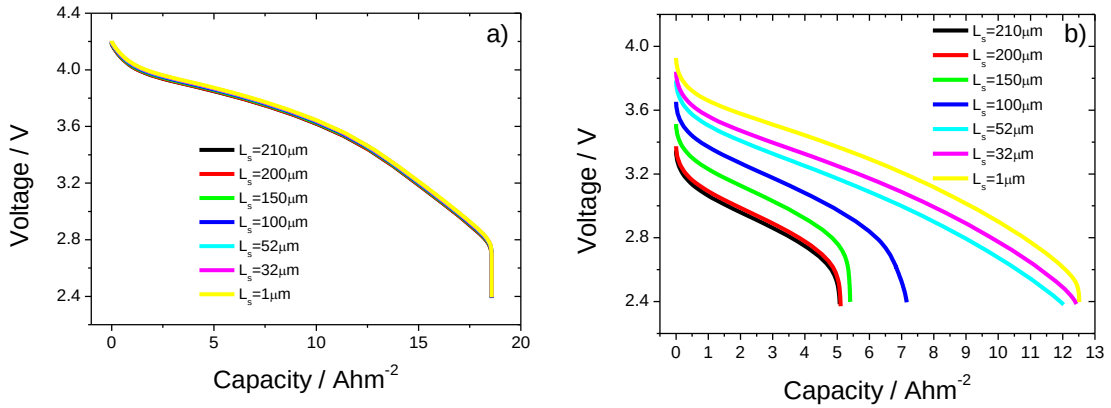

Figure 4.7 - Voltage as a function of the delivered capacity for battery separator membranes with different thicknesses, 70% of porosity and 3.8 of tortuosity: a) 0.15C and b) 5C.

Figure 4.7a) shows that the thickness of the separator membrane does not affect the delivered capacity value of the battery system for a scan rate of 0.15C. This behavior is not observed for higher scan rates (figure 4.7b)), 5C) in which increasing the thickness of the separator leads to a decrease of the delivered capacity.

This fact is correlated with the longer path that lithium ions have to move through the separator membrane which leads to a decreasing delivered capacity value.

Figure 4.8 presents the delivered capacity as a function of the thickness of separator at different scan rates.

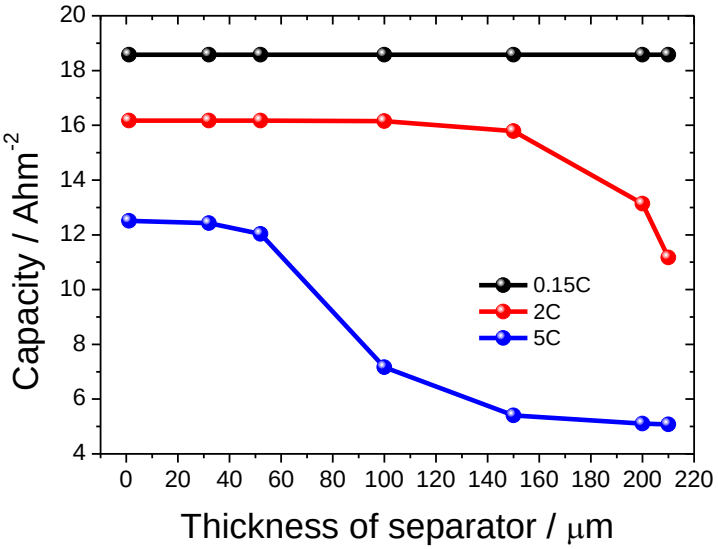

Figure 4.8 - Delivered capacity as a function of the separator thickness at different scan rates: 0.15C, 2C and 5C.

Figure 4.8 shows that the ideal value of the separator thickness is between 1μm and 32μm, leading to proper battery capacity values independently of the scan rate.

Based on these results (figure 4.8), it is concluded that according to the polymer membrane used in the separator with a degree of porosity and tortuosity value assigned, it is possible to determine the maximum thickness value possible for which there is not a decrease of battery capacity for each discharge rate applied.

Normally, it is observed commercial values of thickness of separator membrane and degree of porosity that are < 25μm and 40-70% in which these values are attributed for separator but without referring the importance and the influence of tortuosity value in the separator membrane once that these parameters influence its ionic conductivity value [7, 20]. It is observed that the ideal thickness depends also on the discharge scan rate. Taking into account these results, the thickness value depends on the degree of porosity and tortuosity of the separator membrane.

With alteration of these parameters (degree of porosity and tortuosity value), it will be obtained new maximum thickness values of separator without decreasing the delivered capacity value of battery.

4.5 Conclusions

Separator membranes are essential to obtain good performance of lithium-ion batteries. In this way it is required the optimization of separator parameters such as porosity, tortuosity and thickness taking into account the delivered capacity value of the battery.

Based on a mathematical model that describes the electrochemical and ionic transport processes within the separator, variables such as degree of porosity and tortuosity were included through the Bruggeman exponent at different scan rates.

The Bruggeman coefficient, which depends on the degree of porosity and tortuosity, has a strong influence on the values of the diffusion coefficient and ionic conductivity of lithium ions in the separator and, consequently, on the delivered capacity of the battery. The inclusion of the separator membrane in the simulation model of the battery system does not affect the performance of the battery in comparison to the free electrolyte without polymer membrane. It was then demonstrated the existence of optimal values of the degree of porosity and tortuosity. Independently of the scan rate, the ideal value of the degree of porosity is above 50% and the separator thickness should range between 1μm and 32μm with mechanical integrity in order to maintain good battery performance.

4.6 References

1. Wakihara, M. and O. Yamamoto, Lithium ion batteries: fundamentals and performance1998: Kodansha.
2. Scrosati, B. and J. Garche, Lithium batteries: Status, prospects and future. Journal of Power Sources, 2010. **195**(9): p. 2419-2430.
3. Marom, R., et al., A review of advanced and practical lithium battery materials. Journal of Materials Chemistry, 2011. **21**(27): p. 9938-9954.
4. Etacheri, V., et al., Challenges in the development of advanced Li-ion batteries: a review. Energy & Environmental Science, 2011. **4**(9): p. 3243-3262.
5. Yoshio, M., R.J. Brodd, and A. Kozawa, Lithium-Ion Batteries: Science and Technologies2010: Springer.
6. Manuel Stephan, A., Review on gel polymer electrolytes for lithium batteries. European Polymer Journal, 2006. **42**(1): p. 21-42.
7. Arora, P. and Z. Zhang, Battery Separators. Chemical Reviews, 2004. **104**(10): p. 4419-4462.
8. Huang, X., Separator technologies for lithium-ion batteries. Journal of Solid State Electrochemistry, 2011. **15**(4): p. 649-662.
9. Ramadesigan, V., et al., Modeling and Simulation of Lithium-Ion Batteries from a Systems Engineering Perspective. Journal of The Electrochemical Society, 2012. **159**(3): p. R31-R45.
10. Martínez-Rosas, E., R. Vasquez-Medrano, and A. Flores-Tlacuahuac, Modeling and simulation of lithium-ion batteries. Computers & Chemical Engineering, 2011. **35**(9): p. 1937-1948.
11. Miranda, D., C.M. Costa, and S. Lanceros-Mendez, Lithium ion rechargeable batteries: State of the art and future needs of microscopic theoretical models and simulations. Journal of Electroanalytical Chemistry, 2015. **739**: p. 97-110.
12. Patel, K.K., J.M. Paulsen, and J. Desilvestro, Numerical simulation of porous networks in relation to battery electrodes and separators. Journal of Power Sources, 2003. **122**(2): p. 144-152.
13. Arora, P., et al., Comparison between computer simulations and experimental data for high-rate discharges of plastic lithium-ion batteries. Journal of Power Sources, 2000. **88**(2): p. 219-231.

14. Doyle, M., et al., Comparison of Modeling Predictions with Experimental Data from Plastic Lithium Ion Cells. Journal of The Electrochemical Society, 1996. **143**(6): p. 1890-1903.
15. Ding-Wen, C., et al., Validity of the Bruggeman relation for porous electrodes. Modelling and Simulation in Materials Science and Engineering, 2013. **21**(7): p. 074009.
16. Costa, C.M., et al., Influence of different salts in poly(vinylidene fluoride-co-trifluoroethylene) electrolyte separator membranes for battery applications. Journal of Electroanalytical Chemistry, 2014. **727**(0): p. 125-134.
17. Cannarella, J. and C.B. Arnold, Ion transport restriction in mechanically strained separator membranes. Journal of Power Sources, 2013. **226**: p. 149-155.
18. Costa, C.M., et al., Poly(vinylidene fluoride)-based, co-polymer separator electrolyte membranes for lithium-ion battery systems. Journal of Power Sources, 2014. **245**(0): p. 779-786.
19. Yu, S., et al., Investigation of design parameter effects on high current performance of lithium-ion cells with LiFePO4/graphite electrodes. Journal of Applied Electrochemistry, 2012. **42**(6): p. 443-453.
20. Tye, F.L., Tortuosity. Journal of Power Sources, 1983. **9**(2): p. 89-100.
21. Doyle, M., T.F. Fuller, and J. Newman, Modeling of Galvanostatic Charge and Discharge of the Lithium/Polymer/Insertion Cell. Journal of The Electrochemical Society, 1993. **140**(6): p. 1526-1533.
22. Costa, C.M., M.M. Silva, and S. Lanceros-Mendez, Battery separators based on vinylidene fluoride (VDF) polymers and copolymers for lithium ion battery applications. RSC Advances, 2013. **3**(29): p. 11404-11417.
23. Martins, P., A.C. Lopes, and S. Lanceros-Mendez, Electroactive phases of poly(vinylidene fluoride): Determination, processing and applications. Progress in Polymer Science, 2014. **39**(4): p. 683-706.
24. Michot, T., A. Nishimoto, and M. Watanabe, Electrochemical properties of polymer gel electrolytes based on poly(vinylidene fluoride) copolymer and homopolymer. Electrochimica Acta, 2000. **45**(8–9): p. 1347-1360.
25. Idris, N.H., et al., Microporous gel polymer electrolytes for lithium rechargeable battery application. Journal of Power Sources, 2012. **201**: p. 294-300.

26. Rajendran, S., O. Mahendran, and T. Mahalingam, Thermal and ionic conductivity studies of plasticized PMMA/PVdF blend polymer electrolytes. European Polymer Journal, 2002. **38**(1): p. 49-55.

27. Ferreira, J.C.C., et al., Variation of the physicochemical and morphological characteristics of solvent casted poly(vinylidene fluoride) along its binary phase diagram with dimethylformamide. Journal of Non-Crystalline Solids, 2015. **412**: p. 16-23.

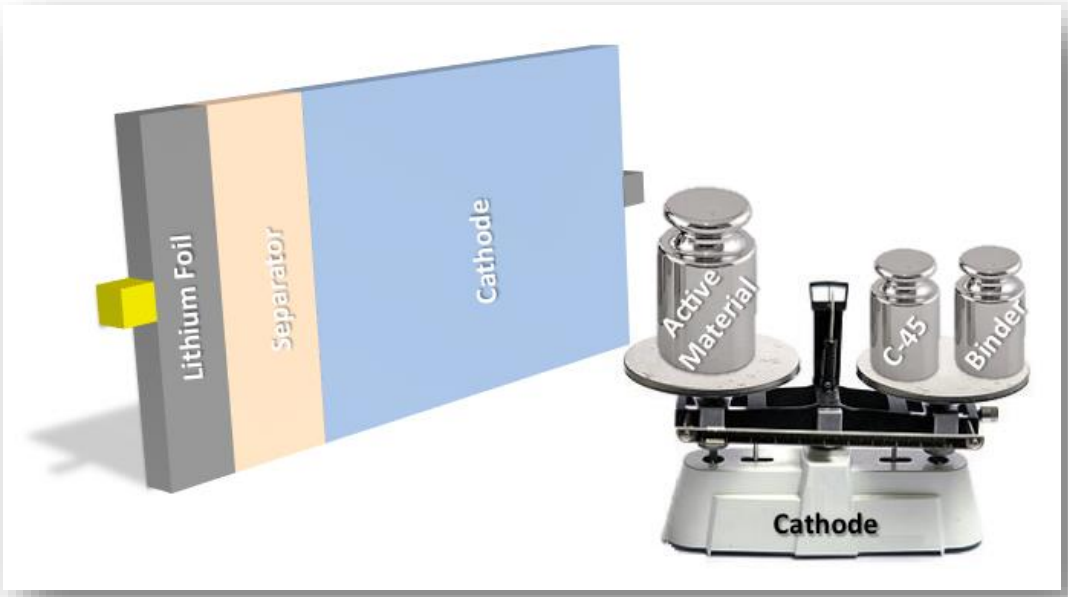

5. Theoretical simulation of the optimal relationship between active material, binder and conductive additive for lithium-ion battery cathodes

This chapter describes the theoretical simulations that have been carried out to evaluate the influence of active material, binder and conductive additive relative contents on electrode performance at various discharge rates. The simulations were performed by the finite element method applying the Doyle/Fuller/Newman model for two different active materials, C-$LiFePO_4$ and $LiMn_2O_4$, and the obtained results were compared with experimental data.

This chapter is based on the following publication:

"Theoretical simulation of the optimal relationship between active material, binder and conductive additive for lithium-ion battery cathodes", D. Miranda, A. Gören, C. M. Costa, M. M. Silva, A. M. Almeida, S. Lanceros-Méndez, submitted.

5.1 Introduction

The rapid technological development of mobile electrical applications lead to the increasingly important question of how to store electrical energy in a more efficient way [1]. Thus, energy storage is critical in modern society, the most used energy storage system being batteries [2], particularly, rechargeable lithium-ion batteries, introduced to the market in 1992 by Sony [3]. Lithium-ion batteries are of increasing importance as power sources as they are lighter, cheaper, show higher energy density, lower self-discharge, no memory effect, prolonged service-life, higher number of charge/discharge cycles, environmental friendliness and higher safety when compared to other battery technologies [4]. There are two main types of batteries, defined as primary and secondary batteries, the latter being rechargeable [5, 6].

The main constituents of lithium-ion batteries are the cathode, anode and the separator membrane [7] and the key issues are to improve specific energy, power, safety and reliability [8]. For the various components of the batteries it is necessary to improve the materials that constitute them, being particularly relevant the cathode, due to its influence on the capacity of the battery [9].

Cathodes are typically constituted by a polymer binder, a conductive additive and an active material, the most used active materials being lithium iron phosphate ($LiFePO_4$), lithium nickel manganese cobalt oxide ($LiNiMnCoO_2$), lithium cobalt oxide ($LiCoO_2$), lithium nickel oxide ($LiNiO_2$), lithium nickel cobalt aluminum ($LiNiCoAlO_2$), lithium titanate oxide ($LiTiO_2$) and lithium manganese spinel oxide ($LiMn_2O_4$), among others [9].

The key characteristics of the active materials include being easily reducible, reacting with lithium in a reversible manner, being a good electronic conductor and stable, i.e. not undergoing structural variations of degradation with the loading and unloading of the battery [4].

Relevant parameters of the cathodes that affect their performance include active mass loading, porosity, thickness and the relation between active material, binder and conductive additive [10-13].

The electrode density depends on the maximum amount of active material, including the lowest possible amount of binder and conductive additive to obtain proper mechanical and electrical properties, respectively [14].

The width of the cathode determines two main factors: the quantity of active material and the resistance to mass transport; finally, the porosity of the electrode affects the effective conductivity and the resistance to mass transfer [15].

For C-$LiFePO_4$ active material, more than 40 electrode formulations have been reported for active material, binder and conductive additive, the highest amount of active material reaching 95% and the lowest amount for binder and conductive additive being 2% and 3%, respectively [14]. For C-$LiFePO_4$ as active material, the minimum and maximum relative percentage of each component in the electrode slurry has been reported as 60 to 95% for the active material, from 2 to 25% for the binder and from 3 to 30% for the conductive additive [14]. Percolation is achieved for a volume fraction of active material of 30% [16].

Taking into account the state of art, it is thus necessary the optimization of the electrode composition, allowing the fabrication of high-quality lithium-ion battery cathodes for applications such as printed batteries [17]. This optimization can be guided by computer simulation of the performance of a battery, based on the electrochemical reactions describing the physical-chemical properties of the materials to be used as electrodes and separators [18].

Thus, this chapter is devoted to the optimization of the cathode formulation relationship (active material, conductive material and binder) for two active materials (C-$LiFePO_4$ and $LiMn_2O_4$) taking also into account the porosity and electronic conductivity. In this way, the study has focus in understanding the optimal relationship of the cathode components for obtaining higher capacity, maintaining constant the width of the battery. The theoretical simulation model was first validated with experimental results.

5.2 Preparation and characterization of the cathodes

For the validation of the theoretical model, cathodes were first prepared and characterized. C-$LiFePO_4$ (LFP, Particle size: D_{10}=0.2 μm, D_{50}=0.5 μm and D_{90}=1.9 μm), carbon black (Super P-C45), poly(vinylidene fluoride) (PVDF, Solef 5130) and N-methyl-2-pyrrolidone (NMP) were acquired from Phostech Lithium, Timcal Graphite & Carbon, Solvay and Fluka, respectively. $LiMn_2O_4$ (LMO) was synthesized via sol gel method as indicated in [19]. The cathode was prepared by mixing LFP or LMO as

active materials, Super P, and the polymer binder in NMP solvent with a weight ratio of 80:10:10 (wt.%).

After complete dissolution of the polymer binder, small amounts of dried mixed solid material (LFP/LMO and Super P) were added to the solution under constant stirring at room temperature. The electrode slurry was maintained under stirring for 3 hours at 1000 rpm to obtain a good dispersion.

The electrode slurry was spread onto an aluminum foil and dried in air atmosphere at 80 ºC in a conventional oven (ED 23 Binder). After complete evaporation of the solvent, the cathodes were dried at 90 ºC in vacuum before being transferred into a glove-box.

Two Swagelok type cells were assembled in the home-made argon-filled glove box: metallic lithium (8 mm diameter) was used as anode material; Whatman glass microfiber filters (grade GF/A) (10 mm diameter) was used as separator; 1M $LiPF_6$ in ethylene carbonate-diethyl carbonate (EC-DEC, 1:1 vol) or in ethylene carbonate-dimethyl carbonate (EC-DMC, 1:1 vol) (Solvionic) were used as electrolyte and the prepared LFP/LMO electrodes were used as cathodes (8 mm diameter).

Charge-discharge measurements were carried out at room temperature at different current densities (C/10 and C/2) in the voltage range from 2.5 to 4.2 V for LFP and from 3.5 to 4.2 V for LMO using a Landt CT2001A Instrument.

5.3 Theoretical simulation model and model parameters

Two lithium half-cell batteries were simulated with the different active materials for the cathode as well as with the different electrolyte solutions. The lithium-ion half-cell battery structure was [anode, (Li metallic) | separator, P(VDF-TrFE) soaked in 1M LiTFSI in PC | cathode, (LFP) or (LMO)].

The main equations governing the operation of the different components of the half-cell batteries (Chapter 3) are based on the Doyle/Fuller/Newman model [20-25] and the finite element method was implemented for the theoretical simulations.

In this work, the influence of the relative percentages of the three components of the cathode (binder, active material and carbon black) in the performance of the battery will be evaluated. The variables introduced in the model will be the percentage of active material, C_1, binder, C_2, and carbon black, C_3, respectively. The relative percentage of

each component affects the value of the porosity (ε_c) of the cathode as well as its electronic conductivity (σ_c). Thus, the porosity of the cathode is represented by [13, 26]:

$$\varepsilon_c = \frac{\left(L - W\left(\frac{C_1}{D_1} + \frac{C_2}{D_2} + \frac{C_3}{D_3}\right)\right)}{L} \tag{1}$$

where L is the thickness of the electrode, W is weight of the electrode per unit area and D_1, D_2 and D_3 are the densities of the active material, the binder and the conductive additive, respectively.

Further, the electronic conductivity of the cathode is represented by [13, 26]:

$$\log \sigma_c = \log \sigma_{3Pure} - b\left(\frac{\phi_2}{\phi_3}\right) \tag{2}$$

where σ_{3Pure} is the measured electronic conductivity of the neat conductive additive. The parameters ϕ_2 and ϕ_3 are described by the following equations:

$$\phi_2 = \frac{m_2}{D_2 \times V_{Total}} \tag{3}$$

$$m_2 = C_2 \times m_{Total} \tag{4}$$

and

$$\phi_3 = \frac{m_3}{D_3 \times V_{Total}} \tag{5}$$

$$m_3 = C_3 \times m_{Total} \tag{6}$$

In equation 2, $log\ \sigma_{3Pure}$ and b are constants, so σ_c depends on the ratio ϕ_2/ϕ_3. Thus,

$$\frac{\phi_2}{\phi_3} = \frac{C_2 \times D_3}{C_3 \times D_2} = \frac{C_2}{C_3} \times \frac{D_3}{D_2} = n \times \frac{D_3}{D_2} \tag{7}$$

with

$$n = \frac{C_2}{C_3} \tag{8}$$

The percentages of the active material, the binder and the carbon black, will be called hereafter C_1, C_2 and C_3, respectively.

Finally, the parameters used for the simulations of the half-cells are indicated in Table 5.1.

The nomenclature of the aforementioned equations and tables is shown in the List of Symbols and Abbreviations.

Table 5.1 - Parameters used for the simulations of the Li/LFP and Li/LMO half-cells.

Li/LFP and Li/LMO cell			
Parameter	**Unit**	**Electrolyte**	**Cathode (LFP/LMO)**
$C_{E,i,0}$	mol/m^3		800/3900
$C_{E,i,max}$	mol/m^3		22806
C_L	mol/m^3	1000	
r	m		$1{,}7\times10^{-6}/1{,}5\times10^{-6}$
L_c	m		$70\times10^{-6}/99\times10^{-6}$
L_s	m	430×10^{-6}	
$k_{ef,i}$	S/m	$(\text{value}^{a)})\times0{,}30^{1,5}/(\text{value}^{b)})\times0{,}35^{1,5}$	$(\text{value}^{a)b)})\times\varepsilon_c{}^{1,5}$
D_i	m^2/s	$(3{,}0\times10^{-10})\times0{,}30^{1,5}/(7{,}5\times10^{-11})\times0{,}35^{1,5}$	$(3{,}0\times10^{-10}/7{,}5\times10^{-11})\times\varepsilon_c{}^{1,5}$
D_{LI}	m^2/s		$8\times10^{-18}/1\times10^{-16}$
k_i	mol/s.m^2		$3\times10^{-13}/2\times10^{-11}$
Brugg or p		1,5	1,5
ε_i		0,30/0,35	ε_c
σ_i	S/m		σ_c
σ_{3Pure}	S/m		100 [27]
i_{1C}	A/m^2	8.66/7.96	
C_1			C_1
C_2			C_2
C_3			C_3
D_1	g/m^3		$3{,}34\times10^6/2{,}93\times10^6$
D_2	g/m^3		1.765×10^6
D_3	g/m^3		1.9×10^6
W	g/m^2		64,6/21.8
b			1
V_{Totalc}	m^3		$4{,}45\times10^{-9}/7{,}25\times10^{-9}$
m_{Totalc}	g		$4{,}11\times10^{-3}/1{,}6\times10^{-3}$
General parameters			
Cut-off voltage	V	2,5/3.4	
F	C/mol	96487	
T	K	298,15	
R	J/mol K	8,314	
t_+^0		0,363	
A_{bat}	m^2	$6.36\times10^{-5}/5{,}02\times10^{-5}$	
Electrolyte	$LiPF_6$ in EC:DEC/ $LiPF_6$ in EC:DMC		
Inert filler	PVDF		

a) Model fits: Ionic condutivity as a function of salt concentration for $LiPF_6$ in EC:DEC [22]:

$$k_l = 0,0911 + 1,910c - 1,052c^2 + 0,1554c^3$$

b) Model fits: Ionic condutivity as a function of salt concentration for $LiPF_6$ in EC:DMC [28]:

$$k_l = 2{,}905\times10^{-4} + 2{,}32702\times10^{-2}c - 1{,}82683\times10^{-2}c^2 + 5{,}1708\times10^{-3}c^3 - 4{,}977\times10^{-4}c^4$$

5.4 Results and discussion

In order to evaluate the optimal relationship between the active material, the conductive material and the polymer binder within the cathodes in order to obtain higher capacity values and optimal performance in lithium ion half-cells, theoretical simulations were performed in two lithium ion half-cells (Li/LFP and Li/LMO) taking into account the equations (Chapter 3 and 5.3) describing the phenomena associated to battery performance. Thus, the delivery capacity and impedance for both half-cells was obtained. Further, the electrode and electrolyte current density was also obtained for the Li/LFP half-cells.

5.4.1 LFP and LMO half-cells: validation of the theoretical model

First, the simulation model was validated by comparing the theoretical and experimental results obtained for the Li/LFP and Li/LMO half-cells (figures 5.1a) and 5.1b)).

Figures 5.1a) and 5.1b) show a comparison of the experimental results and the simulation curves (full line) at C/10 and C/2 discharge rates for Li/LFP and Li/LMO, respectively.

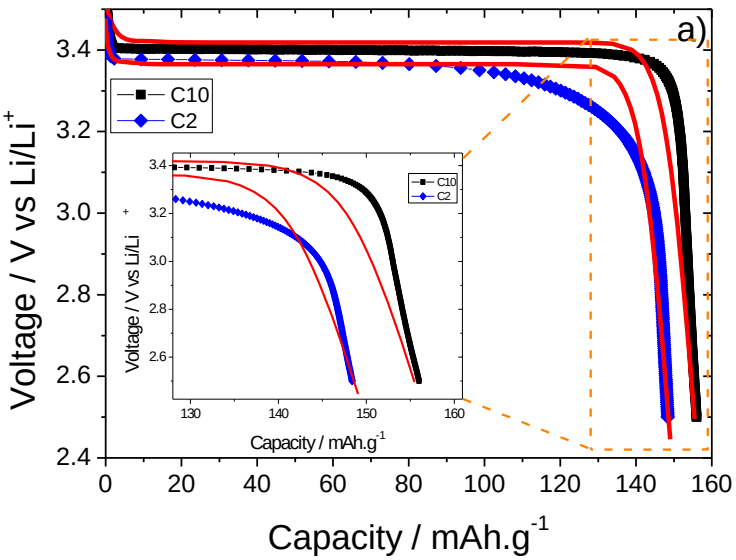

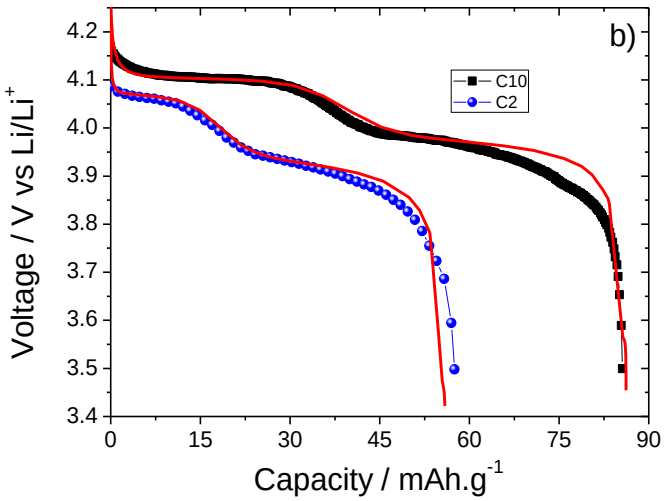

Figure 5.1 - Voltage as a function of the delivered capacity at C/10 and C/2 discharge rates for the a) Li/LFP and b) Li/LMO half-cells.

For both half-cells and discharge rates, a good agreement is observed between the theoretical and experimental values, validating therefore the simulation model.

For Li/LFP, the theoretical capacities values at C/10 and C/2 are 156 mAh.g^{-1} and 149 mAh.g^{-1}, respectively, and the corresponding experimental capacity values are 156 mAh.g^{-1} and 148 mAh.g^{-1} (Figure 5.1a)). Similar agreement is observed for the Li/LMO half-cell, with theoretical and experimental values of 86 mAh.g^{-1} and 56 mAh.g^{-1} at C/10 and C/2, respectively (figure 5.1b)).

In the higher capacity region (magnification in figure 5.1a) of the discharge curves there are small deviations between the theoretical simulations and the experimental results, attributed to corresponding differences in the electronic conductivity values [29]. Further, the theoretical electronic conductivity values described by equation (2) do not take into account the microscopic physico-chemical phenomena associated to electrical resistance that occurs on carbon black particles dispersed together with the active material. Further, the voltage difference between theoretical and experimental values is higher at the C/2 discharge rate than at the C/10 discharge rate, which is associated to internal total resistance effects at high discharge rates [30].

In any case, a good theoretical approximation is obtained for both discharge curves (C/10 e C/2) and half-cells, allowing the validation of the theoretical model.

5.4.2 Influence of the cathode components content in the performance of the half-cell.

The effect of the content of the different components of the cathode in Li/LFP and Li/LMO half-cells performance was first evaluated by taking into account batteries with different active material (C_1) content. Then, for each battery with a specific C_1, C_2 and C_3 were varied in order to obtain discharge curves at a discharge rate of 1C, as shown in figure 5.2a) and 5.2b) for Li/LFP and figure 5.3b) for Li/LMO half-cells, respectively.

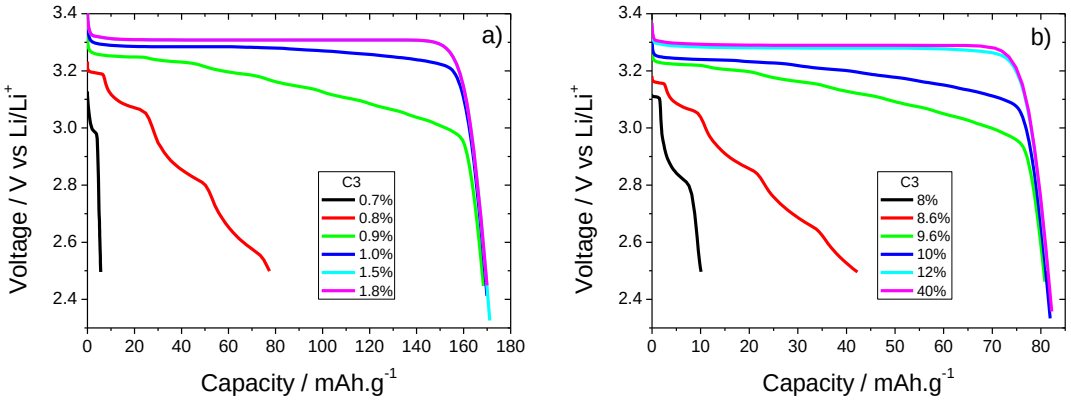

Figure 5.2 - Voltage as a function of delivered capacity for Li/LFP half-cells with C_1: 95% a) and 50% b) at a discharge rate of 1C.

Figure 5.2a) shows a representative Li/LFP half-cell with 95% of C_1 with C_3 varying from 0.7% to 1,8%. When C_3 varies, C_2 changes accordingly. It is observed that when C_3 is below 1% there is instability on battery operation and losses in the capacity value, whereas when C_1 is above 1%, a constant capacity value is obtained. These results show that there is a minimum value of C_3 to maintaining the battery with low internal resistance (see impedance values later in section 5.4.3) and without capacity losses. It is important to notice that the minimum value of C_3 also depends on the active material content, as shown in figure 5.2. Further, the C_3 content only affects the electrical conductivity, the porosity value of the cathode remaining constant at a value of ε=71%. The porosity of the cathode just varies ~ 1% with varying C_3 for a specific C_1 content. Thus, the porosity is more affected by C_1, due to the higher density of the material.

Figure 5.2b) shows the Li/LFP half-cell with C_1=50% and C_3 ranging from 8% to 40%. The behaviour of this half-cell is representative of the other ones with different

active material contents. It is important to notice that with decreasing C_3 there is also a decrease in the value of the capacity, indicative of poor stability in battery operation. For C_3 ranging from 8% to 40% the obtained values of the capacity range from 9.3 $mAh.g^{-1}$ to 81.1 $mAh.g^{-1}$. It is to notice that in this case, the minimum value of C_3 is higher than for the half-cell with 95% of C_1. For the half-cell with a C_1= 50%, the minimum C_3 is 10%. This effect is explained by the balance between the increase of the capacity associated to the higher active material content, and the losses associated to the internal resistance: lower active material content implies a lower ionic current that should be compensated by an electronic conduction to maintain a high performance battery.

Figure 5.3a) and 5.3b) show ten batteries for each half-cell (Li/LFP and Li/LMO) with C_1 contents ranging 50% to 95%. In each of these batteries the C_3 and consequently the C_2 was varied.

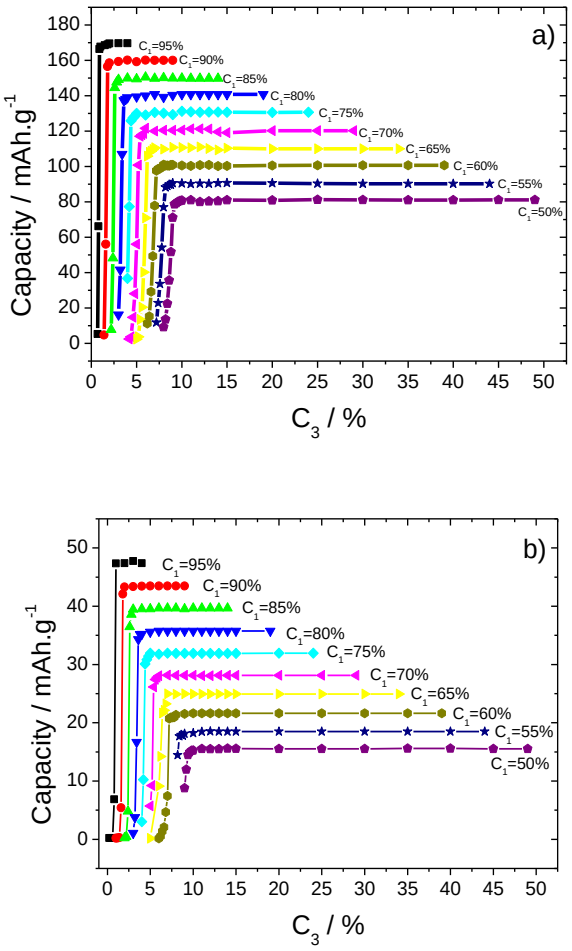

Figure 5.3 - Delivered capacity as a function of C_3 for different C_1 for Li/LFP (a) and Li/LMO (b) half-cells at a discharge rate of 1C.

Figures 5.3a) and 5.3b) also show that for batteries with 95% of C_1 it is possible to vary C_3 between 0.7% and 4%, thus allowing a minimum of 1% for C_2, similar to the minimum of 2% for C_2 content that has been reported experimentally [14].

It is observed that Li/LFP and Li/LMO half-cells show a different minimum C_3, above which a constant capacity value is obtained, leading to higher battery performance. High conductive material content increases the electrical conductivity, but does not contribute to an increase of the capacity of the battery, once the amount of active material (quantity of ions) limits the capacity value, as observed for the two active materials (figure 5.3). For low active material contents, high percentages of conductive material are required, once it is necessary to optimize the electrical conduction to obtain maximum capacity values of the battery, as a low electrical conductivity implies a low profitability of the intercalation of ions within the cathode along the discharge cycle.

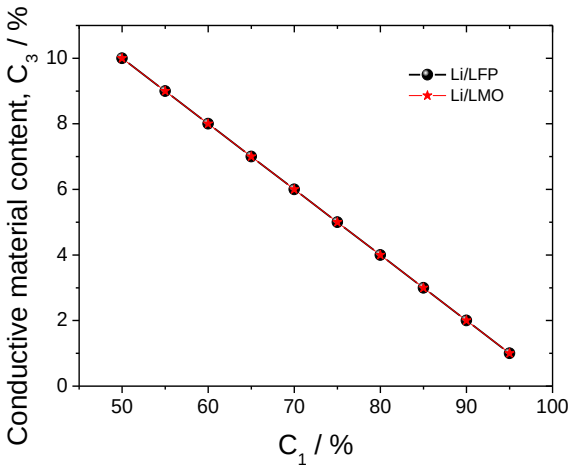

Figure 5.4 - Minimum percentage of C_3 as a function of C_1 for both half-cells at a discharge rate of 1C.

Figure 5.4 shows a summary of minimum percentage of C_3 supporting an optimal battery performance for both half-cells with different amount of C_1. By decreasing the active material content from 95% to 50%, the minimum percentage of C_3 increases linearly. The same behaviour is obtained for both LFP and LMO based batteries.

Table 5.2 shows the ratio (n) between C_2 and C_3 (equation 8) for both half-cells at 1C.

Table 5.2 - Minimum values of n=C_2/C_3 as a function of C_1 for the Li/LFP and Li/LMO half-cells at a discharge rate of 1C.

Half-Cell	**C_1**									
Li/LFP	**50%**	**55%**	**60%**	**65%**	**70%**	**75%**	**80%**	**85%**	**90%**	**95%**
n (C_2/C_3)	40/10	36/9	32/8	28/7	24/6	20/5	16/4	12/3	8/2	4/1
Li/LMO	**50%**	**55%**	**60%**	**65%**	**70%**	**75%**	**80%**	**85%**	**90%**	**95%**
n (C_2/C_3)	40/10	36/9	32/8	28/7	24/6	20/5	16/4	12/3	8/2	4/1

Table 5.2 shows that a constant value of the n is obtained (n= 4) for the different active material contents for both half-cells. Thus, this ratio is independent of the nature and of the type of active material used for half-cell fabrication. The ratio n depends of the electrical conductivity value for neat conductive material that was used in battery.

In summary, in order to obtain an optimal half-cell performance, a minimum of C_3 of 25% has to be used in relation to the C_2. This minimum ratio is validated by using carbon black as conductive material [14].

Figure 5.5 compares the simulated capacity values ($Capacity_{sim}$) with the theoretical capacity values ($Capacity_{theo}$) for the Li/LFP half-cell with different active material contents at 1C discharge rate. Independently of the active material content it is observed a good agreement with small differences between the theoretical and experimental results. The observed differences are attributed to the effect of charge-transfer resistance and the electronic/ionic conductivity value assumed in the theoretical model. $Capacity_{sim}$ were obtained at the minimum ratio n where the battery operates with better stability.

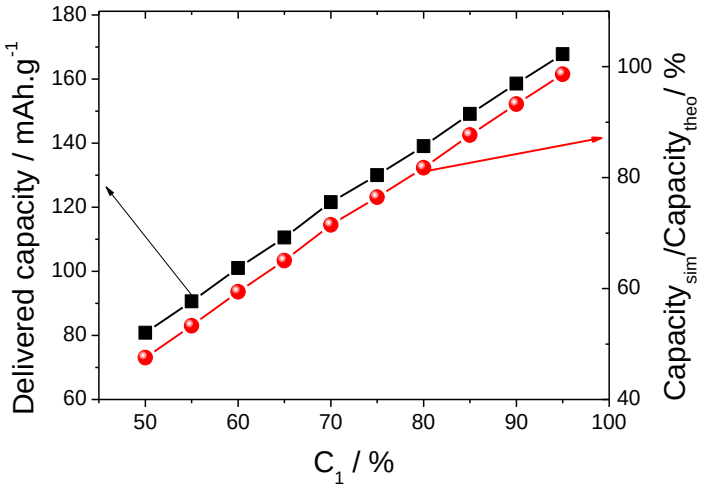

Figure 5.5 - Delivered capacity and $Capacity_{sim}/Capacity_{theo}$ (%) ratio as a function of C_1 for the Li/LFP half-cell at 1C discharge rate.

Figure 5.5 shows that for C_1=50% the decrease of the capacity is also approximately 50% of the theoretical capacity. Therefore, C_1 contents above 50% should be selected for suitable half-cell performance.

Further, the performance of the half-cell was evaluated at low, medium and high discharges rates (1C, 5C and 10C) (Figure 5.6a) and 5.6b)).

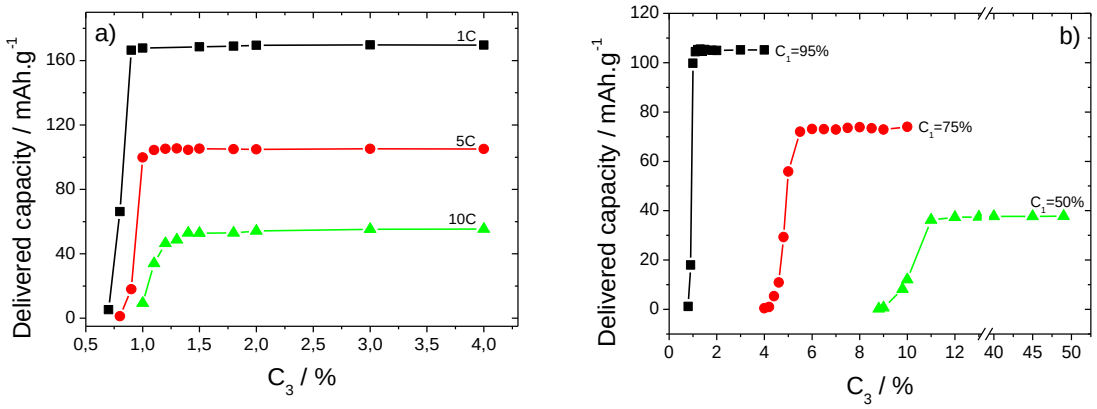

Figure 5.6 - a) Delivered capacity as a function of minimum C_3 for the Li/LFP half-cells: a) C_1=95% at 1C, 5C and 10C discharge rates and b) C_1 = 95%, 75% and 50% at 5C discharge rate.

As mentioned before, the minimum of C_3 to obtain a stable performance in a battery with C_1=95% is 1% at 1C, being obtained (figure 5.6) 1.1% and 1.3% at 5C, 10C discharges rates, respectively (figure 5.6a)). Thus, the high ionic conductivity required for high discharges rates is obtained for electrical conductivity. Thus, it is possible to conclude that once achieved the electrical percolation network for C1 = 95%, the minimum value of C_3 is similar for discharge rate.

Figure 5.6b) also shows that increasing C_1 leads to a decrease of the minimum C_3 to maintaining a stable battery. Further, the minimum C_3 also decreases with decreasing discharge rate (see figure 5.3 and 5.6b)).

Table 5.3 shows the minimum values of *n* obtained for the Li/LFP half-cells with different C_1 at 1C, 5C and 10C discharge rates.

Table 5.3 - Minimum values of the *n* ratio for different C_1 for Li/LFP half-cells at 1C, 5C and 10C discharge rates.

	C_1		
Discharge Rate	**95%**	**75%**	**50%**
1C	n=(4/1) = 4	n=(20/5) = 4	n=(40/10) = 4
5C	n=(3.9/1.1) = 3.54	n=(19.5/5.5) = 3.54	n=(39/11) = 3.54
10C	n=(3.7/1.3) = 2.64	n=(18.5/6.5) = 2.86	n=(37/13) = 2.84

Table 5.3 shows that *n* increases with increasing discharge rate for a given active material content and that for a fixed discharge rate, the variable *n* is independent of the active material content.

Thus, the minimum C_3 depends on C_1 and discharge rate value. However, the ratio *n* is independent of C_1, but depends on the discharge rate. At high discharges rates, it is required high ionic and electrical conduction to obtain a facilitated intercalation process. So, it is important to take into account the minimum value of *n* according to the battery operation discharge rate.

5.4.3 Impedance of the LFP and LMO half-cells

The impedance of the half-cells was evaluated through the Nyquist plots to better understand the conduction phenomena according to the balance of the different cathode components in the Li/LFP and Li/LMO half-cells. Based on the previous sections, the battery resistance was evaluated with the minimum C_3 and ratio *n* for different C_1, as obtained in the previous study at a discharge rate of 1C.

For the different half-cell simulations, the Nyquist plots are characterized by a semicircle at high frequencies (the overall resistance) and an approximately 45º line in the low-frequency range, which can be considered as the Warburg impedance, associated with the lithium-ion diffusion in the bulk of the active material [31].

Figure 5.7a) and 5.7b) shows the Nyquist plot with C_1 of 95% and 50% at 1C discharge rate, respectively. Figure 5.7a) shows a total impedance that corresponds to the sum of the electrolyte resistance (R_e, high frequency intercept with the Z´-axis), surface film resistance (R_f, Li-ion migration resistance through the solid electrolyte interface (SEI) film formed on the cathode surface) and charge-transfer reaction resistance (R_{ct}) ascribed to the lithium-intercalation process. It is observed that an increase of the impedance value is observed below 1.0% of C_3, which explains the

existence of a minimum C_3 in order to maintain the battery operating with high performance and stability at a given discharge rate. At a discharge rate of 1C and a C_3 below 1%, the capacity value decreases significantly for the Li/LFP half-cell with a C_1 of 95%. When the battery is characterized by a high resistance, the normal intercalation process of the cathode along the discharge cycle is affected. The same behaviour is observed for the Li/LFP half-cell with C_1=50% at 1C (figure 5.7b). The total impedance values for C_3 = 9.8%, 10% and 12%, are 0.0034 Ω.m^2, 0.0030 Ω.m^2 and 0.0010 Ω.m^2, respectively. The minimum value of C_3 is 10%, as shown in figure 5.4a), the resistance of the battery increases for lower C_3 contents. Figure 5.7c) shows the Nyquist plot for two Li/LMO half-cells. The total impedance value of Li/LMO with C_1 = 95% and C_3 = 1% being 0.0076 Ω.m^2 and for Li/LMO half-cells with C_1 = 50% and C_3 =10% the real impedance value is 0.016 Ω.m^2. Thus, despite the half-cell with C_1 = 50% showing a higher C_3, the battery resistance value is higher.

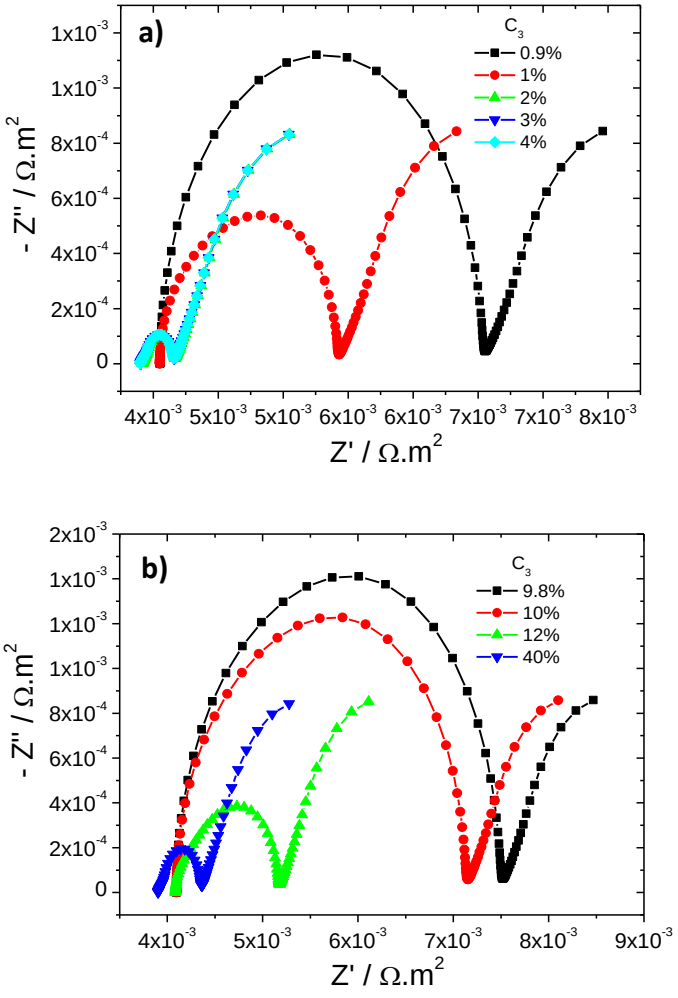

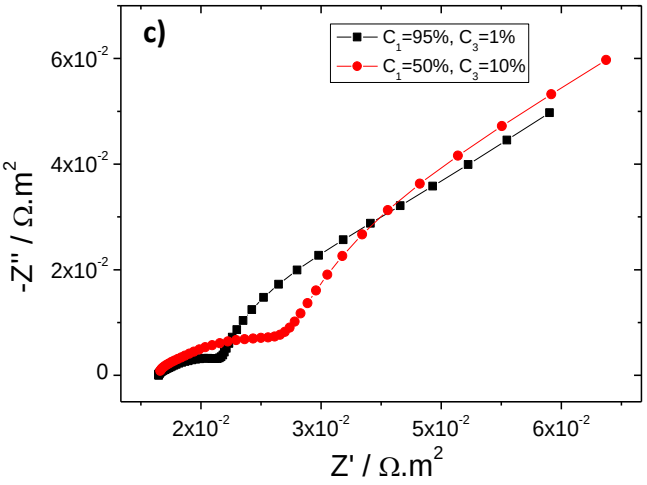

Figure 5.7 - Nyquist plot for the Li/LFP half-cell: a) C_1 = 95% with different C_3 values at 1C discharge rate and b) C_1 = 50% with different C_3 values at 1C discharge rate. Nyquist plot for Li/LMO half-cells: c) C_1 = 95% and 50% and C_3 = 1% and 10% at 1C discharge rate.

Figure 5.8 shows the overall impedance values for the Li/LFP and Li/LMO half-cells obtained for the minimum C_3 at different C_1 and 1C discharge rate, where a considerable increase of the real impedance value below the minimum C_3 for a given C_1 in both batteries is observed.

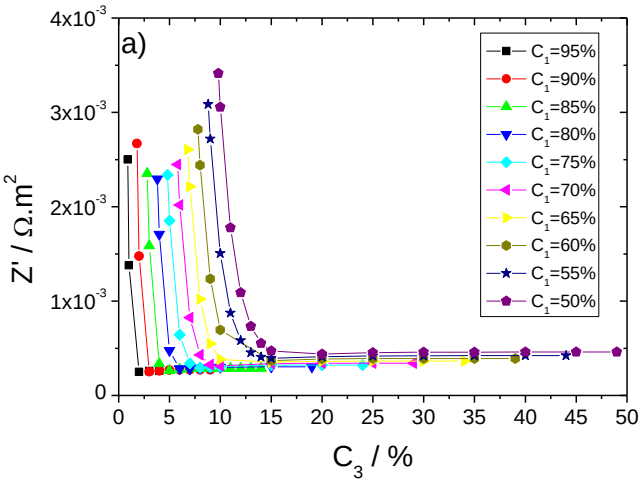

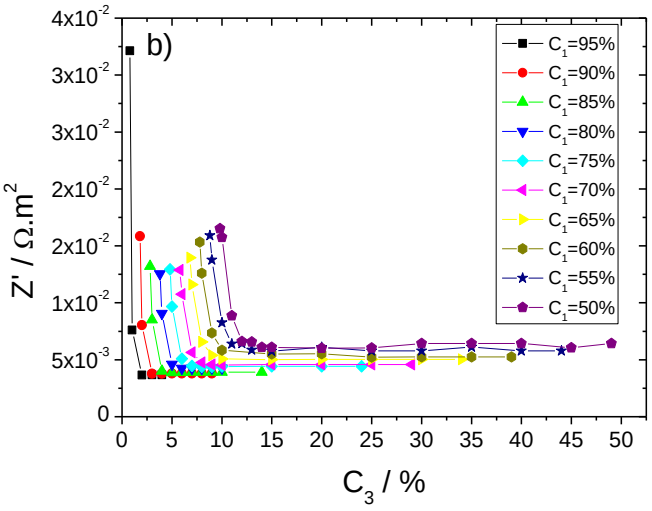

Figure 5.8 - Total impedance as a function of minimum C_3 for different C_1 at 1C discharge rate for: a) Li/LFP and b) Li/LMO half-cells.

For both Li/LFP and Li/LMO half-cells it is observed that above a minimum C_3, the real impedance value remains constant, allowing to optimize the conductive additive content.

5.4.4 Electrolyte and Electrode Current Density for LFP half-cells

The previous sections showed that there is a minimum value of C_3 for a fixed C_1 in order to maintain a good operation of the battery. Now, it is important to qualitatively evaluate the electrolyte and electrode current density in the cathode to investigate the behaviour of ions and electrons during the intercalation process at a given time. For the evaluation of the electrolyte and electrode current density it was chosen the time of 500 s, as this time is within the discharging time range for all evaluated batteries.

The electrolyte current density is defined by the current density of charges associated to lithium ions that exist in the electrolyte present in the pores of the cathode. The electrode current density is the current density of charges associated to electrons moving on the solid phase of the cathode. During the discharge process, the ions move from the separator towards the current collector, through the empty spaces within the cathode (pores). At the same time, the electrons move in the opposite direction, from the current collector to the separator, through the solid phase of the cathode (active and

conductive materials). Figure 5.9 shows a schematic representation of the intercalation process (reduction of lithium ions) within the cathode during the discharge process.

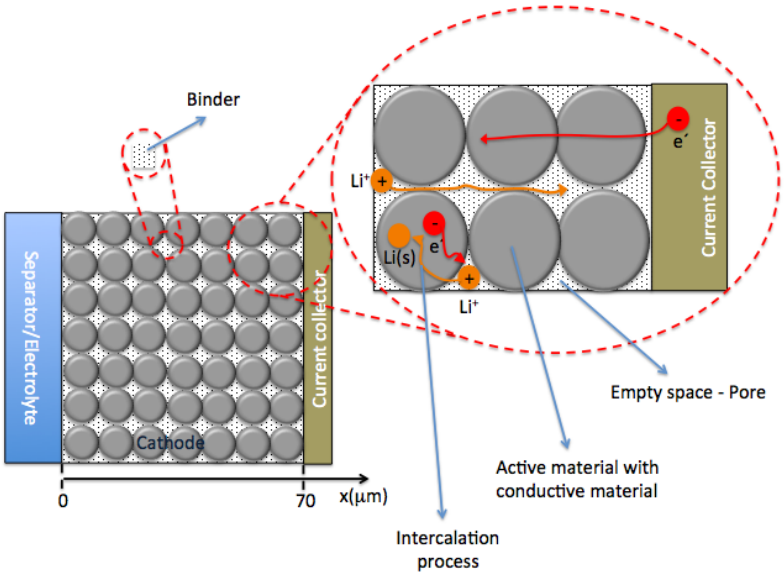

Figure 5.9 - Schematic representation of a battery cathode and the corresponding intercalation process during the discharge mechanism.

In figure 5.9, the boundary between the separator and the cathode is located at x= 0 μm and the interface of the cathode with the current collector is located at x= 70 μm.

Figure 5.10 shows both the electrolyte and the electrode current density along the width of the cathode at the time of 500 s for a Li/LFP half-cell with 95% of active material and 4% of conductive material at 1C discharge rate. As a control parameter, it is shown that the conservation of charge is respected

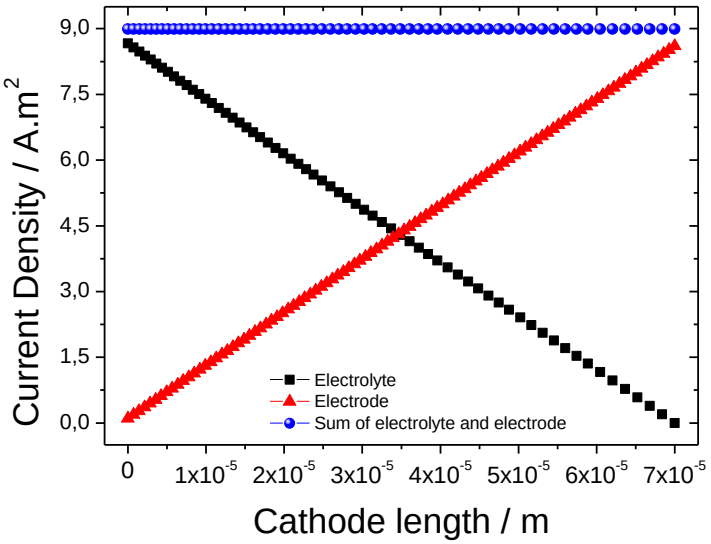

Figure 5.10 - Electrolyte and electrode current density as a function of cathode length for a Li/LFP half-cell with C_1 = 95% and C_3 = 4% of at 1C discharge rate and at 500s. The blue line corresponds the sum of both current densities along the width of the cathode, showing that the divergence of the total electric charge is null.

At t = 500 s, the current density of the electrolyte decreases from x= 0 μm to x= 70 μm, showing that the amount of available lithium ions decreases along of width of the cathode due to the intercalation process. The electrolyte current density close to the current collector is lower than it is at the separator, as ions are subjected to the intercalation process in positions closer to the separator. During the intercalation of ions, they are neutralized or reduced will quickly decreasing the ionic current through the electrode.

The results are shown for the Li/LFP half-cells, being also representative for the Li/LMO half-cell.

Figures 5.11 and 5.12 show the electrolyte and electrode current density along the width of the cathode at a time of 500 s. The simulations were performed in Li/LFP half-cells with C_1 = 95% and 50% with various C_3 at 1C discharge rate.

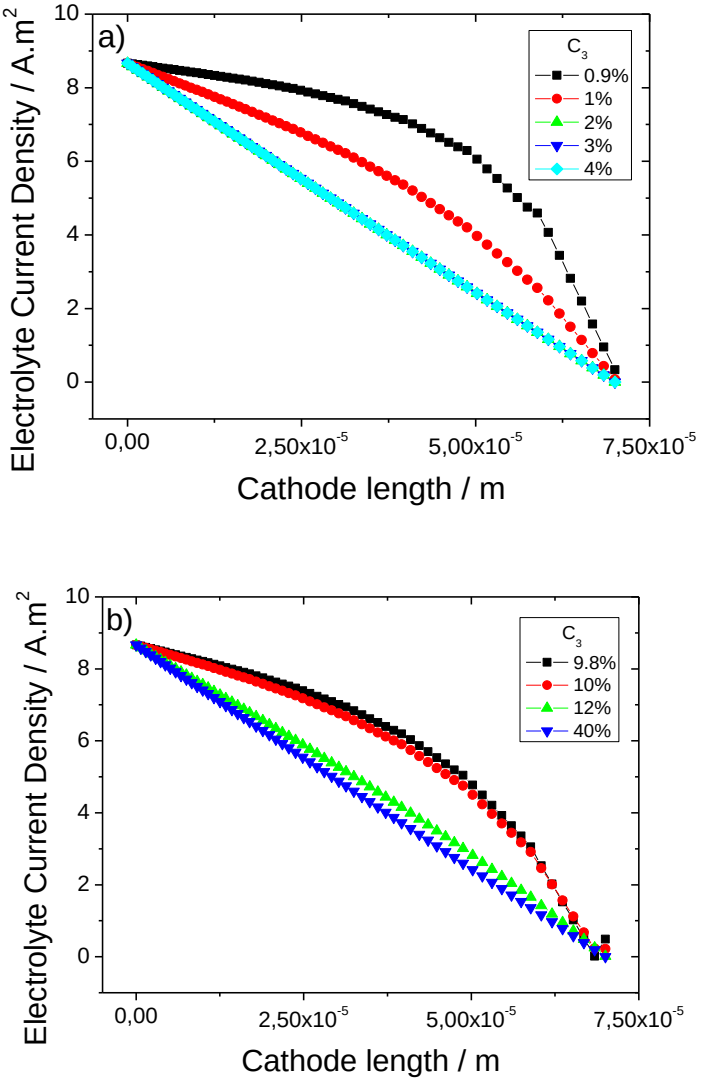

Figure 5.11 - Electrolyte current density as a function of the cathode length for Li/LFP half-cell for various C_3 at 1C discharge rate and at 500s for C_1= 95% (a) and 50% (b).

Regarding the electrolyte current density value for the half-cell with C_1 =95% in the middle position of the cathode at 500 s, it is observed that this value is high for conductive material contents below 1% of minimum C_3, as shown in figure 5.11a). Also, for the half-cell with C_1 = 50% and C_3 below 10% there is a significant increase of the electrolyte current density at the middle position of the cathode, as shown in figure 5.11b). This phenomenon indicates that below a minimum C_3, the intercalation process of ions occur with deeper magnitude in locations closer to the current collector. For low conductive material content, the higher electrical resistance within the solid phase of the cathode, leads to lower electrode current density in locations closer to the separator/cathode interface. Thus, the electrode current density value is higher positions

close to the cathode/current collector interface, leading to a higher intercalation process rate in these regions, as shown in figure 5.12a) and 5.12b).

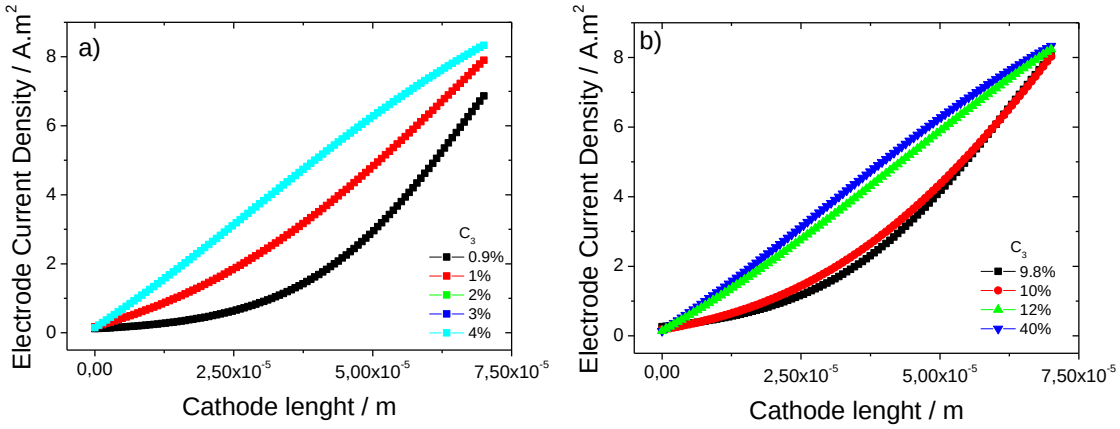

Figure 5.12 - Electrode current density as a function of cathode length for Li/LFP half-cell for various C_3 at 1C discharge rate and 500s for C_1 = 95% (a) and 50% (b).

Figure 5.12 shows that above a minimum C_3 for both half-cells with C_1 = 95% and 50% the electrode current density values are low in the middle position of the cathode, as shown the figures 5.12a) and 5.12b), due to the high electrical resistance of the cathode.

Figure 5.13 shows the electrolyte and electrode current density as a function of time at 20 µm of position inside of cathode in relation to cathode/separator interface. The cathode contains C_1 = 95% and C_3 = 0.9%. The width of cathode is 70 µm.

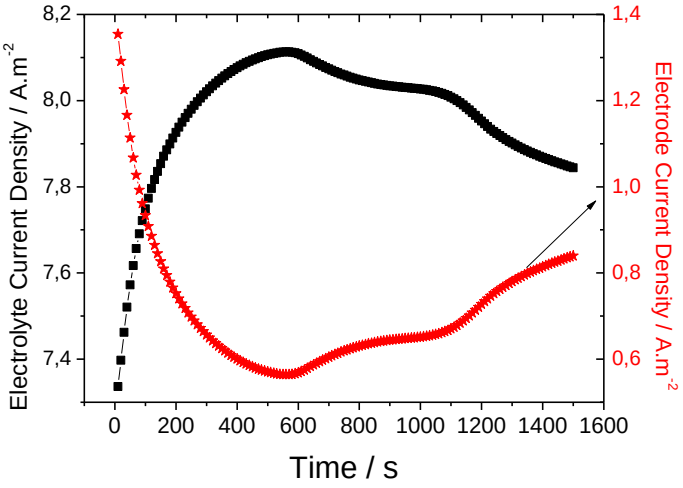

Figure 5.13 - Electrolyte and electrode current density as a function of time for a Li/LFP half-cell with C_1 = 95% and C_3 = 0.9% at 20 µm of position inside of cathode in relation to separator/cathode interface. The width of the cathode is 70 µm.

It is observed that the electrolyte current density increases for the first 600 s and decreases for larger times. The behavior observed for the electrode current density is the opposite of the one observed for the electrolyte current density. The electrolyte and electrode current densities are symmetric to each other. After 600 s, the electrolyte current density decreases, the reason for this fact is due that in this position begins to occur with more intensity the intercalation of the ions taking into account that its density decreases resulting one increase of the electrical resistance.

The behavior of electrolyte and electrode current density as a function of time is independent of the cathode position.

For low conductive material content, the electrons are subjected to higher resistance in their flux, so the lithium ions move deeper inside the cathode before the intercalation process occurs. Thus, at one instant of time of discharge the half-cells with less conductivity material content show the higher electrolyte density current and lower electrode current density in the middle position of cathode.

5.5 Conclusions

The optimization of the electrode formulation based on different active material content, binder and conductive additive is essential for maximizing the electrode properties in lithium-ion batteries. Thus, this work reports on the optimization of the electrode formulation for two active materials: C-$LiFePO_4$ and $LiMn_2O_4$. The theoretical simulations were based on the Doyle/Fuller/Newman theoretical model and the validation of the theoretical model was performed through comparison with experimental results.

It was found that the C_2/C_3 ratio described by the variable *n* should be taken into account in the fabrication of the cathode. Independently of the active material type, the minimum value of the C_2/C_3 ratio is 4 at a discharge rate of 1C. So, when the battery is subjected to a discharge rate of 1C, the relationship $C_3 = 0.25 \times C_2$ should be respected. The minimum value of the C_2/C_3 ratio depends on the discharge rate, as well as the electrical conductivity, which depends on the C_2/C_3 ratio and the electrical conductivity value of neat conductive material.

The ideal relation for the electrode material is 90% of percentage of active material (C_1) for obtain good cycling and the C_2 and C_3 varying between 2 and 8% according the scan rate and respecting the mechanical stability.

5.6 References

1. Evarts, E.C., *Lithium batteries: To the limits of lithium.* Nature, 2015. **526**(7575): p. S93-S95.
2. Tarascon, J.M. and M. Armand, *Issues and challenges facing rechargeable lithium batteries.* Nature, 2001. **414**(6861): p. 359-367.
3. Vincent, C.A., *Lithium batteries: a 50-year perspective, 1959–2009.* Solid State Ionics, 2000. **134**(1–2): p. 159-167.
4. Whittingham, M.S., *Lithium Batteries and Cathode Materials.* Chemical Reviews, 2004. **104**(10): p. 4271-4302.
5. Daniel, C. and J.O. Besenhard, *Handbook of Battery Materials*2012: Wiley.
6. Winter, M. and R.J. Brodd, *What Are Batteries, Fuel Cells, and Supercapacitors?* Chemical Reviews, 2004. **104**(10): p. 4245-4270.
7. Wakihara, M. and O. Yamamoto, *Lithium Ion Batteries: Fundamentals and Performance*2008: Wiley.
8. Scrosati, B. and J. Garche, *Lithium batteries: Status, prospects and future.* Journal of Power Sources, 2010. **195**(9): p. 2419-2430.
9. Fergus, J.W., *Recent developments in cathode materials for lithium ion batteries.* Journal of Power Sources, 2010. **195**(4): p. 939-954.
10. Newman, J., *Optimization of Porosity and Thickness of a Battery Electrode by Means of a Reaction-Zone Model.* Journal of The Electrochemical Society, 1995. **142**(1): p. 97-101.
11. Ramadesigan, V., et al., *Optimal Porosity Distribution for Minimized Ohmic Drop across a Porous Electrode.* Journal of The Electrochemical Society, 2010. **157**(12): p. A1328-A1334.
12. Zheng, H., et al., *Calendering effects on the physical and electrochemical properties of Li[Ni1/3Mn1/3Co1/3]O2 cathode.* Journal of Power Sources, 2012. **208**: p. 52-57.
13. Zheng, H., et al., *Cooperation between Active Material, Polymeric Binder and Conductive Carbon Additive in Lithium Ion Battery Cathode.* The Journal of Physical Chemistry C, 2012. **116**(7): p. 4875-4882.

14. Gören, A., et al., *State of the art and open questions on cathode preparation based on carbon coated lithium iron phosphate.* Composites Part B: Engineering, 2015. **83**: p. 333-345.
15. Martínez-Rosas, E., R. Vasquez-Medrano, and A. Flores-Tlacuahuac, *Modeling and simulation of lithium-ion batteries.* Computers & Chemical Engineering, 2011. **35**(9): p. 1937-1948.
16. Chen, Y.-H., et al., *Selection of Conductive Additives in Li-Ion Battery Cathodes: A Numerical Study.* Journal of The Electrochemical Society, 2007. **154**(10): p. A978-A986.
17. Sousa, R.E., C.M. Costa, and S. Lanceros-Méndez, *Advances and Future Challenges in Printed Batteries.* ChemSusChem, 2015. **8**(21): p. 3539-3555.
18. Miranda, D., C.M. Costa, and S. Lanceros-Mendez, *Lithium ion rechargeable batteries: State of the art and future needs of microscopic theoretical models and simulations.* Journal of Electroanalytical Chemistry, 2015. **739**: p. 97-110.
19. Ram, P., et al., *Improved performance of rare earth doped LiMn2O4 cathodes for lithium-ion battery applications* New Journal of Chemistry, 2016. **40**: p. 6244-6252.
20. Wang, S., L. Lu, and X. Liu, *A simulation on safety of LiFePO4/C cell using electrochemical–thermal coupling model.* Journal of Power Sources, 2013. **244**: p. 101-108.
21. Safari, M. and C. Delacourt, *Modeling of a Commercial Graphite/LiFePO4 Cell.* Journal of The Electrochemical Society, 2011. **158**(5): p. A562-A571.
22. Yu, S., et al., *Model Prediction and Experiments for the Electrode Design Optimization of LiFePO4/Graphite Electrodes in High Capacity Lithium-ion Batteries.* Bulletin of the Korean Chemical Society, 2013. **34**(1): p. 9.
23. Wang, M., et al., *The effect of local current density on electrode design for lithium-ion batteries.* Journal of Power Sources, 2012. **207**: p. 127-133.
24. Srinivasan, V. and J. Newman, *Discharge Model for the Lithium Iron-Phosphate Electrode.* Journal of The Electrochemical Society, 2004. **151**(10): p. A1517-A1529.
25. Dai, Y., L. Cai, and R.E. White, *Simulation and analysis of stress in a Li-ion battery with a blended LiMn2O4 and LiNi0.8Co0.15Al0.05O2 cathode.* Journal of Power Sources, 2014. **247**: p. 365-376.

26. Lestriez, B., *Functions of polymers in composite electrodes of lithium ion batteries.* Comptes Rendus Chimie, 2010. **13**(11): p. 1341-1350.

27. Young, R.J. and P.A. Lovell, *Introduction to Polymers, Third Edition*2011: Taylor & Francis.

28. Van Zee, J.W., et al., *Advances in Mathematical Modeling and Simulation of Electrochemical Processes and Oxygen Depolarized Cathodes and Activated Cathodes for Chlor-alkali and Chlorate Processes*1998: Electrochemical Society.

29. Wang, C. and J. Hong, *Ionic/Electronic Conducting Characteristics of LiFePO4 Cathode Materials: The Determining Factors for High Rate Performance.* Electrochemical and Solid-State Letters, 2007. **10**(3): p. A65-A69.

30. Ning, G., B. Haran, and B.N. Popov, *Capacity fade study of lithium-ion batteries cycled at high discharge rates.* Journal of Power Sources, 2003. **117**(1–2): p. 160-169.

31. Shi, Y., et al., *Graphene wrapped LiFePO4/C composites as cathode materials for Li-ion batteries with enhanced rate capability.* Journal of Materials Chemistry, 2012. **22**(32): p. 16465-16470.

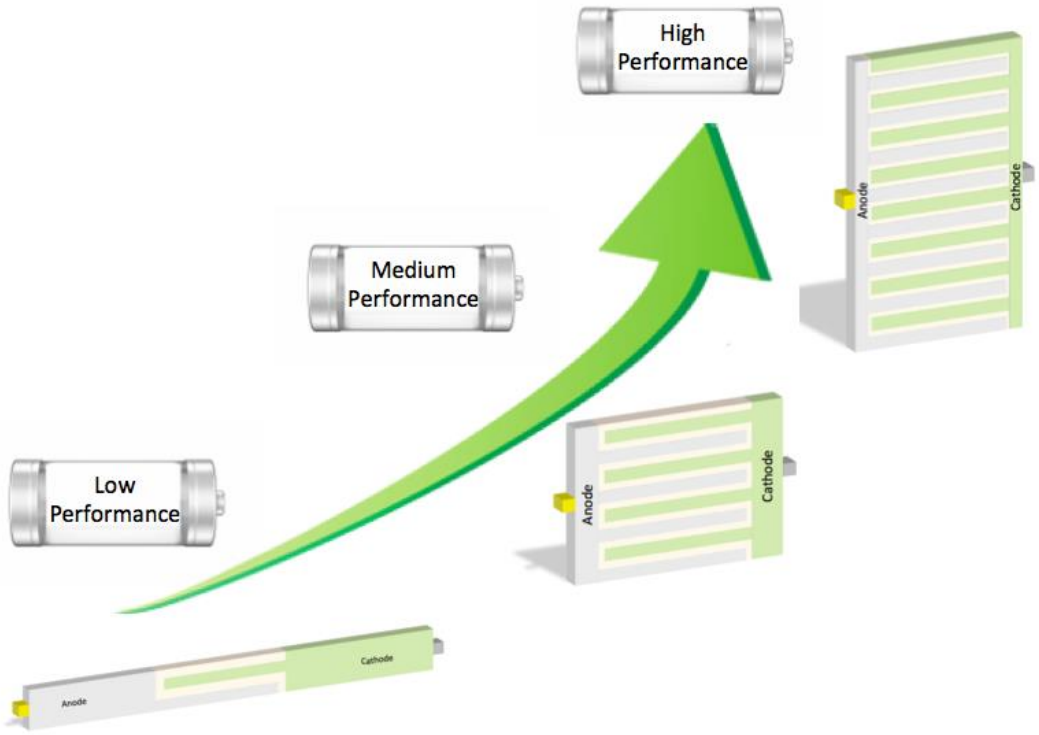

6. Computer simulation evaluation of the geometrical parameters affecting the performance of two dimensional interdigitated batteries

This chapter describes the simulation of the effect of the geometrical parameters of interdigitated batteries, including the number, thickness and the length of the digits, on the delivered battery capacity. This optimization was carried out in two dimensions maintaining the area of the different components constant.

This chapter is based on the following publication:

"Computer simulation evaluation of the geometrical parameters affecting the performance of two dimensional interdigitated batteries", D. Miranda, C. M. Costa, A. M. Almeida, S. Lanceros-Méndez, Journal of Electroanalytical Chemistry 781 (2016) 1-11.

6.1 Introduction

Lithium-ion batteries are nowadays the most relevant and efficient energy storage systems, increasingly used for applications in portable electronic products, such as mobile-phones, computers, e-labels and disposable medical testers, hybrid electric vehicles (HEVs) and electric vehicles (EVs) [1].

The rechargeable battery market is expected to reach $ 22.5 billion dollars and the growth of the lithium- ion battery market in 2016 is expected to reach 25%. The increasing demands of the automotive and mobile phone sectors result in an increasing need for lithium ion battery autonomy, power and capacity [2].

The widespread presence of lithium-ion batteries is due to their advantages in comparison with other battery systems, as they are lighter, cheaper, have higher energy density (between 100 and 265 Wh kg^{-1}), lower self-discharge, no memory effect, prolonged service-life and higher number of charge/discharge cycles [3, 4]. Improving lithium-ion battery performance is nevertheless needed with respect to specific energy, power, safety and reliability [4].

Typically, the performance of a battery is optimized for either power or energy density by modifying the chemistry and materials for electrodes (anode and cathode) and separators in conventional two-dimensional structures [5-7]. This structure is defined as a layer-by-layer configuration such as cathode/separator/anode [8].

Nevertheless, this structure is limited by the slow transport of lithium ions and hindered accessibility to the material at the back of the electrode, close to the current collector [9].

Taking this limitation into account and in order to maximize power and energy density, interdigitated structures are being developed [9]. The interdigitated geometry consists of electrode arrays of rods separated by a solid electrolyte, i.e, lithium salts put directly into the polymeric matrix without organic solvent present in electrolyte. In this way, the surface area of the electrodes increases without additional side reactions on the electrode surfaces [10].

This configuration leads to shorter Li^+ transport paths, reducing ion diffusion lengths and electrical resistance across the entire battery system, as well as to higher energy density of the cell within the same areal footprint [9-11].

In this context, interdigitated batteries using high capacity manganese oxide cathodes and lithium anode have achieved a capacity of up to 29.5 μAh/cm^2, which is 10x the average capacity of rechargeable conventional batteries [12].

Three dimensional (3D) interdigitated architectures have been fabricated by printing concentrated LFP-LTO based inks, showing a high areal energy density of 9.7 J cm^{-2} at a power density of 2.7 mW cm $^{-2}$ [13].

3D printing was also used for the fabrication of batteries based on $Li_4Ti_5O_{12}$ (average particle diameter of 50 nm) and $LiFePO_4$ (average particle diameter of 180 nm). This battery (960 μm × 800 μm, electrode width = 60 μm, spacing = 50 μm) shows a high areal energy density of 9.7 J cm^{-2} at a power density of 2.7 mWcm^{-2} [13].

The interdigitated architecture mostly depends on the aspect ratios (length/width) that can be achieved as well as on the geometry of the electrode. In this way, computer simulations of battery performance are important and critical for evaluating the optimized geometries before experimental implementation [14, 15].

In order to simulate battery operation, the couplings of different physical-chemical levels are needed. Macroscopic models allow geometrical and dimensional optimization of the battery components and mesoscale models are suitable for understanding and improving the different components of the battery: physical-chemical properties of the materials to be used as electrodes and separators and the choice of the most suitable organic solvents for electrolytes [15-17]. Theoretical simulations on 3D battery architectures have been addressed by focusing on determining an optimal electrode cylinder array configuration [18] as well as the planar tessellated electrode geometry of square and circular electrode arrays, in which the cell capacity can be increased by simply adding more electrodes in the plane of the array or increasing the height of the electrodes [19]. Further, a Finite Element Analysis (FEA) electrochemical model has been developed for several of the main 3D battery architectures such as interdigitated cylinders, concentric cylinders and interdigitated plates using a non-porous electrode (particle-scale) electrochemistry model [20]. The effect of the solid electrolytes ionic conductivity was also analyzed for interdigitated structures, the discharge capacity increasing with increasing of ionic conductivity [21, 22].

Theoretical simulation was also used to demonstrate that the electrode thickness can significantly influence many key aspects of a battery such as energy density, temperature response, capacity fading rate and overall heat generation, among others [23].

In 3D pillar structures, template pillar heights (h) and interpillar distances (d) have been evaluated, the optimum pillar height being ~ 70 μm in order to achieve homogeneous lithiation and high cell capacity [24].

The influence of geometry in the performance of conventional and unconventional lithium-ion batteries was studied maintaining the same area of the different components and it has been shown that the geometry with the best performance is the interdigitated structure [25].

Taking into account the state-of-the art on 3D battery architecture simulation and that interdigitated structures maximize the performance of the battery, the goal of this work is focus in the quantitative evaluation of the effect of the variation of the geometrical parameters of the interdigitated structure towards performance optimization of lithium-ion batteries. The considered geometrical parameters are the number, thickness and length of the digits, and the optimization has been performed considering different scan rates. To our knowledge these effects have never been comprehensively reported before and it is important to take them into account before experimentally implementing the adequate geometry of a battery for particular applications, allowing to improve battery design for specific area restrictions. The performance of the battery was determined in two dimensions at different scan rates up to 400C, as the combination of interdigitated structure fabrication with printing technologies allows to obtain interdigitated batteries with small size and thickness and yet with high delivered capacity. The optimization of the interdigitated structure by a FEA was carried out taking into account the number, thickness and length of the digits, while maintaining the area of the different components constant. The results are also compared with a conventional structure. As a result, optimization of the geometrical parameters of interdigitated geometries is achieved, allowing to guide experimental fabrication by providing an essential tool for proper battery design and implementation.

6.2 Theoretical simulation model and parameters

The main components of lithium ion batteries are anode, cathode and separator, that can be simulated by the Doyle/Fuller/Newman model in two dimensions (2D) [26]. The electrochemical model used is presented in Chapter 3.

The nomenclature and the physical meaning of the different symbols are shown in

the List of Symbols and Abbreviations.

In this work, a finite element method is implemented, considering the electrochemical and transport processes in interdigitated lithium ion battery structure such as: [porous positive electrode, ($Li_xMn_2O_4$) | porous separator, poly(vinylidene-trifluoroethylene) (P(VDF-TrFE)) soaked in 1M lithium hexafluorophosphate ($LiPF_6$) in propylene carbonate (PC) | porous negative electrode, (Li_xC_6)], the simulations being performed in 2D. The degree of porosity of the electrodes is defined as the space between the particles of active electrode material and the respective values are shown in Table 6.1.

Figure 6.1 represents a conventional (figure 6.1a)) and an interdigitated (figure 6.1b)) geometry with the identification of the investigated geometrical parameters in three (3D) and two dimensions (2D).

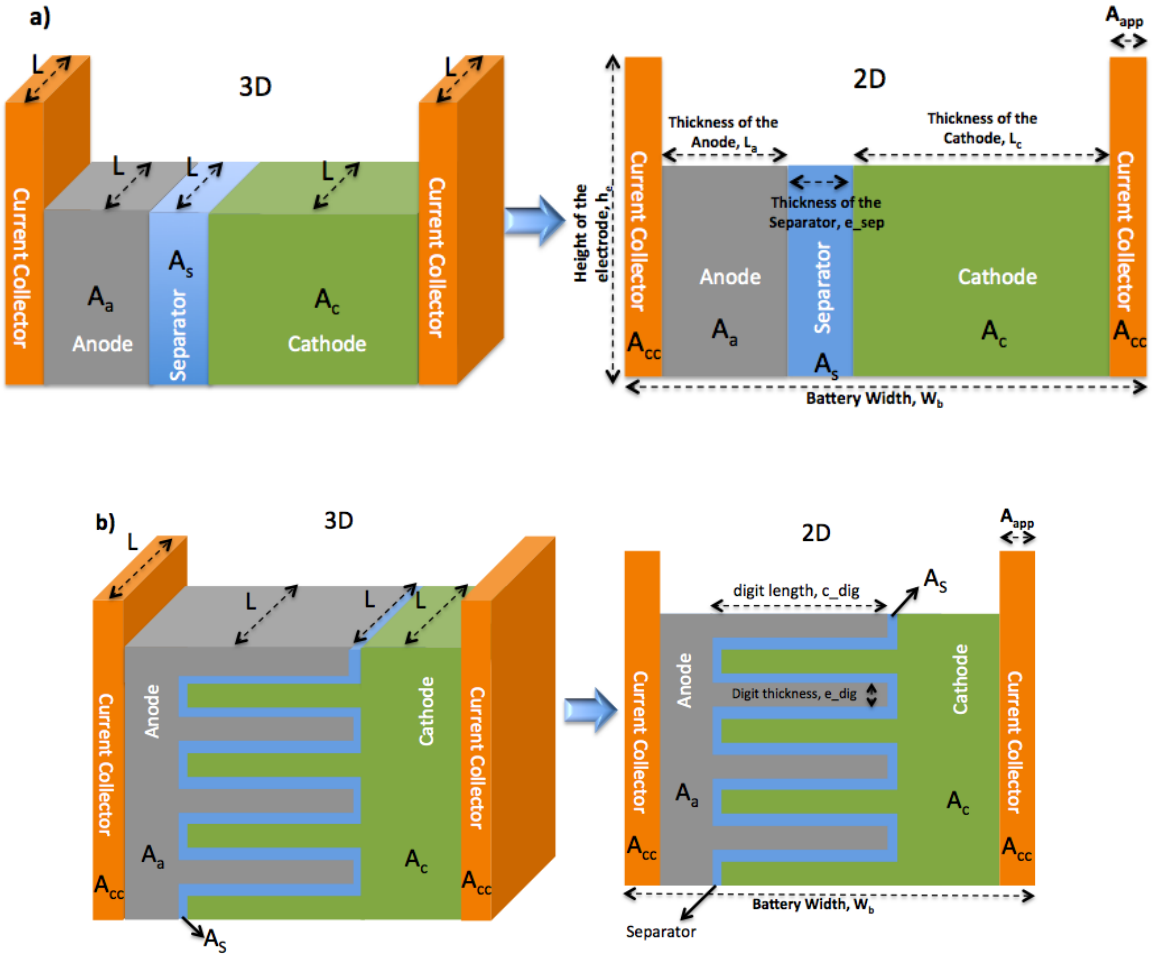

Figure 6.1 - Schematic representation of a conventional (a) and an interdigitated (b) battery with indication of the main geometrical parameters.

In this case, the control of the active mass loading in both electrodes is achieved through the volume of the electrodes. As the study was performed in 2D, the mass loading is related to the area.

Figure 6.1a) shows a 3D interdigitated battery in which the volume of each electrode corresponds to the multiplication of the dimension L by the area of the electrode, A_a and A_c for the anode and the cathode, respectively. For the 2D model, on the other hand, the mass loading is just related with the area of each electrode (figure 6.1b). Here, the cathode area is larger than the anode area ($A_c > A_a$) on all conventional and interdigitated batteries as shown by the values assigned to each electrode (Table 6.1).

The volume of active material for a 3D geometry is determined by the active material content through its initial concentration (initial parameter indicated in table 6.1, $C_{E,i,0}$).

The same principle was applied for the interdigitated geometry (figure 6.1b)).

In order to study the influence of geometrical parameters (number of digits, length and thickness of the digits) in the discharge capacity value at a specific scan-rate, it is necessary to maintain the same area of each component whenever a specific parameter is changed.

Thus, the same active mass loading of both electrodes is maintained, as well as the degree of porosity in the electrolyte and separator, allowing to maintain constant the capacity and just to evaluate the effect of the geometrical parameters.

Figure 6.2 illustrates how the area is maintained for the various battery components (electrodes, separator and current collectors) when varying the number of digits, from 4 to 2, of an interdigitated battery.

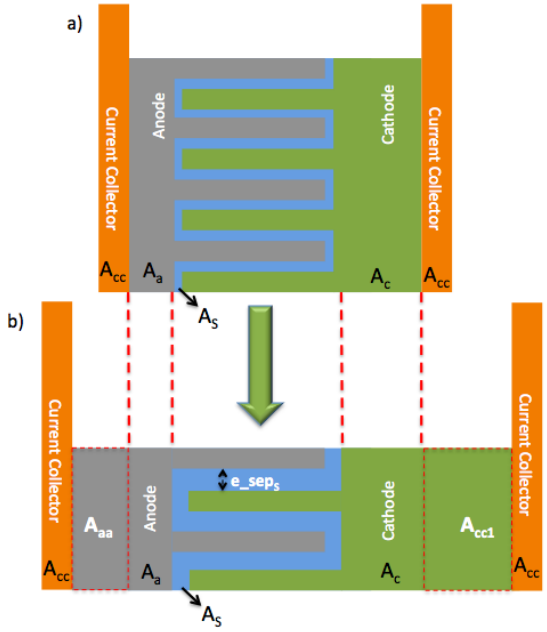

Figure 6.2 - Schematic representation illustrating how the area of each component is maintained constant, while varying the number of digits.

When the number of digits decreases, the area of the active material (mass of the active material) that was interdigitated will be moved to part of the electrode which is not interdigitated.

This fact is illustrated in figure 6.2b) by A_{aa} and A_{cc1} for the anode and the cathode, respectively. In this way, the mass of active material remains constant independently of the variation of the geometrical parameters.

The values of the parameters used for each component of the battery are listed in Table 6.1. In the computer simulations, the length of the digit (c_dig), the thickness (e_dig) and the number were varied while maintaining constant the area of both electrodes (A_a and A_c), separator (A_s) and current collectors (A_{cc}).

Relatively to the parameters of the separator, the constant values are indicated in Table 6.1 and the variable parameter is its thickness (e_sep).

Table 6.1 - Parameters used in the simulations of the conventional and interdigitated battery structures.

Parameters used for the simulation of both conventional and interdigitated structures				
Parameter	**Unit**	**Anode** (Li_xC_6)	**Separator**	**Cathode** ($Li_xMn_2O_4$)
$C_{E,i,0}$	mol/m^3	14870		3900
$C_{E,i,max}$	mol/m^3	26390		22860
C_L	mol/m^3		1000	
r	m	$12,5\times10^{-6}$		8×10^{-6}
K_l	S/m	$6,5\times10^{-1}$	$6,5\times10^{-1}$	$6,5\times10^{-1}$
$K_{eff,i}$	S/m	$(6,5\times10^{-1})\times0,357^{1,5}$		$(6,5\times10^{-1})\times0,444^{1,5}$
K_f	S/m		$(6,5\times10^{-1})\times(4,84\times10^{-2})$	
D_l	m^2/s	$4,0\times10^{-10}$	$4,0\times10^{-10}$	$4,0\times10^{-10}$
$D_{eff,i}$	m^2/s	$(4,0\times10^{-10})\times0,357^{1,5}$	$(4,0\times10^{-10})\times4,84\times10^{-2}$	$(4,0\times10^{-10})\times0,444^{1,5}$
t^0_+		0,363	0,363	0,363
D_{LI}	m^2/s	$3,9\times10^{-14}$		1×10^{-13}
Brugg or p		1,5	8,5	1,5
$\varepsilon_{f,i}$		0,172		0,259
ε_i		0,357	0,70	0,444
τ			3,8	
σ_i	S/m	100		3,8
i_{1C}	A/m^2		17,5	
F	C/mol		96487	
T	K		298,15	
R	J/mol K		8,314	
A_i	m^2	$4,0\times10^{-8}$	$1,8\times10^{-9}$	$8,0\times10^{-8}$
Geometrical parameters used for the conventional structure				
Parameter	**Unit**	**Anode** (Li_xC_6)	**Separator**	**Cathode** ($Li_xMn_2O_4$)
L_i	m	200×10^{-6}	90×10^{-6}	400×10^{-6}
Geometrical parameters used for the interdigitated structure				
Parameter	**Unit**	**Anode** (Li_xC_6)	**Separator**	**Cathode** ($Li_xMn_2O_4$)
c_dig	m	c_dig		c_dig
e_dig	m	e_dig		e_dig
e_sep	m		e_sep	
N		1 to 8		1 to 8

The finite element calculations were carried out using a MATLAB subroutine in order to solve the governing equations of the constituents (electrodes and separator) in an ideal cell without SEI formation. The size of the mesh is one order of magnitude below the dimension of the components.

The value of C-rate was determined from the cathode electrode area taking into account the corresponding active material.

The impedance was measured for each geometry at frequencies ranging from 10 mHz to 1 MHz with a potential perturbation with an amplitude of 0.01 V and with the following parameters: film resistance of the positive electrode: 0.0065 $m^2.S^{-1}$; film resistance of the negative electrode: 1×10^{-5} $m^2.S^{-1}$; double layer capacitance of the positive electrode: 0.2 $F.m^{-2}$; double layer capacitance of the negative electrode: 0.2 $F.m^{-2}$; current collector resistance at each current collector: 1.1×10^{-4} $m^2.S^{-1}$.

6.3 Results

Theoretical model simulations of the lithium-ion battery were applied for studying the influence of different geometrical parameters, including the number of digits (N), their length (c_dig) and thickness (e_dig), in the interdigitated geometry (figure 6.1b)) and the results were compared to those obtained for a conventional structure at low, medium and high discharge rates. In all simulations, the area of the different components, anode, cathode and separator, was maintained constant in order to keep the same amount of active material and to evaluate only the effect of the geometrical differences. Further, the same area was used for the current collectors in all simulations, in order to maintain the same ohmic resistance. The capacity value is in the form of ampere-hour per square meter ($Ah.m^{-2}$) – capacity per unit area depending on the electrode area for optimizing the geometrical parameters.

6.3.1 Conventional geometry

Figure 6.1a) shows the schematic representation of a battery with a conventional geometry (conventional battery). Figure 6.1a) also shows the geometrical variables which are evaluated at various discharge rates in order to investigate their influence in the capacity of the battery: thickness of the anode, L_a, thickness of the cathode, L_c, and thickness of the separator, e_sep.

It is important to notice that for the conventional structure, increasing the thickness of each component implies to increase the area of the battery, once the height of the battery is constant.

The choice of the initial dimensions for the anode and the cathode is related to the fact that the amount of active material for the cathode should be higher in comparison to the active material for the anode. In the discharge process ions move from the anode to the cathode, the active mass loading of the anode working as lithium ions source and, therefore, the higher the mass loading (area in this case) of the anode, the higher will be the capacity value in the discharge process taking into account the area of the cathode and respecting the cell balance.

The intercalation process of ions occurs in the cathode during the discharge process, the area of the cathode being larger in order to increase the number of intercalation ions in this process.

Further, it is also considered that the areas of the conventional and interdigitated geometries are maintained constant [27], in order to allow proper comparison between both battery types and to properly consider the effect of the variation of the geometrical parameters (number, thickness and length of digit) in the interdigitated geometry.

Figure 6.3a) shows the delivered capacity measured at 1C discharge rate as a function of the anode thickness with the cathode and separator widths fixed at 400 μm and 25 μm, respectively. The thickness of the anode was varied from 200 μm to 540 μm, with a step of 20 μm, the cathode and initial anode areas are 8×10^{-8} and 4×10^{-8} m^2, respectively.

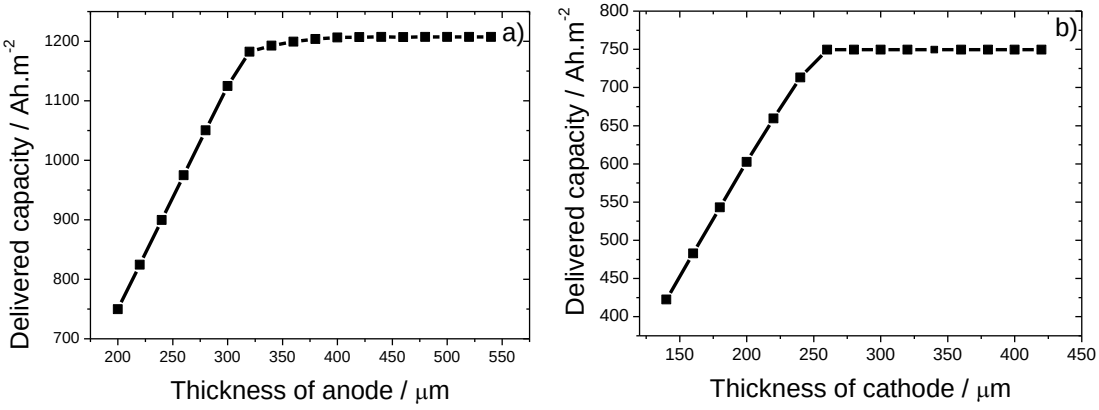

Figure 6.3 - Delivered capacity at 1C discharge rate as a function of the anode thickness for a fixed cathode thickness of 400 μm (a) and as a function of the cathode thickness for a fixed anode thickness of 200 μm (b).

Figure 6.3a) shows that varying the thickness of the anode from 200 μm to 400 μm leads to an increase of the capacity value from 750 $Ah.m^{-2}$ to 1207 $Ah.m^{-2}$, reaching a constant value for the anode thickness above 400 μm.

Figure 6.3b) shows the influence of the variation of the thickness of the cathode (140 to 420μm) for a fixed anode (200μm) and separator thickness (25μm) in that the initial cathode and anode areas are 2.8×10^{-8} and 4×10^{-8} m^2, respectively.

It is observed that varying the thickness of the cathode between 140 μm and 260 μm leads to increased battery capacity values from 422 $Ah.m^{-2}$ to 750 $Ah.m^{-2}$ and that

for cathode thickness larger than 260 μm the capacity of the battery remains constant. The thickness of the cathode is higher in comparison to the thickness of the anode due to the possibility to obtain larger variations of the discharge rates, as presented in figure 6.4.

Taking into account that the ideal value of the cathode thickness is 400 μm (Figure 6.3b)), Figure 6.4 shows the delivered capacity for different anode thicknesses and a constant separator thickness of 90 μm. This separator thickness value allows a simpler variation of the geometrical parameters for the interdigitated geometry, maintaining the areas of the components constant (electrodes and separator) in both geometries (interdigitated and conventional).

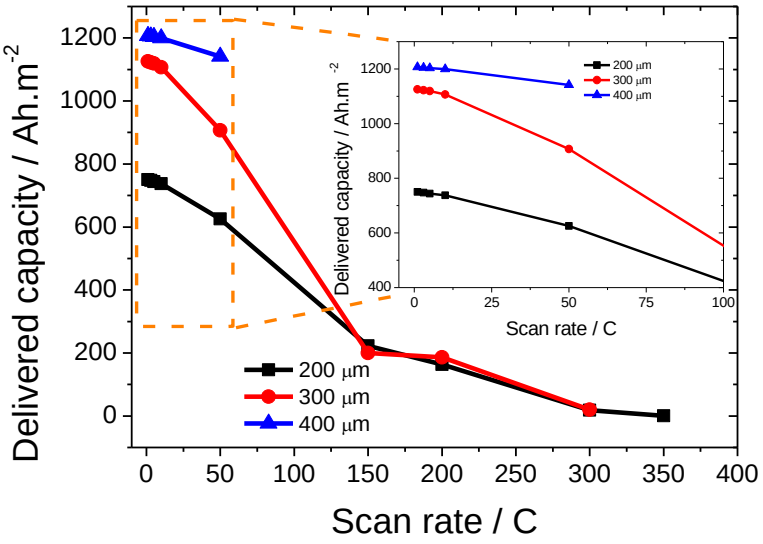

Figure 6.4 - Delivered capacity as a function of the scan rate for three different anode thicknesses and fixed cathode thickness of 400 μm.

Figure 6.4 shows that a conventional geometry with a separator thickness of 90 μm and both electrodes with an equal dimension of 400 μm does not work for discharge rates above 50C.

So, it is important to reduce the thickness of the anode to obtain a battery which operates properly at low, medium and high discharge rates. By decreasing the anode thickness to 300 μm, the battery operates up to a maximum discharge rate of 300C with a capacity value of 20.25 $Ah.m^{-2}$.

When decreasing the thickness of the anode to 200 μm, the battery operates up to a maximum discharge rate of 350C, thereby increasing the discharge rate range.

Thus, the delivered capacity depends on the scan rate and on the thickness of the electrodes, as shown in Figure 6.4. These effects are larger at higher discharge rates, in which an elevated ionic flow between the electrodes is required, i.e., higher ion insertion capacity in the cathode.

6.3.2 Interdigitated geometry

For the interdigitated geometry, it was evaluated the influence of the geometrical parameters (number of digits, width and thickness) on battery capacity at low, medium and high discharge rates. The results were compared with the ones obtained for the conventional geometry (section 6.3.1).

The values of the areas chosen for each battery component are presented in Table 6.1. For the selection of the areas it was taken into account the need of having large areas to allow a wide variation range in the number of digits, keeping the digit thickness and length constant.

Figure 6.1b show the schematic representation of the simulated interdigitated geometry in which number of digits (N), digit length, c_dig, and digit thickness, e_dig, are represented.

6.3.2.1 Influence of the number of digits at different scan rates

Figures 6.5a) and 6.5.b) show the delivered capacity at scan rates from 1C to 400C for a conventional battery structure and an interdigitated structure with 1 to 8 digits with a digit thickness of 20 μm and a digit length of 100 μm. It is observed that a constant capacity is obtained in the range of discharge rates from 1C to 10C for all battery geometries.

This effect is due to the fact that the discharge rates are quite low, allowing the mobility of lithium ions from the anode to the cathode and the full insertion of lithium ions in the cathode. For discharge rates from 50C to 400C, the delivered capacity of the interdigitated geometry is higher than the capacity of the battery with a conventional geometry, the capacity value being related with the increase of the number of digits. The

main difference between both geometries is the path of ions and electrons, i.e, the ohmic resistance [10] and the increased contact surface area of the electrodes, leading to improvement of the insertion of lithium ions in the cathode.

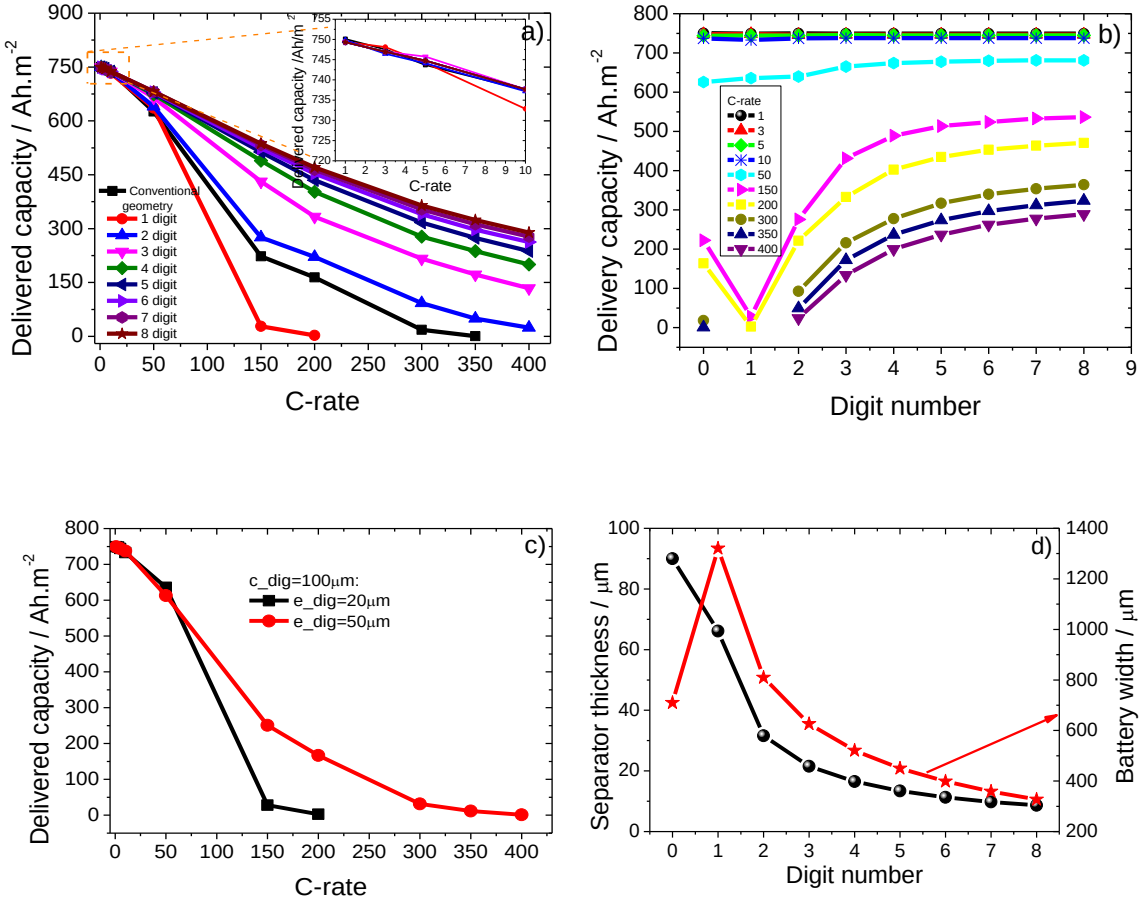

Figure 6.5 - Delivered capacity as a function of the scan rate (a and c) and number of digits (b). Separator thickness and battery width as a function of the number of digits with a fixed c_dig at 400 μm and e_dig at 20 μm (d)**.**

The conventional geometry (Figure 6.5a)) shows a delivered capacity of 0.7 $Ah.m^{-2}$ for 350C whereas for the interdigitated geometries this value is much higher, being 49.68 Ahm^{-2} for of the battery with two digits and 323.77 $Ah.m^{-2}$ for the battery with 8 digits.

On the other hand, the maximum scan rate and the delivered capacity value are lower for the interdigitated battery with one digit when compared with the conventional battery (figure 6.5a)). This behavior is ascribed to the increased length of the interdigitated battery with one digit, maintaining the same area for both geometries.

Figure 6.5b) shows that the delivered capacity remains constant around 737 $Ah.m^{-2}$ for both the interdigitated and the conventional geometries up to 50C discharge rate. On the other hand, for scan rates from 50C to 400C, it is verified an increase of the capacity value from the conventional geometry to the interdigitated geometry with eight digits.

The delivered capacity for the interdigitated geometry with two different digit thicknesses (e_dig= 20 μm and 50 μm) for equal digit length (c_dig=100 μm) shows that the larger thickness improves the delivered capacity of the interdigitated geometry, independently of the scan rate (Figure 6.5c)). This effect is due to the fact that the interdigitated geometry with larger digit thickness (e_dig) leads to shorter battery width between the electrodes, as the area of the components is maintained.

Figure 6.5d) shows that the length of the battery for the conventional geometry is about 700 μm and for the interdigitated geometry with one digit is 1300 μm. Although the thickness of the separator has been decreased from 90 μm to 60 μm in the conventional geometry and the interdigitated geometry with one digit, respectively, the charges should move through longer pathways, leading to higher ohmic losses.

For further analysing the effect of the different geometries, the electrochemical impedance spectra was investigated evaluate the mass transport phenomena during the discharge of the battery [28]. Figure 6.6 shows the typical impedance curve (Nyquist plot) for the conventional and the interdigitated geometry with 8 digits.

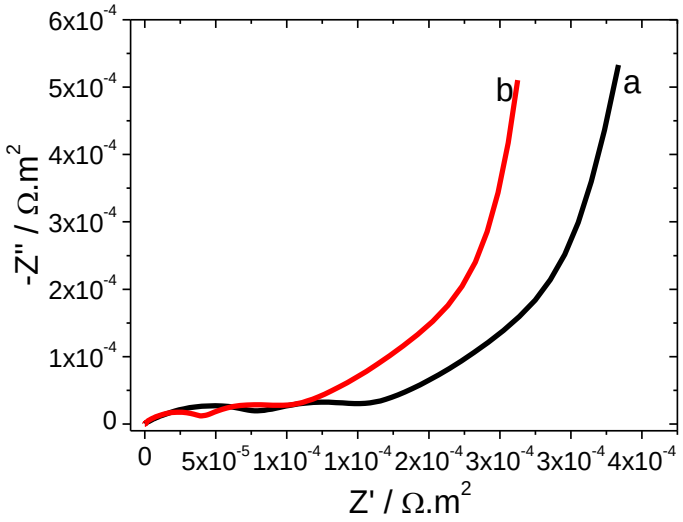

Figure 6.6 - Nyquist plot for the conventional (a) and the interdigitated (b) geometry with 8 digits in frequency range of 1 mHz to 1MHz.

Independently of the geometries, each plot in Figure 6.6 is characterized by two semicircles at high frequencies, representing the ohmic resistance, ionic resistance due to the pores and interfacial charge-transfer resistance. The inclined line in the low-frequency range of Figure 6.6 corresponds to the Warburg impedance, associated with the lithium-ion diffusion in the bulk of the active material [29]. The total impedance represented by the diameter of the semicircles is observed to be higher for the conventional geometry than for the interdigitated geometry.

6.3.2.2 Influence of length and thickness of the digit

In the previous section (6.3.2.1) it was observed that the length and thickness of digit of the interdigitated geometry affect more significantly the delivered capacity at higher scan rates. This effect will be analysed in detail in the following sections for a battery with four digits operating at a discharge rate of 400C. The study of the influence of digit length and digit thickness variation in the delivered capacity is performed for separators either with constant or variable width. The effect of the geometrical parameters is evaluated for a fixed separator thickness, whereas in some cases it is necessary to modify the thickness of the separator in order to keep constant the area of the different components.

6.3.2.2.1 Influence of digit length from 60 μm to 480 μm

Figure 6.7 shows the influence of the digit length for a constant digit thickness of 20 μm in the delivered capacity of a four digits battery (Figure 6.7a)) and the corresponding effects in the width of the battery (Figure 6.7b)) for both constant and variable separators. For the interdigitated geometry with constant separator, the separator thickness value is 16.49 μm, which corresponds to a digit length of 100 μm and a digit thickness of 20 μm.

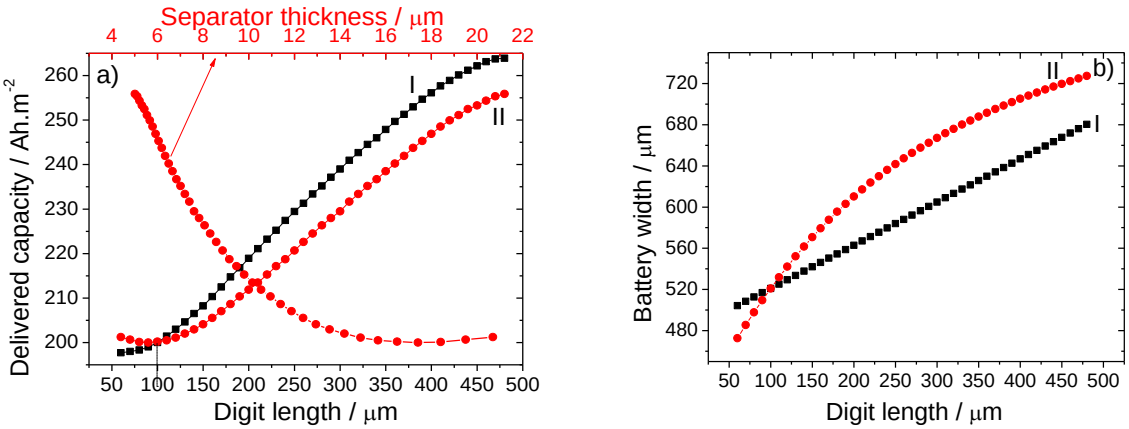

Figure 6.7 - a) Delivered capacity and b) width of the battery as a function of digit length for a four digits battery for a constant (I) and a variable (II) separator.

Independently of the separator type, Figure 6.7a) shows that the delivered capacity increases with increasing digit length due to the increased contact surface between the electrodes and therefore to the decrease of the ion pathways. For digit lengths between 60 μm and 100 μm, the delivered capacity for the variable separator is higher in comparison with the interdigitated geometry with a constant separator.

For digit lengths larger than 100 μm, the interdigitated geometry with a constant separator shows higher delivered capacity (Figure 6.7a)). The reason for this fact is observed in Figure 6.7b) and depends essentiality on the width of the battery. Figure 6.7a) also shows the variation of the delivered capacity as a function of the separator thickness for a variable separator, the delivered capacity decreasing with increasing separator thickness.

It is also observed in Figure 6.7b) that the width of the battery with a constant separator is larger in comparison with the variable separator up to a digit length of 100 μm. The area of the electrodes is thus constant and the thickness of the separator decreases, which implies an increase in the length of the battery to maintain the same area of the electrodes.

This fact is also supported by the impedance curves for the three digit lengths shown in Figure 6.8, which shows that the total impedance of the semicircles decreases as the digit length increases.

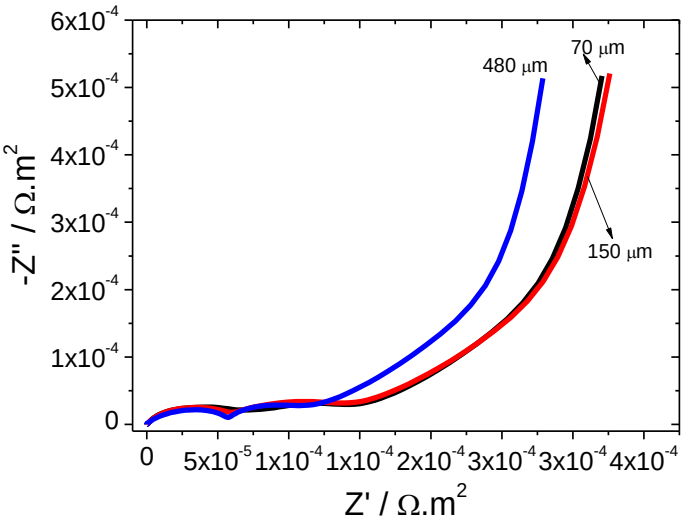

Figure 6.8 - Nyquist plot of interdigitated geometries for three different digit lengths in the frequency range from 1 mHz to 1MHz.

.

6.3.2.2.2 Influence of the digit thickness from 10 µm to 70 µm

Figure 6.9 shows the influence of the digit thickness in the delivered capacity (Figure 6.9a)) and width of the battery (Figure 6.9b)) for both constant and variable separators and with a constant digit length of 100 µm. For the interdigitated geometry with constant separator, the separator thickness value is 16,49 µm, corresponding to a digit length of 100 µm and a digit thickness of 20 µm.

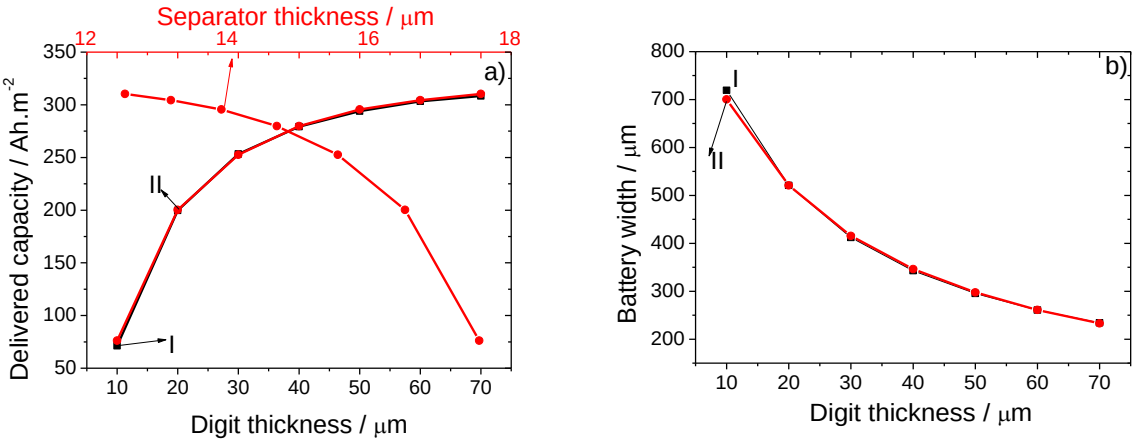

Figure 6.9 - a) Delivered capacity and b) width of the battery as a function of digit thickness for a constant (I) and a variable (II) separator.

Independently of the separator type, Figure 6.9a) shows an increase of the delivered capacity with increasing digit thickness. This effect is due to the increasing contact surface area between each electrode and the separator and the reduction of the width of the battery (Figure 6.9b)). Taking into account the areas of each of the components, the digit thickness increase was limited to 70 μm.

The increase of the delivered capacity as a function of digit thickness is related to the decrease of the battery width for both separator types. Figure 6.9a) also shows that the delivered capacity decreases with increasing separator thickness for the variable separator. Figure 6.10 shows the Nyquist plot for three digits thickness with a constant digit length of 100 μm and four digits, showing that the total impedance decreases with increasing digit thickness, affecting the discharge value of the battery.

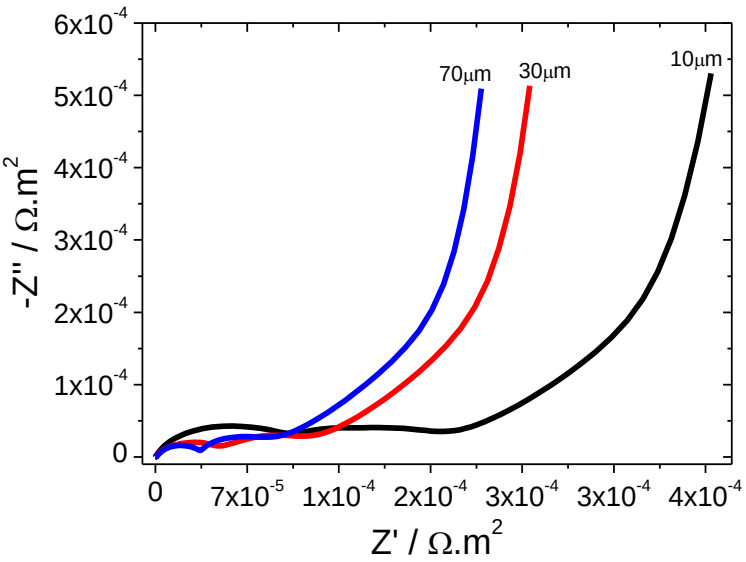

Figure 6.10 - Nyquist plot of the interdigitated geometries for three different digit thicknesses in the frequency range from 1 mHz to 1MHz.

6.3.2.2.3 Maximum limit for digit thickness and length at 200C and 400C

The influence of the maximum limit values for thickness and length in the delivered capacity was evaluated. These so called “digit limits” are the maximum possible values maintaining constant the area of the interdigitated geometry illustrated in the figure 6.11.

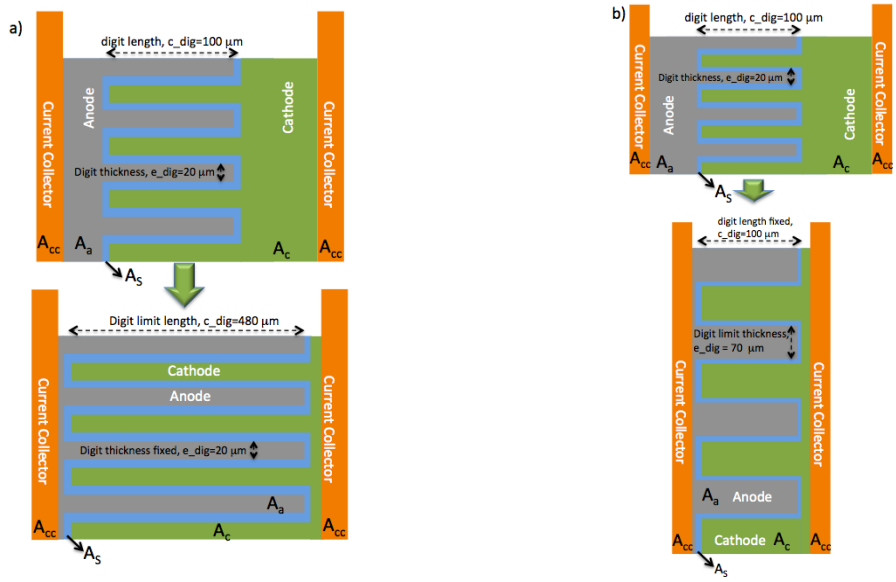

Figure 6.11 - Schematic representation of the: a) digit limit length and b) digit limit thickness for four digits.

The same procedure was carried out for the other interdigitated batteries with different numbers of digits. It is to notice that the maximum length and width of the digit value that can be achieved decreases with increasing number of digits.

Figures 6.12a) and 6.12b) show the delivered capacity for batteries with different number of digits as a function of "digit limit" thickness and length with c_dig= 100µm and e_dig=20µm, respectively, for 200C and 400C.

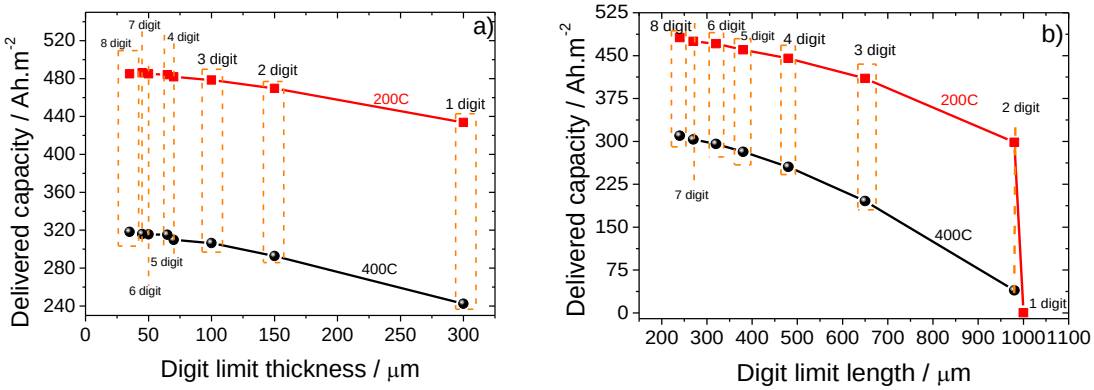

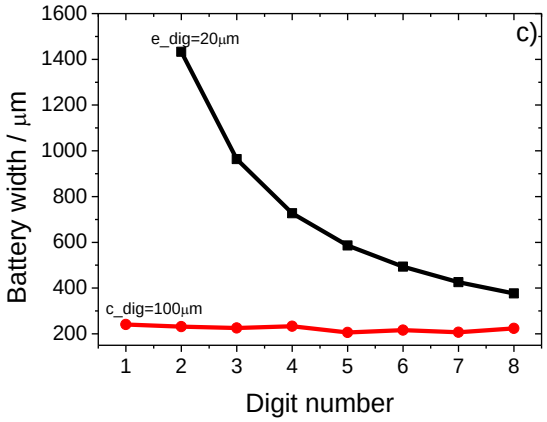

Figure 6.12 - Delivered capacity as a function of digit limit thickness (a) and length (b) at 200C and 400C. c) Width of the battery as a function of the number of digits for c_dig= 100 μm and e_dig=20 μm at 200C and 400C.

It is observed that the delivered capacity of the battery increases with increasing number of digits for both scan rates (figure 6.12a) and 6.12b)). The digit limit thickness (Figure 6.12a)) and length (Figure 6.12b)) decrease with increasing the number of digits, as it implies a decrease of the maximum digit length and thickness (due to the fact that a constant area is maintained), leading to a decrease of the battery width (figure 6.12c)).

Figure 6.12a) also shows that the maximum delivered capacity as a function of digit thickness for 200C is 433 $Ah.m^{-2}$ for 1 digit and 484.42 $Ah.m^{-2}$ for 8 digits, which is related to the increase of the contact surface area between the electrodes and the separator and the decrease of the thickness of the separator, the width of the battery being practically constant (Figure 6.12c)). Similarly, the maximum delivered capacity for 1 digit is 0.2 $Ah.m^{-2}$ and 481.42 $Ah.m^{-2}$ for 8 digits (Figure 6.12b)).

Figures 6.11a) and 6.11b) show that the interdigitated battery with 2 digits and digit limit thickness showed larger capacity when compared with the same battery with digit limit length. The delivered capacity value for the interdigitated battery with 2 digits and digit limit thickness is 469 $Ah.m^{-2}$ and for the corresponding battery with digit limit length is 300 $Ah.m^{-2}$. This fact is due to a higher contribution of the width of battery to the delivered capacity when compared to the contact surface area between the electrodes and the separator.

Finally, Figure 6.12c) shows that the width of the interdigitated battery with 2 digits and length digit limit is 1400 μm, being just 210 μm for the same battery with the thickness digit limit.

6.4. Discussion

Different geometrical parameters have been evaluated for both conventional and interdigitated geometries in order to optimize the performance of the later one.

For the conventional geometry, the effect of the variation of the anode thickness is the increase of the battery capacity due to the increasing active material content (lithium ion content) [30], but Figure 6.4 shows that the limit of lithium ions at the cathode is reached: during the discharge process, the cathode receives lithium ions coming from the anode, but due to its thickness, there is a maximum capacity of insertion of these ions.

Thus, the choice of the anode and cathode dimension is fundamental in the conventional geometry in order to obtain a high delivered capacity, i.e, the cathode thickness should be equal or higher than the anode thickness for the investigated electrochemical system.

Figures 6.5a)-6.5d) show that the interdigitated geometry shows higher delivered capacity in comparison to the conventional geometry, as the former geometry facilitates the mobility of ions between electrodes. At medium and high scan rates a fast mobility of the ions is required, resulting in higher charge flow for both electrons and ions and a larger ion insertion ability in the cathode. In a conventional battery, the mobility of ions is hindered by the larger paths that ions must travel from the anode to the cathode (larger width of the battery), as well as by the larger thickness of the separator (higher resistance to ionic conductivity). Also the charge-transfer resistance value affects the battery performance, as can be seen through the impedance curves (Figure 6.6).

Taking into account the results shown in Figures 6.5 to 6.12 for the interdigitated geometry, it is concluded that paths for ions between the electrodes is substantially reduced, the contact surface between the electrodes is improved and the thickness of the separator is reduced in comparison to conventional geometry, while maintaining the area of the different components constant.

The thickness and the length of the digits are relevant parameters as they are related to the lithium-ion insertion in the cathode material during the discharge process and smaller ion paths lead to the observed variations in the delivered capacity. The ohmic losses related to the width of the battery can be reduced by increasing the contact surface area, resulting in an increase of the delivery capacity in the interdigitated geometry.

6.5. Conclusions

Interdigitated structures are essential for obtaining maximum power and energy density in battery systems. In this way, the optimization of the geometrical parameters such as the number, thickness and length of the digits is required for optimizing battery performance, while maintaining constant the area of the different components. This optimization was performed in this work in two dimensional interdigitated structures, following the Doyle/Fuller/Newman theoretical model.

With respect to the geometry optimization of the interdigitated geometry, it was observed that increasing the number of digits implies an increase in the capacity of the battery due to the smaller path of the lithium ions between electrodes in the intercalation/deintercalation process.

For the same digit number, increasing the thickness and the length of the digits leads to an increase in the capacity of the battery as the width of the battery decreases, leading to reduced ohmic losses associated to charge transport and increased surface contact area of the electrodes, which facilitates the insertion process on the cathode material during the discharge process.

The interdigitated geometry increases the contact surface area between each electrode and the separator and thereby increases the corresponding ion flow. Thus, it is concluded that, if maintaining the same areas for all components, the interdigitated geometry strongly improves the delivered capacity value in comparison to the conventional geometry, this improvement being particularly relevant at high discharge rates.

6.6 References

1. Wakihara, M. and O. Yamamoto, Lithium ion batteries: fundamentals and performance1998: Kodansha.
2. Gonzalez, F. and P. Harrop, Batteries & Supercapacitors in Consumer Electronics 2013-2023: Forecasts, Opportunities, Innovation, 2014, IDTechEx.
3. Whittingham, M.S., Lithium Batteries and Cathode Materials. Chemical Reviews, 2004. **104**(10): p. 4271-4302.
4. Scrosati, B. and J. Garche, Lithium batteries: Status, prospects and future. Journal of Power Sources, 2010. **195**(9): p. 2419-2430.
5. Goriparti, S., et al., Review on recent progress of nanostructured anode materials for Li-ion batteries. Journal of Power Sources, 2014. **257**(0): p. 421-443.
6. Chikkannanavar, S.B., D.M. Bernardi, and L. Liu, A review of blended cathode materials for use in Li-ion batteries. Journal of Power Sources, 2014. **248**(0): p. 91-100.
7. Lee, H., et al., A review of recent developments in membrane separators for rechargeable lithium-ion batteries. Energy & Environmental Science, 2014. **7**(12): p. 3857-3886.
8. Long, J.W., et al., Three-Dimensional Battery Architectures. Chemical Reviews, 2004. **104**(10): p. 4463-4492.
9. Rohan, J.F., et al., Energy Storage: Battery Materials and Architectures at the Nanoscale. ICT - Energy - Concepts Towards Zero - Power Information and Communication Technology2014.
10. Arthur, T.S., et al., Three-dimensional electrodes and battery architectures. MRS Bulletin, 2011. **36**(07): p. 523-531.
11. Pikul, J.H., et al., High-power lithium ion microbatteries from interdigitated three-dimensional bicontinuous nanoporous electrodes. Nat Commun, 2013. **4**: p. 1732.
12. Pikul, J.H., P.V. Braun, and W.P. King, High power primary lithium ion microbatteries. Journal of Physics: Conference Series, 2013. **476**(1): p. 012087.
13. Sun, K., et al., 3D Printing of Interdigitated Li-Ion Microbattery Architectures. Advanced Materials, 2013. **25**(33): p. 4539-4543.

14. Ramadesigan, V., et al., Modeling and Simulation of Lithium-Ion Batteries from a Systems Engineering Perspective. Journal of The Electrochemical Society, 2012. **159**(3): p. R31-R45.
15. Miranda, D., C.M. Costa, and S. Lanceros-Mendez, Lithium ion rechargeable batteries: State of the art and future needs of microscopic theoretical models and simulations. Journal of Electroanalytical Chemistry, 2015. **739**(0): p. 97-110.
16. Martínez-Rosas, E., R. Vasquez-Medrano, and A. Flores-Tlacuahuac, Modeling and simulation of lithium-ion batteries. Computers & Chemical Engineering, 2011. **35**(9): p. 1937-1948.
17. Franco, A.A., Multiscale modelling and numerical simulation of rechargeable lithium ion batteries: concepts, methods and challenges. RSC Advances, 2013. **3**(32): p. 13027-13058.
18. Hart, R.W., et al., 3-D Microbatteries. Electrochemistry Communications, 2003. **5**(2): p. 120-123.
19. Liang, R.H.P., et al., Mathematical modeling and reliability analysis of a 3D Li-ion battery. J. Electrochem. Sci. Eng., 2014. **4**(1): p. 17.
20. Zadin, V., et al., Modelling electrode material utilization in the trench model 3D-microbattery by finite element analysis. Journal of Power Sources, 2010. **195**(18): p. 6218-6224.
21. Itoh, F., G. Inoue, and M. Kawase, Reaction and Mass Transport Simulation of 3-Dimensional All-Solid-State Lithium-Ion Batteries for the Optimum Structural Design. ECS Transactions, 2015. **69**(1): p. 83-90.
22. Zadin, V. and D. Brandell, Modelling polymer electrolytes for 3D-microbatteries using finite element analysis. Electrochimica Acta, 2011. **57**: p. 237-243.
23. Zhao, R., J. Liu, and J. Gu, The effects of electrode thickness on the electrochemical and thermal characteristics of lithium ion battery. Applied Energy, 2015. **139**: p. 220-229.
24. Priimägi, P., et al., Optimizing the design of 3D-pillar microbatteries using finite element modelling. Electrochimica Acta, 2016. **209**: p. 138-148.
25. Miranda, D., et al., Computer simulations of the influence of geometry in the performance of conventional and unconventional lithium-ion batteries. Applied Energy, 2016. **165**: p. 318-328.

26. Doyle, M., et al., Comparison of Modeling Predictions with Experimental Data from Plastic Lithium Ion Cells. Journal of The Electrochemical Society, 1996. **143**(6): p. 1890-1903.
27. Daniel, C., Materials and processing for lithium-ion batteries. JOM, 2008. **60**(9): p. 43-48.
28. Huang, R.W.J.M., F. Chung, and E.M. Kelder, Impedance Simulation of a Li-Ion Battery with Porous Electrodes and Spherical $Li+$ Intercalation Particles. Journal of The Electrochemical Society, 2006. **153**(8): p. A1459-A1465.
29. Zhu, J.G., et al., A new electrochemical impedance spectroscopy model of a high-power lithium-ion battery. RSC Advances, 2014. **4**(57): p. 29988-29998.
30. Favors, Z., et al., Stable Cycling of SiO2 Nanotubes as High-Performance Anodes for Lithium-Ion Batteries. Sci. Rep., 2014. **4**.

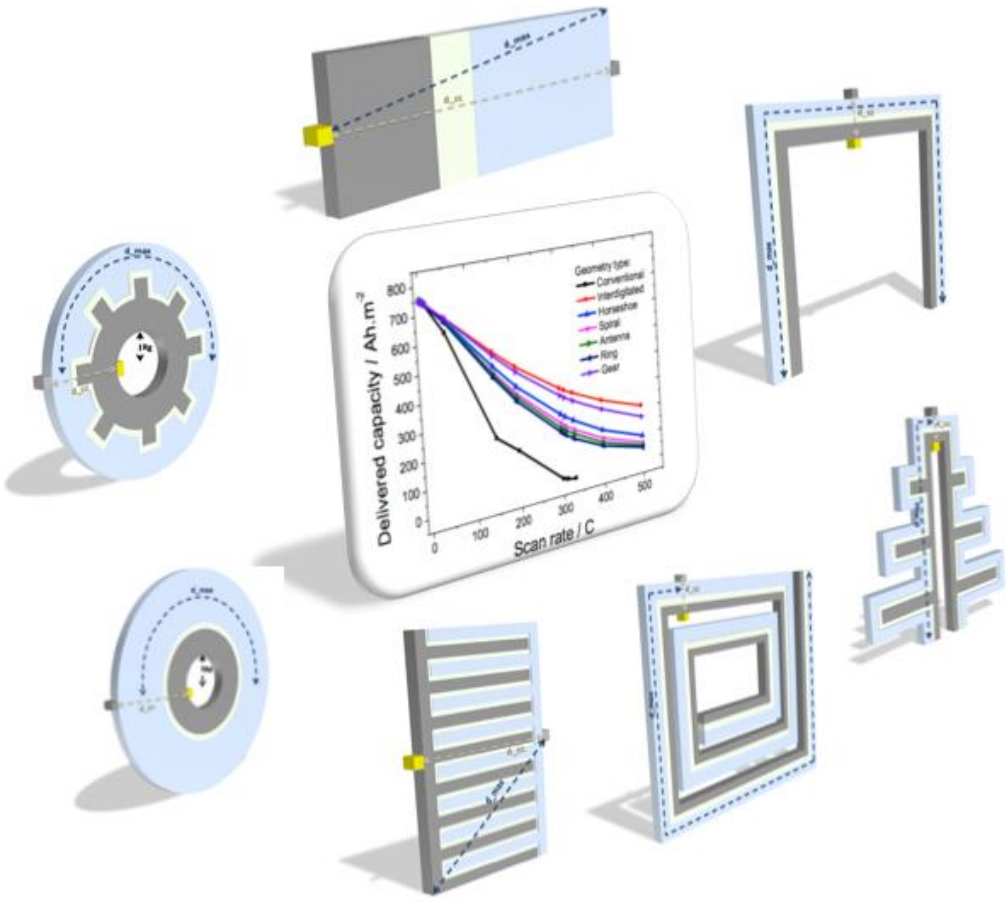

7. Computer simulations of the influence of geometry in the performance of conventional and unconventional lithium-ion batteries

This chapter evaluates the influence of the battery geometry in the performance of lithium-ion batteries. In order to optimize battery performance, different geometries have been evaluated taking into account their suitability for different applications. These different geometries include conventional and interdigitated batteries, as well as unconventional geometries such as horseshoe, spiral, ring, antenna and gear batteries.

This chapter is based on the following publication:

"Computer simulations of the influence of geometry in the performance of conventional and unconventional lithium-ion batteries", D. Miranda, C. M. Costa, A. M. Almeida, S. Lanceros-Méndez, Applied Energy 165 (2016) 318-328.

7.1 Introduction

Energy storage systems are an essential need in a modern society with rapid technological advances, increasing mobility and environmental concerns [1-3], the most used energy storage systems being lithium-ion batteries [4, 5].

Lithium-ion batteries are essential in applications such as mobile-phones and computers, among others. Further, they area also explored for hybrid electric vehicles (HEVs) and electric vehicles (EVs) [6-8].

Lithium-ion batteries dominate the battery market with a share of 75% due to their advantages with respect to other battery systems (NiCd, nickel-cadmium and NiMH, nickel-metal hydride), including high energy density, lightweight, high average discharge rate, no memory effect and high cycle life [9, 10].

The key issues for lithium-ion batteries are related to improving specific energy, power, safety and reliability [5]. These issues strongly depend on the materials for electrodes (anode and cathode) and separator (porous membrane with electrolyte solution) [11-14].

Together with the materials, also the geometry of the battery strongly affects its performance, the interdigitated geometry being the most investigated for this effect [15-17].

The improving specific energy, power, safety and reliability of lithium ion batteries are strongly depend on the materials for electrodes (anode and cathode) and separator (porous membrane with electrolyte solution) [11-14]. Together with the materials, also the geometry of the battery strongly affects its performance, the interdigitated geometry being the most investigated for this effect [15-17].

The interdigitated geometry is based on electrode digits separated by an electrolyte, allowing increased surface area for the electrodes. In this geometry, the Li^+ transport paths are shorter, reducing the electrical resistances across the battery and ion diffusion [16, 18].

As an example, lithium-ion microbatteries with interdigitated electrodes have been fabricated by electrodepositing high capacity electrolytic materials, manganese oxide cathode and lithium anode. The capacity value of these microbatteries is 29.5 $\mu Ah/cm^2\mu m$, with an increase in capacity and power by 10x and 1000x, respectively, in comparison with conventional batteries [16, 19].

Microbatteries based on interdigitated geometries have been fabricated by printing $Li4Ti_5O_{12}$ (LTO) and $LiFePO_4$ (LFP) based inks. These batteries show high energy density, 9.7 J cm^{-2}, at a power density of 2.7 mW cm^{-2} and can be used in microelectronics and biomedical devices [20].

The combination of printing technologies and microbatteries allow to obtain customizable thin batteries with large area and at low-cost [21]. These batteries can be fabricated with specific geometries by different printing (screen, spray and inkjet printing) techniques, depending on the final applications. Thus, it has been demonstrated that it is possible to fabricate microbatteries by ink-jet printed that operate at 90 C [22].

Printed battery applications include radio-frequency identification (RFID), security, thin film medical products and products that require on-board battery power [23]. Thus, evaluation of the possible battery geometries is necessary for optimizing size, fabrication and integration before experimental implementation. The optimization of the geometries can be carried out through computer simulations of battery performance [24].

Battery performance by computer simulation is based in models at different physical levels describing the physical-chemical properties of the materials to be used as electrodes and separators, as well as the operation of the battery [25-27].

These computer simulations are thus essential for battery development as they allow the correlation between theoretical and experimental results through the electrochemical behavior of the batteries [28].

The state-of-the art regarding battery geometry optimization of lithium-ion batteries through simulation models include interdigitated [16, 18, 29, 30], cylindrical [31, 32], spiral wound [33] and prismatic geometries [34]. For these geometries, thermal analysis has been performed [32, 34-36]. Further, different active material shapes for the anode, i.e, different microstructures [37] have been evaluated as well as the effect of thickness [38]. Further, the effect of lithium distribution and concentration [39] and geometric characteristics, i.e, porosity and tortuosity [40] have been computer simulated. Finally, a theoretical analysis of potential and current distributions has been carried out for lithium-ion batteries with planar electrodes [41].

The most relevant geometry for increasing capacity value is the interdigitated geometry [19].

Taking into account the advantages of printing techniques allowing battery fabrication with unconventional geometries, which will improve device integration and overall performance for different application, the novelty of this work is to quantitatively evaluate the effects of seven different lithium-ion battery geometries while maintaining constant the area of the different components. In this way, just the effect of geometry variation is quantified. Five of the evaluated geometries have never been reported before. Battery performance has been determined up to 500C, as microbatteries fabricated by printing batteries are already able to operate at at high scan rates above 90C. In this way, battery geometry will be able to be tailored for specific applications.

The optimization of the seven geometries (conventional, interdigitated, horseshoe, spiral, ring, antenna and gear) was carried out by finite element method simulations through the Doyle/Fuller/Newmann model. The choice of the different geometries is based on their applicability in different devices, including smart-phones, watches, tables, sensors and RFID tags, among others.

7.2 Theoretical simulation model and specific parameters for each geometry

The Doyle/Fuller/Newman model used in this work describes the main equations that govern the operation of a battery and its main components: anode, cathode and separator [42]. The equations of the electrochemical model applied in the simulations are presented in Chapter 3. The nomenclature and definition of the symbols within the equations are shown in the List of Symbols and Abbreviations.

Considering the electrochemical and transport processes in a typical lithium-ion battery structure such as: [anode, (Li_xC_6) | electrolyte/separator, porous membrane of P(VDF-TrFE) soaked in 1M LiTFSi-PC | cathode, ($Li_xMn_2O_4$)], in this work, a finite element method is implemented through the previous equations (Doyle/Fuller/Newman model) for the study of the different geometries shown in table 7.1. The choose of the thickness of separator is based in [43].

The values of the parameters used for the different components of each battery geometry are listed in Table 7.1. The areas of all components were maintained constant in the computer simulations. In the different geometries represented in Table 7.1, d_max and d_cc represent the maximum distance of the ions to the collectors and the distance

between current collectors, respectively. This table also shows the main characteristics of each geometry as well as some potential applications.

Table 7.1 - Parameters used for the simulations, main characteristics and applications for the different battery geometries [44-46].

Parameter	**Unit**	**Anode** (Li_xC_6)	**Separator**	**Cathode** ($Li_xMn_2O_4$)
$C_{E,i,0}$	mol/m^3	14870		3900
$C_{E,i,max}$	mol/m^3	26390		22860
C_L	mol/m^3		1000	
r	m	$12,5\times10^{-6}$		8×10^{-6}
L_i	m	200×10^{-6}		400×10^{-6}
e_sep	m		90×10^{-6}	
$k_{ef,i}$	S/m	$(6,5\times10^{-1})\times0,357^{1,5}$	$(6,5\times10^{-1})\times4,84\times10^{-2}$	$(6,5\times10^{-1})\times0,444^{1,5}$
$D_{ef,i}$	m^2/s	$(4,0\times10^{-10})\times0,357^{1,5}$	$(4,0\times10^{-10})\times4,84\times10^{-2}$	$(4,0\times10^{-10})\times0,444^{1,5}$
D_{LI}	m^2/s	$3,9\times10^{-14}$		1×10^{-13}
Brugg or p		1,5	8,5	1,5
$\varepsilon_{f,i}$		0,172		0,259
ε_i		0,357	0,70	0,444
τ			3,8	
σ_i	S/m	100		3,8
i_{1C}	A/m^2		17,5	
F	C/mol		96487	
T	K		298,15	
R	J/mol K		8,314	
A_i	m^2	$4,0\times10^{-8}$	$1,8\times10^{-9}$	$8,0\times10^{-8}$

Specific parameters for each battery geometry

Conventional battery geometry

Parameter	**Value / m**		**Characteristics**	**Applications**
L_c	400×10^{-6}	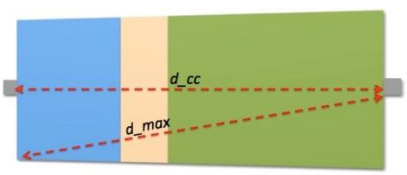	- low surface contact area between electrodes - high separator thickness - high distance between current collectors - high ohmic losses - layer by layer fabrication	Portable devices and electric vehicles
L_a	200×10^{-6}			
e_sep	90×10^{-6}			
d_max	697×10^{-6}			
d_cc	690×10^{-6}			

Interdigitated battery geometry

Parameter	Value / m		Characteristics	Applications
N	8* except unit	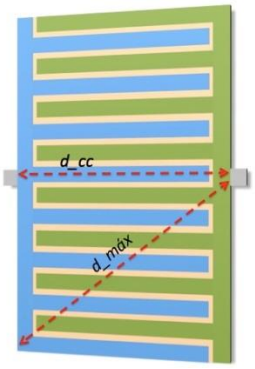	- high surface contact area between electrodes - medium distance between current collectors - thin thickness of separator - digits	Sensors and actuators, electric vehicles, smart cards
c_dig	100×10^{-6}			
e_dig	20×10^{-6}			
e_sep	$8{,}66\times10^{-6}$			
d_max	391×10^{-6}			
d_cc	327×10^{-6}			

Horseshoe battery geometry

Parameter	Value / m		Characteristics	Applications
L_c	$33{,}1\times10^{-6}$	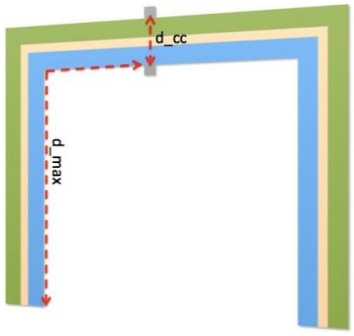	- high surface contact area between electrodes - low distance between current collectors - thin thickness of separator - large space at the center - layer by layer fabrication in u form	Portable devices with empty space for the placement of electronic components at the center of the battery, such as, smart-phones, tablets and portable computers
L_a	$17{,}5\times10^{-6}$			
e_sep	$7{,}71\times10^{-6}$			
d_max	1125×10^{-6}			
d_cc	$58{,}3\times10^{-6}$			

Spiral battery geometry

Parameter	Value / m		Characteristics	Applications
L_c	$28{,}6\times10^{-6}$	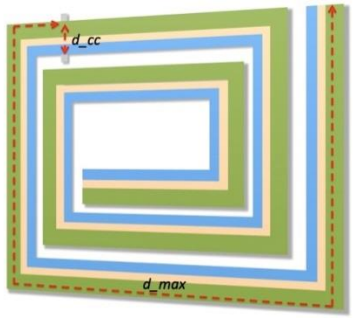	- high surface contact area between electrodes - medium distance between current collectors - medium thickness of separator - low space at the center	Smart cards, smart toys, sensors and actuators
L_a	$17{,}8\times10^{-6}$			
e_sep	$7{,}27\times10^{-6}$			
d_max	1240×10^{-6}			
d_cc	$53{,}7\times10^{-6}$			

Ring battery geometry

Parameter	Value / m
L_c	$27{,}4\times10^{-6}$
L_a	$14{,}5\times10^{-6}$
e_sep	$6{,}40\times10^{-6}$
R_d	430×10^{-6}
d_max	1350×10^{-6}
d_cc	$48{,}4\times10^{-6}$

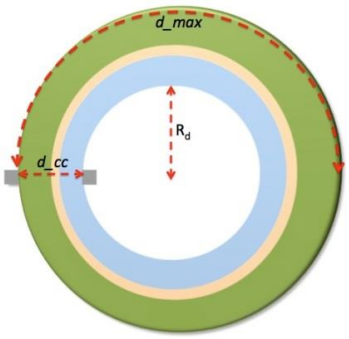

Characteristics	Applications
- high surface contact area between electrodes - low distance between current collectors - thin thickness of separator - large space at the center	Watches, mobile phones, medical devices

Antenna battery geometry

Parameter	Value / m
L_c	$25{,}6\times10^{-6}$
L_a	$16{,}0\times10^{-6}$
e_sep	$5{,}88\times10^{-6}$
d_max	1225×10^{-6}
d_cc	$47{,}5\times10^{-6}$

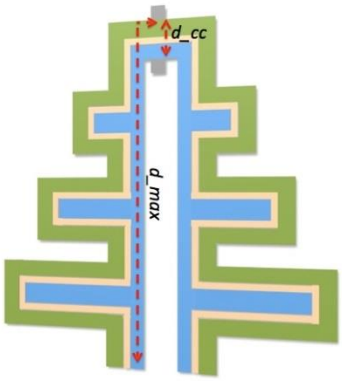

Characteristics	Applications
- high surface contact area between electrodes - medium distance between current collectors - thin thickness of the separator - small space at the center	Smart toys, gift cards, medical devices (e.g. transdermal drug delivery (TDD) systems

Gear battery geometry

Parameter	Value / m
N	8* except unit
e_sep	$12{,}41\times10^{-6}$
R_g	$93{,}9\times10^{-6}$
d_max	294×10^{-6}
d_cc	$135{,}8\times10^{-6}$
e_dig	40×10^{-6}
c_dig	30×10^{-6}

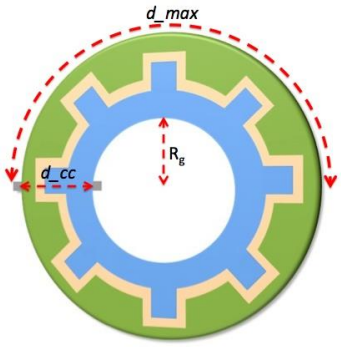

Characteristics	Applications
- high surface contact area between electrodes - small distance between current collectors - thin thickness of separator - large space at the center - digits	Watches, mobile phones, medical devices

7.3 Results and Discussion

Theoretical model simulations were thus applied for studying seven different lithium-ion battery geometries by keeping constant the areas of the anode, cathode, separator and current collectors. The main objective is to evaluate the effect of the geometry in battery performance. The delivery capacity was obtained for all geometries at low, medium and high discharge rates.

7.3.1 Effect of battery geometry

For the different geometries, the current collectors are located in the positions shown in table 7.1. The choice for the specific position of the collectors for each battery geometry is based on having the same electric field applied to the lithium-ions that are located in the places further away in relation to the current collector positions.

Figure 7.1 shows the capacity values obtained for the different geometries for scan rates from 1C up to 500C.

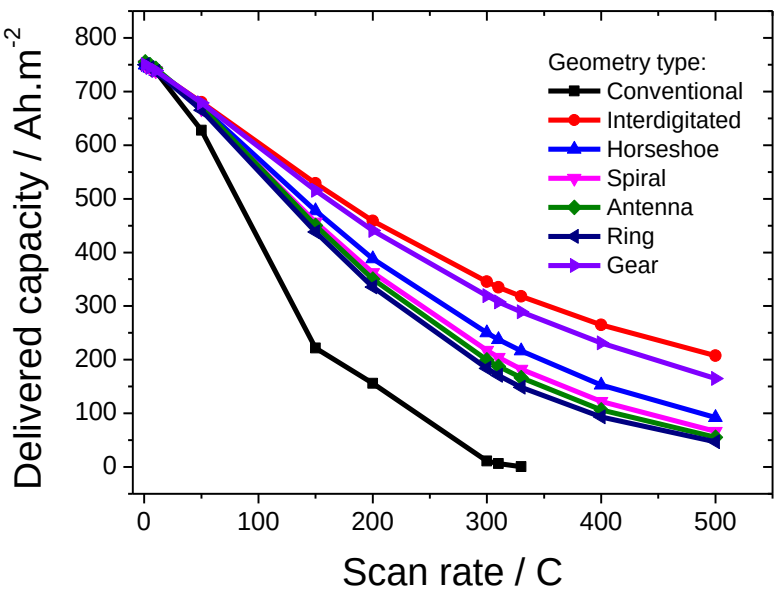

Figure 7.1 – Delivered capacity as a function of scan rate for the different batteries.

For each geometry, increasing scan rate leads to a decrease of the capacity value. This fact is ascribed to ohmic drop polarization [47]. Figure 7.1 shows that the

conventional geometry does not operate above 330C discharge rate, the capacity value at 330C being 0.58 Ahm^{-2}.

At high discharges rates (> 300C) it is observed that the interdigitated and conventional geometries show the highest and the lowest capacity in comparison to the other geometries.

Figure 7.1 also shows that there is a significant difference in the capacity value between the conventional geometry and the remainder geometries for discharge rates above 50C.

At 330C, it is possible to classify the geometries into three groups. The first group is constituted just by the conventional geometry, with a capacity value of 0.58 Ahm^{-2}. The second group is constituted by the ring, antenna and spiral geometries, with a range of capacity values from 149 Ahm^{-2} up to 182 Ahm^{-2}. Finally, the third group is constituted by the gear and interdigitated geometries that show capacity values from 289 Ahm^{-2} up to 318 Ahm^{-2}. The horseshoe geometry is located between the second and the third groups with a capacity value of 216 Ahm^{-2}. The horseshoe geometry shows a higher capacity than the spiral, antenna and ring geometries and a lower capacity than the gear and interdigitated battery geometries.

The reason for the different capacity values is ascribed to variations of the maximum distance and distance between current collectors in the different geometries, as shown in figure 7.2.

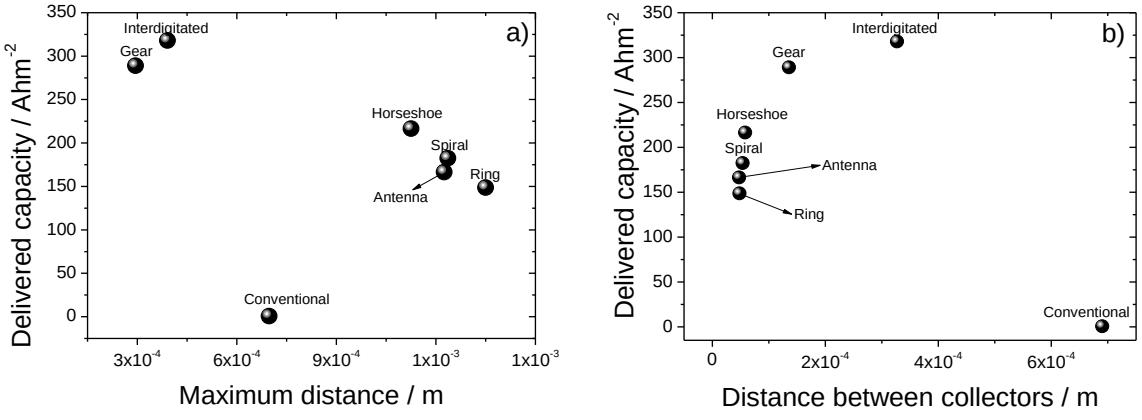

Figure 7.2 - Delivered capacity for the different geometries as a function of a) maximum distance and b) distance between collectors.

Figure 7.2a) shows the maximum distance that the ions move between the electrodes during the discharge process. It is observed that the interdigitated and gear geometries show lower maximum distance between the electrodes than the other geometries, as these geometries show shorter paths for ions to move. The maximum distances for interdigitated and gear geometries are 391 μm and 294 μm, respectively. This fact implies decreasing ohmic losses in the discharge process. Thus, high capacity values are obtained for these batteries at high discharge rates. It is also shown that the conventional geometry shows a lower maximum distance but large capacity losses due to the larger thickness of the separator with respect to the other geometries. This effect is ascribed to the fact that the same area is maintained for all components in the different geometries. The thickness of the separator for the conventional geometry is 90 μm and, therefore, the conventional geometry has an ionic flow that is hindered by the separator at high discharge rates.

The horseshoe geometry, for example, shows a higher maximum distance (1125 μm) than the conventional (697 μm) battery, but its capacity is higher at high discharges rates (C) due to the thinner separator (~ 7,71 μm).

Figure 7.2b) shows the distance between collectors for the different geometries and it is observed that the ring, antenna, spiral and horseshoe batteries present almost the same distance between collectors, being in the range from 47.5 μm to 58.3 μm. In this way, these geometries show a thin separator and therefore an improved ionic flow through the separator. On the other hand, the ring, antenna and spiral geometries show a larger amount of charges (ions and electrons) further from the current collector positions, leading to higher ohmic losses due to increased internal resistance of the battery. The ohmic losses are more significant for the value of the capacity of the battery than the separator thickness. In conclusion, this effect is the main reason for the horseshoe geometry presenting a higher capacity value than ring, spiral and antenna geometries, despite all four geometries having approximately the same separator thickness.

Figure 7.2b) shows that the gear and interdigitated geometries present a higher distance between the collectors and a larger separator thickness than the horseshoe, spiral, ring and antenna geometries. The thickness of the separator for the gear and interdigitated geometries are 12.41 and 8.66 μm, respectively, and the distances between the collectors are 135.8 μm and 327 μm, respectively. However, in the gear

and interdigitated geometries a higher delivery capacity is obtained. The improvement in the delivery capacity is related to the fact that the lower maximum distance of the ions from the collector position overcomes the capacity losses due to the larger thickness of the separator.

Finally, it is also worth noticing that the influence of the geometry on battery performance is higher when the batteries operate at high discharge rates, as shown in figure 7.1 and that the performance depends on the combination of different parameters, including the maximum distance of the ions to the current collector, d_max, the distance between current collectors, d_cc, and the thickness of separator and electrodes.

7.3.2 Influence of the geometrical parameters in battery performance

The influence of specific geometrical parameters of the different geometries (horseshoe, ring and gear) in battery performance is shown in this section. The choice of these geometries is based on the delivered capacity obtained in the previous section as well as their application possibilities. The interdigitated geometry also shows high capacity values but its optimization has been already addressed in the literature. All simulations consider the same area for the different components (anode, cathode, separator and current collectors) and high discharge rates. In the horseshoes geometry, the main parameters studied are the dimensions and current collector positions. For the ring geometry, it was studied the effect of the radius of the ring. Finally, the battery performance of ring and gear geometries was compared.

7.3.2.1 Effect of battery dimensions and current collector positions in the horseshoe geometry

Due to its specific geometrical features, it is particularly important to evaluate the influence of the dimensions of the battery and the position of the current collectors on battery performance for the horseshoe geometry. In this study, simulations were performed at high discharges rates (500C), as effects associated to battery geometry are more clearly observed.

7.3.2.1.1 Current collector positions

Three current collector positions were selected (figure 7.3a)): A, B and C which correspond to 0 μm, 562.5 μm and 1125 μm distance from position A.

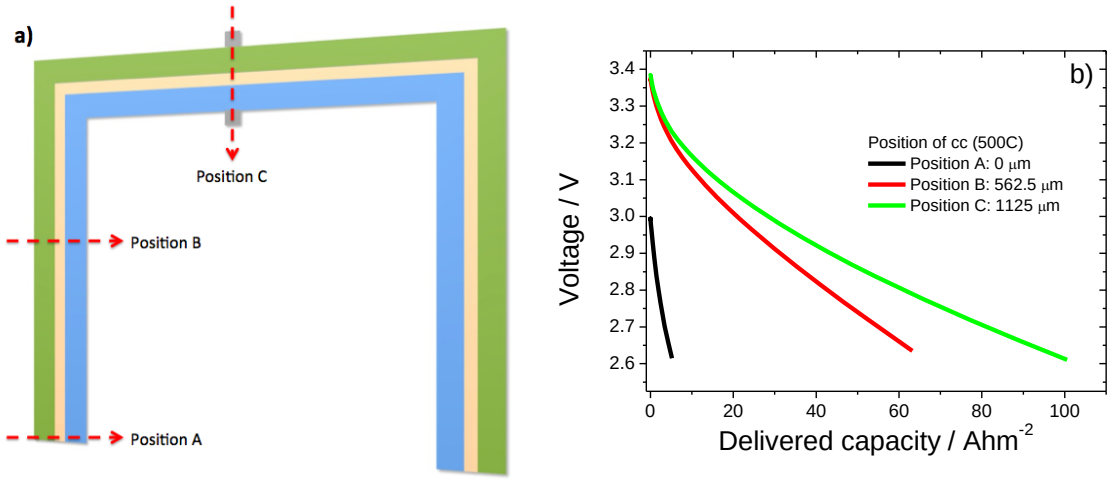

Figure 7.3 - a) Schematic representation of the current collector positions and b) voltage as a function of the delivered capacity for the different current collector positions.

Figure 7.3b) shows that the battery with collectors placed in C results in the highest capacity value in comparison to the other collector positions, due to the lower ohmic losses associated to the movement of the ions to the current collector positions.

Being constant the dimensions of the battery, the observed differences in delivery capacity are just ascribed to the maximum distance of the lithium ions to the collectors (Figure 7.4).

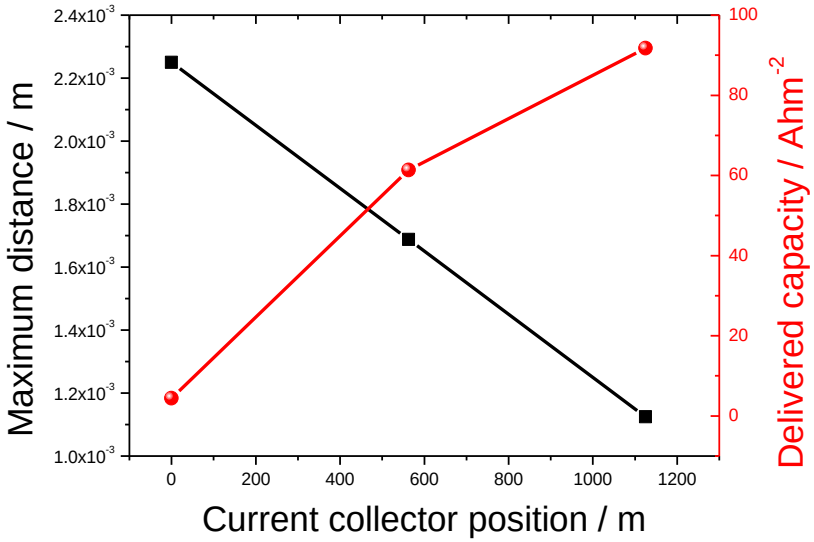

Figure 7.4 - Delivered capacity as a function of current collector positions and maximum distance of lithium ions.

Figure 7.4 shows that the maximum distance of the most distant ions for the 3 collector position A, B and C is 2250 μm, 1687 μm and 1125 μm, respectively, a decrease of the maximum distance of the furthest ions in relation to the collector position leading to shortest paths for ion transport and therefore to lower ohmic losses. Further, for the collectors placed at positions B and A, the magnitude of the electric field applied to the ions located at places far from the electrodes is lower.

When the collectors are placed in the central geometrical position, all ions located far from the electrodes are at similar distances, leading to smaller paths for ion movement and a larger magnitude of the electric field.

So, it is concluded that the current collector position strongly affects battery performance for this geometry.

7.3.2.1.2. Dimensions of the battery

Taking into account the previous results, it is important evaluate the influence of the dimensions of the horseshoe geometry in the performance of the battery at high discharges rates (500C). The dimension under consideration, L_dim in Figure 7.5a), was modified from 50 μm to 750 μm.

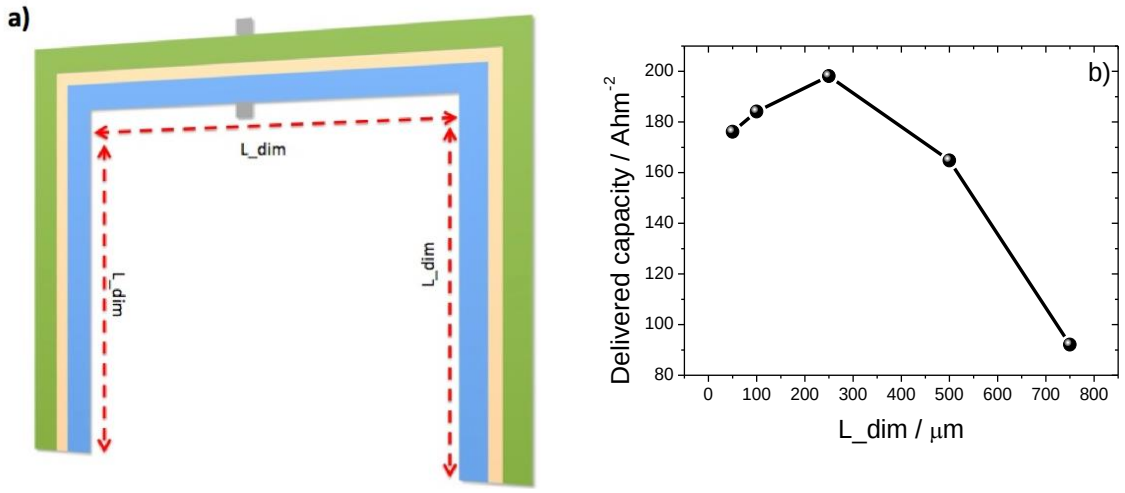

Figure 7.5 - a) Schematic representation of the horseshoe battery dimension, L_dim, and b) delivered capacity as a function of L_dim.

Figure 7.5b) shows that the capacity value increases from 176 Ahm^{-2} to 198 Ahm^{-2} when L_dim increases from 50 μm to 250 μm. For further increase from 250 μm to 750 μm, the capacity values decrease from 198 Ahm^{-2} to 92Ahm^{-2}. In this way, the optimum capacity value is 198 Ahm^{-2} for a horseshoe dimension of 250 μm. It would be expected that by decreasing L_dim, the capacity values would increase due to a reduction of the ohmic losses. In contrast, a decrease of the capacity value is obtained for L_dim from 250 μm to 50 μm. This effect is explained by the balance between the gains in capacity associated to the reduction of the ohmic losses and the higher electric field applied to the most distant ions, and the decrease of the capacity associated to the thickness increase of the electrodes. Other possible reasons for this fact are the increased thickness of the separator (hindering ionic flow through the separator) and the decrease of the surface contact area between electrodes (decreasing ion insertion in the cathode).

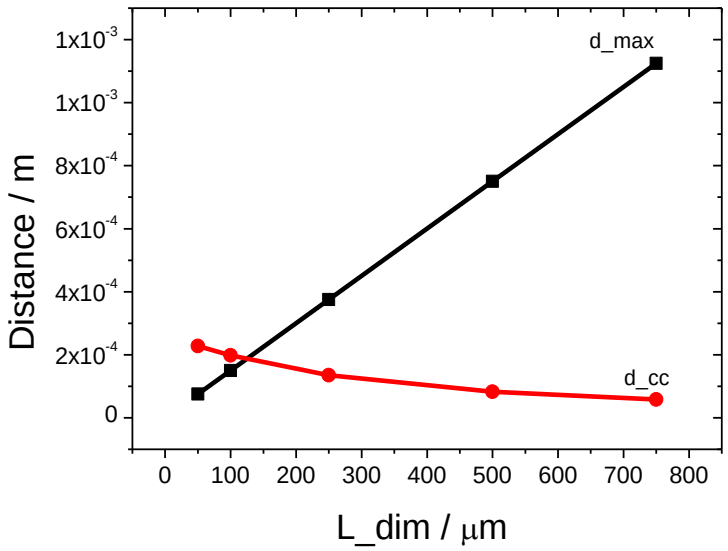

Figure 7.6 - Maximum distance and distance between current collectors as a function of L_dim for the horseshoe geometry.

Figure 7.6 shows that increasing L_dim between 50 μm to 750 μm leads to an increase of the distance of the more distant lithium ions from the collectors, d_max, and a decrease of the distance between collectors, d_cc.

It is important to notice that the lager distance between collectors, d_cc, is due to the increased thickness of separator and electrodes, leading to larger paths for electrons to move.

In the range of L_dim from 250 μm to 50 μm it is observed a decrease of the capacity value. Although, the distance of the most distant ions to the collectors, d_max, is lower, there is a larger impact of the losses on the capacity values. As previously mentioned, these losses are related to the larger thickness of the separator, low surface contact area between electrodes and larger paths for the movement of electrons from the electrodes to the collectors.

7.3.2.2 Influence of the radius in the ring geometry

The influence of the radius of the ring battery in battery performance was investigated. The radius of the ring geometry is defined by R_d, as illustrated in figure 7.7a).

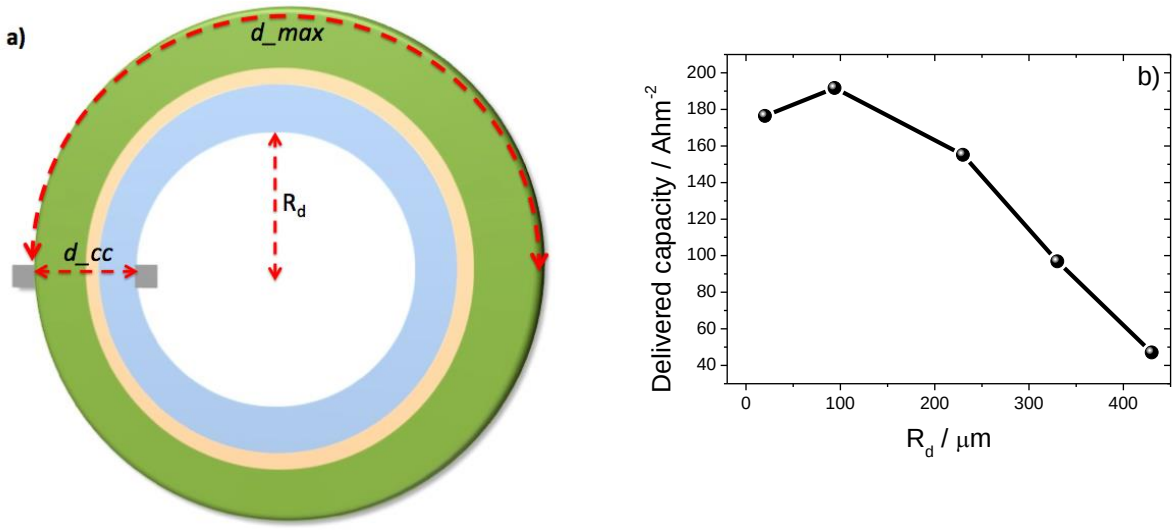

Figure 7.7 - a) Schematic representation of the ring geometry and b) delivered capacity as a function of the radius, R_d.

The maximum distance of the ions that are located in distant places with respect to the collector position, d_max, is half the ring perimeter (Figure 7.7a)).

In section 7.3.1., it was observed that the ring geometry belongs to the group of geometries with medium capacity value, together with the ring, antenna and spiral geometries. The capacity can nevertheless be optimized by varying the radius.

Figure 7.7b) shows the relationship between the radius of the ring and the capacity for high discharges rates (500C).

For a radius of the ring from 20 μm to 93.9 μm it was obtained an increase in the capacity value from 176 Ahm^{-2} to 192 Ahm^{-2}, respectively, due to the balance between maximum distance of ions and thickness of separator as illustrated in figure 7.8. Further, for a radius from 93.9 μm to 430 μm a decrease in the performance of the battery is observed (figure 7.7b)). In this way, an optimum capacity value of 192 Ahm^{-2} is obtained for a ring battery with a radius of 93.9 μm.

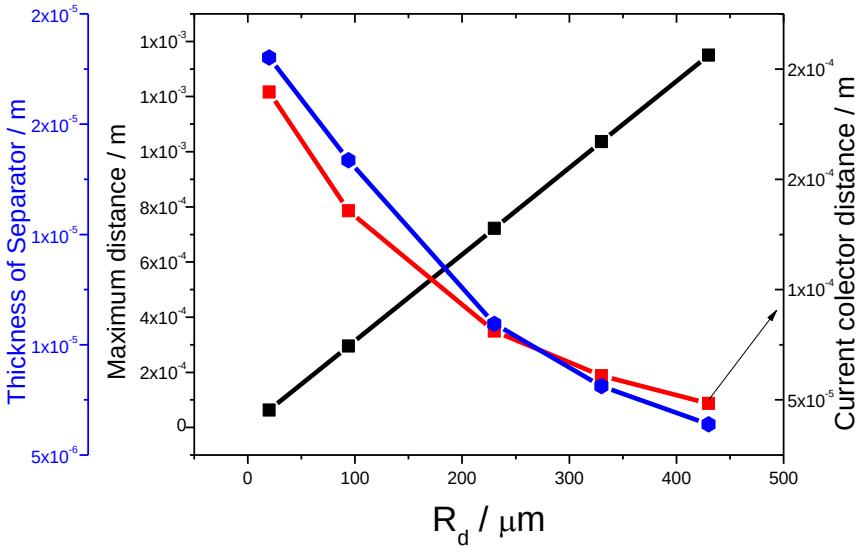

Figure 7.8 - Maximum distance, distance between current collectors and thickness of the separator as a function of R_d.

Figure 7.8 shows that, for R_d from 20 μm to 430 μm, that the thickness of separator decreases from 23 μm to 6.40 μm and that the distance between the collectors decreases from 189.5 μm to 48.35 μm. In this way, the gain in capacity associated to the decreasing thickness of the electrodes and separator are lower than the capacity losses due to the increase of the maximum distances of the ions from the current collector positions.

As a result, the ring geometry can be optimized for specific applications taking into account its radius.

7.3.2.3 Comparative performance of ring and gear battery geometries

A comparative study of the capacity of the ring (figure 7.7a)) and gear battery geometries was performed for a 500C discharge rate. Figure 7.9a) shows the gear geometry, which is characterized by the presence of digits in both electrodes, each digit defined by its thickness (e_dig) and length (c_dig). Further, *Rg* defines the radius of the gear geometry. The simulated gear shows 8 digits in both electrodes (figure 7.9a)). The maximum distance of the most distant ions to the collector position (d_max) is the same for both gear and ring geometries. The maximum distance in these geometries is half the perimeter.

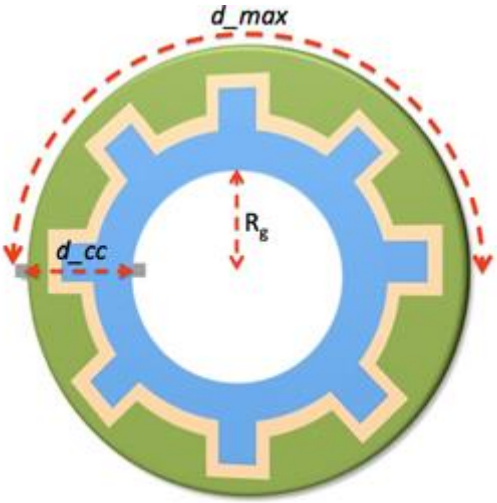

Figure 7.9 – Schematic representation of the gear geometry.

The comparative effect of Rg variation (93.9 μm and 20 μm) in both gear and ring geometries is illustrated in figure 7.10. In both cases, the values of the thickness and the length of the digit is 40 μm and 30 μm, respectively.

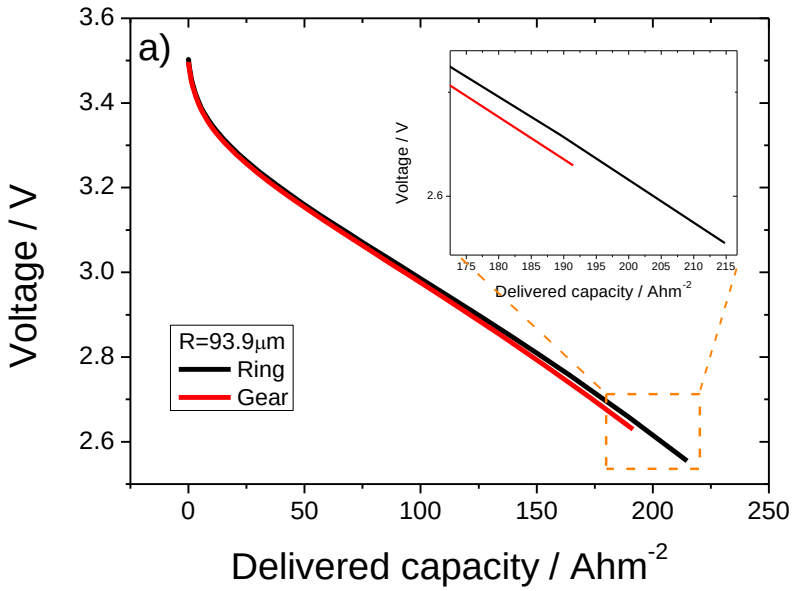

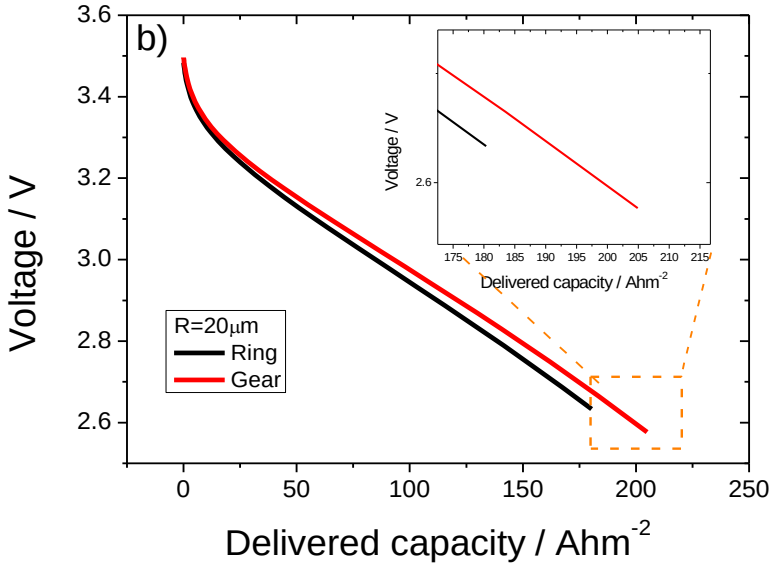

Figure 7.10 – Voltage as a function of the delivered capacity for the ring and gear geometries with different Rg: a) 93.9 μm and b) 20 μm.

Figure 7.10a) shows the capacity values for both geometries and a Rg of 93.9 μm. It is relevant to notice that the gear and ring geometries show the same distance between collectors, d_cc, but that the gear geometry presents a lower separator thickness due to the presence of the digits. It would be expected a higher capacity value in the gear geometry than for the ring geometry, as the digits of the former increase the surface contact area between the electrodes and decreases the thickness of the separator. However, it is observed that the value of the capacity for the gear geometry is lower than for the ring geometry. Both geometries show the same maximum distance of 294.8 μm and therefore the same ohmic losses.

On the other hand, when Rg decreases to 20 μm, the opposite behavior is observed with respect to the capacity values (figure 7.10b)): the gear geometry show larger capacity that the ring geometry.

The larger capacity obtained for the gear geometry is associated to the lower separator thickness and larger contact surface area between electrodes due to the fact that the same area was maintained for the different battery components (electrodes, separator and current collectors).

The larger capacity of the ring geometry for the larger Rg is explained in figure 7.11 in terms of the electrolyte potential and electrolyte current density vectors (black arrows) in the different regions of the battery at a specific discharge time.

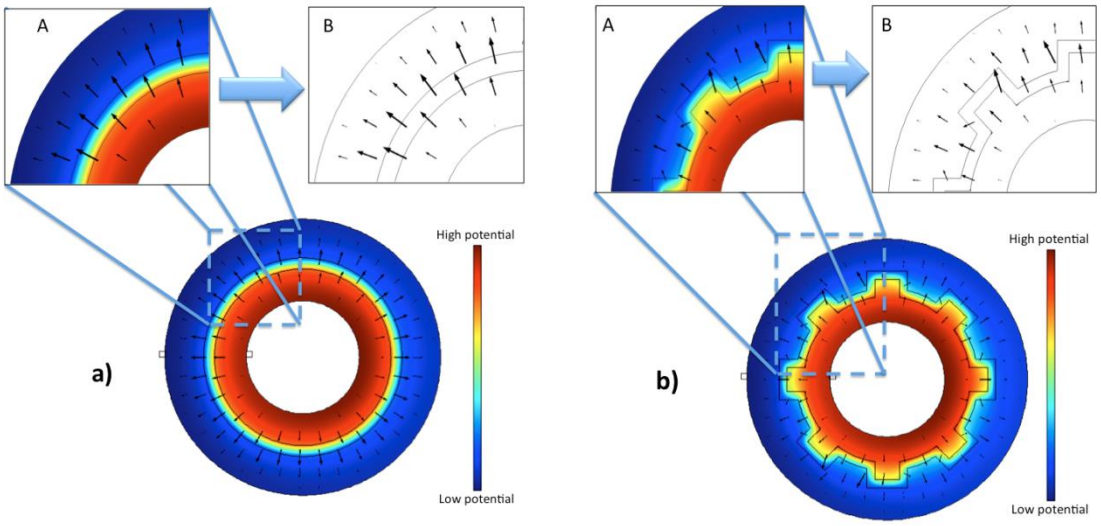

Figure 7.11 - Electrolyte potential and electrolyte current density vectors for a) ring and b) gear geometries.

The gear geometry shows lower capacity due to lithium ion accumulation in the vertices of the digits, leading to a higher charge density in these regions and a heterogeneity in the electric potential that leads to local electric fields (images A in figure 7.11). Local electric fields mean lower ionic flow between electrodes and the electrolyte current density shows different orientations instead of the radial orientation observed for the ring geometry (images B in figures 7.11), that does not show local accumulations of lithium ions.

Figure 7.12 shows the capacity values of the gear and ring geometries at 500C for a Rg of 20 μm. The ring geometry shows a separator thickness of 42.6 μm and the gear geometry of 23.4 μm: the different separator thickness is due to the presence of the digits in the gear geometry that lead to an increase of the contact surface area between the electrodes. A study was thus carried out in which the area of the separator is duplicated from the gear to the ring geometries.

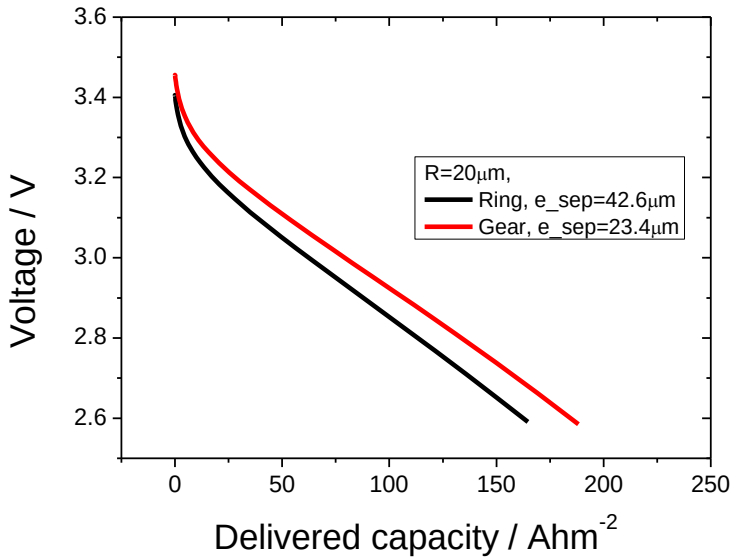

Figure 7.12 - Voltage as a function of the delivered capacity for the ring and gear geometries with different separator thickness.

Figure 7.12 show that the gear geometry shows a higher capacity value than the ring geometry. In contrast with the previous study, the losses associated to the accumulation of lithium ions in the vertices of the digits is not significant in comparison with the gains of capacity associated to the decrease of the thickness of the separator and the increase in contact surface area between the electrodes. The gear geometry shows an optimal thickness for the separator value that allows a better ionic flow through the separator.

In conclusion, when there is a need to decrease the radius of a circular battery for specific applications, it is important to introduce digits in the electrodes (gear geometry).

7.4 Conclusions

Geometry optimization is essential for maximizing energy density in lithium-ion batteries. This work reports on the optimization of specific battery geometries, based on their potential applicability.

Seven geometries were theoretical simulated based on the Doyle/Fuller/Newman theoretical model, including conventional, interdigitated, horseshoe, spiral, ring, antenna and gear batteries.

It is shown that, independently of the geometry, high discharge rates require higher ion insertion capacity on the cathode (high surface contact area between electrodes), smaller paths for charges to move between collectors and electrodes (reduced ohmic losses), thin thickness of the separator (improved ionic flow) and optimized current collector positions to decrease the loss of magnitude of the electric field applied to the most distant ions.

At 330C, capacity values of conventional, ring, spiral, horseshoe, gear and interdigitated geometries are 0,58 Ahm^{-2}, 149 Ahm^{-2}, 182 Ahm^{-2}, 216 Ahm^{-2}, 289 Ahm^{-2} and 318 Ahm^{-2}, respectively.

It is also shown that battery capacity can be tailored for the different geometries taking into account geometrical parameters such as maximum distance of the most distant ions, d_max, distance between of current collectors, d_cc and thickness of separator and electrodes, once the materials are selected. In this way, new battery geometries with optimized performance can be fabricated to allow better integration into specific devices.

7.5 References

1. Tarascon, J.-M., Key challenges in future Li-battery research. Vol. 368. 2010. 3227-3241.
2. Wakihara, M. and O. Yamamoto, Lithium Ion Batteries: Fundamentals and Performance2008: Wiley.
3. Dunn, B., H. Kamath, and J.-M. Tarascon, Electrical Energy Storage for the Grid: A Battery of Choices. Science, 2011. **334**(6058): p. 928-935.
4. Thackeray, M.M., C. Wolverton, and E.D. Isaacs, Electrical energy storage for transportation-approaching the limits of, and going beyond, lithium-ion batteries. Energy & Environmental Science, 2012. **5**(7): p. 7854-7863.
5. Scrosati, B. and J. Garche, Lithium batteries: Status, prospects and future. Journal of Power Sources, 2010. **195**(9): p. 2419-2430.
6. Dunn, J.B., et al., The significance of Li-ion batteries in electric vehicle life-cycle energy and emissions and recycling's role in its reduction. Energy & Environmental Science, 2015. **8**(1): p. 158-168.
7. Zhang, Q., et al., Nanomaterials for energy conversion and storage. Chemical Society Reviews, 2013. **42**(7): p. 3127-3171.
8. Patry, G., et al., Cost modeling of lithium-ion battery cells for automotive applications. Energy Science & Engineering, 2015. **3**(1): p. 71-82.
9. Vincent, C.A., Lithium batteries: a 50-year perspective, 1959–2009. Solid State Ionics, 2000. **134**(1–2): p. 159-167.
10. Park, J.K., Principles and Applications of Lithium Secondary Batteries2012: Wiley.
11. Roy, P. and S.K. Srivastava, Nanostructured anode materials for lithium ion batteries. Journal of Materials Chemistry A, 2015. **3**(6): p. 2454-2484.
12. Goriparti, S., et al., Review on recent progress of nanostructured anode materials for Li-ion batteries. Journal of Power Sources, 2014. **257**(0): p. 421-443.
13. Chikkannanavar, S.B., D.M. Bernardi, and L. Liu, A review of blended cathode materials for use in Li-ion batteries. Journal of Power Sources, 2014. **248**(0): p. 91-100.

14. Costa, C.M., M.M. Silva, and S. Lanceros-Mendez, Battery separators based on vinylidene fluoride (VDF) polymers and copolymers for lithium ion battery applications. RSC Advances, 2013. **3**(29): p. 11404-11417.
15. Roberts, M., P. Johns, and J. Owen, Micro-scaled Three-Dimensional Architectures for Battery Applications, in Nanotechnology for Lithium-Ion Batteries, Y. Abu-Lebdeh and I. Davidson, Editors. 2013, Springer US. p. 245-275.
16. Pikul, J.H., et al., High-power lithium ion microbatteries from interdigitated three-dimensional bicontinuous nanoporous electrodes. Nat Commun, 2013. **4**: p. 1732.
17. Arthur, T.S., et al., Three-dimensional electrodes and battery architectures. MRS Bulletin, 2011. **36**(07): p. 523-531.
18. Long, J.W., et al., Three-Dimensional Battery Architectures. Chemical Reviews, 2004. **104**(10): p. 4463-4492.
19. Pikul, J.H., P.V. Braun, and W.P. King, High power primary lithium ion microbatteries. Journal of Physics: Conference Series, 2013. **476**(1): p. 012087.
20. Sun, K., et al., 3D Printing of Interdigitated Li-Ion Microbattery Architectures. Advanced Materials, 2013. **25**(33): p. 4539-4543.
21. Gaikwad, A.M., A.C. Arias, and D.A. Steingart, Recent Progress on Printed Flexible Batteries: Mechanical Challenges, Printing Technologies, and Future Prospects. Energy Technology, 2015. **3**(4): p. 305-328.
22. Delannoy, P.E., et al., Ink-jet printed porous composite LiFePO4 electrode from aqueous suspension for microbatteries. Journal of Power Sources, 2015. **287**: p. 261-268.
23. Sousa, R.E., C.M. Costa, and S. Lanceros-Mendez, Advances and Future Challenges in Printed Batteries. ChemSusChem, 2015. **Accepted**.
24. Ramadesigan, V., et al., Modeling and Simulation of Lithium-Ion Batteries from a Systems Engineering Perspective. Journal of The Electrochemical Society, 2012. **159**(3): p. R31-R45.
25. Miranda, D., C.M. Costa, and S. Lanceros-Mendez, Lithium ion rechargeable batteries: State of the art and future needs of microscopic theoretical models and simulations. Journal of Electroanalytical Chemistry, 2015. **739**(0): p. 97-110.

26. Martínez-Rosas, E., R. Vasquez-Medrano, and A. Flores-Tlacuahuac, Modeling and simulation of lithium-ion batteries. Computers & Chemical Engineering, 2011. **35**(9): p. 1937-1948.
27. Franco, A.A., Multiscale modelling and numerical simulation of rechargeable lithium ion batteries: concepts, methods and challenges. RSC Advances, 2013. **3**(32): p. 13027-13058.
28. Arora, P., et al., Comparison between computer simulations and experimental data for high-rate discharges of plastic lithium-ion batteries. Journal of Power Sources, 2000. **88**(2): p. 219-231.
29. Rohan, J.F., et al., Energy Storage: Battery Materials and Architectures at the Nanoscale, ICT - Energy - Concepts Towards Zero - Power Information and Communication Technology, InTech, Editor 2014.
30. Oltean, G., et al., A Li-Ion Microbattery with 3D Electrodes of Different Geometries. ECS Electrochemistry Letters, 2014. **3**(6): p. A54-A57.
31. Zhang, X., Thermal analysis of a cylindrical lithium-ion battery. Electrochimica Acta, 2011. **56**(3): p. 1246-1255.
32. Jeon, D.H. and S.M. Baek, Thermal modeling of cylindrical lithium ion battery during discharge cycle. Energy Conversion and Management, 2011. **52**(8–9): p. 2973-2981.
33. Harb, J.N. and R.M. LaFollette, Mathematical Model of the Discharge Behavior of a Spirally Wound Lead-Acid Cell. Journal of The Electrochemical Society, 1999. **146**(3): p. 809-818.
34. Hatchard, T.D., et al., Thermal Model of Cylindrical and Prismatic Lithium-Ion Cells. Journal of The Electrochemical Society, 2001. **148**(7): p. A755-A761.
35. Miranda, Á.G. and C.W. Hong, Integrated modeling for the cyclic behavior of high power Li-ion batteries under extended operating conditions. Applied Energy, 2013. **111**: p. 681-689.
36. Ping, P., et al., Thermal behaviour analysis of lithium-ion battery at elevated temperature using deconvolution method. Applied Energy, 2014. **129**: p. 261-273.
37. Zhao, R., J. Liu, and J. Gu, The effects of electrode thickness on the electrochemical and thermal characteristics of lithium ion battery. Applied Energy, 2015. **139**: p. 220-229.

38. Elul, S., Y. Cohen, and D. Aurbach, The influence of geometry in 2D simulation on the charge/discharge processes in Li-ion batteries. Journal of Electroanalytical Chemistry, 2012. **682**: p. 53-65.
39. Bates, A., et al., Modeling and simulation of 2D lithium-ion solid state battery. International Journal of Energy Research, 2015: p. n/a-n/a.
40. Lim, C., et al., Geometric Characteristics of Three Dimensional Reconstructed Anode Electrodes of Lithium Ion Batteries. Energies, 2014. **7**(4): p. 2558.
41. Taheri, P., et al., Theoretical Analysis of Potential and Current Distributions in Planar Electrodes of Lithium-ion Batteries. Electrochimica Acta, 2014. **133**: p. 197-208.
42. Doyle, M., et al., Comparison of Modeling Predictions with Experimental Data from Plastic Lithium Ion Cells. Journal of The Electrochemical Society, 1996. **143**(6): p. 1890-1903.
43. Miranda, D., et al., Modeling separator membranes physical characteristics for optimized lithium ion battery performance. Solid State Ionics, 2015. **278**: p. 78-84.
44. Costa, C.M., et al., Poly(vinylidene fluoride)-based, co-polymer separator electrolyte membranes for lithium-ion battery systems. Journal of Power Sources, 2014. **245**(0): p. 779-786.
45. Dai, Y., L. Cai, and R.E. White, Simulation and analysis of stress in a Li-ion battery with a blended LiMn2O4 and LiNi0.8Co0.15Al0.05O2 cathode. Journal of Power Sources, 2014. **247**: p. 365-376.
46. Park, J., et al., Numerical Simulation of the Effect of the Dissolution of LiMn2O4 Particles on Li-Ion Battery Performance. Electrochemical and Solid-State Letters, 2011. **14**(2): p. A14-A18.
47. Zhang, X., W. Shyy, and A. Marie Sastry, Numerical Simulation of Intercalation-Induced Stress in Li-Ion Battery Electrode Particles. Journal of The Electrochemical Society, 2007. **154**(10): p. A910-A916.

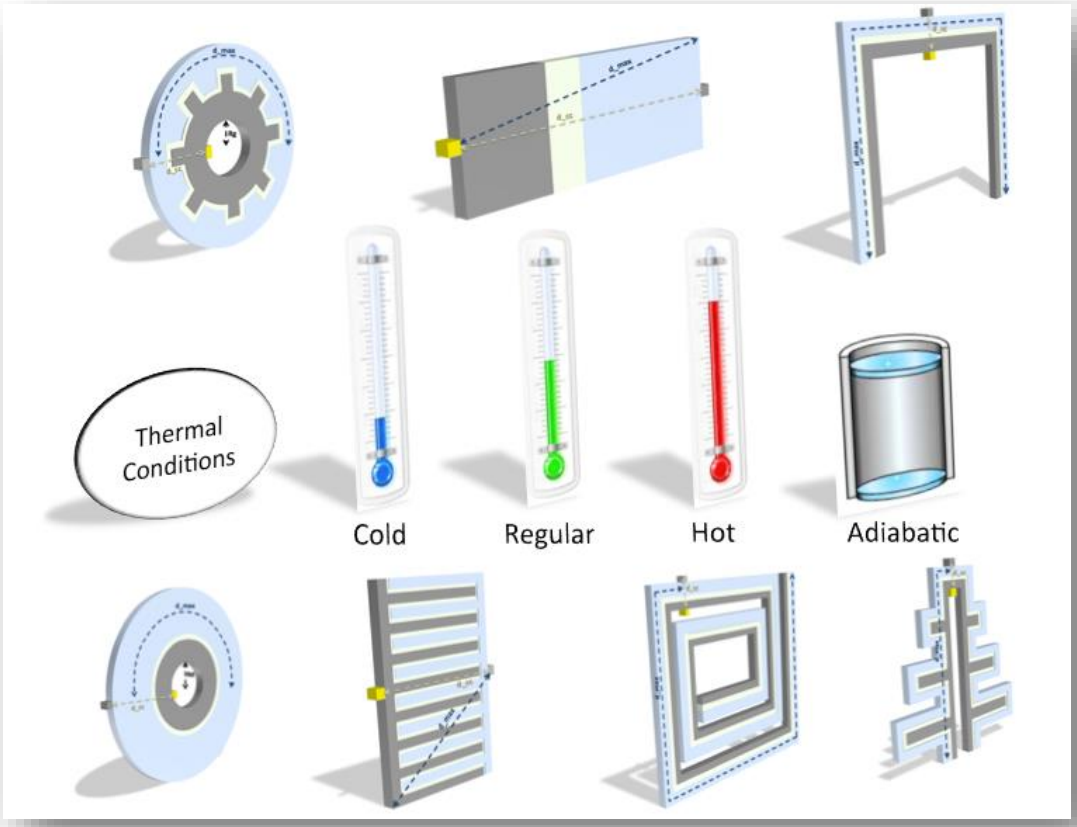

8. Computer simulation of the effect of different thermal conditions in the performance of conventional and unconventional lithium-ion battery geometries

This chapter describes the effect of the thermal conditions (isothermal, adiabatic, cold, regular and hot) in the performance of batteries with conventional, interdigitated, horseshoe, spiral, ring, antenna and gear geometries. The simulations are based on the Newman/Doyle/Fuller model with the addition of the thermal model.

This chapter is based on the following publication:

"Computer simulation of the effect of different thermal conditions in the performance of conventional and unconventional lithium-ion battery geometries", D. Miranda, C. M. Costa, A. M. Almeida, S. Lanceros-Méndez, *submitted.*

8.1 Introduction

Electrical energy is increasingly being obtained through renewable sources, such as, solar, wind, waves, bioenergy and geothermal energy, leading to the need of efficient energy storage systems [1-4].

These energy storage systems are essential for portable electronic devices such as mobile phone and computers but also for transportation systems, i.e, power hybrid electric vehicles (HEVs) and pure electric vehicles (EVs) [5].

Lithium-ion batteries are the most used energy storage systems, being the main type of battery for many applications [6,7].

Lithium-ion batteries are light weight, show high energy density (210Wh kg^{-1}), low charge loss, no memory effect, prolonged service-life and high number of charge/discharge cycles [8,9].

The basic constituents of a lithium-ion battery are the anode, the cathode and the separator and the main issues for improving its performance are specific energy, power, safety and reliability [10].

Li-ion batteries are extremely sensitive to certain temperature ranges that depend on the materials of their constituents and typically can operate between -20 ºC up to ~50-60 ºC [11,12]. The cycling performance of the battery increases with increasing temperature but if the limit range of temperature is exceeded, exothermic reactions can occur, increase of the internal pressure, and rupture or even explosion of the battery [13,14].

For certain applications, such as when high discharge rates are needed for short operation time, the thermal management of batteries is fundamental to optimize battery performance [2,14].

The influence of the thermal conditions in lithium ion battery performance is analyzed in each components but also through of heat dissipation systems [15]. The electrode thickness influences the battery in many key aspects such as its performance and overall heat generation [16].

Each active material has different ionic and electrical conductivity values and its size strongly affects the generation of heat [17].

Thus, the effect of particle size for $LiMn_2O_4$ was studied by using a thermal model and the higher generation of heat generation was observed for larger particles size [18]. Further, the geometry of the batter also influences its thermal behavior [14,19].

The thermal behavior of batteries with cylindrical, prismatic and pouch cell geometries was analyzed under different electrical loads and cooling conditions [20].

In relation to cylindrical cell geometries, it is observed an decreasing heat transfer resistance with increasing radius due to adiabatic condition at the cell core. On the other hand, differential temperature across the cell thickness must be considered for prismatic cells [20].

The thermal behavior of a lithium ion battery during galvanostatic discharge was analyzed by computer simulation showing that higher cell temperatures raise the risk of thermal runaway and more rapid degradation of the cell [21].

Due to the relevance of maintaining proper battery temperatures, thermal management system (TMS) are implemented with the objective to avoid overheating of battery packs [22]. Applied cooling systems include air cooling [23], liquid cooling [24], heat pipe cooling [25], and PCM cooling [26].

New lithium-ion unconventional battery geometries, such as ring, spiral, horseshoe, antenna and gear, [19] can be produced by printing techniques for better integration in small, portable and wearable devices.

Taking into account the relevance of the thermal behavior of lithium-ion batteries, the goal of this work is to evaluate the effect of different thermal conditions, including isothermal, adiabatic and environmental conditions, in the performance of batteries with seven different geometries: conventional, interdigitated, horseshoe, spiral, ring, antenna and gear [19].

8.2 Preparation and measurement of the full-cell

For the validation of the theoretical thermal model, a full-cell was developed.

For the preparation of the electrodes, anode and cathode, carbon coated lithium iron phosphate, C-$LiFePO_4$ (LFP, Particle size: D10=0.2 μm, D50=0.5 μm and D90=1.9 μm), poly(vinylidene fluoride) (PVDF, Solef 5130) and N,N'-dimethyl propylene urea (DMPU) were acquired from Phostech Lithium, Solvay and LaborSpirit, respectively. Timrex SLG3 graphite particles and carbon black (Super P-C45) were obtained from Timcal Graphite & Carbon.

The electrodes were prepared by mixing LFP (for the cathode) or graphite (for the anode) as active materials, Super P, and the PVDF polymer binder in DMPU solvent with a weight ratio of 80:10:10 (wt.%), i.e, 1 g of solid material for 2.25 mL of DMPU [27].

First, the polymer was dissolved in the solvent and, after this process, small amounts of dried mixed solid material (LFP or graphite and Super P) were added to the solution under constant stirring at room temperature. Good dispersion was achieved by maintaining the electrode slurry under stirring for 2 hours at 1000 rpm, then 1h in an ultrasonic bath and then stirred again for 1 hour. After the mixing process of the materials, the electrode slurry was spread onto a copper foil for the anode and aluminum foil for the cathode and dried in air atmosphere at 80 ºC in a conventional oven (ED 23 Binder). Finally, the electrodes were dried at 90 ºC in vacuum over the night before being transferred into the glove-box.

Two Swagelok type cells were assembled in a home-made argon-filled glove box: the graphite based electrodes (8 mm diameter) were used as anode material; glass microfiber separators (Whatman grade GF/A) (10 mm diameter) were used as separators; 1M $LiPF_6$ in ethylene carbonate-diethyl carbonate (EC-DEC, 1:1 vol) (Solvionic) was used as electrolyte and LFP based electrodes were used as cathode material (8 mm diameter).

The prelithiation of the graphite electrodes was previously achieved by placing them in direct contact with an electrolyte-wetted Li foil for 2 hours, under slight pressure. The active mass loading of the anode and cathode used in the full cell were ~ 1.20 and 2.92 $mg.cm^{-2}$, respectively.

The full battery was cycled at 25 ºC from 2.5 V to 3.8 V at C/10 rate (C = 170 $mA.g^{-1}$) using a Landt CT2001A Instrument.

8.3 Theoretical model: parameters, initial values and boundary conditions

8.3.1 Theoretical simulation model

Simulations were performed by applying the electrochemical model based on the Newman/Doyle/Fuller equations with addition of the thermal behaviour. This electrochemical model describes the electrochemical processes that occurs in battery components, electrodes, separator and current collectors, including the thermal behaviour. The simulations were carried out by implementing the finite element method for different 2D battery geometries in a typical lithium-ion battery structure: [porous negative electrode, (Li_xC_6) | porous membrane of glass micro fiber soaked in 1M lithium hexafluorophosphate ($LiPF_6$) in ethylene carbonate-diethyl carbonate (EC-DEC) | porous positive electrode, (Li_xFePO_4)]. The degree of porosity of the electrodes, defined as the space between the particles of active electrode material, is shown in table 8.1 for both electrodes.

The finite element calculations describing the electrochemical and thermal behavior were carried out using a MATLAB subroutine to solve the main equations describing the behavior of the different battery constituents (electrodes and separator) in an ideal cell without solid electrolyte interface (SEI) formation, as presented in Chapter 3. The size of the mesh was refined according to the dimensions of the different geometries of the battery.

The value of C-rate was determined by the area of the cathode considering the mass of active material.

The impedance was measured for each geometry at frequencies ranging from 10 MHz to 1 MHz with a potential perturbation amplitude of 0.01 V and with the following parameters: film resistance of the positive electrode: 0.0065 $m^2 \cdot S^{-1}$; film resistance of the negative electrode: 1×10^{-5} $m^2 \cdot S^{-1}$; double layer capacitance of the positive electrode: 0.2 $F.m^{-2}$; double layer capacitance of the negative electrode: 0.2 $F.m^{-2}$; current collector resistance at each current collector: 1.1×10^{-4} $m^2.S^{-1}$ [28].

8.3.2 Specific parameters and initial values

The values of the parameters used for the different components of each battery geometry are listed in Table 8.1. The areas of all components were maintained constant in the computer simulations as shown in [29].

Table 8.1 - Values of the parameter values used in the simulations. The nomenclature is indicated in the List of Symbols and Abbreviations.

Electrochemical parameters and initial values				
Parameter	**Unit**	**Anode (Li_xC_6)**	**Separator**	**Cathode (Li_xFePO_4)**
$C_{E,i,0}$	mol/m^3	14870		3900
$C_{E,i,max}$	mol/m^3	31507		21190
C_L	mol/m^3		1000	
r	m	$12{,}5\times10^{-6}$		8×10^{-6}
L_i	m	200×10^{-6}	90×10^{-6}	400×10^{-6}
$k_i(T)$	S/m	a)	a)	a)
$k_{ef,i}$	S/m	$k_i(T)\times0{,}357^{1,5}$	$k_i(T)\times4{,}84\times10^{-2}$	$k_i(T)\times0{,}444^{1,5}$
$K_{t298,15,i}$	m/s	2×10^{-11}		2×10^{-11}
$K_{t,i}(T)$	m/s	b)		b)
$D_i(T)$	m^2/s	c)	c)	c)
$D_{ef,i}$	m^2/s	$D_i(T)\times0{,}357^{1,5}$	$D_i(T)\times4{,}84\times10^{-2}$	$D_i(T)\times0{,}444^{1,5}$
D_{LI}	m^2/s	$3{,}9\times10^{-14}$		$3{,}2\times10^{-13}$
$D_{LI}(T)$		d)		d)
Brugg or p		1,5	8,5	1,5
$\varepsilon_{f,i}$		0,172		0,259
ε_i		0,357	0,70	0,444
τ			3,8	
σ_i	S/m	100		11.8
i_{1C}	A/m^2		17,5	
F	C/mol		96487	
R	J/mol K		8,314	
$E_{ad,i}$	J/mol	5.1×10^3		39×10^3
$E_{ak,i}$	J/mol	58×10^3		29×10^3
Thermal parameters and initial values				
Parameter	**Unit**	**Anode (Li_xC_6)**	**Separator**	**Cathode (Li_xFePO_4)**
$C_{p,i}$	J/(kg.K)	1437.4	1978.16	1260.2
ρ_i	kg/m^3	2660	1008.98	1500
λ_i	W/(m.K)	1,04	0,344	1,48
h	W/(m^2.K)	1,0	1,0	1,0
$T\infty_{,cold}$	K	265,15	265,15	265,15
$T\infty_{,reg}$	K	298,15	298,15	298,15
$T\infty_{,hot}$	K	316,15	316,15	316,15
$T_{0,adi}$	K	298,15	298,15	298,15
$T_{0,cold}$	K	265,15	265,15	265,15
$T_{0,reg}$	K	298,15	298,15	298,15
$T_{0,hot}$	K	316,15	316,15	316,15
Area of each component of the battery				
Parameter	**Unit**	**Anode (Li_xC_6)**	**Separator**	**Cathode (Li_xFePO_4)**
A_i	m^2	$4{,}0\times10^{-8}$	$1{,}8\times10^{-9}$	$8{,}0\times10^{-8}$

Auxiliary equations:

a) Ionic conductivity as a function of temperature [30]:

$$k_i(T) = c\times(-10.5+(0.0740\times T)-((6.96\times10^{-5})\times(T^2))+(0.668\times c)-$$
$$-(0.0178\times c\times T)+((2.8\times10^{-5})\times c\times(T^2))+(0.494\times c^2)-((8.86\times10^{-4})\times(c^2)*(T)))^2$$

b) Reaction rate coefficient of the electrodes as a function of temperature [31]:

$$K_{t,i}(T)= k_{t298,15,i}\times exp(-(E_{ak,i}/R)\times(1/T-1/298{,}15))$$

c) Diffusion coefficient of the salt in the electrolyte as a function of temperature [30]:

$$D_i(T) = 10\text{^}(-(0.22\times c)-4.43-((54)/(T-229-(5\times c))))$$

d) Diffusion coefficient of Li ions in the electrode as a function of temperature [31]:

$$D_{LI}(T) = D_{LI}\times exp(-(E_{ad,i}/R)\times(1/T-1/298{,}15))$$

Table 8.2 shows the schematic representation of each of the evaluated geometries, conventional, interdigitated, gear, horseshoe, spiral, antenna and ring, as well as the values of the relevant dimensions for battery characterizations such as distance between collectors and thickness of the electrodes and separator, among others.

Table 8.2 - Schematic representation of the different battery geometries and the corresponding dimensions. The nomenclature is indicated in the List of Symbols and Abbreviations.

Battery design	Dimensions (m)	
	Parameter	**Value / m**
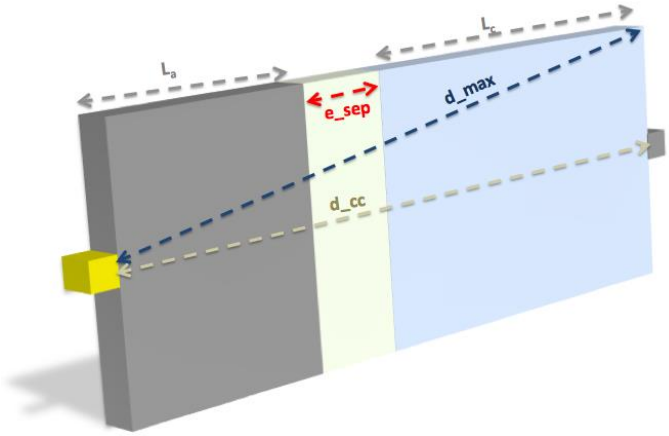 Conventional	L_c	400×10^{-6}
	L_a	200×10^{-6}
	e_sep	90×10^{-6}
	d_max	697×10^{-6}
	d_cc	690×10^{-6}
	Parameter	**Value / m**
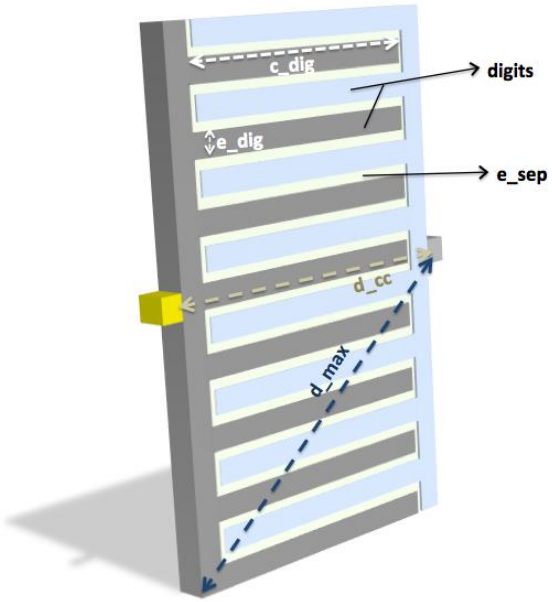 Interdigitated	*N*	8 digits
	c_dig	100×10^{-6}
	e_dig	20×10^{-6}
	e_sep	8.66×10^{-6}
	d_max	391×10^{-6}
	d_cc	327×10^{-6}

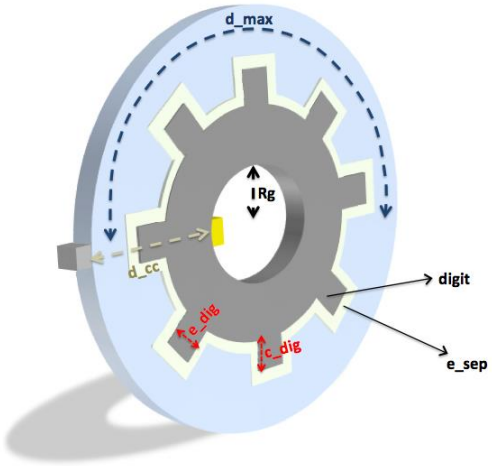

Gear

Parameter	Value / m
N	8 digits
e_sep	12.41×10^{-6}
Rg	93.9×10^{-6}
d_max	294×10^{-6}
d_cc	135.8×10^{-6}
e_dig	40×10^{-6}
c_dig	30×10^{-6}

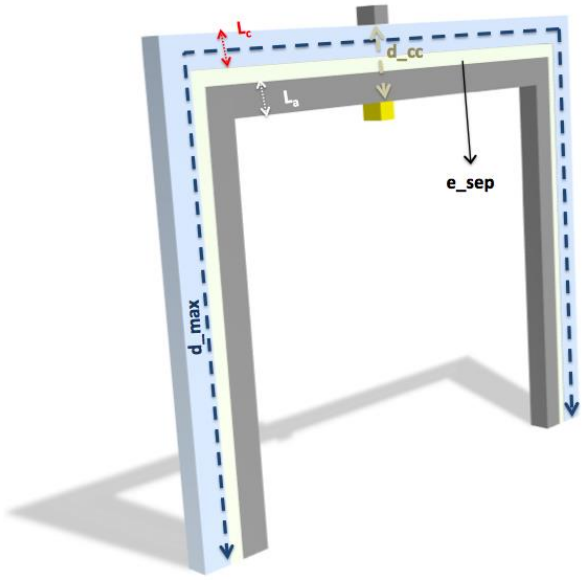

Horseshoe

Parameter	Value / m
L_c	$33{,}1\times10^{-6}$
L_a	17.5×10^{-6}
e_sep	7.71×10^{-6}
d_max	1125×10^{-6}
d_cc	58.3×10^{-6}

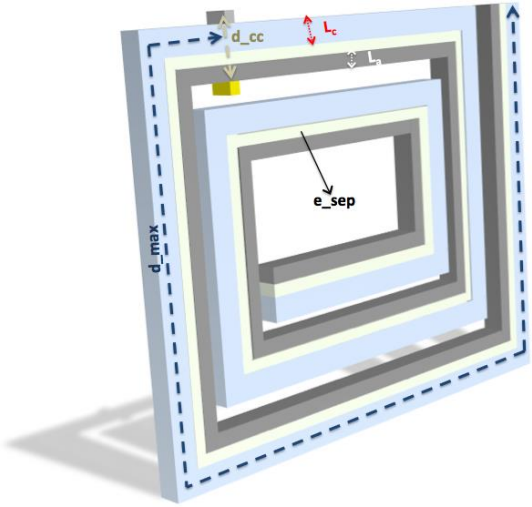

Spiral

Parameter	Value / m
L_c	28.6×10^{-6}
L_a	17.8×10^{-6}
e_sep	7.27×10^{-6}
d_max	1240×10^{-6}
d_cc	53.7×10^{-6}

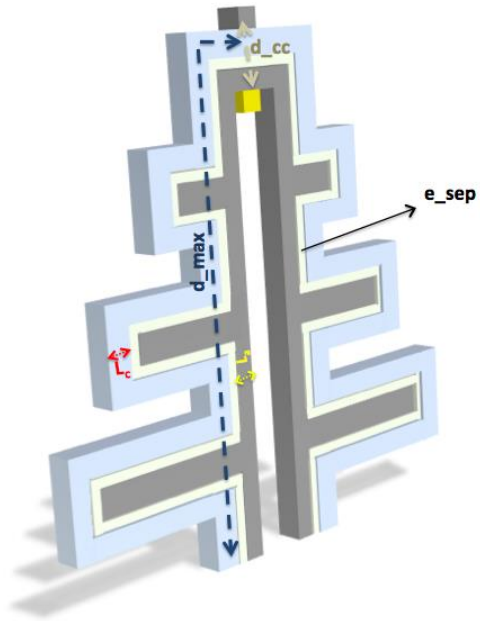

Antenna

Parameter	Value / m
L_c	25.6×10^{-6}
L_a	16.0×10^{-6}
e_sep	5.88×10^{-6}
d_max	1225×10^{-6}
d_cc	47.5×10^{-6}

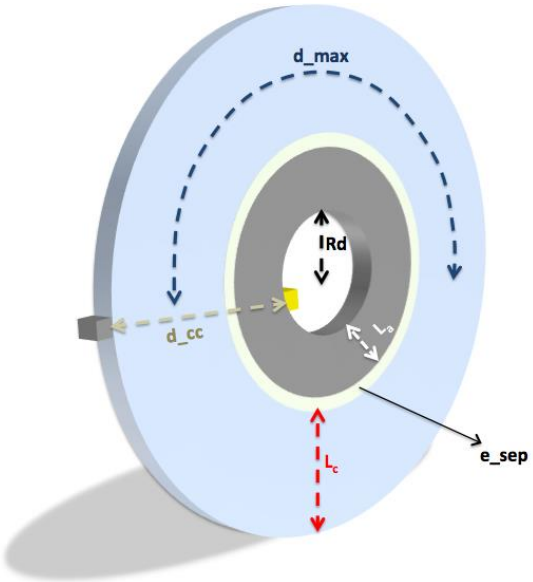

Ring

Parameter	Value / m
L_c	27.4×10^{-6}
L_a	14.5×10^{-6}
e_sep	6.40×10^{-6}
R_d	430×10^{-6}
d_max	1350×10^{-6}
d_cc	48.4×10^{-6}

8.3.3 Boundary conditions

The boundary conditions were defined accordingly to the electrochemical (Newman/Doyle/Fuller) and thermal models. The boundary conditions are schematically presented in Figure 1 and defined in Table 8.3.

As the boundary conditions are the same for all geometries, just the ones for conventional geometry will be presented, as an example. Table 4 shows these boundary conditions addressing the schematic representation of the conventional geometry, illustrated in Figure 8.1.

In Table 8.3 and Figure 8.1, the boundary conditions are identified from 1 to 7.

According to Figure 8.1, the boundary condition 1 indicates that there is no ion flux. Regarding the thermal model in the adiabatic condition, there is no heat transfer with the external environment, as defined by boundary condition 1. Also, at adiabatic condition the external temperature is not applicable (boundary condition 6). In contrast, for the thermal model with different conditions (cold, regular and hot temperatures) there is heat transfer with the external environment (boundary condition 1) and an external temperature was defined according to the applied thermal condition (boundary condition 6).

For the interfaces between the electrodes and the separator, as well as between the electrodes and the current collectors/external medium, the boundary conditions 2, 3, 4, 5 were defined. These boundary conditions define the value of the ionic conductivity/diffusion, concentration of lithium ions and electric conductivity for both sides of the interface border.

Finally, the boundary condition 7 defines the values of the ionic diffusion and concentration of the lithium salt along the radius of the spherical particles of active material.

Table 8.3 - Summary of the boundary conditions implemented in the conventional geometry. The nomenclature is indicated in the List of Symbols and Abbreviations.

Boundaries	Boundary Condition	Model
Boundary 1	No ion flux occurs.	**Electrochemical model** (Newman, Doyle, Fuller)
Boundary 2	$D_{ef,a}\left.\frac{\partial c_{L,a}}{\partial x}\right\|_{x=2^-}=0$ $k_{ef,a}\left.\frac{\partial \phi_{L,a}}{\partial x}\right\|_{x=2^-}=0$	
Boundary 3	$D_{ef,a}\left.\frac{\partial c_{L,a}}{\partial x}\right\|_{x=3^-}=D_{ef,s}\left.\frac{\partial c_{L,s}}{\partial x}\right\|_{x=3^+}$ $c_{L,a}\|_{x=3^-}=c_{L,s}\|_{x=3^+}$ $\sigma_{ef,a}\left.\frac{\partial \phi_{E,a}}{\partial x}\right\|_{x=3^+}=0$	
Boundary 4	$D_{ef,s}\left.\frac{\partial c_{L,s}}{\partial x}\right\|_{x=4^-}=D_{ef,c}\left.\frac{\partial c_{L,c}}{\partial x}\right\|_{x=4^+}$ $c_{L,s}\|_{x=4^-}=c_{L,c}\|_{x=4^+}$ $\sigma_{ef,a}\left.\frac{\partial \phi_{E,c}}{\partial x}\right\|_{x=4^-}=0$	
Boundary 5	$D_{ef,c}\left.\frac{\partial c_{L,c}}{\partial x}\right\|_{x=5^+}=0$ $\sigma_{ef,c}\left.\frac{\partial \phi_{E,c}}{\partial x}\right\|_{x=5^+}=i_{app}$ $k_{ef,c}\left.\frac{\partial \phi_{L,c}}{\partial x}\right\|_{x=5^+}=0$	
Boundary 7	$At\ r=0: D_{Li,i}\frac{\partial c_{E,i}}{\partial r}=0$ $At\ r=r_i: -D_{Li,i}\frac{\partial c_{E,i}}{\partial r}=J_i$ $i=a,c$	
Boundary 1	$\lambda_i \nabla T\|_{x=1}=0, i=a,s,c$	**Thermal Model** (Adiabatic condition)
Boundary 6	T_∞, the external temperature is not applicable.	

Boundary 1	$\lambda_i \nabla T\big\|_{x=1} = h(T_\infty - T)$	**Thermal Model** (cold, regular and hot temperatures)
Boundary 6	T_∞ , the external temperature according to the thermal conditions applied.	

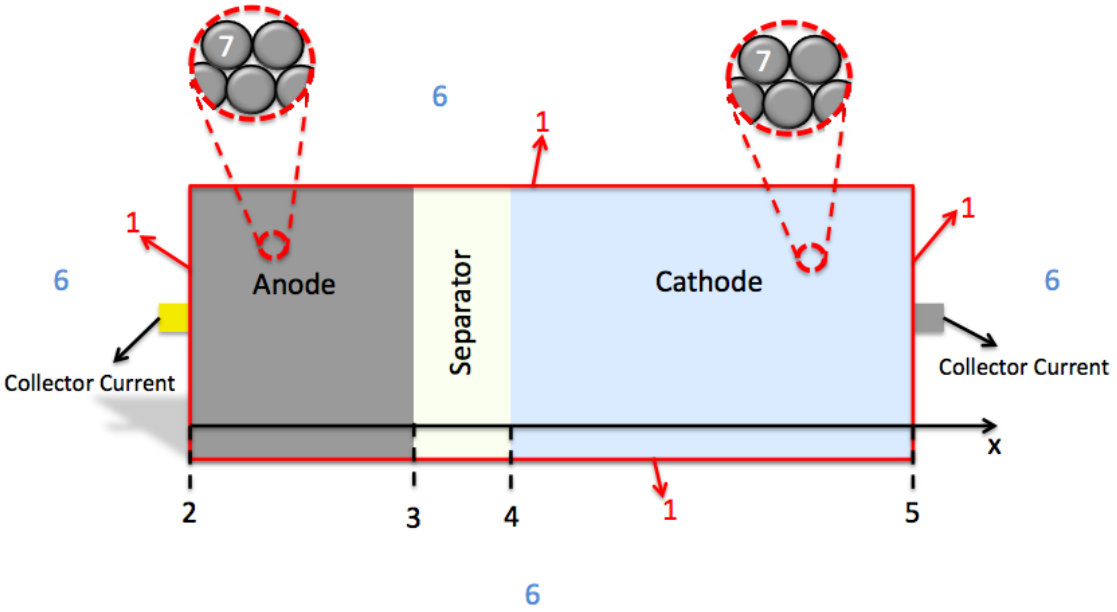

Figure 8.1 - Schematic representation of the boundary conditions applied in the conventional geometry.

8.4 Results and discussion

Theoretical model simulations were thus applied in all different lithium-ion battery geometries in different thermal conditions: isothermal, adiabatic and environmental conditions (cold, regular and hot temperatures) keeping constant the area of the components.

The theoretical model was first validated with the experimental results obtained for the developed full cell.

The main objective is to evaluate how the performance of the batteries with different geometries are affected by the thermal conditions.

8.4.1 $LiC_6/LiFePO_4$ full-cell: Validation of the theoretical model

The simulation model was validated by comparing the theoretical and experimental results obtained for the $LiC_6/LiFePO_4$ full-cell with conventional geometry (figure 8.2). Figure 8.2 shows experimental and simulation curves for the full-cell at 298 K and at scan rate of C/10 (0.51 $A.m^{-2}$).

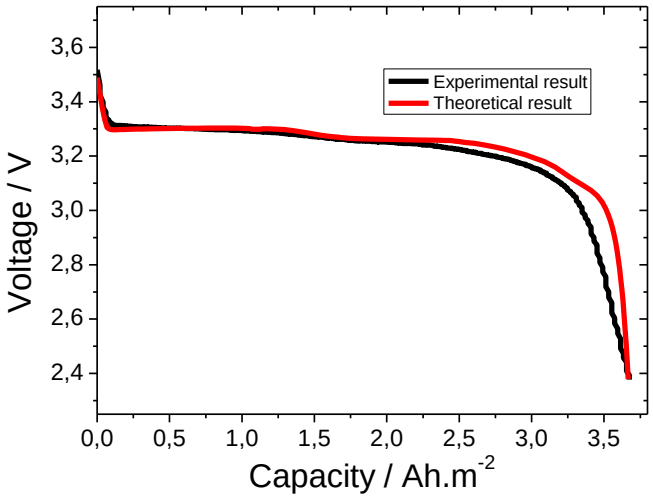

Figure 8.2 - Voltage as a function of the delivered capacity at C/10 rate for the $LiC_6/LiFePO_4$ full-cell with a conventional geometry.

Figure 8.2 shows a good agreement between experimental and theoretical results. There is a slight deviations of the capacity of the real full-cell relative to the theoretical

model below 3.2 V, attributed to corresponding differences in the electronic conductivity values and also to the exact temperature value during the discharge process [31].

However, the good theoretical approximation allows the validation of the theoretical model.

8.4.2 Battery performance of the various battery geometries at different thermal conditions

Theoretical model simulations with thermal conditions were carried out for all geometries at different thermal conditions (isothermal, adiabatic and environmental (cold, regular and hot temperatures) varying scan rate between 1C to 500C.

8.4.2.1 Isothermal condition

Firstly, all geometries were tested at scan rates between lC to 500C for a constant temperature of 298 K, i.e, without applying the thermal equations.

A similar study has been already presented for all these geometries with lithium manganese oxide ($LiMn_2O_4$, LMO) as active material [19], which leads to differences based on the specific electric and ionic conductivity values and lithium diffusion coefficients, among others, of the active materials [33].

Thus, the present investigations also allow to evaluate the influence of active material on battery performance.

Figure 8.3 shows the discharge capacity value as a function of the scan rate for all geometries under isothermal condition.

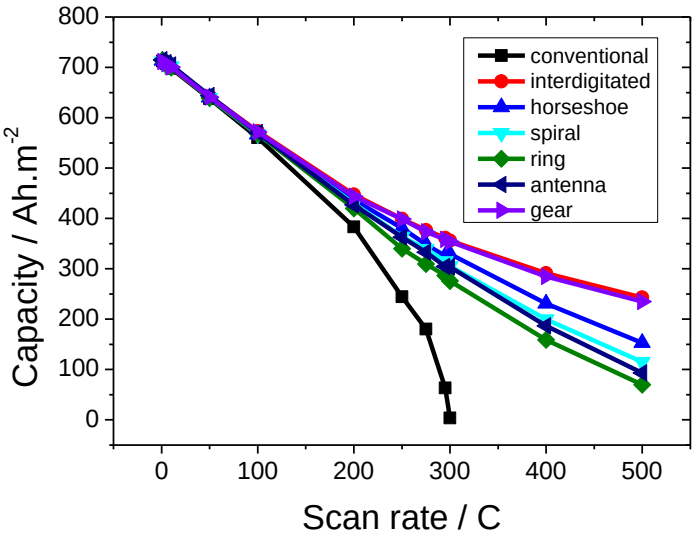

Figure 8.3 - Delivered capacity as a function of scan rate for all geometries under isothermal condition.

For low scan rates, no significant differences arise and all geometries show high capacity. At medium and high scan rates, the discharge capacity of the geometries follow this order: interdigitated, gear, horseshoe, spiral, antenna, ring and conventional.

It can be observed that the conventional geometry operates just up to 300C and for this scan rate, its discharge capacity value is 3.61 $Ah.m^{-2}$. It is also observed that all other geometries may operate at higher rates up to 500C.

The interdigitated geometry shows the best performance for all scan rates. At 300C, its capacity is 356 $Ah.m^{-2}$, which is 98 times higher than the one for the conventional geometry.

The gear geometry closely follows the interdigitated one and at 300C, the capacity value is 354 $Ah.m^{-2}$.

The different discharge capacity values observed for the geometries is ascribed to different internal resistance values, variations of the maximum distance, and distance between current collectors in the different geometries, as well as to variations of the dimensions of the components (electrodes and separator), as shown in table 8.2.

Thus, the main reason for the conventional geometry not operating at scan rates above 300C is due to the high thickness of the electrodes and separator in comparison to the other geometries, which limits the diffusion of ions.

The interdigitated and gear geometries show lower maximum distance values (d_max) and higher contact surface area between the electrodes than any other geometry, as can be seen in table 8.2.

During the discharge process, the geometry effect is more significant for higher scan rates once it is required elevated mobility of ions and electrons.

By comparison with the literature [19], it is observed that the results with $LiFePO_4$ or $LiMn_2O_4$ as active material are similar.

8.4.2.2 Adiabatic condition

All geometries were tested under adiabatic condition with an initial temperature of 298.15 K before the discharge process for all geometries. Figure 8.4a) and 8.4b) show the discharge capacity value and the temperature for all geometries at scan rate between 1C and 500C, respectively.

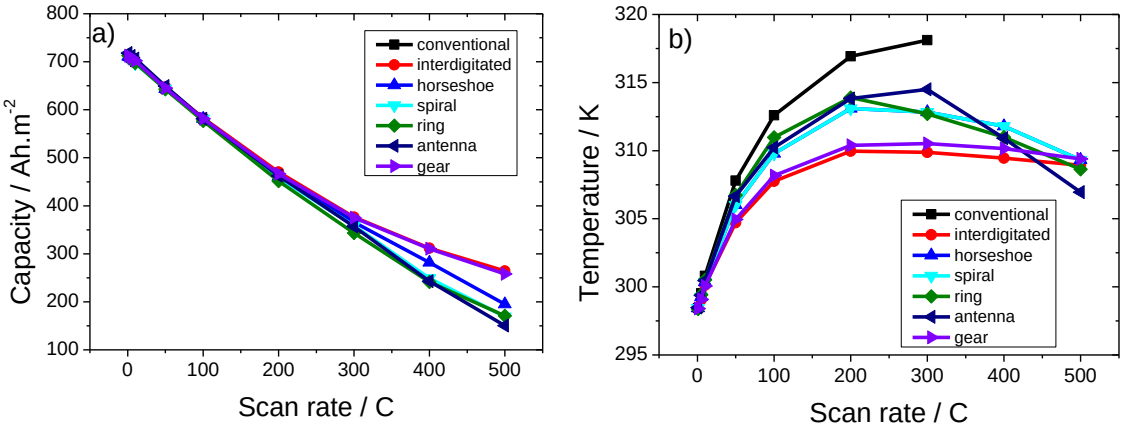

Figure 8.4 - Delivered capacity (a) and temperature (b) as a function of the scan rate for all geometries under adiabatic condition.

The discharge capacity value decreases when increasing the scan rate as it is shown in figure 8.4a). Up to 200 C, the discharge capacity value is practically the same for all geometries, being the differences observed in the discharge capacity value after 300 C for the different geometries attributed to variation in the internal resistance of the batteries due to geometrical effects, as previously indicated.

The discharge capacity value is higher under adiabatic conditions when compared to isothermal condition for the same scan rates. The reason for this effect is due that

heat produced for each geometry will be internally absorbed, leading to a temperature increase (figure 8.4b)), which in turn affects the diffusion and ionic conductivity values (Chapter 3, Table 3.1).

As previously observed, the conventional geometry only operates up to 300C and its discharge capacity value is 367.05 Ah/m^2. For this geometry, the discharge value in the adiabatic condition is higher relative to the isothermal condition (3.61 Ah/m^2), due to the increase of temperature and the corresponding effect on the diffusion and ionic conductivity values [34].

The conventional geometry has higher internal resistance due to longer distance between current collectors and larger thickness of the separator. Thus, it is observed that the higher discharge capacity caused by the increase of the temperature it is not sufficient to overcome the losses associated to the high internal resistance.

Figure 8.4b) shows that the battery temperature increases with the scan rate up to 300 C for all geometries, due to the heat produced by ohmic losses [35]. For scan rates above 300 C it is observed that the temperature decreases as the scan rate increase, as the heat produced is not totally absorbed during the discharge cycle due to the low discharge time.

Figure 8.4b) also shows that the interdigitated and gear geometries present lower temperature values relatively to the other geometries. The main reason for this behavior is due to the smaller separator thickness, lower maximum distances that ions cross until their intercalation (d_max) and higher contact surface between the electrodes.

In adiabatic conditions, the interdigitated geometry shows higher discharge capacity value for all scan rates in comparison to the other geometries, including the conventional geometry. As for the temperature value, the conventional geometry has higher value when compared to other geometries due to its higher internal resistance.

To evaluate the internal resistance of the battery, impedance measurements were carried out for the conventional and interdigitated geometries at 298.15 K.

Figure 8.5 shows the Nyquist plot for both geometries in the adiabatic condition at frequencies between 1 MHz to 0.1 mHz.

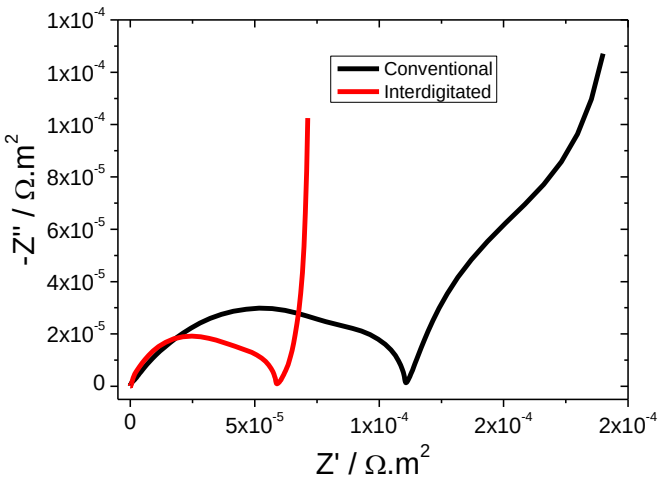

Figure 8.5 - Nyquist plot for conventional and interdigitated geometries under adiabatic condition.

The Nyquist plots are composed of semicircles (overall resistance) at higher and medium frequency and a straight line at lower frequencies [36] as it is illustrated in figure 8.5. Figure 8.5 shows that the conventional geometry shows higher internal overall resistance when compared to the interdigitated geometry. The internal overall resistance is $1.10 \times 10^{-4}\ \Omega.m^2$ and $5.94 \times 10^{-5}\ \Omega.m^2$ for conventional and interdigitated geometries, respectively.

Thus, considering the thermal model, the battery performance is a balance between the higher discharge capacity value caused by the increase of the temperature and the losses related to the internal overall resistance.

8.4.2.3 Environmental conditions

All geometries were subjected to three thermal external conditions considering initial thermal equilibrium with the environmental, whose temperature is cold, 265.15 K, figures 8.6a) and 8.6b); regular, 298.15 K, figures 8.6c) and 8.6d); and hot, 316.15 K, figures 8.6e) and 8.6f).

For each case, the heat produced during the discharge process is exchanged with the exterior and for each geometry, the discharge capacity, the total heat (irreversible, reversible and ohmic heat) and internal temperature were evaluated as a function of the scan rate.

Figures 8.6a) and 8.6b) show the discharge capacity value and temperature as a function of the scan rate between C at 250 C, respectively, for cold condition and all geometries.

None of the batteries can operate at scan rates above 250 C, as the low temperature (265.15 K) severely limits the diffusion and the ionic conductivity of the electrolyte solution [17]. The battery performance for all geometries is identical to the one observed for isothermal and adiabatic condition but with lower discharge capacity values. The conventional geometry only operates up to a scan rate of 17 C, for which the discharge capacity value is 454 Ah.m^{-2}.

At 250 C the discharge capacity values are 234 Ah.m^{-2}, 194 Ah.m^{-2}, 158 Ah.m^{-2}, 212 Ah.m^{-2}, 280 Ah.m^{-2} and 319 Ah.m^{-2} for horseshoe, spiral, antenna, ring, interdigitated and gear geometries, respectively. The interdigitated geometry shows the best performance under isothermal and adiabatic condition but for cold conditions the values for both geometries are very close. However, the gear geometry shows slightly better performance than the interdigitated geometry as the gear geometry has smaller distance between current collectors and lower distances for ions to move until their intercalation.

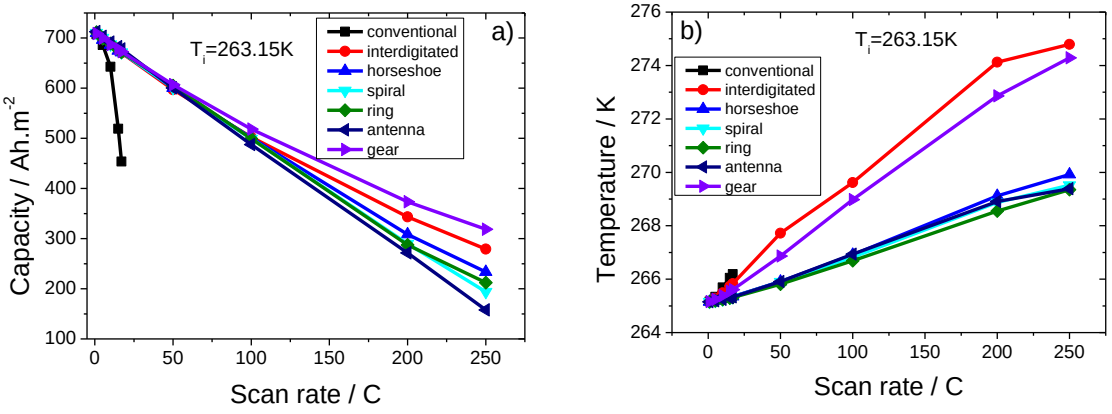

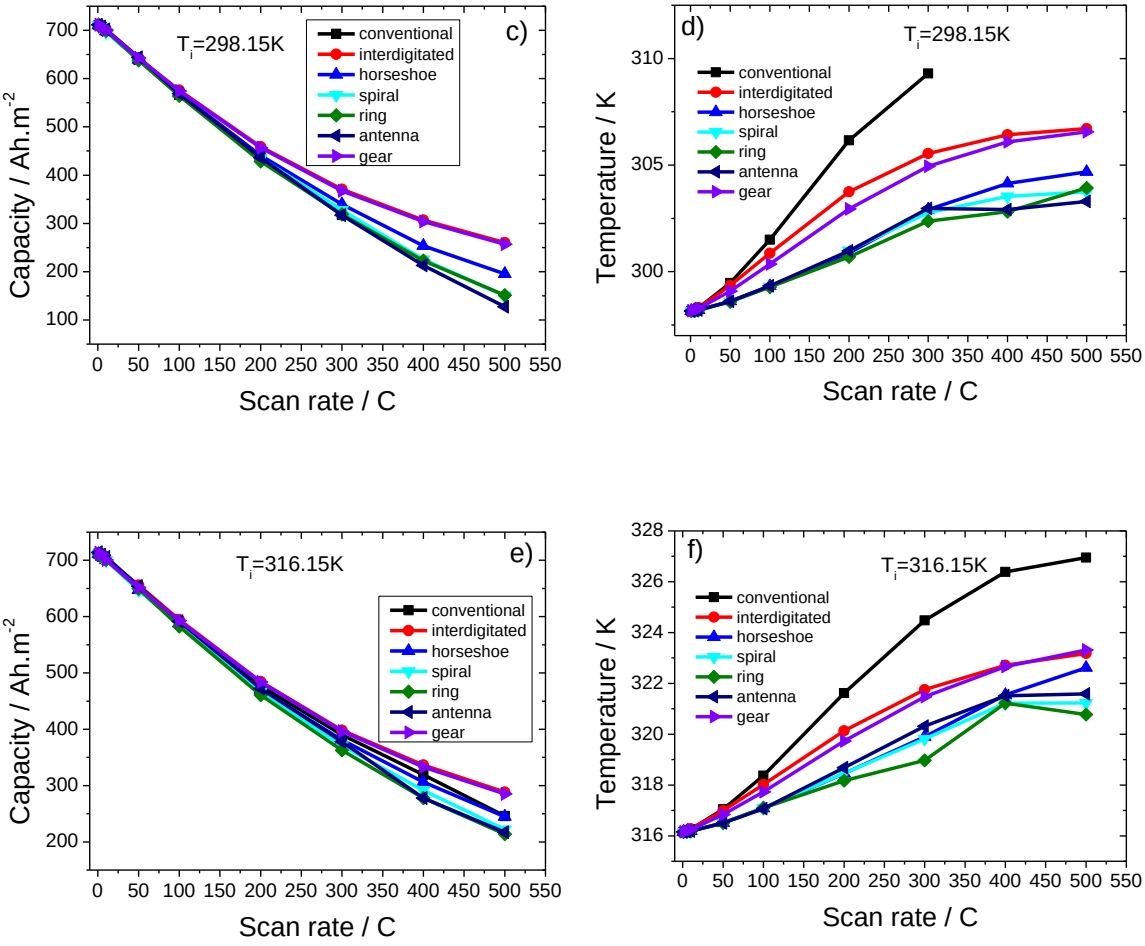

Figure 8.6 - Delivered capacity (left) and final temperature (right) as a function of the scan rate for all geometries under cold (a and b), regular (c and d) and hot (e and f) conditions.

In relation to the temperature (figure 8.6b)), the conventional geometry reaches higher temperatures in comparison to the other geometries due to its higher internal overall resistance. The higher temperature value observed for interdigitated and gear geometries is due to the lower exchange of heat with the exterior when compared to the other geometries resulting in higher discharge capacity values. The contact area between the battery and the exterior for the interdigitated and gear geometries is lower, affecting therefore the heat transfer process.

Figures 8.6c) and 8.6d) show the discharge capacity and temperature values, respectively for all geometries as a function of the scan rate (C to 500 C) for regular environmental condition (298.15K).

For this thermal condition, the conventional geometry can operate up to 300 C and all other geometries up to 500 C. At 300 C, the conventional geometry has the lowest discharge capacity value (318 $Ah.m^{-2}$) and interdigitated geometry has the highest discharge capacity value (371 $Ah.m^{-2}$) in comparison to the other geometries.

As it was observed under adiabatic condition, the increases of the diffusion and conductivity value due to the increase of temperature value leads to an increase in battery discharge capacity. It is to notice that the horseshoe, spiral, antenna and ring geometry does not reflect the increase in battery performance once these geometries have elevated distances for ions and electrons to move during the discharge process.

Figure 8.6c) shows that the conventional geometry presents highest temperature value once it absorbs the heat produced due its internal overall resistance value. For this thermal condition, it is also observed that interdigitated and gear geometries have higher temperature value in comparison to the horseshoe, spiral, antenna and ring geometries for the same reason that was observed for the cold condition.

Figures 8.6e) and 8.6f) show the discharge capacity and temperature values, respectively, for all geometries as a function of the scan rate (1C to 500 C) for hot condition (316.15 K).

For this thermal condition, differences in discharge capacity value are just observed at scan rates above 400 C for all geometries. For this temperature, the conventional geometry operates up to 500 C. Further, the differences in the discharge capacity values are small in comparison to the isothermal, adiabatic, cold and environmental conditions for all geometries

As previously observed, the interdigitated and gear geometries show the best discharge values in comparison to the other geometries. Relatively to the temperature behavior (figure 8.6f)), the conventional geometry has the higher temperature value for all scan rates due to the higher separator thickness. The temperature behavior for the other geometries (figure 8.6f)) is the same as observed for adiabatic and environmental conditions.

It is important refer that the conventional geometry reach temperature above 323 K for scan rates above 300 C where the organic solvent of the electrolyte solution can start to evaporate [37].

8.4.3 Total heat at low and high discharge rates

The total dissipated heat for the different geometries was evaluated with the objective to relate the increases of the temperature with the total heat produced by the battery.

The generated heat in the battery comes from three sources: reaction, reversible and ohmic. The total heat of the different components (anode, separator and cathode) was determined for all geometries under adiabatic conditions at low scan rate (1C) and high scan rate (300C) once the conventional geometry only operates up to this scan rate.

Figure 8.7a), 8.7b) and 8.7c) show the total heat in the anode, separator and cathode, respectively, for all geometries at 1C as a function of time.

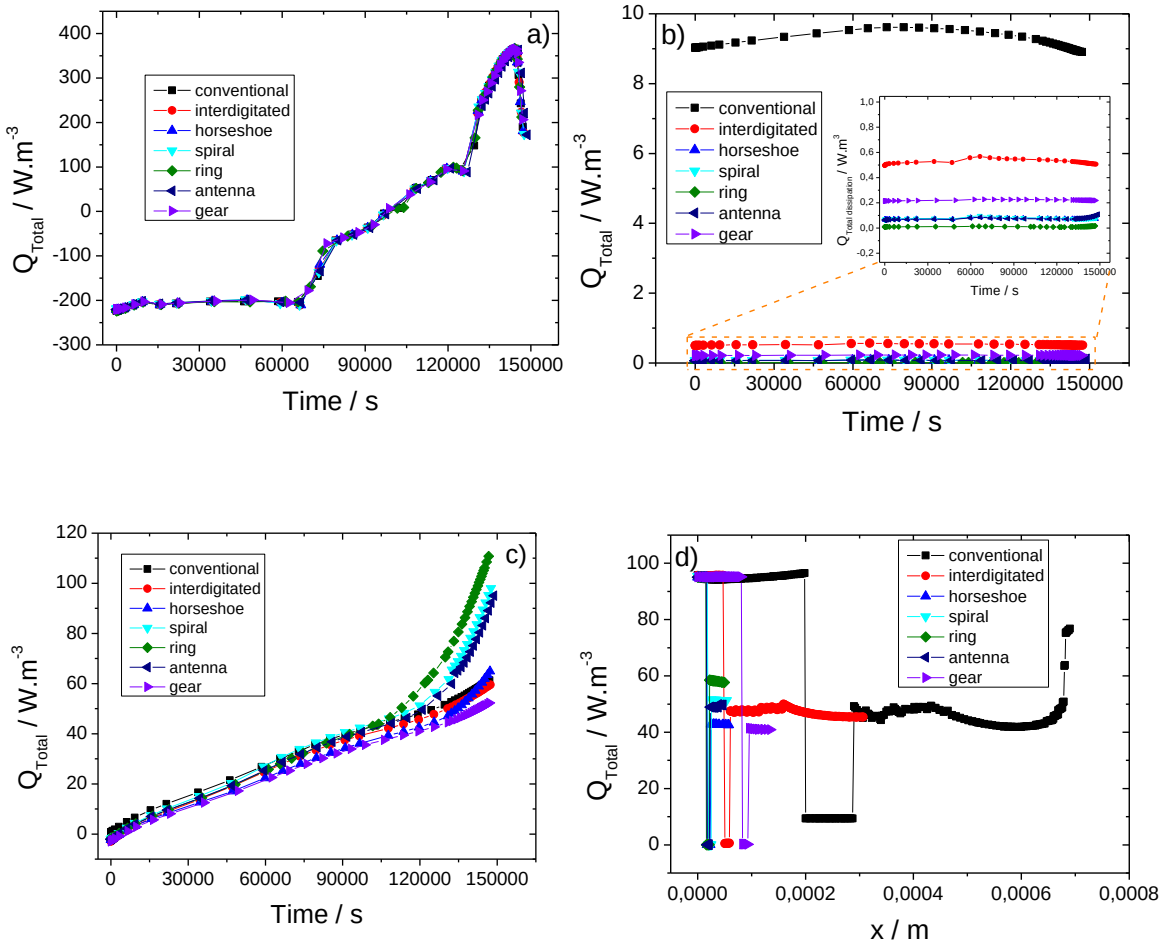

Figure 8.7 - Total heat in the anode (a), separator (b) and cathode (c) for all geometries at 1C as a function of the time. d) Total heat along the battery for all geometries at 1C after 120 000s.

The total discharge time for all geometries at 1C is around 150 000s. Figure 8.7d) shows the total heat for all geometries at different places between current collectors at time of 120 000s

Figure 8.7a) and 8.7c) show that the total heat produced by the electrodes (anode and cathode, respectively) is the same at all instants of time along the discharge cycle.
For all geometries, the total dissipated heat for anode changes between -220 W/m^3 to 370 W/m^3 and for cathode varies between 0 W/m^3 to 110 W/m^3, as a function of time.

All geometries produce the same amount of heat in each electrode, being therefore identical the effect of losses associated with the internal resistance caused by the diffusion and conductivity of the ions and the electrical conduction.
The heat produced is the same in all geometries as at low discharge rates, a low ionic mobility is required and the internal resistance has not significant effects in the produced heat.

For the separator, figure 8.7b) shows that the total dissipated heat for conventional geometry is higher in comparison to the other geometries. Thus, for the conventional geometry the varies from 8.8 W/m^3 to 9.5 W/m^3 as a function of time and for other geometries varies between 0.01 W/m^3 to 0.56 W/m^3.

This fact is due to the higher separator thickness for the conventional geometry in comparison to the other geometries that affects the mobility of the ions and in turn the produced heat.

Figure 8.7d) shows the total heat at a time of 120 000 s in different points between current collectors for all geometries, where the heat is produced according the results of the figure 8.7a) to 8.7c).

As represented in figure 8.7d) at 1C, the total heat of the electrodes is very close for all geometries, the difference being verified for the separator due to their thicknesses.

Further, the evolution of the temperature of the battery as a function of time for all geometries is shown in figure 8.8 at 1C.

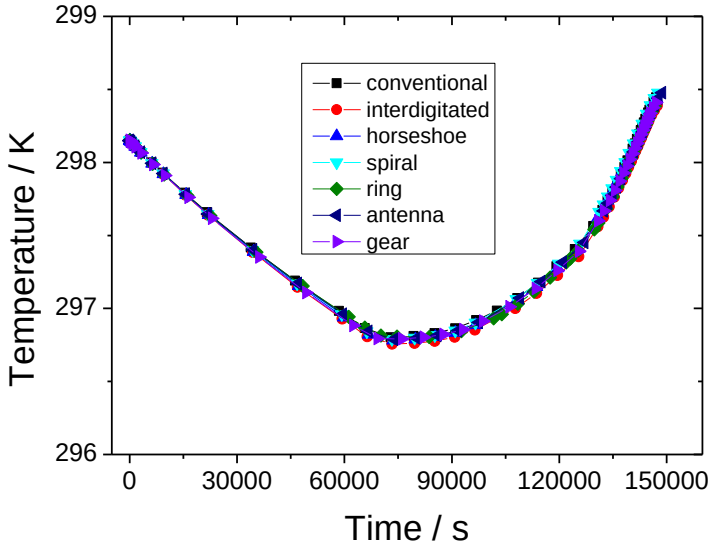

Figure 8.8 - Temperature of the battery as a function of time for all geometries at 1C.

Figure 8.8 shows that the temperature of the batteries along to the discharge time is independent of the geometry.

Figures 8.9a) 8.9b) and 8.9c) show the total dissipated heat as a function of time in the anode, separator and cathode, respectively, for all geometries at 300 C. This condition is selected at the higher scan rate will be produce a larger effect of the internal resistance during to the discharge process.

Figure 8.9a) shows that the geometries that produce a lower amount of heat in the anode are the gear and the interdigitated geometries.

In contrast, the conventional, ring, spiral and antenna geometries produce larger amounts of heat along to the discharge time.

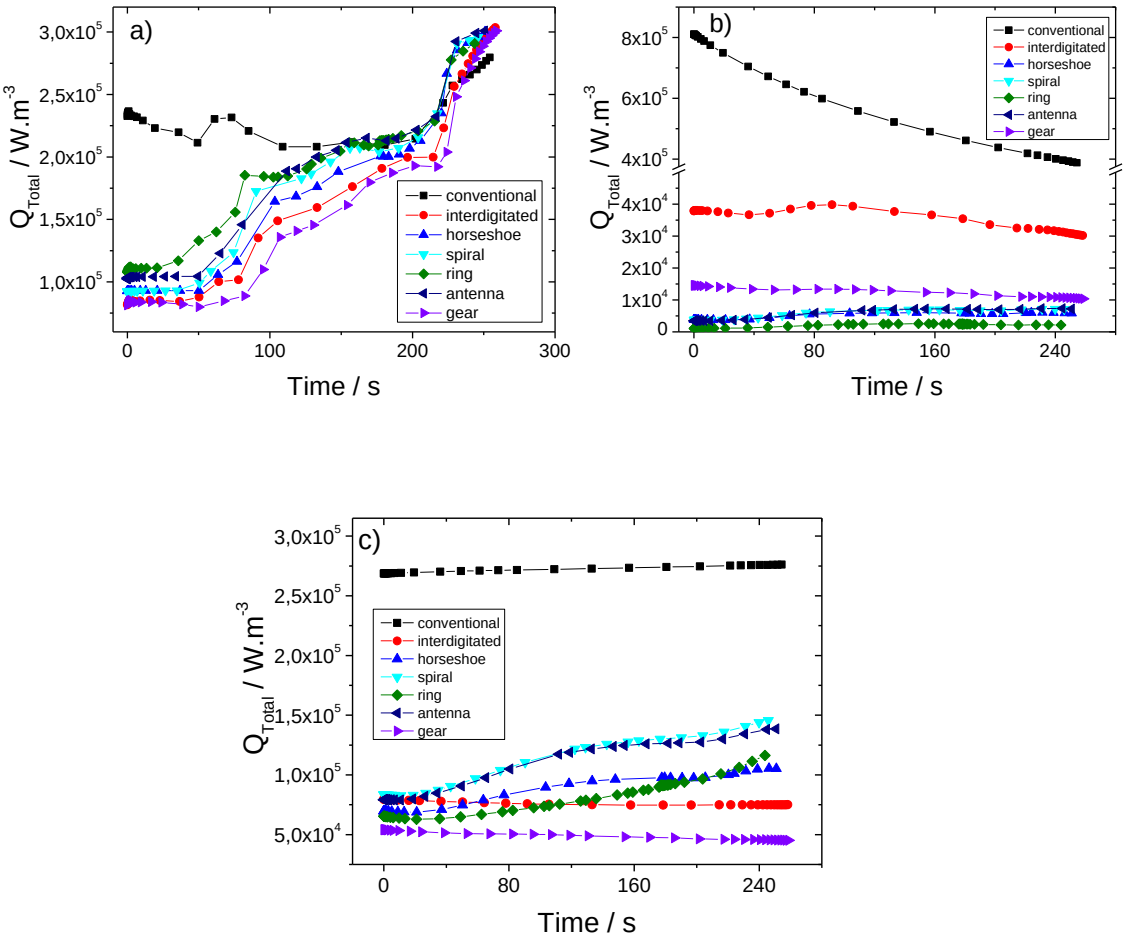

Figure 8.9 - Total heat for anode (a), separator (b) and cathode (c) for all geometries at 300C as a function of time.

It is to notice that, the antenna, ring and spiral geometries show small distance between current collectors and also small separator thickness as well as longer distances for the ions to move (d_max) that implies higher dissipated heat due to ohmic losses. It is interesting to notice that close to the end of the discharge time, the ring, antenna, spiral and horseshoe geometries approach to the conventional geometry behavior since the total dissipated heat for these geometries increases over time due to the contribution of the ions located in places more distant from the collectors.

Identical behavior is observed for the cathode (figure 8.9c)), where the conventional geometry shows higher total dissipated heat (270 kW/m^3) in comparison to the other geometries and the geometry with the lower total dissipated heat is the gear geometry (50 kW/m^3).

Relatively to the separator (figure 8.9b)), the conventional geometry also shows higher total dissipated heat in comparison to the other geometries, with values between 388 kW/m^3 and 810 kW/m^3. The interdigitated and gear geometries show intermediate values of 39 kW/m^3 and 14 kW/m^3, whereas the dissipate heat is between 1071W/m^3 to 7200W/m^3 for the other geometries. In this case, the conventional geometry shows higher total dissipated heat due to the higher separator thickness in comparison to the other geometries (Table 8.2) and the interdigitated and gear geometries show intermediate values due to the separator thickness and distance between current collectors.

Figures 8.10a) and 8.10b) show the total heat in different positions on the battery between the current collectors for all geometries after 50 s at 300C.

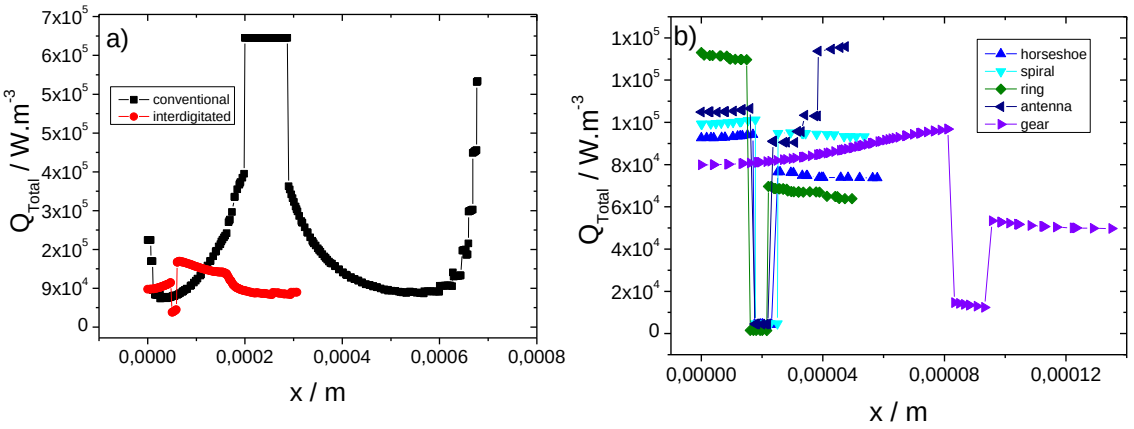

Figure 8.10 - Total heat along the battery after 50 s at 300C for conventional and interdigitated geometries (a) and for the remaining geometries (b).

Figure 8.10a) shows that batteries with conventional geometry generate higher heat due to the thickness of the separator. Figure 8.10 also shows that the interdigitated and gear geometries generate lower heat values in all positions between the current collectors due to the lower thickness of separator.

The geometries that produced lower total dissipated heat are the interdigitated and gear geometries associated to internal resistance related to the thickness of the separator, distance between current collectors and smaller distance of ions until intercalation.

Figure 8.11 shows the evolution of the temperature of the battery as a function of time with the different geometries at 300C.

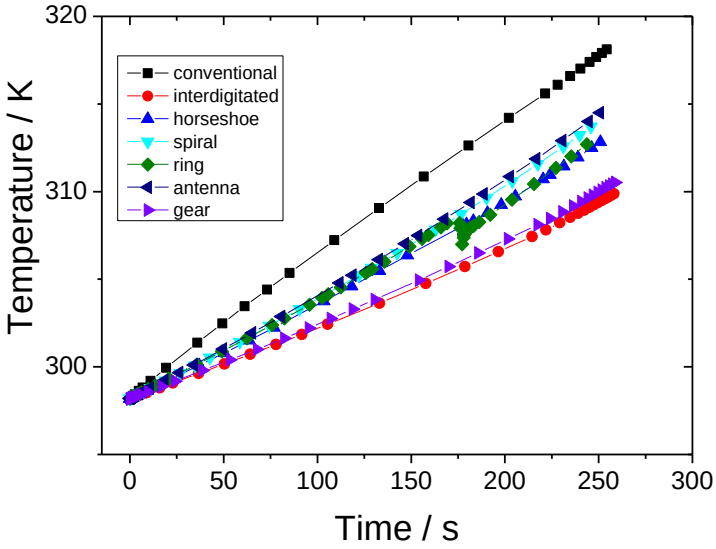

Figure 8.11 - Temperature as a function of time for all geometries at 300C.

Figure 8.11 shows that the temperature of the different batteries increases linearly in time. The conventional geometry temperature increases from 298.15 K to 318.10 K, whereas for the interdigitated and gear geometries the increase is the lowest reaching a maximum of 310 K after 260 s discharge time.

8.4.4 Ohmic heat for ring geometry with different radius

For understanding the contribution of the mobility of the ions and the corresponding resistance for the production of heat and its influence into battery performance, this section analyzes the ohmic heat produced in a ring geometry for different radius at 500C and under adiabatic conditions. The selected radius are 93.9 μm, 230 μm, 330 μm and 430 μm (Figure 8.12)), the ohmic heat being associated to the Joule effect caused by the ohmic losses due to the different paths the charges have to move to the current collectors (d_max) and also to differences in the thickness of the separator. The variation of the radius is carried out while maintaining constant the area of all components of battery (electrodes, separator and current collectors).

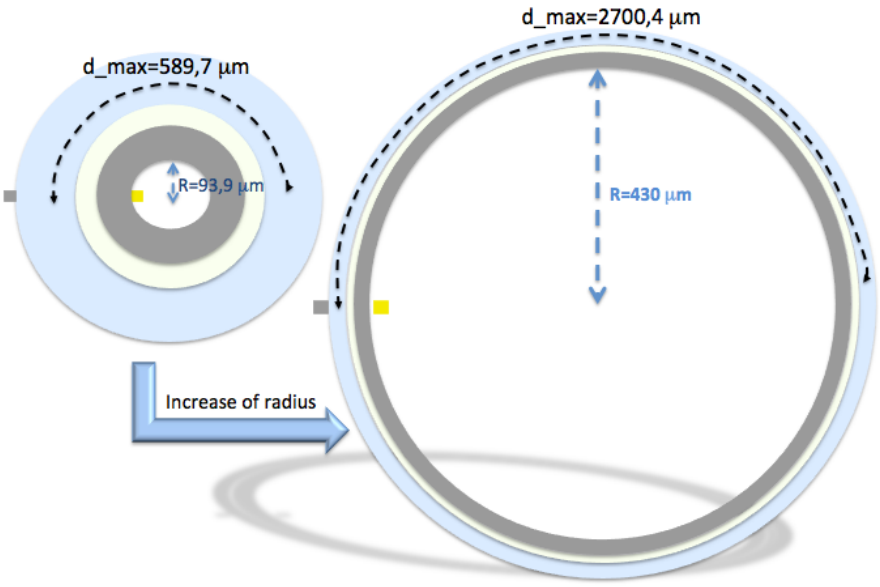

Figure 8.12 - Schematic representation of the ring geometry for the radius of 93.9 µm and 430 µm.

Simulations show (Figure 8.13 a)) that the capacity of the battery decreases with increasing the radius of the ring. The ring geometry with bigger radius has smaller thickness for electrodes and separator, lower distance between the current collector, and higher maximum distance for the ions (d_max) that implies lower battery performance due to the higher internal resistance.

It is observed in figure 8.13b) that the temperature of the battery increases over time for all radii, being the increase larger for the larger radius.

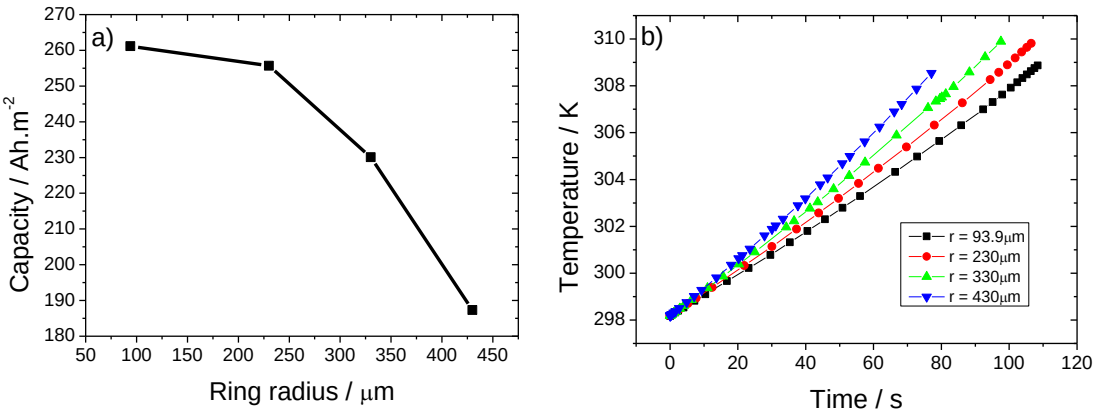

Figure 8.13 - a) Capacity as a function of ring radius and b) temperature as a function of time for all ring radius at 500 C.

The heat for each component (electrodes and separator) as a function of time for the batteries with the different radius is shown in figure 8.14.

Figure 8.14 a) and 8.14c) show that for both electrodes (anode and cathode) the generated heat increase with increasing radius.

As previously indicated, higher ohmic losses are observed for the geometry with the larger radius due to the increase of the path the charges have to move during the discharge process.

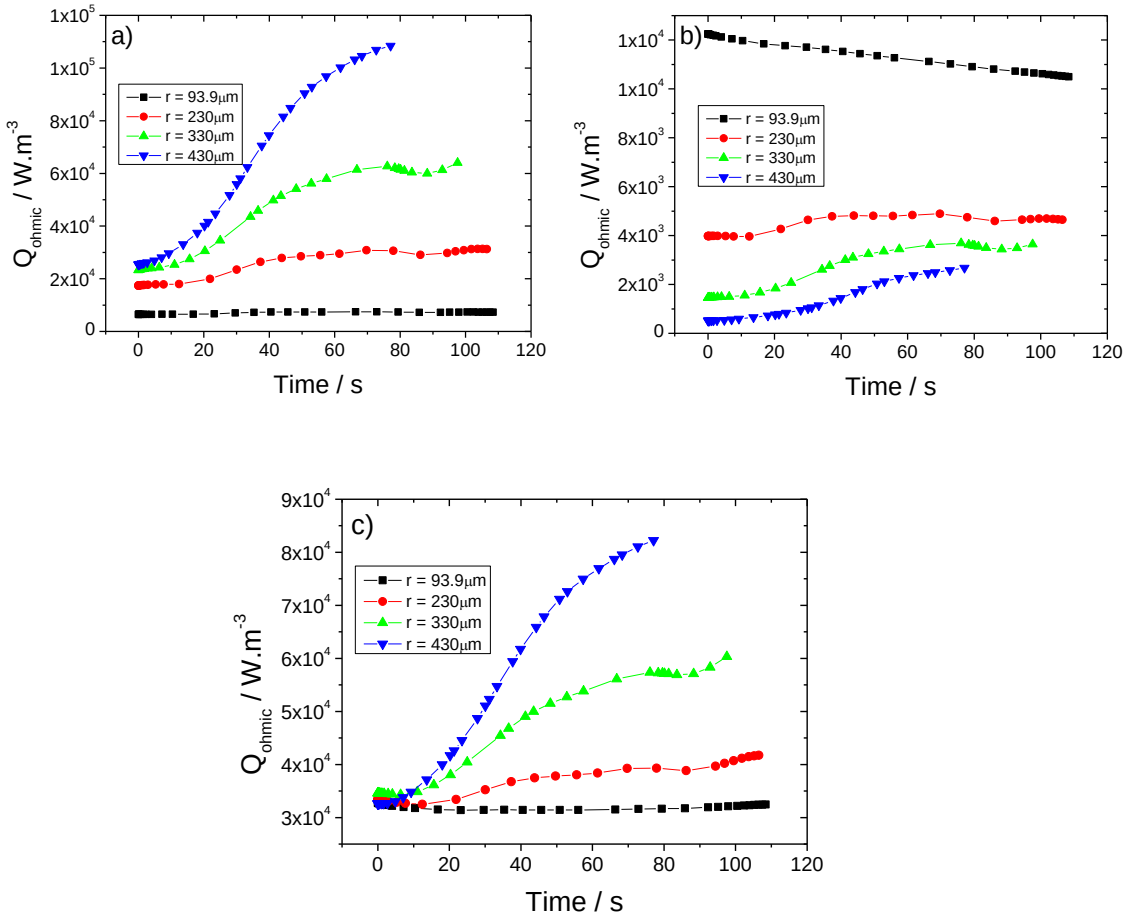

Figure 8.14 - Ohmic heat for anode (a), separator (b) and cathode (c) as a function of the time at 500 C for various ring radius.

Figure 8.14b) shows the ohmic heat at the separator for the ring geometries with different radius. Contrary to the observations for the electrodes (figure 8.14a) and 8.14c)), the higher ohmic heat is observed for the battery with the smaller radius. In this case, the ring geometry with smaller radius produce higher ohmic heat due to the higher separator thickness, that will affect the diffusion and conduction behavior of the ions and consequently to increase by the Joule effect that translate in higher ohmic heat.

Figure 8.15 shows the ohmic heat fin the battery along different positions between the current collectors for the ring geometry with different radius at 70 s and 500 C.

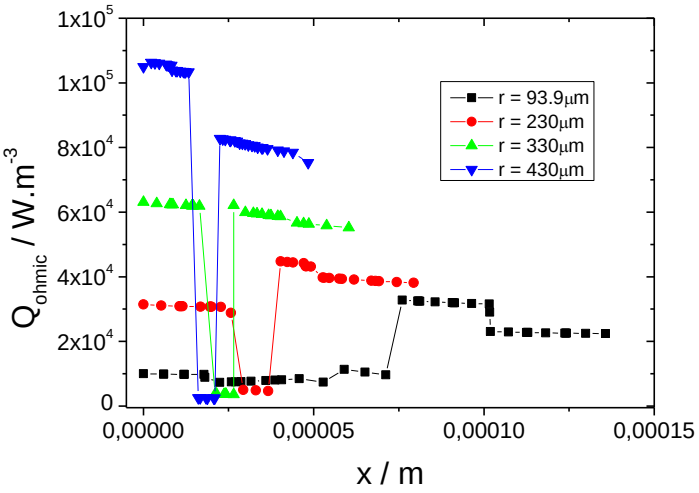

Figure 8.15 - Ohmic heat along different places between the current collectors of the battery after 70 s at 500C for ring geometry with different radius.

Considering figure 8.15, it is observed higher ohmic heat for the electrodes of the ring geometry with higher radius due to the larger distance the ions have to move until intercalation.

In relation to the separator, the higher ohmic heat is observed for the smaller radius due to higher separator thickness.

Figure 8.16 shows the impedance curves for the ring geometry with different radius in order to determine the internal resistance value.

Independently of the radius of the ring geometry, the Nyquist plot is characterized by two semicircles at high frequencies identified in the figure 8.16 where the overall resistance that is the sum of the two semicircles that represent the ohmic resistance, which is related to the contact film resistance and resistance contributions from the charge-transfer reaction resistance in the high and medium frequency range. At low-frequency range, the inclined line corresponds to the Warburg impedance, associated to the lithium-ion diffusion in the bulk of the active material [38]. The diameter of the semicircles corresponds to the total impedance and its value is 5×10^{-5} Ω.m^2, 6×10^{-5} Ω.m^2, 8×10^{-5} Ω.m^2 and 9×10^{-5} Ω.m^2 for 93.9 μm, 230 μm, 330 μm and 430 μm, respectively.

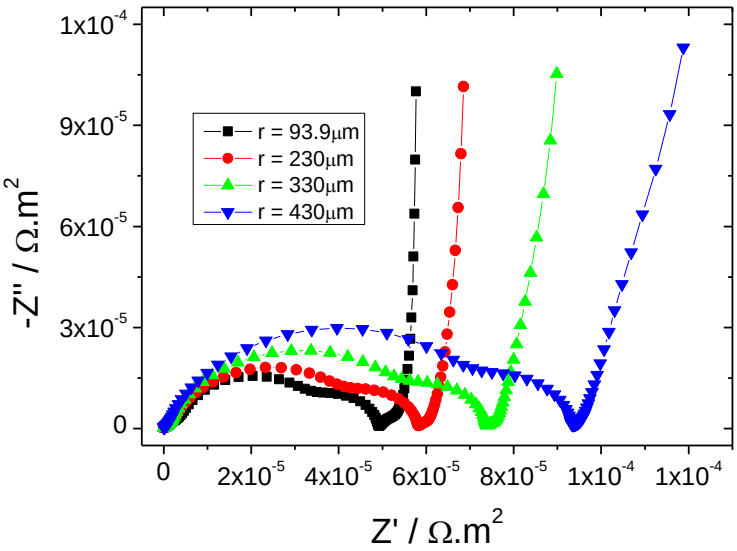

Figure 8.16 - Nyquist plot for the ring geometry with different radius at 500 C.

It is observed that the ring geometry with small radius shows the lowest resistance value due to the smaller paths that the ions placed distant from current collectors have to move.

To understand the effect of the maximum distance of ions until the intercalation process, figure 8.17 shows the ionic current density vectors for the ring geometry with small (figure 8.17a) and higher (figure 8.17b)) radius that correspond to the ionic charge at the time of 70 s at 500C. This magnitude is represented as a vector on the 2D graphics shown in figure 8.17, indicating the direction of the ions.

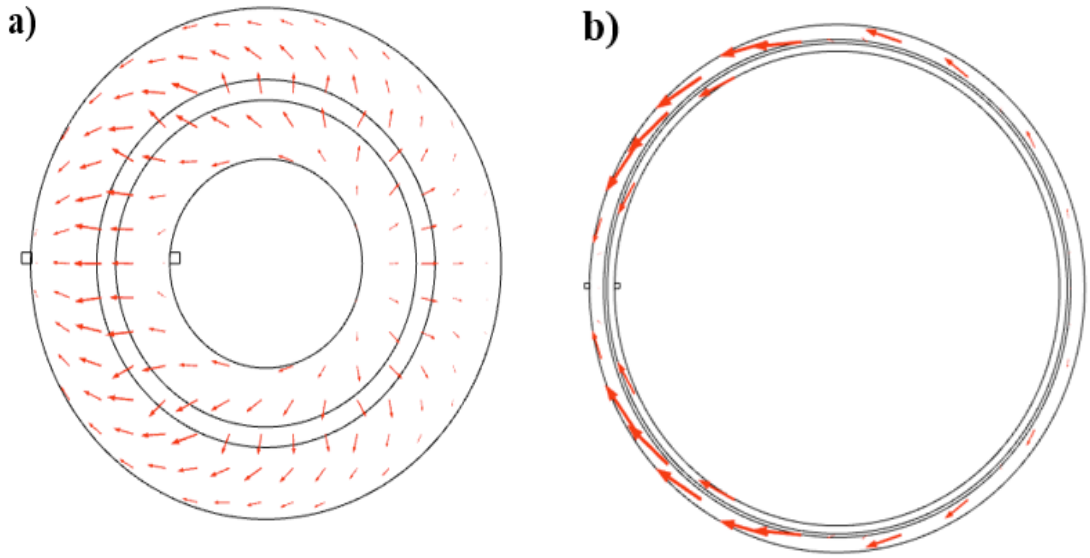

Figure 8.17 - Ionic current density vectors of the ring geometry for a) R= 93.9 μm and b) R=430 μm.

Figure 8.17a) shows that for the battery with the smaller radius, the most distant ions have a shorter maximum distance to travel to the current collectors. In relation of the battery with bigger radius (figure 8.17b)), it is observed a similar behavior. Figure 8.17b) also shows that for places closer to the current collectors, the ionic current density is more intense, the ring geometry with higher radius dissipating more ohmic heat.

It is concluded that battery performance for each geometry can be optimized considering the geometrical parameters that will be influence the thermal behavior.

8.5 Conclusions

Thermal conditions are a critical issue in lithium-ion batteries as they influence the battery performance and safety. For maximizing the battery performance, it is essential to carry out the geometry optimization considering the thermal modelling. This work shows the effect of the thermal conditions for different geometries: conventional, interdigitated, horseshoe, spiral, ring, antenna and gear geometries. The simulations were based on the Newman/Doyle/Fuller model with addition of isothermal, adiabatic, cold, ambient and hot conditions.

Under isothermal and adiabatic conditions, the best geometries are interdigitated and gear geometries due to higher battery performance and low temperature values relatively to the other geometries and the main reason for this behavior is the smaller separator thickness, lower distances for the ions to move (d_max) and higher contact surface area of the electrodes. For cold condition (265.15 K), the best battery performance is obtained for the gear geometry and for other conditions (ambient and hot), the best results are obtained for the gear and interdigitated geometries.

The generated heat is due to the internal resistance related to the maximum distances that ions move until its intercalation (d_max) and also to the thickness of the separator.

Thus, it is shown how battery performance can be optimized for specific geometries taking into account different thermal conditions.

8.6 References

1. Dunn, B., H. Kamath, and J.-M. Tarascon, *Electrical Energy Storage for the Grid: A Battery of Choices.* Science, 2011. **334**(6058): p. 928-935.
2. Lin, X., et al., *High temperature electrical energy storage: advances, challenges, and frontiers.* Chemical Society Reviews, 2016. **45**(21): p. 5848-5887.
3. Turner, J.A., *A Realizable Renewable Energy Future.* Science, 1999. **285**(5428): p. 687-689.
4. Varun, I.K. Bhat, and R. Prakash, *LCA of renewable energy for electricity generation systems—A review.* Renewable and Sustainable Energy Reviews, 2009. **13**(5): p. 1067-1073.
5. Ibrahim, H., A. Ilinca, and J. Perron, *Energy storage systems—Characteristics and comparisons.* Renewable and Sustainable Energy Reviews, 2008. **12**(5): p. 1221-1250.
6. Ozawa, K., *Lithium Ion Rechargeable Batteries: Materials, Technology, and New Applications*2012: Wiley.
7. Park, J.K., *Principles and Applications of Lithium Secondary Batteries*2012: Wiley.
8. Tarascon, J.-M., *Key challenges in future Li-battery research.* Philosophical Transactions of the Royal Society A: Mathematical, Physical and Engineering Sciences, 2010. **368**(1923): p. 3227-3241.
9. Tarascon, J.M. and M. Armand, *Issues and challenges facing rechargeable lithium batteries.* Nature, 2001. **414**(6861): p. 359-367.
10. Scrosati, B. and J. Garche, *Lithium batteries: Status, prospects and future.* Journal of Power Sources, 2010. **195**(9): p. 2419-2430.
11. Khateeb, S.A., et al., *Design and simulation of a lithium-ion battery with a phase change material thermal management system for an electric scooter.* Journal of Power Sources, 2004. **128**(2): p. 292-307.
12. Buchmann, I. and C.E. Inc, *Batteries in a Portable World: A Handbook on Rechargeable Batteries for Non-engineers*2001: Cadex Electronics.
13. Balakrishnan, P.G., R. Ramesh, and T. Prem Kumar, *Safety mechanisms in lithium-ion batteries.* Journal of Power Sources, 2006. **155**(2): p. 401-414.

14. Wang, Q., et al., *Thermal runaway caused fire and explosion of lithium ion battery.* Journal of Power Sources, 2012. **208**: p. 210-224.
15. Zhao, R., et al., *A review of thermal performance improving methods of lithium ion battery: Electrode modification and thermal management system.* Journal of Power Sources, 2015. **299**: p. 557-577.
16. Zhao, R., J. Liu, and J. Gu, *The effects of electrode thickness on the electrochemical and thermal characteristics of lithium ion battery.* Applied Energy, 2015. **139**: p. 220-229.
17. Park, M., et al., *A review of conduction phenomena in Li-ion batteries.* Journal of Power Sources, 2010. **195**(24): p. 7904-7929.
18. Du, W., et al., *Effect of cycling rate, particle size and transport properties on lithium-ion cathode performance.* International Journal of Heat and Mass Transfer, 2010. **53**(17–18): p. 3552-3561.
19. Miranda, D., et al., *Computer simulations of the influence of geometry in the performance of conventional and unconventional lithium-ion batteries.* Applied Energy, 2016. **165**: p. 318-328.
20. Yeow, K., et al. *3D thermal analysis of Li-ion battery cells with various geometries and cooling conditions using Abaqus*. in *Proceedings of the SIMULIA Community Conference*. 2012.
21. Cai, L. and R.E. White, *Mathematical modeling of a lithium ion battery with thermal effects in COMSOL Inc. Multiphysics (MP) software.* Journal of Power Sources, 2011. **196**(14): p. 5985-5989.
22. Mills, A. and S. Al-Hallaj, *Simulation of passive thermal management system for lithium-ion battery packs.* Journal of Power Sources, 2005. **141**(2): p. 307-315.
23. Sabbah, R., et al., *Active (air-cooled) vs. passive (phase change material) thermal management of high power lithium-ion packs: Limitation of temperature rise and uniformity of temperature distribution.* Journal of Power Sources, 2008. **182**(2): p. 630-638.
24. Pesaran, A.A., *Battery thermal management in EV and HEVs: issues and solutions.* Battery Man, 2001. **43**(5): p. 34-49.

25. Rao, Z., et al., *Experimental investigation on thermal management of electric vehicle battery with heat pipe.* Energy Conversion and Management, 2013. **65**: p. 92-97.
26. Gören, A., et al., *High performance screen-printed electrodes prepared by a green solvent approach for lithium-ion batteries.* Journal of Power Sources, 2016. **334**: p. 65-77.
27. Srinivasan, V. and J. Newman, *Discharge Model for the Lithium Iron-Phosphate Electrode.* Journal of The Electrochemical Society, 2004. **151**(10): p. A1517-A1529.
28. Northrop, P.W.C., et al., *Efficient Simulation and Model Reformulation of Two-Dimensional Electrochemical Thermal Behavior of Lithium-Ion Batteries.* Journal of The Electrochemical Society, 2015. **162**(6): p. A940-A951.
29. Miranda, D., et al., *Computer simulation evaluation of the geometrical parameters affecting the performance of two dimensional interdigitated batteries.* Journal of Electroanalytical Chemistry, 2016. **780**: p. 1-11.
30. Gerver, R.E. and J.P. Meyers, *Three-Dimensional Modeling of Electrochemical Performance and Heat Generation of Lithium-Ion Batteries in Tabbed Planar Configurations.* Journal of The Electrochemical Society, 2011. **158**(7): p. A835-A843.
31. Bae, S., et al., *Quantitative performance analysis of graphite-LiFePO4 battery working at low temperature.* Chemical Engineering Science, 2014. **118**: p. 74-82.
32. Wang, C. and J. Hong, *Ionic/Electronic Conducting Characteristics of LiFePO4 Cathode Materials: The Determining Factors for High Rate Performance.* Electrochemical and Solid-State Letters, 2007. **10**(3): p. A65-A69.
33. Shetzline, J.A. and S.E. Creager, *Quantifying Electronic and Ionic Conductivity Contributions in Carbon/Polyelectrolyte Composite Thin Films.* Journal of The Electrochemical Society, 2014. **161**(14): p. H917-H923.
34. Prada, E., et al., *Simplified Electrochemical and Thermal Model of LiFePO4-Graphite Li-Ion Batteries for Fast Charge Applications.* Journal of The Electrochemical Society, 2012. **159**(9): p. A1508-A1519.

35. Okamoto, E., et al., *Analysis of Heat Generation of Lithium Ion Rechargeable Batteries Used in Implantable Battery Systems for Driving Undulation Pump Ventricular Assist Device.* Artificial Organs, 2007. **31**(7): p. 538-541.
36. Solchenbach, S., et al., *A Gold Micro-Reference Electrode for Impedance and Potential Measurements in Lithium Ion Batteries.* Journal of The Electrochemical Society, 2016. **163**(10): p. A2265-A2272.
37. Aurbach, D., et al., *Design of electrolyte solutions for Li and Li-ion batteries: a review.* Electrochimica Acta, 2004. **50**(2–3): p. 247-254.
38. Zhu, J.G., et al., *A new electrochemical impedance spectroscopy model of a high-power lithium-ion battery.* RSC Advances, 2014. **4**(57): p. 29988-29998.

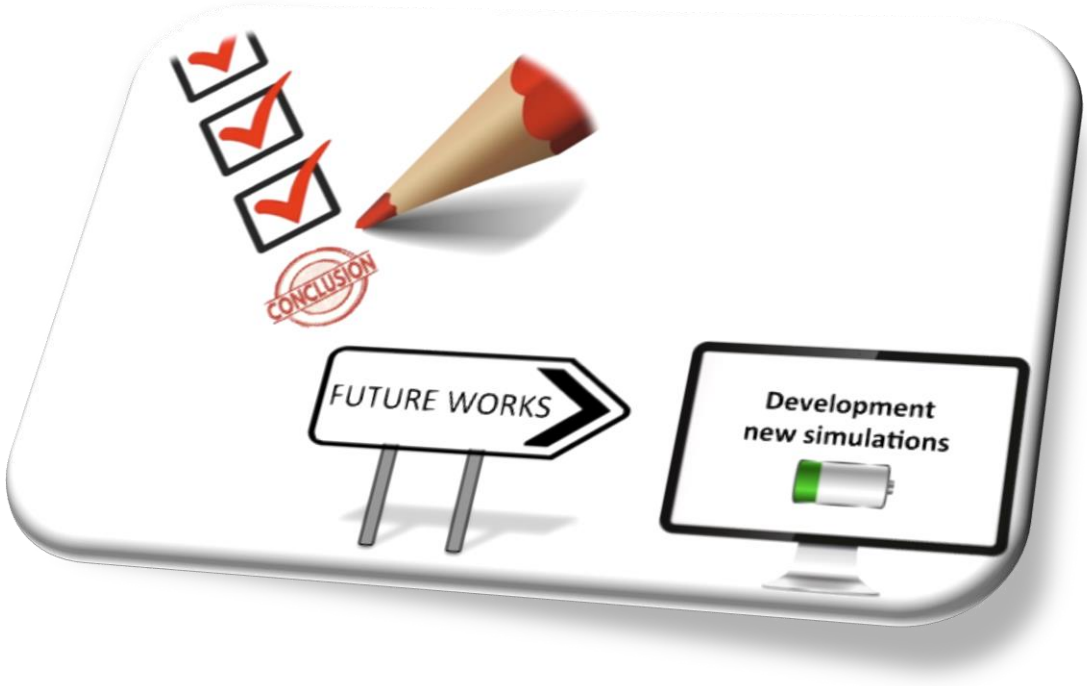

9. Conclusions and future work

This chapter presents the main conclusions of the present work, devoted to the optimization of lithium-ion battery performance through computer simulation. Further, some ideas for future works area also presented.

9.1 Conclusions

Rapid technological advances in portable electronic products (mobile-phones, computers, e-labels, e-packaging and disposable medical testers, among others) and hybrid electric vehicles (HEVs) or electric vehicles (EVs) lead to an increasing need for larger lithium ion battery autonomy with high-power and capacity.

Typically, in order to increase the performance of a battery (power and energy density), new materials for electrodes (cathode and anode) and separators are developed and new geometries are explored.

Computer simulations of battery performance are an essential tool for understanding the main parameters that affect battery behavior before fabrication. Thus, it is important to develop simulations for optimizing battery performance as these simulations allow to predict the factors that affect battery performance. In this work, the effect of the geometrical parameters of battery separator membranes (porosity, turtuosity, Bruggeman coefficient and thickness) were first simulated. Then, the optimal percentage of binder, active material and conductive additive in lithium-ion battery cathodes was evaluated. The choice of battery geometry is important for implementation into devices and therefore, the influence of the geometry of the battery in their performance was evaluated at different thermal conditions. Thus, these simulations allows to develop lithium ion battery prototypes with higher performance for different applications. It is important to refer that the simulations should be developed according to the final application of the battery as well as according to its fabrication process.

In this work it has been demonstrated that the ionic conductivity of the separator depends on the value of the Bruggeman coefficient, which is related with the degree of porosity and tortuosity of the separator membrane. The optimal value of the degree of porosity should be above 50% and the separator thickness should range between 1 μm at 32 μm for improved battery performance.

The optimization of the electrode formulation is independent of the active material type and the minimum value of *n,* defined as the percentage of binder content/percentage of conductive material, is 4 at 1C discharge rate, the minimum value of *n* depending on the discharge rate. Also, the electrical conductivity of the cathode depends on *n* and on the electrical conductivity of the conductive material, being therefore relevant the selection of the conductive material.

The influence of different battery geometries (conventional, interdigitated, horseshoe, spiral, ring, antenna and gear) was studied in order to tune battery geometry for specific applications.

Maintaining constant the area of the different components, the interdigitated geometry reach the higher delivery capacity at medium and high discharges rates. The delivered capacity depending on geometrical parameters such as the maximum distance of the ions to move to the current collector, distance between of current collectors and the thickness of the separator and electrodes.

The effect of the geometrical parameters of interdigitated batteries, including number, thickness and length of the digits, was evaluated and the delivered capacity of the battery increases with increasing the number of digits as well as with increasing thickness and length of the digits.

With respect to the different thermal conditions (isothermal, adiabatic, cold, regular and hot conditions), the gear and interdigitated geometries shows the highest delivery capacity at medium and higher discharge rates.

In conclusion, the theoretical simulation presented in this work allows to understand and optimize the components of the batteries before experimental implementation.

9.2 Future work

The theoretical simulation of lithium-ion batteries represents a strong growing research field with the objective of optimizing their performance before experimental implementation. Once conventional and interdigitated geometries are strongly implemented in the manufacture of lithium ion batteries and following the thermal study, it is important to evaluate the influence of the thermal conditions on the performance of these two geometries when different cathode active materials are used ($LiFePO_4$, $LiMn_2O_4$ and $LiCoO_2$). Thus, at different thermal conditions it can be find the most suitable active material for the cathode in both geometries (conventional and interdigitated) in order to obtain high battery performance.

Following the present work on the effect of different thermal conditions of the performance of lithium ion batteries, it will be relevant to evaluate the battery performance at different external conditions, such as pressure.

In order to further improve the theoretical models applied to lithium ion batteries, it will be necessary to develop simulation studies at different scales in order to better understand the physical, chemical and electrochemical processes and phenomena associated with the operation of the batteries. As example, the process of insertion/extraction of lithium ions and the overall battery operation and ionic diffusion/conductivity through of separator membrane can be studied from different points of view and at different physical and chemical scales: nanoscale, mesoscale, microscale and macroscale. For all models at the different physical-chemical scales, there are a number of relevant variables particularly relevant for battery performance.

It can be also explored the development of specific designs of batteries for areas such as energy harvesting.

With the scarce lithium resources and the emergence of sodium and magnesium batteries, it is important to develop theoretical models for these new batteries. Thus, it would be interesting to applied the methodologies developed in this work for sodium and magnesium ion batteries. Thus, it would be possible to understand the similarities and differences between the various types of batteries (Li-ion, Na-ion and Mg-ion) in order to be used in different application areas.